Mechanistic Study on Lithium–Oxygen Battery-Degradation Mechanism in TEGDME Solution by Mass Spectrometry

(質量分析による TEGDME 溶液中のリチウム酸素電池の劣化メカニズムに関する機構的研究)

Yanan GAO

Graduate School of Chemical Sciences and Engineering

Hokkaido University

2023

Acknowledgement

First of all, I am very grateful to my supervisor, Prof. Hidenori Noguchi. He has given me many detailed and constructive suggestions for my research and writing based on his rich experience and knowledge. His rigorous scientific attitude has deeply impressed and influenced me. Without his help, it would be difficult for me to complete my Ph.D. thesis. I am so appreciative and lucky to meet such a nice supervisor.

Second, I would like to express my deep and sincere gratitude to Professor Kohei Uosaki for his continuous support and valuable guidance during my Ph.D. study. Prof. Uosaki has provided insightful guidance to my research and also helped me analyze the experimental results and discuss research strategies. His proficiency, wisdom, and unparalleled guidance ensured the progress of my Ph.D. project, and these influences will benefit me throughout my whole life. I would also like to express my sincere appreciation to Prof. Uosaki for the great platform he has provided.

Then, I would like to thank Dr. Hitoshi Asahina, who taught me a lot about assembly of the Li-oxygen battery cell and operation of the QMS and GC/MS. I am also very grateful to Dr. Toshihiko Mandai for supplying me with isotope molecules. I want to also thank NIMS Battery Research Platform staff Ms. Hiromi Otsuka for

guidance of the cell assemble and initial material preparation for cell assembly, Ms. Yoko Kubota for arranging the use of super dry room and Mr. Kyosuke Matsushita for arranging the use of XRD equipment.

Additionally, I would like to thank Professor Yan Fang, who often communicate with me on the phone to help me relieve the stress in my life and study.

Finally, I am grateful to my parents for their continuous and selfless support of all my choices, and their hard-working quality has always inspired me in my life. I am grateful to my grandparents for their continuous support and love. Many thanks to my brother, who always sends me a lot of my favorite snacks so that I can always taste the taste of home even after being away from home for almost 4 years.

Yanan GAO

Tsukuba

May, 2023

Contents

Chapter 1: Introduction

1.1 General introduction

Over the past decades, the massive use of fossil fuels and electricity has greatly improved our standard of living. Energy, especially electricity, is at the heart of modern society. Today, more than 80% of the world's domestic and industrial electricity consumption comes from fossil fuels such as coal, petroleum, and natural gas. Human demand for available energy is expected to increase by 56% by 2040. However, the massive consumption of fossil fuels will lead to the depletion of natural resources and the production of large amounts of greenhouse gases (e.g., CO_2), leading to the ecological degradation of our environment. As a result, nuclear power and renewable fuels will increasingly be used alongside coal, petroleum, and natural gas to generate electricity. As human demand for energy continues to grow, the deployment of renewable energy sources is certainly necessary to reduce CO_2 emissions and their impact on climate change. Tremendous efforts and investments have been made to find reliable, renewable, and environmentally friendly energy sources to accommodate the development of a sustainable modern society. Clean energy sources, such as

hydroelectric power, solar cells, and wind turbines, are considered sustainable energy sources, but their production and availability vary depending on geographic location, amount of sunlight, season, and weather.

Electrochemical energy and energy storage systems will play an important role in shifting the future energy networks to clean, renewable energy sources. Which can be applied to the electric vehicles (EVs), hybrid electric vehicles (HEVs), portable electronic devices and even large energy stations. Lithium-ion batteries (LIBs) are currently the most popular type of electrochemical energy storage (**Figure 1-1(a)**) and have been commercialized by Sony since 1991. Due to their relatively high energy density, the LIBs will continue to evolve to provide much higher energy density. LIBs now are the technology of choice for electric vehicles and will play a key role for many years to come. To date, commercially available LIBs in typical electric vehicles can deliver energy densities of about 250 Wh kg^{-1}, corresponding to 170-200 Wh km. It is well known that LIBs have penetrated everywhere in our daily life, such as computers, communication devices, etc. Although LIBs have been a great success in the clean energy field so far, there have been constant demands for improving the capacity and performance of LIBs as this has not been able to meet the emerging needs of society. As shown in **Fig. 1-1(a)**, current Li-ion batteries, with a maximum specific energy of

approximately 250 Wh kg^{-1}, do not have sufficient energy, rate, durability, or affordability to match the performance of conventional automotive gasoline/internal combustion engines. Novel batteries of higher energy density are required for electric vehicles for long driving distance. For example, the energy density of 500Wh kg^{-1} is needed for 500km driving distance (**Fig. 1-1(a)**).

In contrast, the highest theoretical specific energy (up to 11429 Wh kg^{-1}) is obtained by combining a lithium anode with an oxygen cathode, the lithium-oxygen battery (LOB) (**Figure 1-1(b)**). And its actual capacity of 1700 Wh kg^{-1} matches the available energy density of gasoline. In addition, the LOBs have an unlimited supply of oxygen from the air and is therefore also known as lithium-air battery (LAB). Since LAB is still in its infancy, air contains many components other than oxygen including N_2, H_2O, and CO_2, which interfere with battery reactions. fundamental studies are not on LAB but on LOB, which uses pure oxygen as an active material. In this thesis, both the Li-air battery (LAB) and Li-O_2 battery (LOB) below are referred as the Li-O_2 cells (LOB).

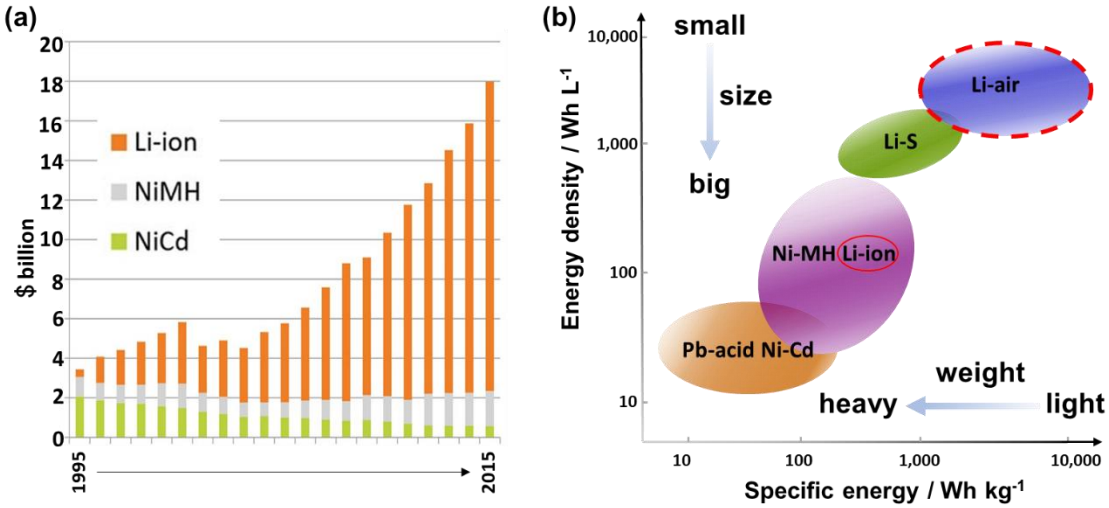

Figure 1-1. (a) Bar graph demonstrating the increase in financial support for LIB relative to NiCd and NiMH batteries from 1995 to 2015. (b) Comparison of specific energy and energy density of various batteries.

Figure 1-2 shows the difference between LIB and LOB. In LIBs, the negative electrode is carbon, and the positive electrode is composed of transition metal oxides, such as cobalt, manganese, and iron. Both are immersed in an electrolyte with lithium salt dissolved in it. When charging, lithium ions move from the positive electrode (cathode) to the negative electrode (anode) porous carbon, embedded in the carbon material; when discharging, lithium ions are de-embedded from the negative electrode and return to the positive electrode. The final battery capacity depends on how much material can hold the lithium ions, i.e., it is determined by the volume and mass of the electrodes.

LOB is a chemical battery with the active metal, lithium, as the negative electrode

and air (oxygen in it) as the positive electrode, and the basic chemical reactions that occur are the same as in a normal chemical battery. The main feature and source of advantage of this kind of battery lies in the use of lithium metal and oxygen as the negative and positive electrodes. This makes LOBs thinner and lighter than LIBs, with a much higher theoretical energy density.

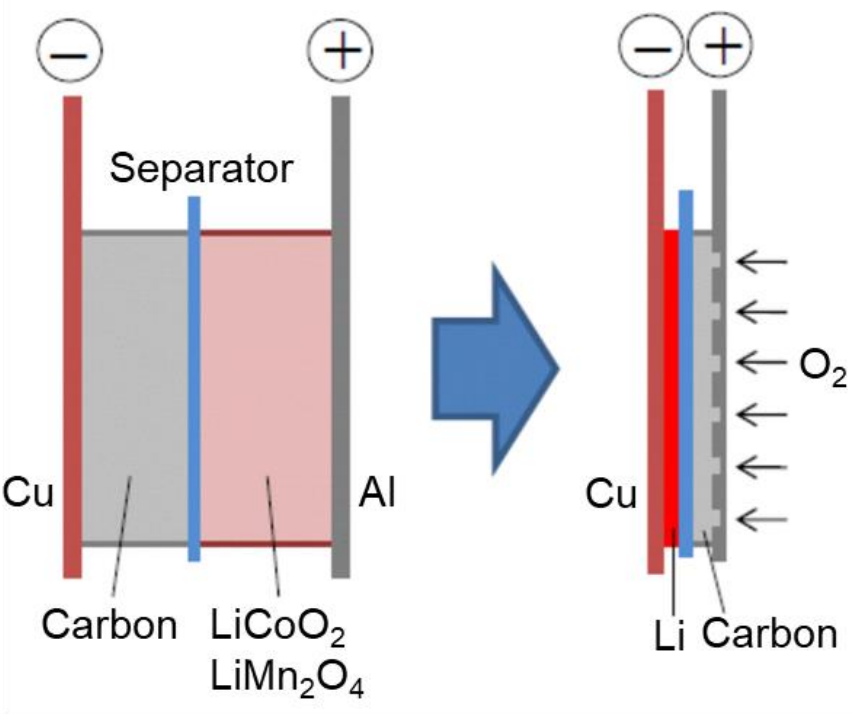

Figure 1-2. Comparison of conventional LIB (left) and LOB (right).

1.2 Fundamental of lithium-(air) oxygen battery

As shown in **Figure 1-3**, LOBs composed of metal lithium and air−O_2 as anode and cathode active materials, and an electrolyte solution containing Li^+ are one of the

most studied classes of LOBs. The carbon cathode is a conductive porous matrix that enables electrochemical contact between oxygen and lithium ions in the electrolyte solution. The essence of the battery process is the dissolution/deposition of lithium metal at the anode and oxygen reduction reaction (ORR)/oxygen evolution reaction (OER) at the cathode.

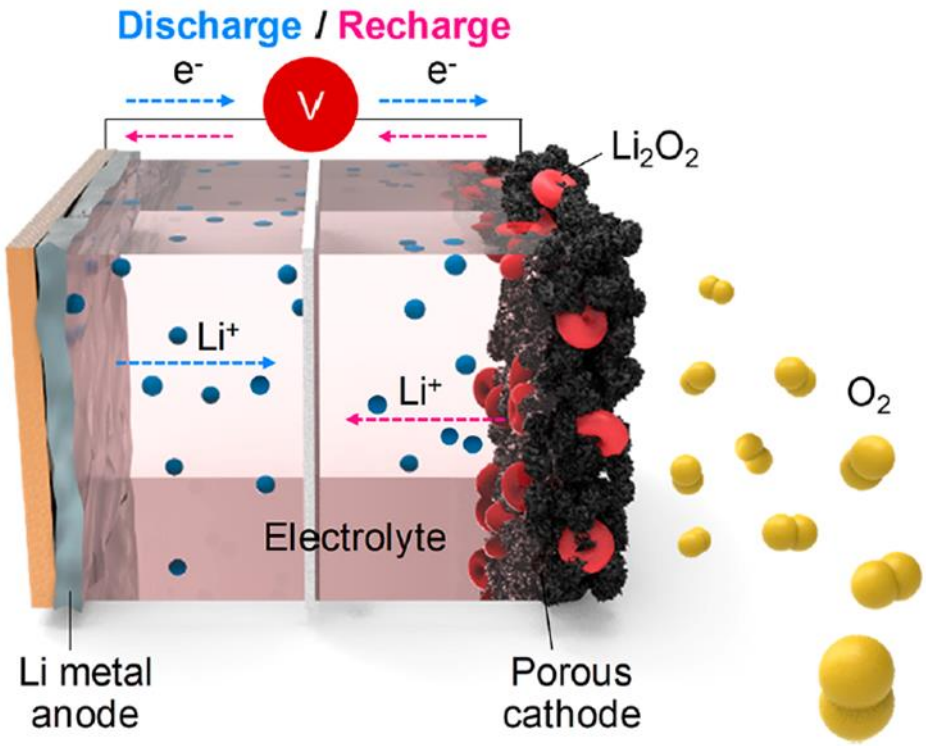

Figure 1-3. Scheme of conventional LOB. [1]

1.2.1 Fundamental electrochemistry in conventional LOBs

As described below, the cathode rection in a nonaqueous LOB produces a mixture

of lithium oxides, of which lithium peroxide Li_2O_2 is considered to be the ideal product. During discharge, lithium is oxidized at the lithium anode and oxygen is reduced at the cathode;

$$Li(s) \leftrightarrow Li^+ + e^- \rightarrow O_2^- \quad U_0 = 0 \text{ V vs. } Li^+/Li \qquad (1)$$

$$2Li^+ + 2e^- + O_2(g) \leftrightarrow Li_2O_2(s) \quad U_0 = 2.96 \text{ V vs. } Li^+/Li \qquad (2)$$

Therefore, the overall battery reaction is;

$$2Li(s) + O_2(g) \leftrightarrow Li_2O_2(s) \quad U_0 = 2.96 \text{ V vs. } Li^+/Li \qquad (3)$$

1.2.2 Components of LOBs

1.2.2.1 Lithium metal anode

Lithium metal is a promising anode material because of its extremely high specific capacity. The theoretical energy of LOBs does not take into account accessories such as electrode structure/mass, electrolyte/diaphragm, current collector, etc. The theoretical specific electrochemical capacity of lithium is calculated by the following equation;

$$C_{Li}^{w} = \frac{n_{Li}F}{w_{Li}} \quad (4)$$

C_{Li}^{w} is used to represent the number of electrons that can be released when 1 kg of metallic lithium is oxidized according to the reaction (4).

n_{Li} is the number of electrons per Li atom when it is oxidized (n_{Li} = 1).

F is the Faraday's constant (96487 As mol^{-1} or 26.802 Ah mol^{-1}).

w_{Li} is the weight of one mole of Li metal (6.941×10^{-3} kg mol^{-1}).

As mentioned above, the theoretical specific capacity of Li metal equals to 3860 Ah kg^{-1}. LOBs have attracted much attention due to their theoretical specific energy, which depends mainly on the use of lithium metal as the anode. Even the theoretical specific energy of LOBs is 4-5 times higher than that of traditional LIBs. Additionally, the lithium electrode has the most negative reduction voltage (-3.04 V vs. standard hydrogen electrode). To date, considerable effort has been devoted to introduce lithium as a practical anode in order to meet the growing demand for advanced, lightweight, high-energy batteries.[2,3,4]

1.2.2.2 Electrolyte

The major difference between non-aqueous and aqueous LOBs is the electrolyte. Since the electrolyte connects the anode and cathode of the battery and has a significant impact on the reactions that occur at the anode and cathode, the properties of the electrolyte will have a significant effect on the overall discharge and charge operation of the non-aqueous LAB.

Table 1-1. Requirements on electrolytes for the nonaqueous LOBs.[5]

Conductivity	• Sufficiently high for the anticipated rate capability
Stability	• Within potential window used on discharge and charge
	• In contact with O_2 and its reduced species on discharge
	• In contact with Li_2O_2 and its intermediates on charge
	• In contact with the anode or a stable SEI formed on the anode
Low volatility	• To minimise evaporation at the porous O_2 cathode
O_2 solubility and diffusivity	• To ensure adequate rate of mass transport to the cathode
Able to wet the electrode surfaces	
Promotes some solubility of Li_2O_2	Interaction with intermediates for high rate and packing density of Li_2O_2
Safety, low cost and toxicity	

It is well known that cycle efficiency and dendrites at the interface between the lithium anode and the electrolyte are important factors for the duration lifetime of lithium-air batteries, but the reaction at the interface between the air cathode and the electrolyte is a more critical factor for LOB operation. In particular, the formation and decomposition of the cathode product Li_2O_2 places high demands on the performance

of the electrolyte. Thus, electrolyte with a wide range of properties as shown in **Table 1-1** are needed to achieve high capacity and long lifetime of LOBs. The properties of some common electrolytes used in LOBs are shown in **Table 1-2**.

Table 1-2. Physical properties of solvents mostly used in electrolyte for non-aqueous LOBs.[6]

Solvent		Molecular weight	Structure	Dielectric constant ε (25 °C)	Dipole moment (μ)	Donor number (kcal mol^{-1})	Viscosity η (cP) (25 °C)	Oxygen solubility (mM cm^{-3})	Boiling/ melting point (°C)	Vapor pressure (kPa, 25 °C)	Density (g cm^{-3}, 25 °C)
Carbonate	PC	102		64.92	4.94 (18 °C)	15.1	2.53	3.2	241.7/−48.8	0.160 (55 °C)	1.1951
	EC	88		89.78 (40 °C)	4.87 (25 °C)	16.4	1.930 (40 °C)	1.71	248.2/36.4	3.371 (95.21 °C)	1.3383
	DMC	90		3.107		17.2	0.59 (20 °C)	7.29	91/4.6	2160	1.063
	EMC	104		2.958			0.65	7.95	110/−53	0.89	1.006
	DEC	118		2.820 (20 °C)	0.90 (25 °C)	16	0.748	7.92	126.8/−74.3	1.3 (23.8 °C)	0.96926
Ether	TEGDME	222		7.79		16.6	4.05	4.43	275/−30	<1.33	1.009
	DME	90		7.2	1.71 (25 °C)	20	0.455	9.57	84.5/−58	6.4 (20 °C)	0.86370
Sulfone	DMSO	78		46.45	4.06 (25 °C)	29.8	1.991	2.1	189/18	56	1.1
	TMS	120						1.59	285/28	1.33	1.261
Amide	DMF	73		36.71	3.24 (25 °C)	26.6	0.802		153/−61	0.49	0.94387
	DMA	87		37.78	3.71 (30 °C)	27.8	0.927		166.1/−20	0.17	0.936337
Ionic liquid	[C$_4$mim][Ntf$_2$]	419.36					44		/−1		1.429
	[C$_4$mim][BF$_4$]	226.02	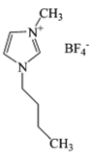				92		/−71		1.26

1.2.2.3 Cathode

In the nonaqueous LOBs. since the product of the cathode, Li_2O_2, is stored in the

cathode pores. the air electrode is used as both an electrode and a reservoir for the ideal discharge product, Li_2O_2. The capacity of the LOB is usually measured in mAh cm^{-2}, that will depend on the amount of Li_2O_2 deposit in the micropores and/or on the surface of the air electrode.

As mentioned above, the cathodic reaction of nonaqueous LOBs produces Li_2O_2 as the ideal product. However, the actual product is a series of oxides mixtures of lithium oxides. Several different discharge and charge mechanisms have been proposed for the ORR and OER process at at the air cathode. [3,7-15]

The two main discharge reaction mechanisms for ORR at the air cathode are as follows:

Discharge mechanism I;

$$O_2 + e^- \rightarrow O_2^- \qquad (5)$$

$$O_2^- + Li^+ \rightarrow LiO_2 \qquad (6)$$

$$LiO_2 + Li^+ + e^- \rightarrow Li_2O_2 \qquad (7)$$

Discharge mechanism II;

$$O_2 + e^- \rightarrow O_2^- \qquad (8)$$

$$2O_2^- \leftrightarrow O_2 + O_2^- \qquad (9)$$

$$O_2^- + 2Li^+ \rightarrow Li_2O_2 \qquad (10)$$

In the charging process, two main OERs at the air cathode are as follows:

Charge mechanism I;

$$Li_2O_2 \rightarrow O_2 + 2Li^+ + 2e^- \qquad (11)$$

Charge mechanism II;

$$Li_2O_2 \rightarrow LiO_2 + Li^+ + e^- \qquad (12)$$

$$LiO_2 \rightarrow O_2 + Li^+ + e^- \qquad (13)$$

Advanced air cathode design plays an important role in improving the catalytic activity of ORR and OER, preventing parasitic reactions of carbon substrates and polymer binders, and achieving excellent electrochemical performance in the LABs. Air cathodes can be modified to meet the following requirements.

(1) High chemical and electrochemical stability and minimal side reactions over a wide voltage range.

(2) High specific surface area and mesopore volume allow adequate storage of discharge products (Li_2O_2).

(3) High quality conductivity for O_2 and Li^+ ion diffusion, high electronic conductivity for fast reaction rates.

(4) Robust and high catalytic activity for Li_2O_2 growth.

The conductive substrate and catalyst should be integrated and considered as an effective air cathode. Based on materials engineering, carbon, which provides a large surface area and pore volume to carry the discharge products Li_2O_2, is typically selected. Early studies in the LAB field Super P, Vulcan XC 72R, and Ketjenblack, etc. have been used as cathodes.[16,17] These materials have a relatively small surface area but a fairly large specific pore volume. Therefore, calculating the specific discharge capacity of such a carbon in Li-O_2 cell cathodes may yield a carbon exceeding 2000 mAh g^{-1}.[18]

1.2.3 Evolution of LOBs

Electrochemical developments in the ORR and OER fields in the early 1960s laid an important theoretical foundation for the establishment of lithium-air batteries[19,20]. An electrochemical couples of Li and O_2 for batteries were proposed in the early 1970s.[21,22,23,24,25] Much effort was expanded in developing aqueous LABs systems with alkaline electrolytes (e.g., KOH) and quasi-neutral electrolytes (e.g., NaCl and KNO3). In 1976, Littauer and Tsai introduced the concept of LAB and proposed the use of aqueous alkaline solutions as electrolytes.[22,23] However, these batteries were not rechargeable, and the detailed battery performance was unknown. It was not until the late 1990s that research began to receive renewed attention. In 1996, Abraham et al. accidentally discovered a rechargeable LAB consisting of a lithium metal anode, a gel-type polymer electrolyte and a carbon air electrode with a catalyst when Li^+ was embedded in graphite through a gel polymer electrolyte and detected the production of Li_2O_2 in the carbon electrode by Raman spectroscopy.[26] However, lithium-air batteries at the current stage have a low cycle life (only three charge-discharge cycles) because the overpotential during charging cannot be controlled and the generated Li2O2 is non-conductive and covers the electrodes. Thus, LAB technology encountered a severe challenge at that time. Fortunately, in 2002, Read et al.[27] pointed out that the cycle

performance, discharge capacity, etc. of Li-O_2 batteries are highly dependent on the electrolyte solution and air cathode. In 2006, Bruce et al.[28] improved cyclability of a cell assembled by Li/PC-$LiPF_6$/Super P carbon black using electrolytic manganese dioxide (EMD) and demonstrated that Li_2O_2 could be decomposed during charging by using mass spectrometry, which is an important first step in producing reversible Li-O_2 batteries. This period was an important germination period for lithium-air batteries.

Scheme 1-1 presents several milestones of research in the field of lithium-air batteries. Based on the work of Bruce et al., LAB research has increased dramatically, also driven by advances in materials science and increasing demand for renewable energy. In 2010, the Battery 500 project, founded by IBM and the European Union, established the Lithium Air Battery with Split Oxygen Collection and Redox Processes (LABOHR) project, and declared its intention to advance the commercialization of Li-air batteries for applications automotive field.[29] To meet the requirements of the energy storage market, it is crucial to improve the safety, reversibility, and lifetime of lithium-air batteries. Based on this, researches on various lithium-air batteries mechanisms are also ongoing. A series of ether, dimethyl sulfoxide (DMSO), amides, nitriles, and ionic liquids based electrolytes have been studied experimentally and theoretically.[30-35] In 2012, the growth mechanism of main discharge product, Li_2O_2, was proposed. Toroid-

shaped Li_2O_2 exhibits higher discharge capacity than thin-film Li_2O_2.[36] In 2013, redox mediators (RMs) were proposed as special additives to electrolytes to promote ORR and OER kinetics, reduce the overpotential and improve energy efficiency.[37] For the anode, several protection strategies were employed to minimize Li metal degradation and dendrite formation, including membrane modification, in situ/in situ protective layer deposition, and Li alloy alternation, etc. One of the works in 2019 was effective to protect the lithium anode from passivation and side reactions, by coating a Nafion-Al2O3 composite layer on the lithium anode surface.[38] Recently, Yu et al. assembled a practical solid-state LAB and achieved significant breakthroughs in energy density, safety, and stability. Although the currently available solid-state electrolytes (SSEs) are costly and can only be manufactured on a small scale, which has greatly limited the development of solid-state batteries. In general, however, this solid-state LAB exhibits good electrochemical performance, safety, and environmental compatibility, making it an important milestone in the LAB development.

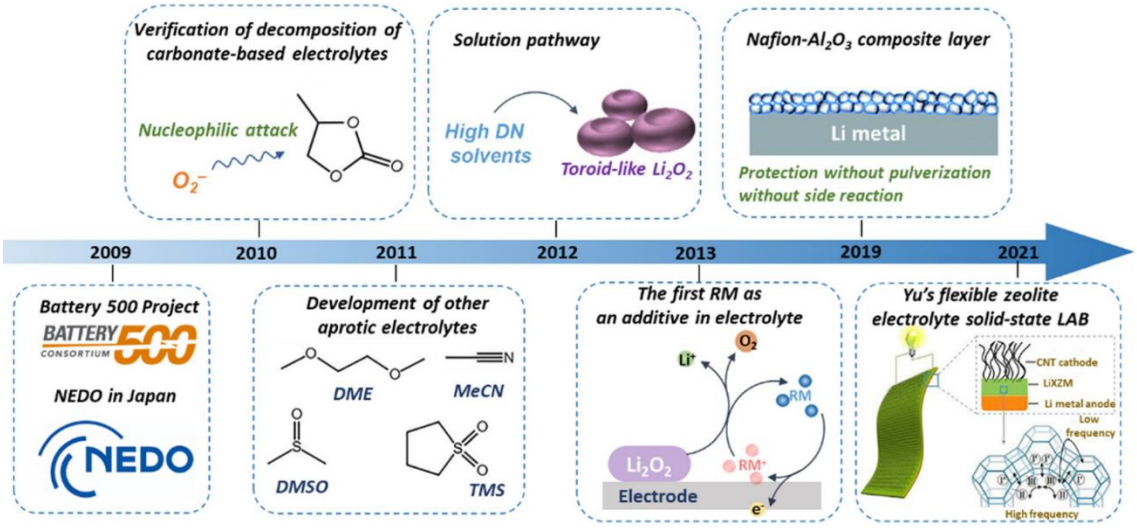

Scheme 1-1. The evolution and major milestones of LABs.[39]

1.2.4 Challenges of LOBs

Recent diligent research has resulted in the selection of appropriate solvents, electrolyte salts, and appropriate redox-mediate additives to improve the actual cell capacity, resulting in a significant reduction in high overpotential and carbon/electrolyte corrosion. As a result, the rechargeability of lithium-air batteries has been significantly improved.[37,40-46] Thus, while the high energy density of the LOB is impressive, there are still many practical challenges in achieving the theoretical energy density. In particular, low cyclability has hindered the practical application of LAB technology. This is mainly due to the occurrence of parasitic reactions, i.e., reactive oxygen species generated during the electrochemical process significantly degrade the cathodes and electrolytes; the situation is becoming worse by the presence of high

overpotentials **(Figure 1-4)**. Therefore, as shown in **Figure 1-5**, dendrite formation of the Li anode, passivation and degradation of the cathode, and degradation of the electrolyte are the most pressing issues for lithium-air batteries in order to make LOB practical.[2,47-52]

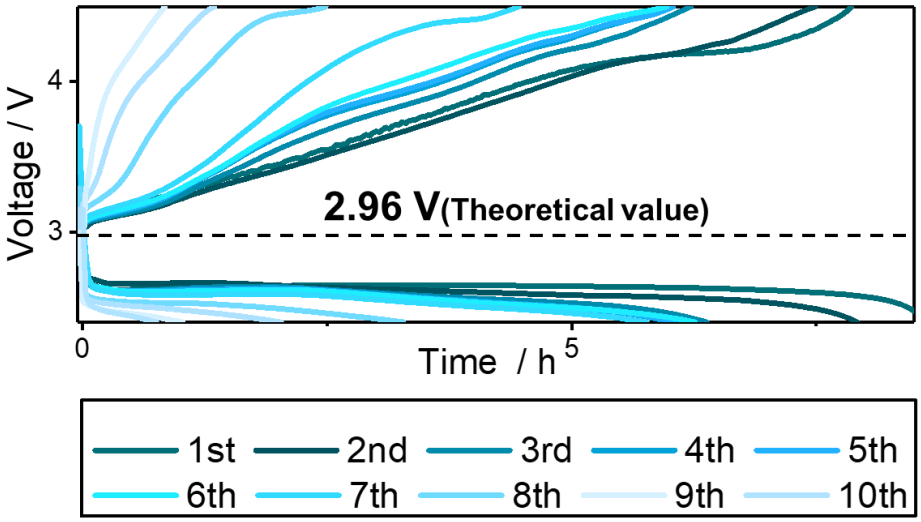

Figure 1-4. The constant current discharge/charge cycles of a ether based lithium-oxygen cell.

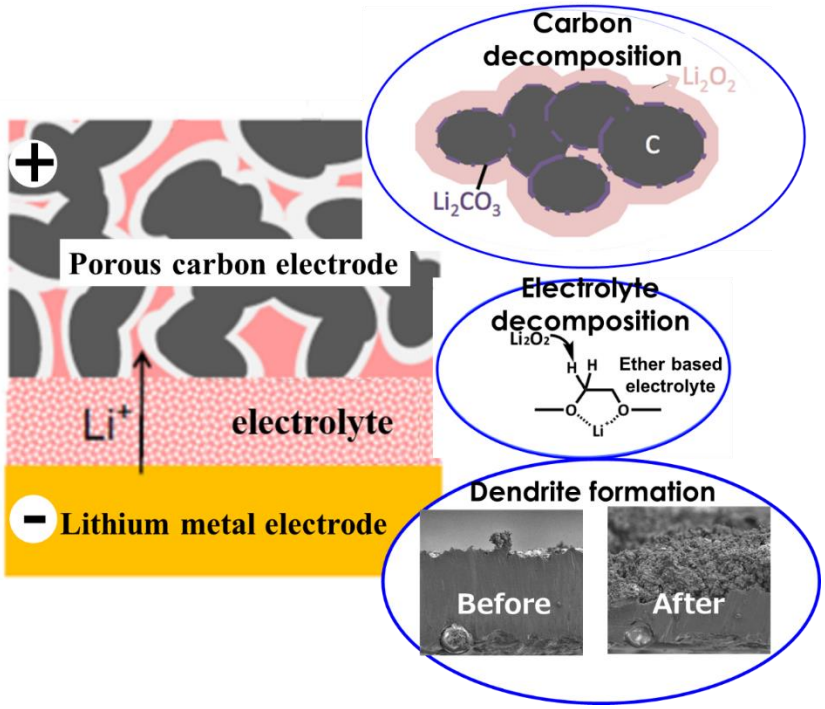

Figure 1-5. Three critical challenges in current LABs.

1.2.4.1 Anode/Lithium dendrite formation/degradation

Lithium metal as the lightest metal (standard atomic weight 6.941 g mol^{-1}, density = 0.53 g cm^{-3}) is the preferred anode of choice for LABs. Compared to embedded lithium anodes, lithium metal anodes provide maximum positive charge and higher energy density with a specific capacity of up to 3860 mAh g^{-1}. However, the implementation of lithium metal anodes is considered to be problematic. The main manifestations are dendrite formation and degradation of lithium.[2,4]

Due to the high Fermi energy level and negative reduction potential, lithium as

the anode of a LAB has a higher operating voltage, which reacts violently with the liquid electrolyte to form a solid electrolyte interface (SEI), temporarily passivates the lithium and prevents further reactions. SEI is a multilayer structure, and this chemical heterogeneity can lead to the non-uniform current distribution and dendrite growth. Unlike the appearance of the smooth coating on the lithium metal surface, if the dendrites penetrate the separator and contact the cathode, as shown in **Figure 1-6(a)** this can lead to a short circuit in the battery and cause serious safety hazards.

In general, side reactions such as SEI formation between the lithium metal and cross-contaminants irreversibly deplete the lithium and electrolyte solution, resulting in a significant drop in coulombic efficiency (CE). If the formed SEI is self-limiting and stable throughout the cycle life, the CE of the Li anode will be greatly improved after the first cycle, but unfortunately, after repeated stripping/plating, the morphology of the lithium surface will changes and the natural SEI will repeatedly rupture and repair itself as shown in **Figure 1-6(b)**. This can lead to undesired electrolyte solution depletion and uneven and uncontrolled deposition of lithium, such as sharp needles (**Figure 1-7(a)**) or dendritic patterns. These dendrites act as ‘hot spots’ and become preferred sites for lithium ion deposition in further cycles due to the fast reaction kinetics and short diffusion length. This leads to continuous growth of dendrites, which

not only leads to changes in volume and morphology, but can also lead to thermal runaway and explosion due to short circuiting of the LOBs.

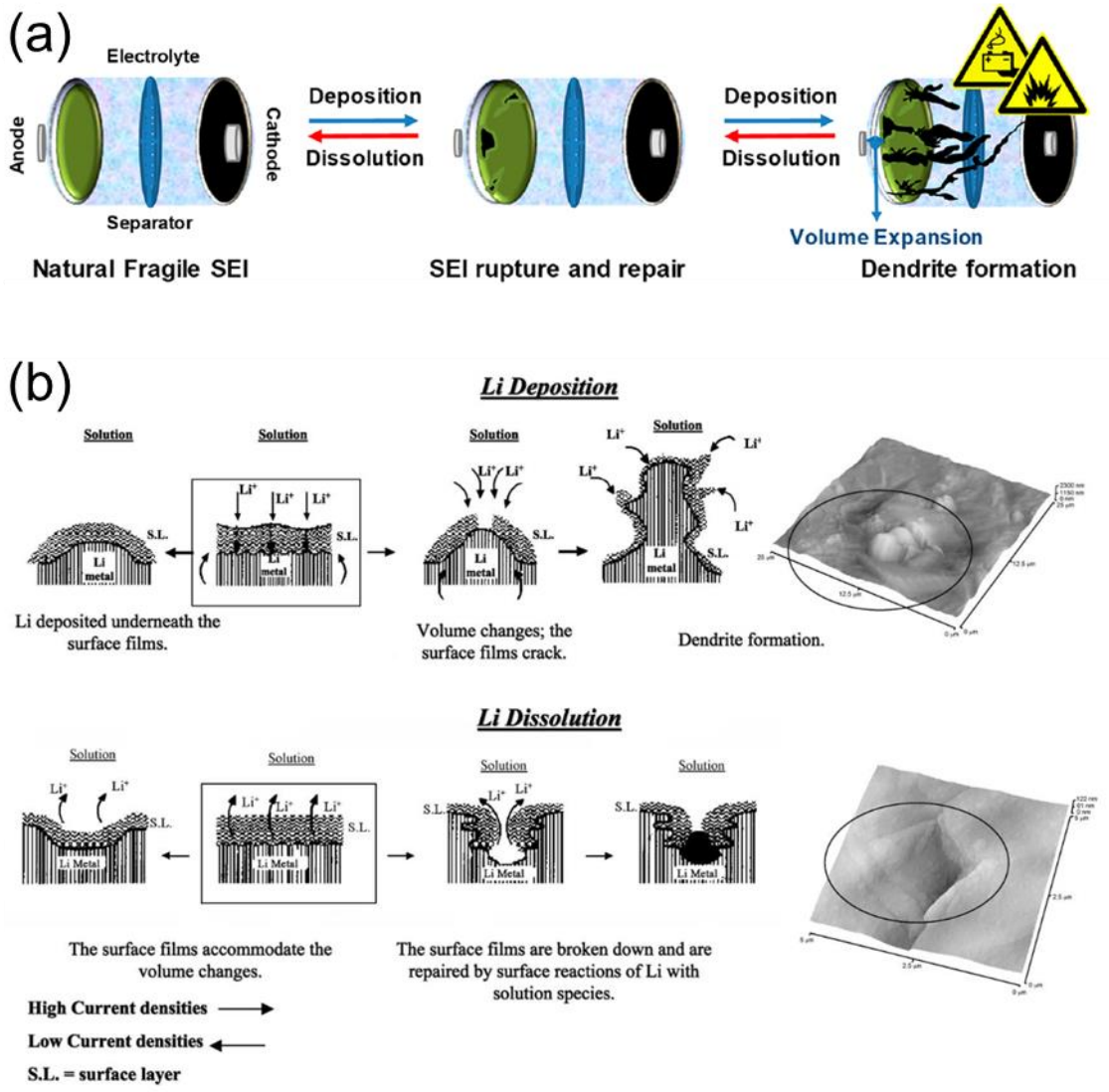

Figure 1-6. (a) dendrite formation and concomitant safety issues originating from the rupture and repair of the fragile solid electrolyte interface (SEI);[1] (b) Description of the morphology and failure mechanisms of lithium electrodes during Li deposition and Li dissolution and relevant AFM images describing selected phenomena: the beginning of dendrite formation and non-uniform Li dissolution accompanied by breakdown and repair of the surface films. (Li electrodes in an EC-DMC/LiPF6solution.)[53]

1.2.4.2 Electrolyte decomposition

Electrolytes are currently the biggest obstacle to the LOBs development, and as a result, more extensive research is being focused to them. LOBs has problems such as low O_2 solubility, lithium oxide disintegration, and lithium anode instability in various electrolytes. Therefore, to achieve a more efficient cell configuration, the ideal electrolyte needs to have the following characteristics: (1)high O_2 solubility and diffusivity; (2)low viscosity; (3)compatibility with lithium metal anodes and other cell components; (4)high boiling point and low volatility; and (5)strong chemical stability against reactive intermediates and products, such as reactive oxygen species, during charging and discharging.[54-60] Since first-generation electrolytes, organic carbonates, are unstable in the presence of superoxide radicals, research on second-generation electrolytes was initiated in terms of solvents and salts.

organic carbonates-based electrolyte. As mentioned above, early studies of LABs used organic carbonates as solvents. In 2006, Ogasawara et al. demonstrated a Li-O_2 rechargeable cell using alkyl carbonate with about 50 cycles.[61] In 2010, Mizuno et al. demonstrated a Li-O_2 cell with nearly 60% capacity retention rate after 100 cycles of discharge and recharge. and proposed Li_2CO_3 and Li_2O_2 as the main discharge

products.[62] One year later, Freunberger et al. described the cathodic decomposition pathway of carbonates in an oxygen environment.[63] As shown in **Figure 1-7** they proposed a degradation mechanism in the electrochemical process. The results show that in this type of LOB, there is no Li_2O_2 formation and that the products of such as Li_2CO_3, HCOOLi, etc., are irreversible during the charging and discharging processes. This results in irreversible degradation of the electrolyte. Moreover, by-products generated by parasitic reaction can accumulate on the cathode surface, increasing the overpotential, causing capacity fading and eventually leading to battery die. Therefore, it is necessary to the search for better and more stable solvents.

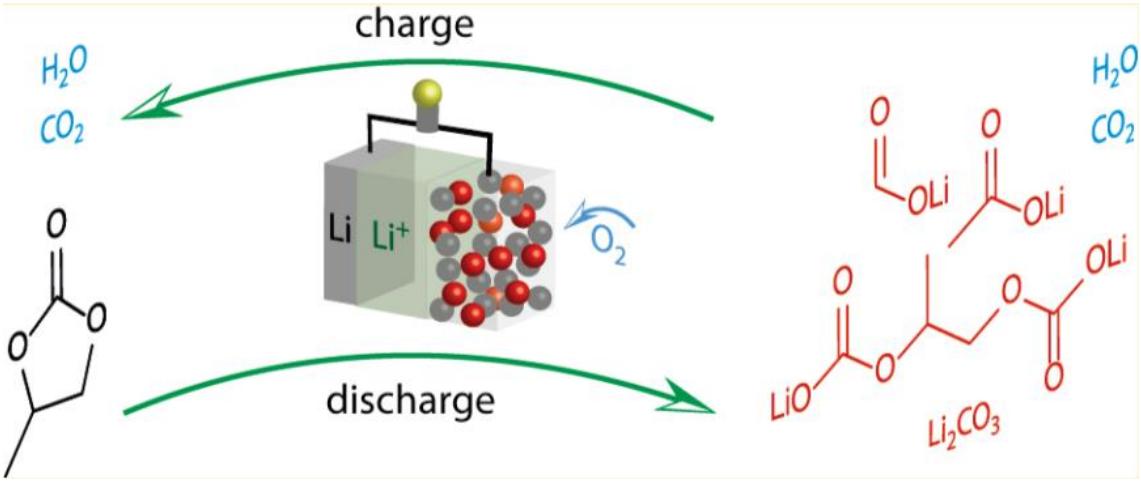

Figure 1-7. Mechanism representation of charge−discharge of Li−O_2 cell with 1 M $LiPF_6$ in propylene carbonate.[63]

Ether-based electrolyte. Ethers are also of interest for LABs because of their stability at high overpotential (>4.5 V), compatibility with lithium metal anodes, low

price, and low volatility such as tetraethylene glycol dimethyl ether (TEGDME).[64] The use of ethers (DME (dimethoxyethane) and DOL (1,3-dioxolane)) as electrolyte solvents has been studied since 2006 by Read et al.[65] and other ether-based solvents include TEGDME and 2-methyltetrahydrofuran (2-Me-THF).[66,67,68] It was confirmed that ether-based solvents are more chemically inert than organic carbonates. This is due to the high oxygen solubility and low viscosity of the ether-based solvents. Later, McCloskey et al.[55] used in situ quantitative differential electrochemical mass spectrometry (DEMS), non-in situ XRD, and Raman to investigate the mechanism of DME solvent-based LOBs. They confirmed that Li_2O_2 is the main discharge product in DME-based solvents, and that O_2 production is detected during charging, but in smaller amounts than the O_2 consumed during discharge. Thus, it was assumed that Li_2O_2 would react electrochemically with DME during the charging process. The degradation of DME and other ether-based solvents was further confirmed by Sharon et al.[69] by the mechanism shown in **Scheme 1-2**. The ether decomposition forms H_2O, CO_2, HCO_2Li, CH_3CO_2Li, etc. suggesting that it is related to nucleophilic attack of O_2 during the discharge process. Subsequently, in 2017, Sharon et al.[70] investigated the different stability responses of various glycol dimethyl ethers to oxygen species formed in Li-O_2 cells and concluded that TEGDME is the most stable ether solvent in Li-O_2

cells, and attributed the reason to the active site in the polyether molecule, that vary by chain length, oxygen numbers, spatial conformation, and oxygen atom interaction with the lithium ions.

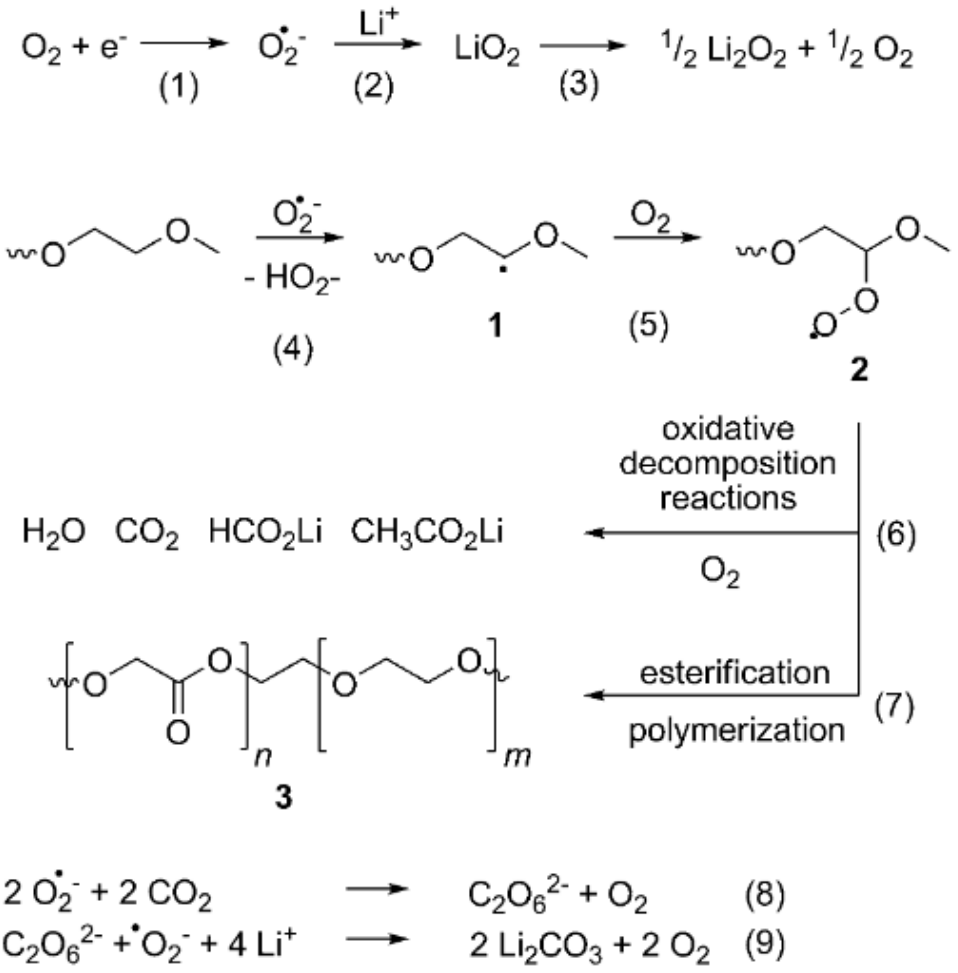

Scheme 1-2. Proposed mechanism for reactions that occur during dis-charge.[68]

DMSO-based electrolyte. Ether solvents are nonpolar and have a fairly low level of ability to dissolve lithium salts. This leads to LABs exhibiting low rates and capacities. Therefore, solvents with high donor number (DN), such as dimethyl

sulfoxide (DMSO), should be considered. Peng et al.[31] reported a Li-O_2 cell with DMSO as solvent and porous gold as cathode, with a capacity retention of about 95% after 100 cycles. However, the cell capacity was limited by the pore volume of the gold electrode. Subsequently, Sharon et al.[71] demonstrated significant degradation of DMSO using carbon electrodes with larger pore volumes and proposed a degradation mechanism Figure 1-8(a). This is due to the fact that DMSO is susceptible to nucleophilic attack by reducing oxygen species, forming sulfone and dimethylsulfone. In 2014, Shao-Horn et al.[72] examined the reactivity of DMSO with Li_2O_2. They found that Li_2O_2 particles formed during discharge gradually converted to LiOH after prolonged exposure to the DMSO-based electrolyte, as shown in **Figure 1-8 (b)**, and the amount of LiOH increased with time. Other investigations[73-75] further support the instability of DMSO solvents, observing the formation of carbonate species, dimethyl sulfone ($DMSO_2$), and the byproduct lithium sulfate/sulfate/sulfone. The poor compatibility of DMSO with lithium metal anode prevents the formation of a stable passivation layer (SEI). These findings suggest that DMSO may not be a suitable solvent for use in long-life rechargeable LOBs.

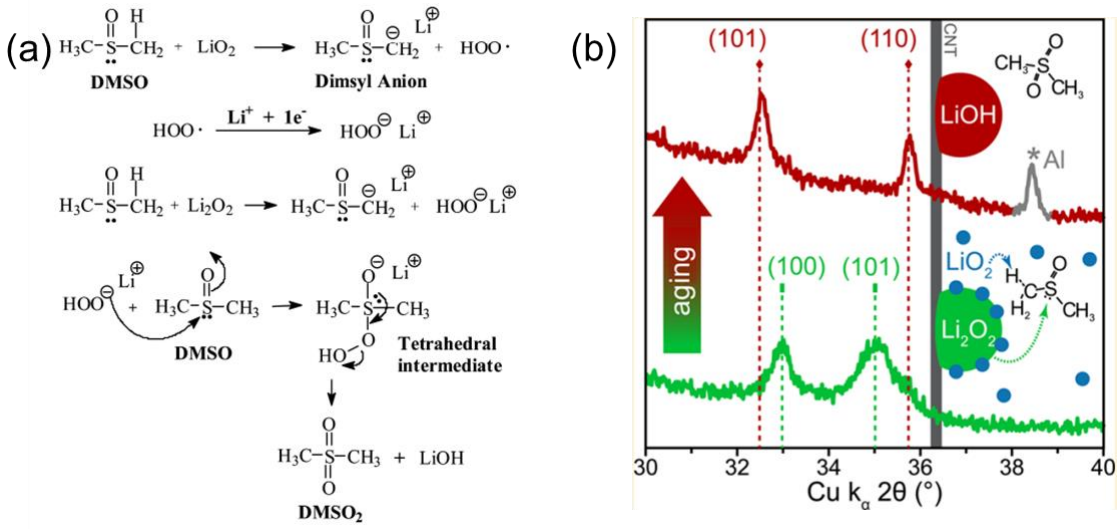

Figure 1- 8. (a) Proposed mechanism of degradation of DMSO.[71] [b] XRD patterns showing evolution of LiOH.[72]

Amide-based electrolyte. The unsatisfactory stability of DMSO has led to a search for new solvent candidates that are suitable against reactive oxygen species. The electronegativity of N in amide (OQC-N) is lower than that of O in ester (OQC-O). The N atom acts as a better electron donating group, and the C center in OQC-N is less positive than the C center in OQC-O. Therefore, amides are expected to be more stable electrolytes against nucleophilic attack. Bryantsev et al.[32,76] also showed successively by calculation that the free energy barrier to nucleophilic attack of amides is indeed greater than that of DMSO and esters. However, Chen et al.[77] demonstrated that the solvent cycling stability of amides does not apply to oxygen reduction applications. **Scheme 1-3** shows the oxidative cleavage of amides and the further degradation of

various substances including dimethylamine, acetate, carbonate, and various N-O substances. Therefore, the stability of amide-based solvents is questionable. Although amides are more stable against superoxide radicals than ether-based solvents, small alkyl amide (e.g., DMA = 293 Pa at 25 ^{o}C) with high vapor pressure as the solvent will be a problem for long-term operation.[78] Another significant drawback of amide-based solvents is the high reactivity towards lithium metal.[79] The reaction between amide-based solvents and lithium metal is very violent and not allow for reversible cycling of lithium metal for LOB rechargeable battery operation. Thus, its use in Li-O_2 batteries has not been widely explored at this time.

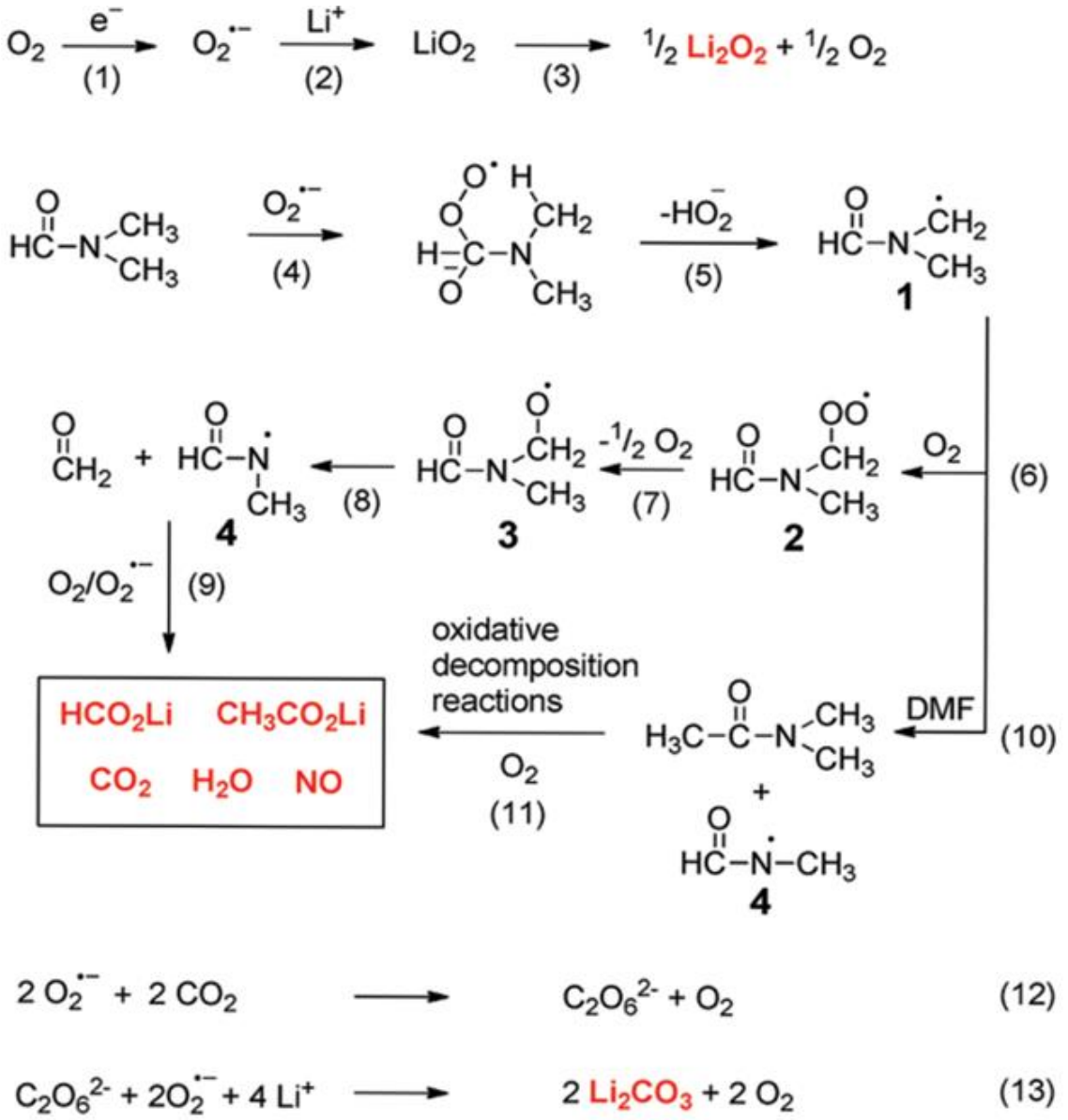

Scheme 1-3. Proposed mechanism for degradation of dimethylacetamide during oxygen reduction reactions.[77]

Ionic liquid (IL)-based electrolyte. On the other hand, room temperature ionic liquids such as 1-alkyl-3-methylimidazolium have attracted attention because of their special properties such as low flammability, hydrophobicity, low vapor pressure, wide potential window, and high thermal stability.[80,81] It shows a discharge capacity of 5,000

mAh g^{-1} at a very low discharge current of 0.01 mA cm^{-2}, and is hydrophobic with negligible vapor pressure. Thus, the ionic liquid Hg/1-ethyl-3-methyl imidazolium imide is considered as a promising candidate for LAB electrolytes.[82] However, several disadvantages of ionic liquids may be a limiting factor for their wide application. In addition to high manufacturing costs, the poor diffusion mobility of Li^+ and dissolved O_2 in ionic liquids may limit the battery performance. Oxygen supply has been identified as the rate-limiting step in the formation of lithium-oxygen compounds (LiO_x) in IL-based electrolytes.[83] ILs have higher viscosity than DME and DMSO, resulting in high mass transfer resistance and high interfacial polarization voltage.[84] Therefore, more advanced and stable solvents are essential for long-term cycling and practical applications of LOBs.

In conclusion, it was found that in the highly reactive environment of the LOB, almost all available non-protonic solvents are more or less degraded. Four modes of degradation mechanisms of metallic Li anodes can be listed: nucleophilic attack, H atom abstraction, acid/base reaction, and reductive degradation. Despite significant progress has been made in recent years, no solvent has yet been found that is compatible with Li metal anode yet can ultimately withstand nucleophilic attack from highly reactive reducing oxygen species. Solvent stability in rechargeable LOBs is a major

issue to be addressed. Despite their inherent drawbacks, ethers, DMSO, DMA, and ILs are by far the most commonly used solvents in academic research. The search for aprotic solvents for LOBs will undoubtedly continue. More advanced and stable solvents are essential for long-term cycle and practical application of LOBs.

1.2.4.3 Carbon cathode decomposition and passivation

Carbon cathodes are widely used in Li-O_2 batteries because of their high conductivity, light weight, low cost, and flexible structure. Despite its promising properties, carbon cathode seems to have stability problems in LOBs. (1)Since ORR and OER occur on the surface of carbon cathode. Active substances produced during ORR an OER, such as reactive oxygen species ($O_2^{-\cdot}$, $Li_{2-x}O_2$, $^1O_2$), are highly reactive due to their oxidative, nucleophilic, and basic nature, leading to carbon degradation. (2)Carbon materials are degraded due to the natural defects and functional groups on the carbon surface. This degradation occurs primarily at high overpotentials. (3)Additionally, environmental factors such as humidity and blockage of the porous carbon cathodes can also lead to irreversible cathode degradation.[85-87]

As shown in **Figure 1-12**, Thotiyl et al. demonstrated that $^{13}CO_2$ is generated during charging of a Li-O_2 cell containing a ^{13}C cathode and that the carbon cathode is

ultimately decomposed in this cell.[88] Analysis of cathodes in different discharge and charge states showed that carbon decomposition occurs at high voltages during charging. Other studies have shown that Li_2CO_3 oxidation and CO_2 release occur below 4 V.[63,88] Analysis of consecutive cycles showed that Li_2CO_3 from carbon decomposition accumulates in the cell. A comparison of hydrophobic and hydrophilic carbons suggested that the latter are more stable due to the absence of reactive surface groups. The preferential reactivity of functional groups on carbon has also been observed by other researchers and is relevant during discharge.[89]

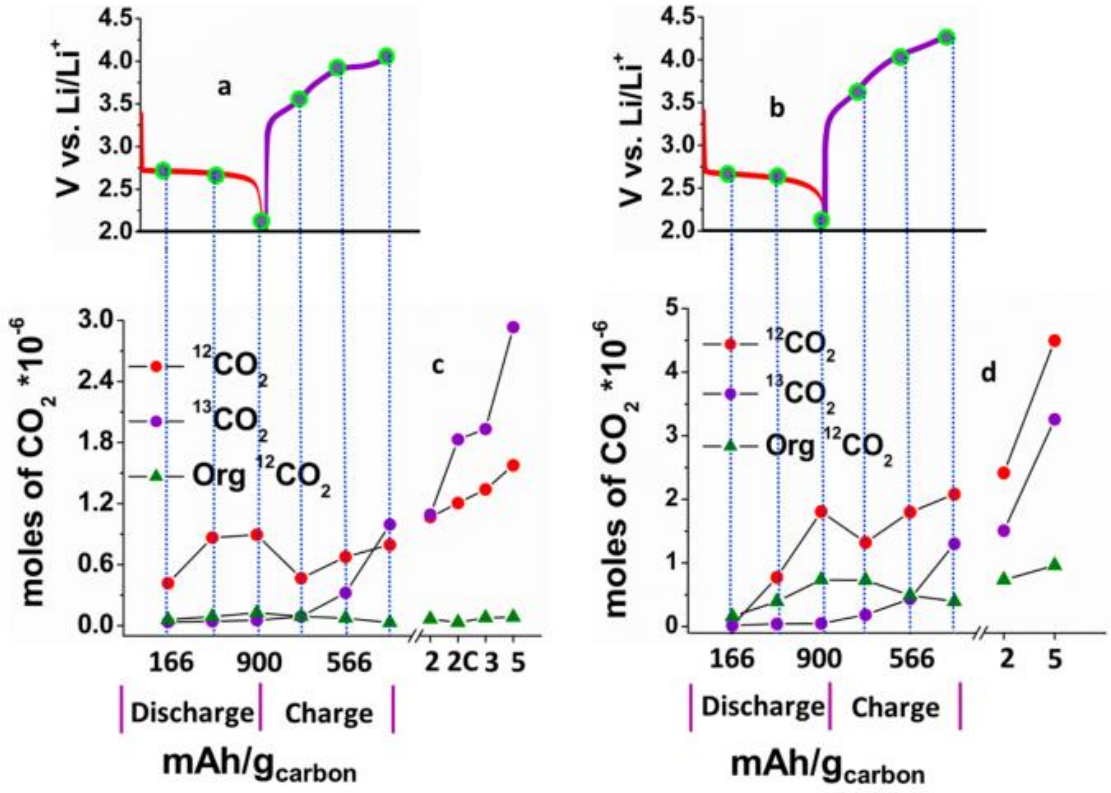

Figure 1-12. (Upper) Discharge−charge curves on the first cycle for Li−O_2 cells containing a DMSO (a) and tetraglyme (b)-based electrolyte and a ^{13}C cathode. (Lower) Moles of CO_2 evolved during chemical treatment of the removed cathodes due to decomposition of (red) the electrolyte, (purple) the cathode, and (green) electrolyte (organic fragments) during cycling to the point indicated by the markers on the plot.[88]

In summary, despite their promising properties, carbon-based materials appear to have stability problems in lithium-air batteries. Therefore, there is a need for a stable material that can serve as an alternative. However, the use of a redox medium in the charging process of Li-O_2 cells can significantly reduce the degradation of cell components.[90] Gao et al.[91] demonstrated a dual dielectric cell with a media, including a cathode containing ^{13}C, and showed that the use of a redox medium improves the

stability of the carbon cathode. As shown in **Figure 1-13**, Li_2CO_3 accumulated rapidly in the standard cell, but degradation and accumulation were significantly less in the cell with dual media. Thus, the use of redox mediators has rekindled the possibility of using carbon in lithium-air batteries.

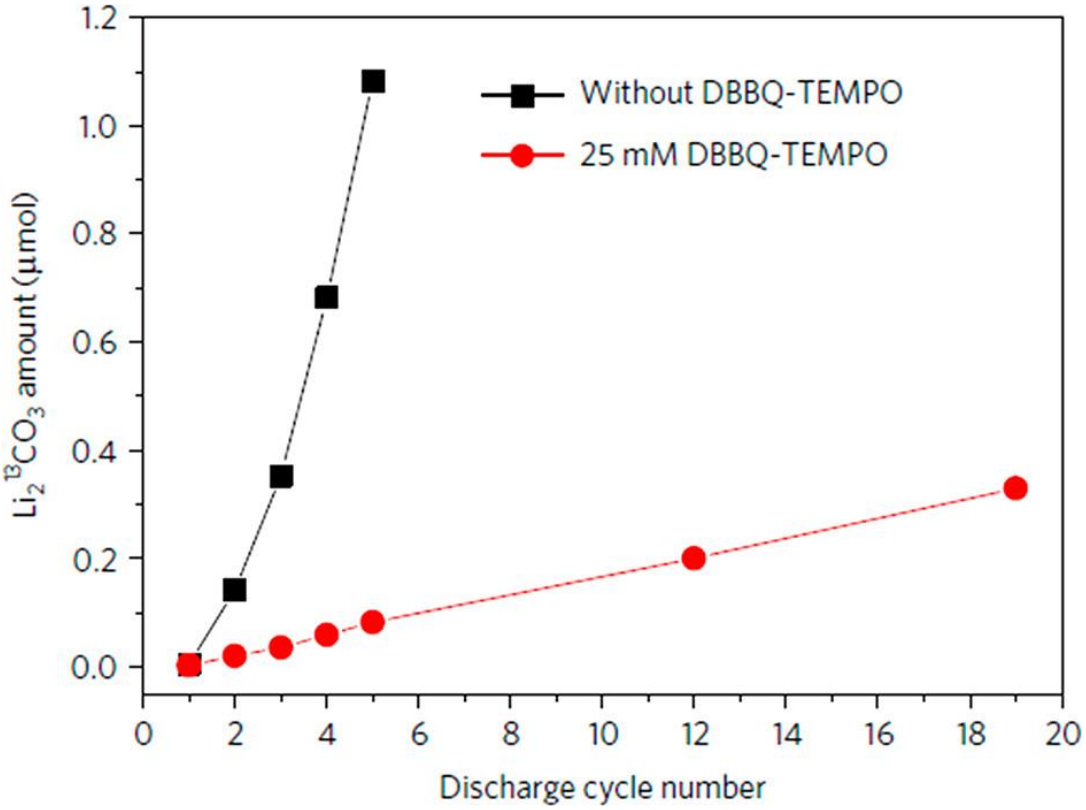

Figure 1-13. Amounts of $Li_2{}^{13}CO_3$ at the end of discharge of successive cycles of cells contain ^{13}C cathodes, with and without dual mediators.[91]

1.3 Characterization tools for LOB mechanism study

LOBs have attracted considerable interest over the past several decades because of their very high theoretical energy density and transition metal-free cathode. As

mentioned above, even LOB has a serious issue of low cyclability due to the degradation of positive electrode (carbon) and electrolyte solution, and the degradation/dendrite formation of negative Li metal electrode. To improve the cyclability, it is essential to clarify the mechanism of LOB degradation[92,93]. Thus, many characterization techniques of microscopy, diffraction, and spectroscopy combined with electrochemical responses have been developed for the electrodes and electrolyte degradation mechanism investigation.

1.3.1 Microscopic techniques

Electron microscopy (EM) is the imaging technique most commonly used in battery research and is generally divided into two categories, scanning electron microscopy (SEM) and transmission electron microscopy (TEM). The typically short de Broglie wavelength of the electron beam is $<10^{-10}$ m. When the electron beam interacts with the sample to be measured, energy conversion occurs and various electrons and X-rays are excited. As shown in **Figure 1-14**, in 2010, Huang et al[92] reported that the lithiation process of a single SnO_2 nanowire anode could be clearly monitored by using TEM. SEM and TEM are mainly used to characterize electrode materials, and their image resolution can even reach 0.05 nm through spherical

aberration calibration[93]. However, conventional SEM and TEM operate under high vacuum conditions, making it impossible to apply such measurements to battery with volatile electrolytes. The electron transport depth of common electrode materials is usually < 10^{-6} m, while practical lithium electrode is > 10^{-5} m thick. Moreover, the high-energy electron beams may damage the sample.

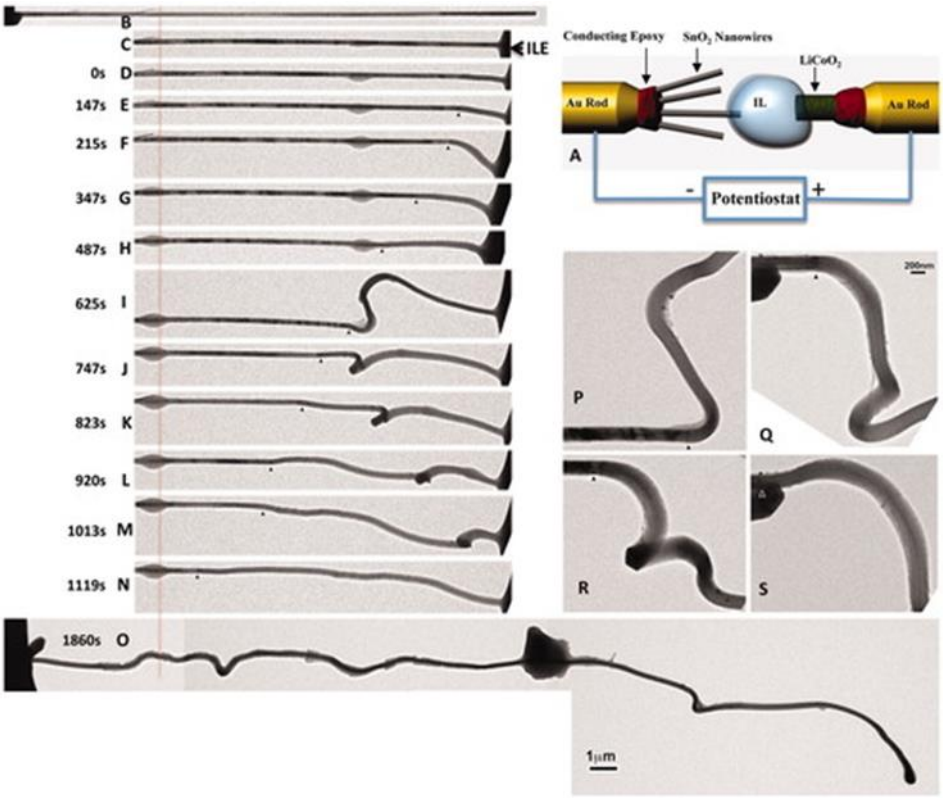

Figure 1-14. Time-lapse structure evolution of a SnO_2 nanowire anode during charging at –3.5 V against a $LiCoO_2$ cathode.[92]

1.3.2 X-ray diffraction technique

X-ray diffraction (XRD) is an extremely important technique for structural

analysis, and in situ XRD measurements provide valuable information, and very high-resolution responses can be obtained using X-ray beams from synchrotron radiation sources[94]. Real-time detection of structural information during electrochemical processes is of more reliable significance for the study of battery degradation mechanisms. As shown in **Figure 1-15**, the reversibility of lithium anodes was investigated by microfocus synchrotron X-ray diffraction (μ-XRD) technique in 2013 by Shui et al..[95] As the charge-discharge cycles were repeated, diffraction peaks attributed to LiOH began to rise at the contact between the anode and the separator. It is hypothesized that LiOH is formed by metallic Li in an alkaline environment and subsequently accumulates in SEI. During the discharge-charge cycles, the total amount of LiOH gradually increases with cycle time, which indicates the continuous expansion of the hydroxide passivation layer. At the same time, only partial recovery of metallic Li was detected during the following recharge step, indicating that the amount of metallic Li anode gradually decreases with the growth of LiOH, or charge-discharge cycles, until it is completely consumed. Synchrotron XRD can detect the structural changes in battery in real time without any damage, but this technique is more limited to monitoring and analyzing the degradation process of the electrode, and does not contribute much to the degradation process of the electrolyte.

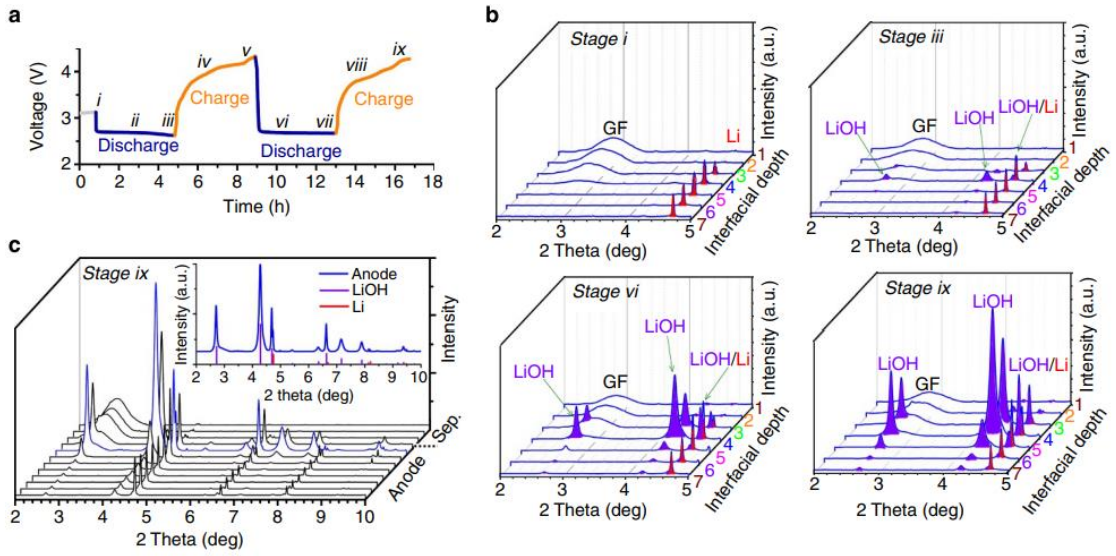

Figure 1-15. The change in anodic lithium during discharge–charge cycling. (a) Discharge–charge voltage profile of the operando Li–O_2 cell as a function of cycling time. The stages at which XRD data sets were collected are marked as i, ii, iiiy on the curve. (b) Four representative XRD sets taken at the cycling stage i, iii, vi, and ix; each set consisted of seven selected XRD patterns collected at various anode–separator interfacial depths (marked as 1, 2, … 7 of different colors on the right of each set). (c) An expanded XRD data set at stage ix covering the whole anode through adjacent separator region. The inset is a representative XRD pattern taken from the position marked by a blue line that includes references of Li and LiOH.[95]

1.3.3 Electrochemical quartz crystal microbalance (EQCM) technique

EQCM is an in-situ surface-sensitive technique based on the piezoelectric response of a thin quartz crystals that vibrates due to the surface loading. The behavior of the EQCM is related to the Sauerbrey equation, i.e., $\Delta f = -C_f \Delta m$ (Cf in Hz g^{-1} is the EQCM mass sensitivity). It establishes a linear relationship between the change in mass (Δm) loading on the thin quartz crystal and the natural frequency of the crystal

(Δf)[96]. The principle is that metal Au or Pt deposited on a quartz crystal is used as a working electrode, and the electrochemical response of this working electrode in a three-electrode cell is measured together with the change in the frequency response of the quartz crystal. By measuring Δm and charge, the mass per electron (m.p.e.) values of the various electrochemical processes measured by the EQCM can be calculated, and by comparing these values with the mass of materials that may have been deposited or dissolved on the surface[97,98], the reaction products that occur on the surface of the working electrode of the Li-air cell can be inferred. As can be seen in **Figure 1-16**, Tomita, et al.[99] carried out EQCM to clarify the cathode reaction mechanism at a gold electrode in a 0.1 M $LiPF_6$ DMSO solution. Illustrated how the major impurities, HF and H_2O, affect the potential dependent products distribution during discharge at the cathode, thereby demonstrating that low cyclability is due to impurities in solution.

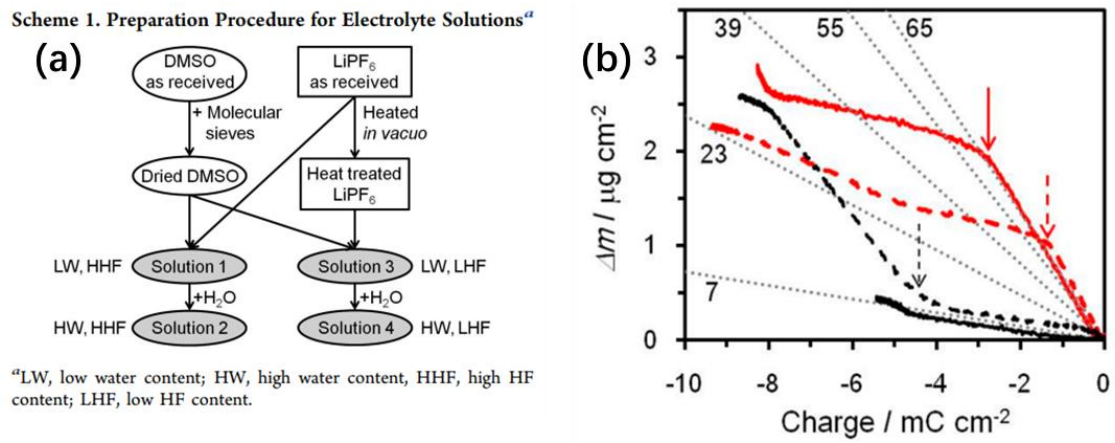

Figure 1-16. (a) Electrolyte solutions. (b) Mass changes as a function of integrated charge obtained from the results in Figure 1 in solutions 1 (red, solid line), 2 (red,broken line), 3 (black, solid line), and 4 (black, broken line).[99]

1.3.4 Mass spectroscopic (MS) techniques

The main spectroscopic techniques used in battery research include Fourier transform infrared spectroscopy (FTIR)[100], Raman[101], solid-state nuclear magnetic resonance (NMR)[102], X-ray absorption near edge structure (XANES), extended X-ray absorption fine structure (EXAFS)[103], and mass spectrometry (MS)[104]. These commonly used spectroscopic can obtain the basic structure of the reaction product components on the electrode surface, but the accuracy of the structural information still needs to be confirmed by a determined mass number. Therefore, the introduction of mass spectrometry to mass analysis is particularly necessary.

Mass spectrometry has been used as a tool to study volatile products formed by

the reaction between the carbon cathode and the electrolyte solution interface[105]. Connecting an electrochemical cell to a high vacuum mass spectrometer via capillary, typically tens of meters long, prevents the transfer of solution from the cell to the mass system, but allows the transfer of volatile products from the electrochemical cell to the spectrometer. This method, therefore, can be used to monitor the voltage-dependent formation of gaseous products generated[106]. It is thus of greater significance for the voltage dependence of electrolytes and electrodes degradation. Combined with investigations of emissions from lithium batteries[107,108,109], a wide variety of species are expected. Since no state-of-the-art analytical system is known to detect all expected emission components without cross-sensitivity, Nedjalkov et al.[110] combined different spectroscopic and chemical analytical techniques. Gas chromatography-mass spectrometry (GC-MS) was introduced to detect large molecules, particularly volatile organic compounds. Small molecules/components were determined by quadrupole mass spectrometry (QMS). **As shown in Figure 1-17**, a combination of GC-MS and QMS was used to measure gas emissions from lithium batterie under different failure scenarios, showing a wide variety of chemical species.

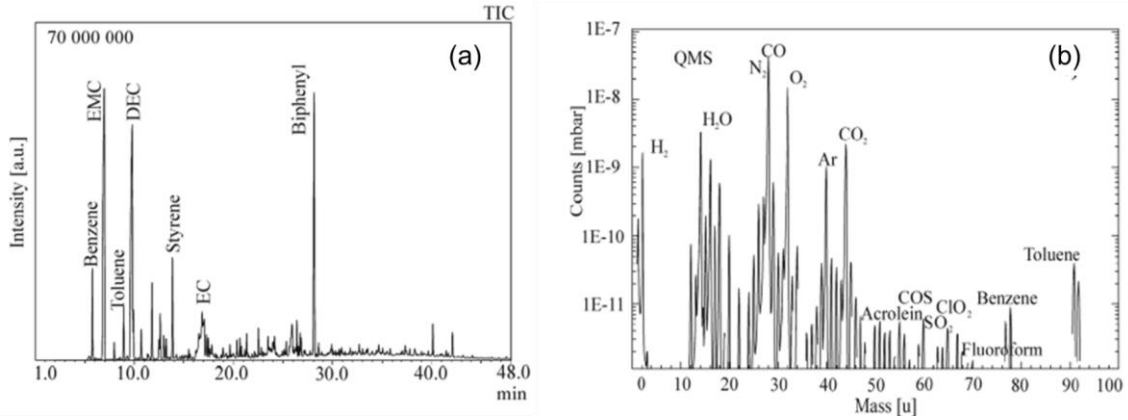

Figure 1-17. (a) Results of the gas chromatography-mass spectrometry (GC-MS) analysis. (b) the quadrupole mass spectrometry (QMS) analysis.[110]

1.4 Objectives and outline of this thesis

In this thesis, experimental study on the degradation mechanism of LOB was carried out in order to understand and solve the problem of low cyclability performance of lithium-oxygen batteries. So far, the main reaction of LOB is the Li_2O_2 generation and decomposition, i.e., $2Li + O_2 \rightleftarrows Li_2O_2$. Since the solvent of the electrolyte in the LOB is usually organic, the side reactions in the battery generate CO_2, H_2O, and organics along with the main reaction. As the major degradation processes are the decomposition of electrolytes and carbon cathode by reacting with reactive oxygen such as super oxide and singlet oxygen generated during both discharge and charging process, the detection of decomposed products is the key to understand the degradation processes. on-line quadrupole mass spectrometry (QMS), ex-situ GC/MS (thermal separation probe-gas chromatogram/mass spectrometry (TSP-GCMS)), and

in-situ GC/MS (cold trap pre-concentrator-gas chromatogram/mass spectrometry (CTPC-GC/MS)) were introduced to detect or real-time monitor of generated organic and inorganic products during the whole electrochemical process in TEGDME based LOB.

In **Chapter 2**, experimental details of chemicals, electrolytes preparation, cell assembly, electrochemical process, as well as configuration of mass spectrometry systems are provided.

In **Chapter 3**, on-line QMS and TSP-GCMS were employed for real time monitoring of generated gaseous products during charging in TEGDME based LOB, which is operated in pure oxygen not in air. To understand the energetics of the product formation during charging process quantitatively, linear voltage sweep (LSV: 0.05 mV s^{-1}) and voltage step modes were employed in additional to constant current charging.

In **Chapter 4**, on-line QMS was introduced combining with isotope experiments, $^{12}CD_3$_TEGDME and $^{13}CH_3$_TEGDME as exchange of solvent TEGDME, and $^{18}O_2$ as exchange of discharge gas $^{16}O_2$, to follow and analysis products generation during charging process. By combining the analysis with isotopic results, all the measured mass numbers can be assigned to the corresponding molecules and thus inferring the

side reactions in the battery during charging.

In **Chapter 5**, on-line CTPC-GC/MS system was constructed to detect reaction products of LABs during discharge and charging in real-time with high accuracy. By installing the cold trap between the cell and the GC/MS and adjusting the cold trapping temperature, all the volatile products generated during the cell reaction processes could be collected and analyzed by GC/MS without exposure to the ambient atmosphere. The generations of organic molecules were followed over time by repeatedly sampling the head-space gas of the cell for a very short time, e.g., 15s, for a fixed period of time, e.g., 40 min, during the cell operation. By controlling the sampling time and period, loss of generated molecules by gas flow can be minimized.

In **Chapter 6**, the general conclusions, and a brief prospect are given.

References

1. Kwak, W.-J.; Rosy; Sharon, D.; Xia, C.; Kim, H.; Johnson, L. R.; Bruce, P. G.; Nazar, L. F.; Sun, Y.-K.; Frimer, A. A.; Noked, M.; Freunberger, S. A.; Aurbach, D., Lithium–Oxygen Batteries and Related Systems: Potential, Status, and Future. Chemical Reviews 2020, 120 (14), 6626-6683.

2. Bruce, P. G.; Freunberger, S. A.; Hardwick, L. J.; Tarascon, J.-M., Li–O2 and Li–S batteries with high energy storage. Nature materials 2012, 11 (1), 19-29.

3. Laoire, C. O.; Mukerjee, S.; Abraham, K. M.; Plichta, E. J.; Hendrickson, M. A., Elucidating the Mechanism of Oxygen Reduction for Lithium-Air Battery Applications. The Journal of Physical Chemistry C 2009, 113 (46), 20127-20134.

4. Xu, W.; Wang, J.; Ding, F.; Chen, X.; Nasybulin, E.; Zhang, Y.; Zhang, J.-G., Lithium metal anodes for rechargeable batteries. Energy & Environmental Science 2014, 7 (2), 513-537.

5. Imanishi, N.; Luntz, A. C.; Bruce, P., The lithium air battery: fundamentals. Springer: 2014.

6. Ma, Z.; Yuan, X.; Li, L.; Ma, Z.-F.; Wilkinson, D. P.; Zhang, L.; Zhang, J., A review of cathode materials and structures for rechargeable lithium–air batteries. Energy & Environmental Science 2015, 8 (8), 2144-2198.

7. Laoire, C. O.; Mukerjee, S.; Abraham, K. M.; Plichta, E. J.; Hendrickson, M. A.,

Influence of Nonaqueous Solvents on the Electrochemistry of Oxygen in the Rechargeable Lithium−Air Battery. The Journal of Physical Chemistry C 2010, 114 (19), 9178-9186.

8. Peng, Z.; Freunberger, S. A.; Hardwick, L. J.; Chen, Y.; Giordani, V.; Bardé, F.; Novák, P.; Graham, D.; Tarascon, J.-M.; Bruce, P. G., Oxygen Reactions in a Non-Aqueous Li+ Electrolyte. Angewandte Chemie International Edition 2011, 50 (28), 6351-6355.

9. Lu, Y.-C.; Gasteiger, H. A.; Crumlin, E.; McGuire, R.; Shao-Horn, Y., Electrocatalytic Activity Studies of Select Metal Surfaces and Implications in Li-Air Batteries. Journal of The Electrochemical Society 2010, 157 (9), A1016.

10. Sawyer, D. T.; Chiericato, G.; Angelis, C. T.; Nanni, E. J.; Tsuchiya, T., Effects of media and electrode materials on the electrochemical reduction of dioxygen. Analytical Chemistry 1982, 54 (11), 1720-1724.

11. Aurbach, D.; Daroux, M.; Faguy, P.; Yeager, E., The electrochemistry of noble metal electrodes in aprotic organic solvents containing lithium salts. Journal of Electroanalytical Chemistry and Interfacial Electrochemistry 1991, 297 (1), 225-244.

12. Fujinaga, T.; Sakura, S., Polarographic Investigation of Dissolved Oxygen in Nonaqueous Solvent. Bulletin of the Chemical Society of Japan 1974, 47 (11), 2781-2786.

13. McCloskey, B. D.; Scheffler, R.; Speidel, A.; Girishkumar, G.; Luntz, A. C., On the Mechanism of Nonaqueous Li–O2 Electrochemistry on C and Its Kinetic Overpotentials: Some Implications for Li–Air Batteries. The Journal of Physical

Chemistry C 2012, 116 (45), 23897-23905.

14. 121 Cao, R.; Walter, E. D.; Xu, W.; Nasybulin, E. N.; Bhattacharya, P.; Bowden, M. E.; Engelhard, M. H.; Zhang, J.-G., The Mechanisms of Oxygen Reduction and Evolution Reactions in Nonaqueous Lithium–Oxygen Batteries. ChemSusChem 2014, 7 (9), 2436-2440.

15. Xue, K.-H.; McTurk, E.; Johnson, L.; Bruce, P. G.; Franco, A. A., A Comprehensive Model for Non-Aqueous Lithium Air Batteries Involving Different Reaction Mechanisms. Journal of The Electrochemical Society 2015, 162 (4), A614.

16. Black, R.; Lee, J.-H.; Adams, B.; Mims, C. A.; Nazar, L. F., The Role of Catalysts and Peroxide Oxidation in Lithium–Oxygen Batteries. Angewandte Chemie International Edition 2013, 52 (1), 392-396.

17. Lu, Y.-C.; Gasteiger, H. A.; Parent, M. C.; Chiloyan, V.; Shao-Horn, Y., The Influence of Catalysts on Discharge and Charge Voltages of Rechargeable Li–Oxygen Batteries. Electrochemical and Solid-State Letters 2010, 13 (6), A69.

18. Woo, H.; Kang, J.; Kim, J.; Kim, C.; Nam, S.; Park, B., Development of carbon-based cathodes for Li-air batteries: Present and future. Electronic Materials Letters 2016, 12 (5), 551-567.

19. Liaxg, C. C.; Juliard, A. L., The overpotential of oxygen reduction at platinum electrodes. Journal of Electroanalytical Chemistry (1959) 1965, 9 (5), 390-394.

20. Kozawa, A., Effects of anions and cations on oxygen reduction and oxygen evolution reactions on platinum electrodes. Journal of Electroanalytical Chemistry

(1959) 1964, 8 (1), 20-39.

21. Bennion, D. N.; Littauer, E. L., Mathematical Model of a Lithium-Water Electrochemical Power Cell. Journal of The Electrochemical Society 1976, 123 (10), 1462.

22. Littauer, E. L.; Tsai, K. C., Anodic Behavior of Lithium in Aqueous Electrolytes: II . Mechanical Passivation. Journal of The Electrochemical Society 1976, 123 (7), 964.

23. Littauer, E. L.; Tsai, K. C., Corrosion of Lithium in Alkaline Solution. Journal of The Electrochemical Society 1977, 124 (6), 850.

24. Littauer, E. L.; Tsai, K. C.; Hollandsworth, R. P., Anodic Behavior of Lithium in Aqueous Electrolytes: III Influence of Flow Velocity, Contact Pressure, and Concentration. Journal of The Electrochemical Society 1978, 125 (6), 845.

25. Blurton, K. F.; Sammells, A. F., Metal/air batteries: Their status and potential — a review. Journal of Power Sources 1979, 4 (4), 263-279.

26. Abraham, K. M.; Jiang, Z., A Polymer Electrolyte-Based Rechargeable Lithium/Oxygen Battery. Journal of The Electrochemical Society 1996, 143 (1), 1.

27. Read, J., Characterization of the Lithium/Oxygen Organic Electrolyte Battery. Journal of The Electrochemical Society 2002, 149 (9), A1190.

28. Ogasawara, T.; Débart, A.; Holzapfel, M.; Novák, P.; Bruce, P. G., Rechargeable

Li2O2 Electrode for Lithium Batteries. Journal of the American Chemical Society 2006, 128 (4), 1390-1393.

29. Girishkumar, G.; McCloskey, B.; Luntz, A. C.; Swanson, S.; Wilcke, W., Lithium−Air Battery: Promise and Challenges. The Journal of Physical Chemistry Letters 2010, 1 (14), 2193-2203.

30. Yao, X.; Dong, Q.; Cheng, Q.; Wang, D., Why Do Lithium–Oxygen Batteries Fail: Parasitic Chemical Reactions and Their Synergistic Effect. Angewandte Chemie International Edition 2016, 55 (38), 11344-11353.

31. Peng, Z.; Freunberger, S. A.; Chen, Y.; Bruce, P. G., A Reversible and Higher-Rate Li-O2 Battery. Science 2012, 337 (6094), 563-566.

32. Bryantsev, V. S.; Uddin, J.; Giordani, V.; Walker, W.; Addison, D.; Chase, G. V., The Identification of Stable Solvents for Nonaqueous Rechargeable Li-Air Batteries. Journal of The Electrochemical Society 2013, 160 (1), A160-171.

33. McCloskey, B. D.; Bethune, D. S.; Shelby, R. M.; Mori, T.; Scheffler, R.; Speidel, A.; Sherwood, M.; Luntz, A. C., Limitations in Rechargeability of Li-O2 Batteries and Possible Origins. The Journal of Physical Chemistry Letters 2012, 3 (20), 3043-3047.

34. Xu, D.; Wang, Z.-l.; Xu, J.-j.; Zhang, L.-l.; Wang, L.-m.; Zhang, X.-b., A stable sulfone based electrolyte for high performance rechargeable Li–O2 batteries. Chemical Communications 2012, 48 (95), 11674-11676.

35. Elia, G. A.; Hassoun, J.; Kwak, W. J.; Sun, Y. K.; Scrosati, B.; Mueller, F.; Bresser, D.; Passerini, S.; Oberhumer, P.; Tsiouvaras, N.; Reiter, J., An Advanced Lithium–Air Battery Exploiting an Ionic Liquid-Based Electrolyte. Nano Letters 2014, 14 (11), 6572-6577.

36. Xu, D.; Wang, Z.-l.; Xu, J.-j.; Zhang, L.-l.; Zhang, X.-b., Novel DMSO-based electrolyte for high performance rechargeable Li–O2 batteries. Chemical Communications 2012, 48 (55), 6948-6950.

37. Chen, Y.; Freunberger, S. A.; Peng, Z.; Fontaine, O.; Bruce, P. G., Charging a Li–O2 battery using a redox mediator. Nature Chemistry 2013, 5 (6), 489-494.

38. Kwak, W.-J.; Park, J.; Nguyen, T. T.; Kim, H.; Byon, H. R.; Jang, M.; Sun, Y.-K., A dendrite- and oxygen-proof protective layer for lithium metal in lithium–oxygen batteries. Journal of Materials Chemistry A 2019, 7 (8), 3857-3862.

39. Wu, Z.; Tian, Y.; Chen, H.; Wang, L.; Qian, S.; Wu, T.; Zhang, S.; Lu, J., Evolving aprotic Li–air batteries. Chemical Society Reviews 2022, 51 (18), 8045-8101.

40. Johnson, L.; Li, C.; Liu, Z.; Chen, Y.; Freunberger, S. A.; Ashok, P. C.; Praveen, B. B.; Dholakia, K.; Tarascon, J.-M.; Bruce, P. G., The role of LiO2 solubility in O2 reduction in aprotic solvents and its consequences for Li–O2 batteries. Nature Chemistry 2014, 6 (12), 1091-1099.

41. Aetukuri, N. B.; McCloskey, B. D.; García, J. M.; Krupp, L. E.; Viswanathan, V.; Luntz, A. C., Solvating additives drive solution-mediated electrochemistry and enhance toroid growth in non-aqueous Li–O2 batteries. Nature Chemistry 2015, 7

(1), 50-56.

42. Burke, C. M.; Pande, V.; Khetan, A.; Viswanathan, V.; McCloskey, B. D., Enhancing electrochemical intermediate solvation through electrolyte anion selection to increase nonaqueous Li–O2 battery capacity. Proceedings of the National Academy of Sciences 2015, 112 (30), 9293-9298.

43. Liu, T.; Frith, J. T.; Kim, G.; Kerber, R. N.; Dubouis, N.; Shao, Y.; Liu, Z.; Magusin, P. C. M. M.; Casford, M. T. L.; Garcia-Araez, N.; Grey, C. P., The Effect of Water on Quinone Redox Mediators in Nonaqueous Li-O2 Batteries. Journal of the American Chemical Society 2018, 140 (4), 1428-1437.

44. Gao, X.; Chen, Y.; Johnson, L.; Bruce, Peter G., Promoting solution phase discharge in Li–O2 batteries containing weakly solvating electrolyte solutions. Nature Materials 2016, 15 (8), 882-888.

45. Wang, Y.; Liang, Z.; Zou, Q.; Cong, G.; Lu, Y.-C., Mechanistic Insights into Catalyst-Assisted Nonaqueous Oxygen Evolution Reaction in Lithium–Oxygen Batteries. The Journal of Physical Chemistry C 2016, 120 (12), 6459-6466.

46. Sun, B.; Guo, L.; Ju, Y.; Munroe, P.; Wang, E.; Peng, Z.; Wang, G., Unraveling the catalytic activities of ruthenium nanocrystals in high performance aprotic Li–O2 batteries. Nano Energy 2016, 28, 486-494.

47. Hardwick, L. J.; Bruce, P. G., The pursuit of rechargeable non-aqueous lithium–oxygen battery cathodes. Current Opinion in Solid State and Materials Science

2012, 16 (4), 178-185.

48. Kraytsberg, A.; Ein-Eli, Y., Review on Li–air batteries—Opportunities, limitations and perspective. Journal of Power Sources 2011, 196 (3), 886-893.

49. Shao, Y.; Ding, F.; Xiao, J.; Zhang, J.; Xu, W.; Park, S.; Zhang, J.-G.; Wang, Y.; Liu, J., Making Li-Air Batteries Rechargeable: Material Challenges. Advanced Functional Materials 2013, 23 (8), 987-1004.

50. Shao, Y.; Park, S.; Xiao, J.; Zhang, J.-G.; Wang, Y.; Liu, J., Electrocatalysts for Nonaqueous Lithium–Air Batteries: Status, Challenges, and Perspective. ACS Catalysis 2012, 2 (5), 844-857.

51. Luo, Z.-K.; Liang, C.-S.; Wang, F.; Xu, Y.-H.; Chen, J.; Liu, D.; Sun, H.-Y.; Yang, H.; Fan, X.-P., Optimizing Main Materials for a Lithium-Air Battery of High Cycle Life. Advanced Functional Materials 2014, 24 (14), 2101-2105.

52. Beyer, H.; Metzger, M.; Sicklinger, J.; Wu, X.; Schwenke, K. U.; Gasteiger, H. A., Antimony Doped Tin Oxide–Synthesis, Characterization and Application as Cathode Material in Li-O2 Cells: Implications on the Prospect of Carbon-Free Cathodes for Rechargeable Lithium-Air Batteries. Journal of The Electrochemical Society 2017, 164 (6), A1026.

53. Aurbach, D.; Zinigrad, E.; Cohen, Y.; Teller, H., A short review of failure mechanisms of lithium metal and lithiated graphite anodes in liquid electrolyte solutions. Solid State Ionics 2002, 148 (3), 405-416.

54. Lu, Y.-C.; Gallant, B. M.; Kwabi, D. G.; Harding, J. R.; Mitchell, R. R.; Whittingham, M. S.; Shao-Horn, Y., Lithium–oxygen batteries: bridging mechanistic understanding and battery performance. Energy & Environmental Science 2013, 6 (3), 750-768.

55. McCloskey, B. D.; Bethune, D. S.; Shelby, R. M.; Girishkumar, G.; Luntz, A. C., Solvents' Critical Role in Nonaqueous Lithium–Oxygen Battery Electrochemistry. The Journal of Physical Chemistry Letters 2011, 2 (10), 1161-1166.

56. Kowalczk, I.; Read, J.; Salomon, M., Li-air batteries: A classic example of limitations owing to solubilities. Pure and applied chemistry 2007, 79 (5), 851-860.

57. Walker, W.; Giordani, V.; Uddin, J.; Bryantsev, V. S.; Chase, G. V.; Addison, D., A Rechargeable Li–O2 Battery Using a Lithium Nitrate/N,N-Dimethylacetamide Electrolyte. Journal of the American Chemical Society 2013, 135 (6), 2076-2079.

58. Piana, M.; Wandt, J.; Meini, S.; Buchberger, I.; Tsiouvaras, N.; Gasteiger, H. A., Stability of a Pyrrolidinium-Based Ionic Liquid in Li-O2 Cells. Journal of The Electrochemical Society 2014, 161 (14), A1992.

59. Wan, H.; Mao, Y.; Liu, Z.; Bai, Q.; Peng, Z.; Bao, J.; Wu, G.; Liu, Y.; Wang, D.; Xie, J., Influence of Enhanced O2 Provision on the Discharge Performance of Li–air Batteries by Incorporating Fluoroether. ChemSusChem 2017, 10 (7), 1385-1389.

60. Guo, H.; Luo, W.; Chen, J.; Chou, S.; Liu, H.; Wang, J., Review of Electrolytes in

Nonaqueous Lithium–Oxygen Batteries. Advanced Sustainable Systems 2018, 2 (8-9), 1700183.

61. Read, J.; Mutolo, K.; Ervin, M.; Behl, W.; Wolfenstine, J.; Driedger, A.; Foster, D., Oxygen Transport Properties of Organic Electrolytes and Performance of Lithium/Oxygen Battery. Journal of The Electrochemical Society 2003, 150 (10), A1351.

62. Mizuno, F.; Nakanishi, S.; Kotani, Y.; Yokoishi, S.; Iba, H., Rechargeable Li-Air Batteries with Carbonate-Based Liquid Electrolytes. Electrochemistry 2010, 78 (5), 403-405.

63. Freunberger, S. A.; Chen, Y.; Peng, Z.; Griffin, J. M.; Hardwick, L. J.; Bardé, F.; Novák, P.; Bruce, P. G., Reactions in the Rechargeable Lithium–O2 Battery with Alkyl Carbonate Electrolytes. Journal of the American Chemical Society 2011, 133 (20), 8040-8047.

64. Laoire, C.; Mukerjee, S.; Plichta, E. J.; Hendrickson, M. A.; Abraham, K. M., Rechargeable Lithium/TEGDME- LiPF6/O2 Battery. Journal of The Electrochemical Society 2011, 158 (3), A302.

65. Read, J., Ether-Based Electrolytes for the Lithium/Oxygen Organic Electrolyte Battery. Journal of The Electrochemical Society 2006, 153 (1), A96.

66. McCloskey, B. D.; Scheffler, R.; Speidel, A.; Bethune, D. S.; Shelby, R. M.; Luntz, A. C., On the Efficacy of Electrocatalysis in Nonaqueous Li–O2 Batteries. Journal

of the American Chemical Society 2011, 133 (45), 18038-18041.

67. Zhang, J.; Sun, B.; Xie, X.; Kretschmer, K.; Wang, G., Enhancement of stability for lithium oxygen batteries by employing electrolytes gelled by poly(vinylidene fluoride-co-hexafluoropropylene) and tetraethylene glycol dimethyl ether. Electrochimica Acta 2015, 183, 56-62.

68. Freunberger, S. A.; Chen, Y.; Drewett, N. E.; Hardwick, L. J.; Bardé, F.; Bruce, P. G., The Lithium–Oxygen Battery with Ether-Based Electrolytes. Angewandte Chemie International Edition 2011, 50 (37), 8609-8613.

69. Sharon, D.; Etacheri, V.; Garsuch, A.; Afri, M.; Frimer, A. A.; Aurbach, D., On the Challenge of Electrolyte Solutions for Li–Air Batteries: Monitoring Oxygen Reduction and Related Reactions in Polyether Solutions by Spectroscopy and EQCM. The Journal of Physical Chemistry Letters 2013, 4 (1), 127-131.

70. [61] Sharon, D.; Hirshberg, D.; Afri, M.; Frimer, A. A.; Aurbach, D., The importance of solvent selection in Li–O2 cells. Chemical Communications 2017, 53 (22), 3269-3272.

71. [63] Sharon, D.; Afri, M.; Noked, M.; Garsuch, A.; Frimer, A. A.; Aurbach, D., Oxidation of Dimethyl Sulfoxide Solutions by Electrochemical Reduction of Oxygen. The Journal of Physical Chemistry Letters 2013, 4 (18), 3115-3119.

72. Kwabi, D. G.; Batcho, T. P.; Amanchukwu, C. V.; Ortiz-Vitoriano, N.; Hammond, P.; Thompson, C. V.; Shao-Horn, Y., Chemical Instability of Dimethyl Sulfoxide in

Lithium–Air Batteries. The Journal of Physical Chemistry Letters 2014, 5 (16), 2850-2856.

73. Younesi, R.; Norby, P.; Vegge, T., A New Look at the Stability of Dimethyl Sulfoxide and Acetonitrile in Li-O2 Batteries. ECS Electrochemistry Letters 2014, 3 (3), A15.

74. Mozhzhukhina, N.; Méndez De Leo, L. P.; Calvo, E. J., Infrared Spectroscopy Studies on Stability of Dimethyl Sulfoxide for Application in a Li–Air Battery. The Journal of Physical Chemistry C 2013, 117 (36), 18375-18380.

75. Lee, H.; Lee, D. J.; Lee, J.-N.; Song, J.; Lee, Y.; Ryou, M.-H.; Park, J.-K.; Lee, Y. M., Chemical aspect of oxygen dissolved in a dimethyl sulfoxide-based electrolyte on lithium metal. Electrochimica Acta 2014, 123, 419-425.

76. Bryantsev, V. S.; Giordani, V.; Walker, W.; Blanco, M.; Zecevic, S.; Sasaki, K.; Uddin, J.; Addison, D.; Chase, G. V., Predicting Solvent Stability in Aprotic Electrolyte Li–Air Batteries: Nucleophilic Substitution by the Superoxide Anion Radical (O2•–). The Journal of Physical Chemistry A 2011, 115 (44), 12399-12409.

77. Chen, Y.; Freunberger, S. A.; Peng, Z.; Bardé, F.; Bruce, P. G., Li–O2 Battery with a Dimethylformamide Electrolyte. Journal of the American Chemical Society 2012, 134 (18), 7952-7957.

78. Nasirzadeh, K.; Zimin, D.; Neueder, R.; Kunz, W., Vapor-Pressure Measurements of Liquid Solutions at Different Temperatures: Apparatus for Use over an

Extended Temperature Range and Some New Data. Journal of Chemical & Engineering Data 2004, 49 (3), 607-612.

79. Sharon, D.; Hirsberg, D.; Afri, M.; Garsuch, A.; Frimer, A. A.; Aurbach, D., Reactivity of Amide Based Solutions in Lithium–Oxygen Cells. The Journal of Physical Chemistry C 2014, 118 (28), 15207-15213.

80. Kuboki, T.; Okuyama, T.; Ohsaki, T.; Takami, N., Lithium-air batteries using hydrophobic room temperature ionic liquid electrolyte. Journal of Power Sources 2005, 146 (1), 766-769.

81. Zhang, D.; Li, R.; Huang, T.; Yu, A., Novel composite polymer electrolyte for lithium air batteries. Journal of Power Sources 2010, 195 (4), 1202-1206.

82. Nanjundiah, C.; McDevitt, S. F.; Koch, V. R., Differential Capacitance Measurements in Solvent-Free Ionic Liquids at Hg and C Interfaces. Journal of The Electrochemical Society 1997, 144 (10), 3392.

83. Nakamoto, H.; Suzuki, Y.; Shiotsuki, T.; Mizuno, F.; Higashi, S.; Takechi, K.; Asaoka, T.; Nishikoori, H.; Iba, H., Ether-functionalized ionic liquid electrolytes for lithium-air batteries. Journal of Power Sources 2013, 243, 19-23.

84. Sawyer, D. T.; Roberts, J. L., Electrochemistry of oxygen and superoxide ion in dimethylsulfoxide at platinum, gold and mercury electrodes. Journal of Electroanalytical Chemistry (1959) 1966, 12 (2), 90-101.

85. Ottakam Thotiyl, M. M.; Freunberger, S. A.; Peng, Z.; Bruce, P. G., The carbon electrode in nonaqueous Li–O2 cells. Journal of the American Chemical Society 2013, 135 (1), 494-500.

86. Itkis, D. M.; Semenenko, D. A.; Kataev, E. Y.; Belova, A. I.; Neudachina, V. S.; Sirotina, A. P.; Hävecker, M.; Teschner, D.; Knop-Gericke, A.; Dudin, P.; Barinov, A.; Goodilin, E. A.; Shao-Horn, Y.; Yashina, L. V., Reactivity of Carbon in Lithium–Oxygen Battery Positive Electrodes. Nano Letters 2013, 13 (10), 4697-4701.

87. Zhou, W.; Li, J.; Nie, H.; Zhang, Y.; Xi, X.; Zhang, H., Carbon electrode for nonaqueous Li-O2 battery: the influence of surface oxygen species. Electrochimica Acta 2014, 138, 410-416.

88. Mahne, N.; Renfrew, S. E.; McCloskey, B. D.; Freunberger, S. A., Electrochemical Oxidation of Lithium Carbonate Generates Singlet Oxygen. Angewandte Chemie International Edition 2018, 57 (19), 5529-5533.

89. Carboni, M.; Brutti, S.; Marrani, A. G., Surface Reactivity of a Carbonaceous Cathode in a Lithium Triflate/Ether Electrolyte-Based Li–O2 Cell. ACS Applied Materials & Interfaces 2015, 7 (39), 21751-21762.

90. Liang, Z.; Lu, Y.-C., Critical Role of Redox Mediator in Suppressing Charging Instabilities of Lithium–Oxygen Batteries. Journal of the American Chemical Society 2016, 138 (24), 7574-7583.

91. Gao, X.; Chen, Y.; Johnson, L. R.; Jovanov, Z. P.; Bruce, P. G., A rechargeable lithium–oxygen battery with dual mediators stabilizing the carbon cathode. Nature

Energy 2017, 2 (9), 17118.

92. Huang, J. Y.; Zhong, L.; Wang, C. M.; Sullivan, J. P.; Xu, W.; Zhang, L. Q.; Mao, S. X.; Hudak, N. S.; Liu, X. H.; Subramanian, A.; Fan, H.; Qi, L.; Kushima, A.; Li, J., In Situ Observation of the Electrochemical Lithiation of a Single SnO2 Nanowire Electrode. Science 2010, 330 (6010), 1515-1520.

93. Kühne, M.; Börrnert, F.; Fecher, S.; Ghorbani-Asl, M.; Biskupek, J.; Samuelis, D.; Krasheninnikov, A. V.; Kaiser, U.; Smet, J. H., Reversible superdense ordering of lithium between two graphene sheets. Nature 2018, 564 (7735), 234-239.

94. Alcántara, R.; Jaraba, M.; Lavela, P.; Tirado, J., Electrochemical, 6Li MAS NMR, and X-ray and Neutron Diffraction Study of LiCo x Fe y Mn2-(x+ y) O4 Spinel Oxides for High-Voltage Cathode Materials. Chemistry of materials 2003, 15 (5), 1210-1216.

95. Shui, J.-L.; Okasinski, J. S.; Kenesei, P.; Dobbs, H. A.; Zhao, D.; Almer, J. D.; Liu, D.-J., Reversibility of anodic lithium in rechargeable lithium–oxygen batteries. Nature Communications 2013, 4 (1), 2255.

96. Xie, Q.; Li, Z.; Deng, C.; Liu, M.; Zhang, Y.; Ma, M.; Xia, S.; Xiao, X.; Yin, D.; Yao, S., Electrochemical quartz crystal microbalance monitoring of the cyclic voltammetric deposition of polyaniline. A laboratory experiment for undergraduates. Journal of chemical education 2007, 84 (4), 681.

97. Aurbach, D.; Zaban, A., The Use of EQCM for the Study of Nonactive Metal

Electrodes in Propylene Carbonate-LiAsF6 Solutions: Significance of the Data Obtained. Journal of the Electrochemical Society 1995, 142 (7), L108.

98. Aurbach, D.; Moshkovich, M., A Study of Lithium Deposition-Dissolution Processes in a Few Selected Electrolyte Solutions by Electrochemical Quartz Crystal Microbalance. Journal of the Electrochemical Society 1998, 145 (8), 2629.

99. Tomita, K.; Noguchi, H.; Uosaki, K., Effect of Water and HF on the Distribution of Discharge Products at Li–O2 Battery Cathode. ACS Applied Energy Materials 2018, 1 (7), 3434-3442.

100. Ostrovskii, D.; Ronci, F.; Scrosati, B.; Jacobsson, P., Reactivity of lithium battery electrode materials toward non-aqueous electrolytes: spontaneous reactions at the electrode–electrolyte interface investigated by FTIR. Journal of power sources 2001, 103 (1), 10-17.

101. Dokko, K.; Mohamedi, M.; Anzue, N.; Itoh, T.; Uchida, I., In situ Raman spectroscopic studies of LiNi x Mn 2− x O 4 thin film cathode materials for lithium ion secondary batteries. Journal of Materials Chemistry 2002, 12 (12), 3688-3693.

102. Grey, C. P.; Dupré, N., NMR studies of cathode materials for lithium-ion rechargeable batteries. Chemical reviews 2004, 104 (10), 4493-4512.

103. Totir, D. A.; Bae, I. T.; Hu, Y.; Antonio, M. R.; Stan, M. A.; Scherson, D. A., In situ Fe K-edge X-ray absorption fine structure of a pyrite electrode in a

Li/polyethylene oxide (LiClO4)/FeS2 battery environment. The Journal of Physical Chemistry B 1997, 101 (47), 9751-9756.

104. Gireaud, L.; Grugeon, S.; Pilard, S.; Guenot, P.; Tarascon, J.-M.; Laruelle, S., Mass spectrometry investigations on electrolyte degradation products for the development of nanocomposite electrodes in lithium ion batteries. Analytical chemistry 2006, 78 (11), 3688-3698.

105. Imhof, R.; Novák, P., Oxidative electrolyte solvent degradation in lithium-ion batteries: an In Situ differential electrochemical mass spectrometry investigation. Journal of The Electrochemical Society 1999, 146 (5), 1702.

106. Lanz, M.; Novák, P., DEMS study of gas evolution at thick graphite electrodes for lithium-ion batteries: the effect of γ-butyrolactone. Journal of power sources 2001, 102 (1-2), 277-282.

107. Abraham, D.; Roth, E.; Kostecki, R.; McCarthy, K.; MacLaren, S.; Doughty, D., Diagnostic examination of thermally abused high-power lithium-ion cells. Journal of power sources 2006, 161 (1), 648-657.

108. Larsson, F.; Andersson, P.; Blomqvist, P.; Lorén, A.; Mellander, B.-E., Characteristics of lithium-ion batteries during fire tests. Journal of Power Sources 2014, 271, 414-420.

109. Ohsaki, T.; Kishi, T.; Kuboki, T.; Takami, N.; Shimura, N.; Sato, Y.; Sekino, M.; Satoh, A., Overcharge reaction of lithium-ion batteries. Journal of power sources

2005, 146 (1-2), 97-100.

110. Nedjalkov, A.; Meyer, J.; Köhring, M.; Doering, A.; Angelmahr, M.; Dahle, S.; Sander, A.; Fischer, A.; Schade, W., Toxic gas emissions from damaged lithium ion batteries—analysis and safety enhancement solution. Batteries 2016, 2 (1), 5.

Chapter 2: Experimental

2.1 Materials

Porous carbon sheet (KJCNT; donated by KJ Specialty Paper) was used as a cathode material because of their uniform and simple pore structures than Ketjenblack and carbon nanotube cathodes, used in more practical cells. The KJCNT sheet was cut into disc with 16 mm in diameter and then baked in a tube furnace at 900℃ for 3 hr under an Ar atmosphere to remove internal sodium and polymer binders etc., and then transferred to dry room for use. Lithium cions (thickness 200 um, diameter 16 mm) were obtained from Honjo Metal Co., Ltd.. $LiNO_3$ (99%) was obtained from Wako Pure Chemical Industries. LiTFSI (99.9%) (battery grade) is obtained from Kishida Chemical Co., Ltd. and used as received. Battery grade TEGDME (98%) is obtain from Kishida Chemical Co., Ltd. and used as received. High purity TEGDME (≥99%) is obtained from Sigma-Aldrich. Isotopes of $^{12}CD_3$_TEGDME and $^{13}CH_3$_TEGDME were synthesized and provided by Dr. Mandai in NIMS. 1M LiTFSI dissolved in TEGDME was used as electrolyte, the water content in electrolyte was measured around 40 ppm by using Karl Fischer Moisture Meter CA-21. Polyethylene (PE)

membrane separator (thickness 20 um) was obtained from W-SCOPE Corp, cut into 19.5 mm diameter disc, and then dried in a vacuum oven at 40 ℃ for 10 hr before use. Stainless steel mesh (thickness 200 um, diameter 16.7 mm, aperture ratio 73%) was obtained from Hohsen Corp. Isotope $^{18}O_2$ (≥98 atom%) was purchased from Taiyo Nippon Sanso Corp. The impurities and analysis value by gas chromatogram in $^{18}O_2$ are ^{16}O ~ 1.2 atom%, ^{17}O ~ 0.1 atom%, ^{18}O ~ 98.7 atom%. Molecular structure of salt LiTFSI, isotope solvent CH_3_TEGDME, CD_3_TEGDME, and $^{13}CH_3$_TEGDME are shown in **Figure 2-1.**

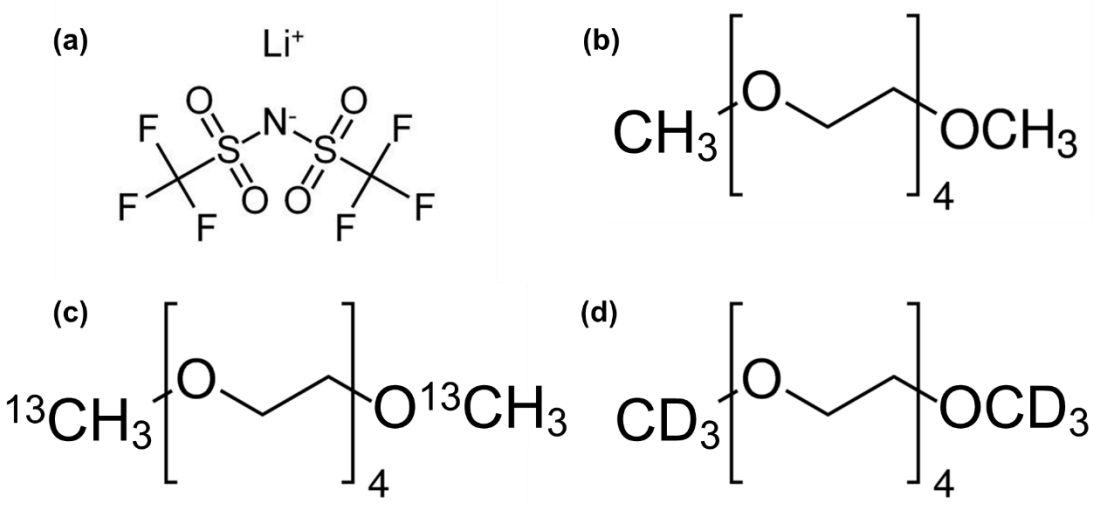

Figure 2-1. Molecule structure of (a) LiTFSI, (b) TEGDME, (c) $^{13}CH_3$_TEGDME, and (d) CD_3_TEGDME.

Li metal anode. Coin shaped Li metal foil (16 mm ϕ and 200 μm thick; Honjo Metal) was used as received.

Electrolyte solution. Lithium bis(trifluoromethanesulfonyl)imide (LiTFSI) (Li battery grade from Kishida Chemical) and two types of tetraethylene glycol dimethyl ether (TEGDME) (BG-TEGDME: Li battery Grade: ~98% from Kishida Chemical, and HP-TEGDME: ≥99% from Sigma-Aldrich) were used as received, and HP-TEGDME was also dried by 4A molecular sieves for 2 days. The water amount of BG-TEGDME, HP-TEGDME and molecular sieves dried HP-TEGDME are around 45, 250 and 45, respectively. 1 M LiTFSI BG-/HP-TEGDME and 1 M LiTFSI HP-TEGDME solution prepared in the dry room has a water content of around 40 and 200 ppm determined by Karl Fischer titration. Gas chromatograms of head space gas of the cells prepared using BG-TEGDME (bottom panel) and HP-TEGDME (top panel) are shown in **Figure 2-2**.

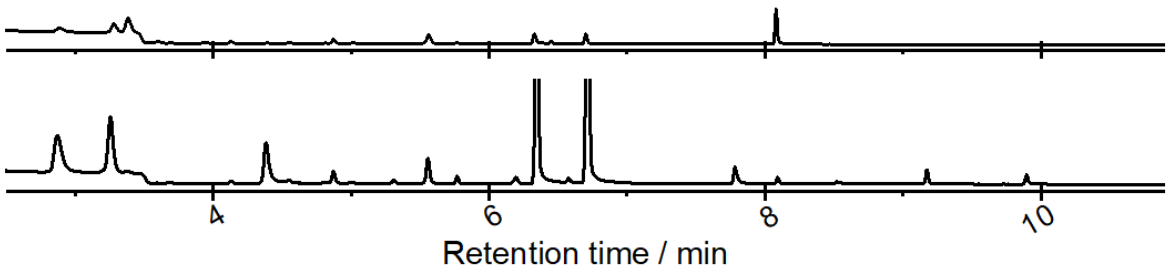

Figure 2-2. Gas chromatograms of head space gas sampled by CTPC-GC/MS of the cells prepared using BG-TEGDME (bottom panel) and HP-TEGDME (top panel).

Separator. Polyethylene (PE) membrane (20 μm thick, W-SCOPE) was cut to 19.5 mm in diameter and dried in a vacuum oven (Model: DP300; Yamato Scientific Co., Ltd.) at 40℃ for 10 hr before use.

KJCNT cathode. CNT-based carbon sheet (KJCNT; donated by KJ Specialty Paper) was used as cathode after baking treatment because of their uniform and simple pore structure compared to Ketjenblack and carbon nanotube-based cathodes, which was used for more practical cells. KJCNT sheets were cut into 16 mm diameter and baked in an Ar atmosphere a at 900℃ for 3 hr in a tube furnace to increase porosity. The morphology of KJCNT sheets before and after baking were evaluated by SEM. As is shown in **Figure 2-3** that after baking, the binder in KJCNT was completely removed and a porous surface appear.

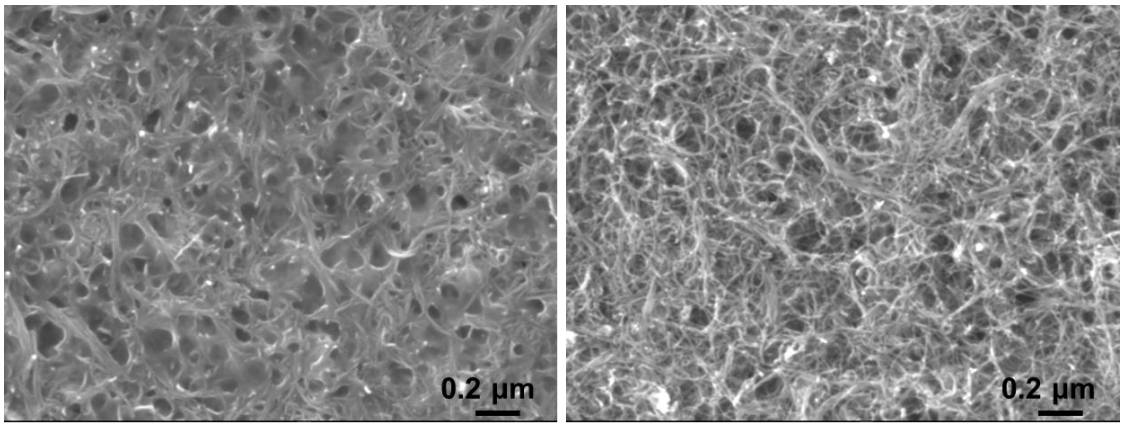

Figure 2-3. Scanning electron microscope images (SEM, JIB-4501, JEOL) of the KJCNT cathode before (left) and after (right) baking.

The pore size distribution of KJCNT sheet after pre-treatment was determined by a specific Brunauer-Emmette-Teller (BET) (3Flex, Micromeritics) method and mercury intrusion porosimetry (AutoPore IV 95000, Micromeritics) methods. The BET results shown in **Figure 2-4(a)** indicates that the pore size distribution was in the ranges between 0.01 and 0.2 μm. The mercury intrusion, which can evaluate a wider pore size range, confirmed that the pore size distribution was mainly from 0.01 to 0.2 μm, with only a few macropores larger than 10 μm (**Figure 2-4 (b)**). No adsorption data were obtained for KJCNT before baking, indicating that almost no pores are present before baking treatment. For comparison, BET results of Ketjenblack and regular carbon nanotube sheet are shown in **Figure 2-4 (c)** and **(d)**, respectively.

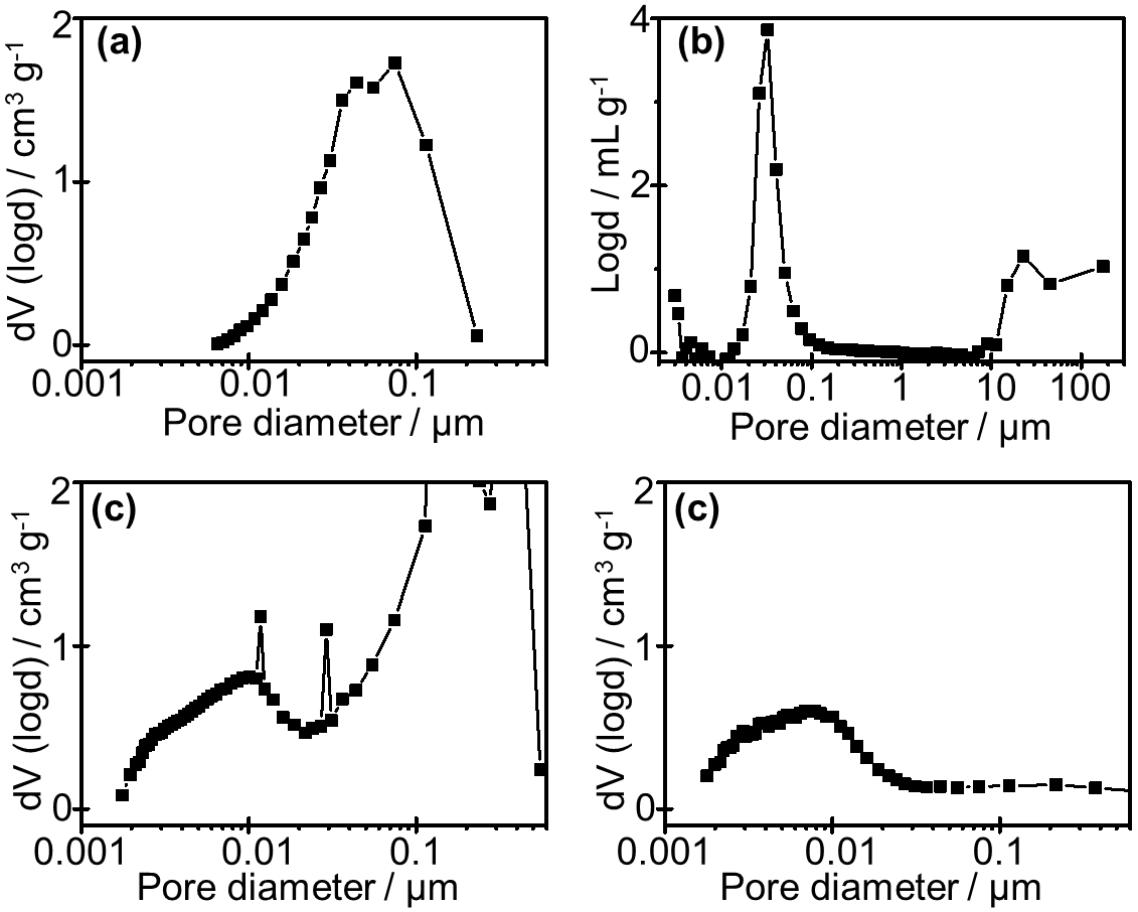

Figure 2-4. The pore size distribution of the KJCNT cathode after baking treatment was determined by (a) specific Brunauer-Emmette-Teller (BET) (3Flex, Micromeritics) and (b) mercury intrusion porosimetry (AutoPore IV 95000, Micromeritics) methods, the pore size distribution (c) and (d) that of Ketjenblack and regular carbon nanotube sheet determined by BET.

The above results indicate that the baked KJCNT is suitable as a cathode for LAB.

The pretreated KJCNT was then transferred to a dry room for use.

2.2 Cell assembly

A custom-made test cell (stainless steel; inner diameter 45 mm, inner height 15 mm) equipped with gas inlet and outlet ports was assembled in a dry-booth (dew point less than -90℃) in a dry-room (dew point less than -60℃) by stacking a Li metal foil (diameter 16 mm, thickness 200 μm), a PE membrane (diameter 19.5 mm, thickness 20 μm), on top of which 15 μL of the 1M LiTFSI TEGDME solution was placed as uniformly as possible, a CNT-based porous carbon sheet (diameter 16 mm, thickness 50 μm), and a stainless steel mesh (diameter 16.7 mm, thickness 200 μm, and 73% aperture: Hohsen), and a conductive spring to provide the cell assembly with a pressure of 35 kPa. A schematic diagram of the cell is shown in **Figure 2-5**.

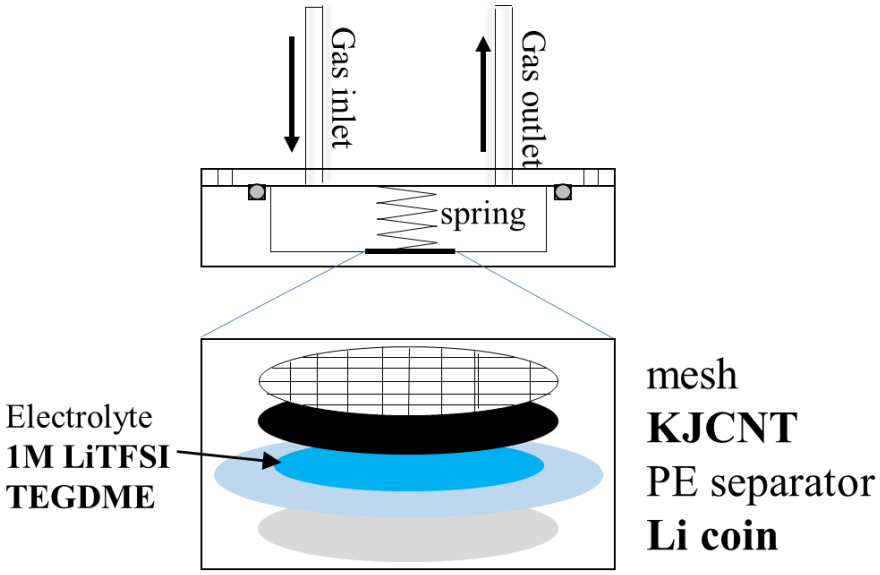

Figure 2-5. Fabrication of Lithium-oxygen cell

2.3 Measurements

2.3.1 Electrochemical Measurements

After assembly, the cell was purged with O_2 flowing at 2 cc/min for 2 hr before the electrochemical operation. The discharge under O_2 flow rate at 2 cc/min was carried out by a galvanostatic electrochemical tester (HJ1020mSD8, Hokuto Denko Corp) with a current density of 0.2 mA/cm^2 and cutoff potential at 2 V (vs. Li+/Li) or cut off time of 10 hr. Then 2 hr rest with O_2 flowing at 2 cc/min (for GC/MS experiments), or switch O_2 to He purge at 20 cc/min for 1 hr 40 min to totally exchange the inside cell O_2 to He, then decrease the He gas flow rate to 5 cc/min for 20 min (for QMS measurements). Then the charging process, keep O_2 or He flow at 2 or 5 cc/min for GC/MS or QMS experiments, is conducted using either a galvanostatic electrochemical tester with a current density of 0.2 mA/cm^2, a cutoff potential of 4.8 V (vs. Li+/Li), and a constant current with a cutoff time of 10 hr, or a potentiostat/galvanostat (HZ-7000, Hokuto Denko) to measure linear sweep voltammetry (LSV) in the range of open-circuit potential (OCP) to 4.8 V with at a sweep rate of 50 mV s^{-1}.

2.3.2 Mass spectroscopic measurements

2.3.2.1 Theory of mass spectrometry

2.3.2.1.1 Theory of gas chromatography

Gas chromatography represents a form of separation technique in which an introduced gas carries a mixture of sample gases pass through a column containing a liquid or solid stationary phase. Separation is then achieved by the distribution of analytes between the mobile and stationary phases.

The distribution of analytes between stationary and mobile phases can be described using partition coefficient;

$$K = \frac{C_S}{C_G} \quad (2\text{-}1)$$

where C_S is the concentration of components in the stationary phase or at the solid surface and C_G is the concentration of components in the gas phase.

$$\beta = \frac{V_m}{V_s} \quad (2\text{-}2)$$

$$K' = \frac{K}{\beta} = \frac{C_S}{C_G} \quad (2\text{-}3)$$

β is the phase ratio. K' is the capacity factor.

This equation allows estimating the retention of a given system. Larger values of K' result in longer retention times because column length, inner diameter, and stationary phase film thickness are all increase. Conversely, lower capacity factor K', result in a shorter retention and analysis time.

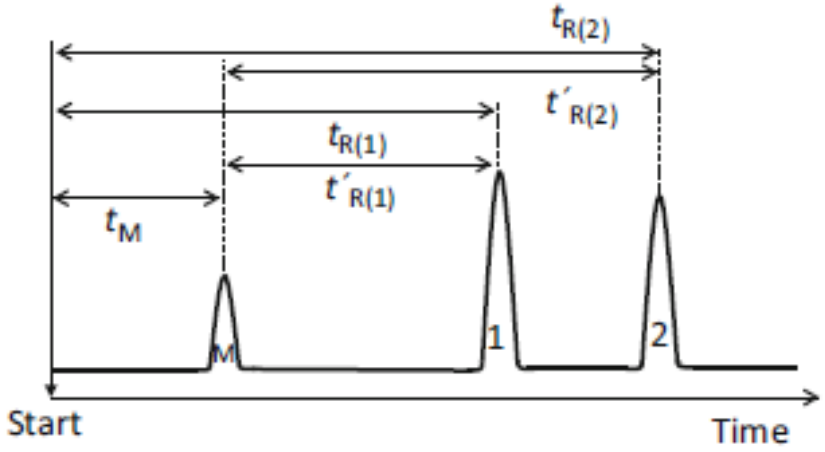

Figure 2-5. Chromatogram.[1] t_M: Total retention time of the mobile phase. $t_{R(1)}$: Total retention time of component 1. $t'_{R(1)}$: Reduced retention time of component 1.

Figure 2-5 shows a typical chromatogram generated from a GC run. First, the peak of the mobile phase occurs at the shortest retention time. The mobile phase compound 1 and compound 2 then reach the detector with longer retention times. Retention of compounds depends on the interaction with the stationary phase and the volatility of the components. The volatility of the component. For example, whether

the retention force is purely dispersive (London force) or induced dipole-dipole, dipole-dipole, or H-bridging forces, depends on the composition of the stationary phase and analyte and the composition of the analyte[1]. Once the stationary phase reaches a certain polarity, the polar analytes are retained to a higher degree than non-polar analytes. When the stationary phase is changed to a non-polar system, the elution sequence is reversed.

The van Deemter equation (2-4) is used to describe the gas chromatography process. This equation evolved from earlier work and was later extended with Glueckauf's theory. Taking into account the mass transfer resistance between the two phases due to diffusion, the equation is derived.

The general form for the van Deemter equation is

$$H = A + \frac{B}{u} + Cu \quad (2\text{-}4)$$

where

$A = 2\lambda d_p$ = eddy diffusion term

$B = 2\gamma Dg$ = longitudinal or ordinary diffusion term

$C = (8/\pi^2)[k/(1 + k)^2](d^2_f /D_l)$ = nonequilibrium or resistance to mass transfer term

The basic Van Deemter equation shows the dependence of the theoretical plate height H for gas velocity u on the constants A, B and C.

Figure 2-6 shows the Van Deemter curve and its various dependencies. A presents eddy diffusion, which describes the path of analyte molecules through the stationary phase. Assuming a packed column, the trajectory of the analyte molecule depends on the homogeneity of the stationary phase, i.e., the narrow particle size distribution. This is explained by the coefficient λ, which describes the packing uniformity and the particle size d_p in van Deemter equation (2-4). Additionally, A is independent of gas velocity and is only affected by the characteristics of the stationary phase. B describes longitudinal diffusion, and can be described by the diffusion coefficient of the analyte in the mobile phase D_b and the labyrinth factor of the pore network γ. The increase in B in the Van-Deemter equation is due to the fact that increase in diffusion with time, as the molecules to be analyzed stay longer in the column as the gas velocity decreases. Finally, C describes the resistance to mass transfer, which describes the delay in mass transfer and leads to a broadening of the peak. C is affected by the capacity factor K', the thickness of the chromatographic layer d_f and the diffusion coefficient D_s in the

stationary phase. By increasing the gas velocity, the *C* is linearly enhanced as mass transfer is further delayed at higher flow rates.

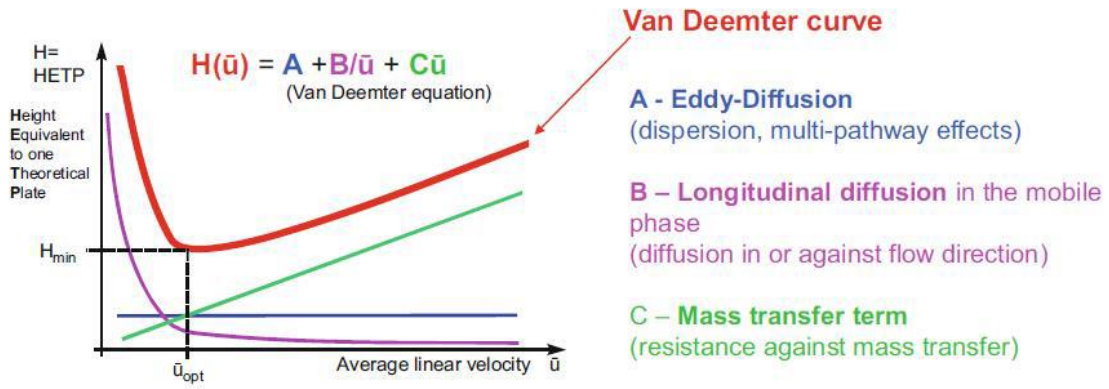

Figure 2-6. Van Deemter curve for a packed column.[1]

2.3.2.1.2 Theory of quadrupole magnetic field

The quadrupole magnetic field is represented by its linear dependence on the coordinate positions. In the Cartesian coordinates x, y, z

$$E = E_0 (\lambda x + \sigma y + \gamma z) \quad (2\text{-}5)$$

where λ, σ and y are weighting constants and E_0 is a position-independent factor, possibly as a function of time. In a perfect magnetic field, since the ion motion can be considered independently in each direction, the three directions are not coupled to each other, thus, greatly simplifies the analysis of the ion motion. For ions in a quadrupole

magnetic field, the force e*E* acting on the ion increases with the ion's displacement from zero.

The field is bounded by the Laplace equation. Assuming no space charge inside the electrode structure

$$\nabla \cdot E = 0 \qquad (2\text{-}6)$$

Thus,

$$\lambda + \sigma + \gamma = 0 \qquad (2\text{-}7)$$

The simplest way of satisfying equation (2-7) which obviously implies that

$$\lambda = -\sigma;\ \gamma = 0 \qquad (2\text{-}8)$$

In order to express these conclusions more concretely, it is necessary to determine the form of the potential to be applied. This is done by integration, since $-(d\Phi/dx) = E_x$ etc. The potential energy Φ can be appropriately expressed as follow:

$$\Phi = -1/2 \cdot E_0 (\lambda x^2 + \sigma y^2 + \gamma z^2) \qquad (2\text{-}9)$$

Consider equation (2-8)

$$\Phi = - 1/2 \cdot E_0 \lambda(x^2 - y^2) \quad (2\text{-}10)$$

The isopotential lines are shown in **Figure 2-7(a)**. They are a set of rectangular hyperbolic curves in the xy-plane, which geometrically have a quadruple symmetry about the z-axis. As shown in **Figure 2-7(b)**, this potential is generated by a set of four hyperbolic cylinders with opposite charges at adjacent electrodes. If the minimum distance between the opposing electrodes is $2r_0$ and the potential between the opposing electrodes is Φ_0, then equation (2-10) becomes

$$\Phi = \Phi_0 (x^2 - y^2) / 2r_0^2 \quad (2\text{-}11)$$

$$\text{Since } \lambda = -1 / r_0^2$$

In practice, round rods that are very close to the correct hyperbolic rods are usually used, but these lead to field failures and impose certain limitations. **Fig. 2-7(b)** represents the electrode structure of a mass filter.

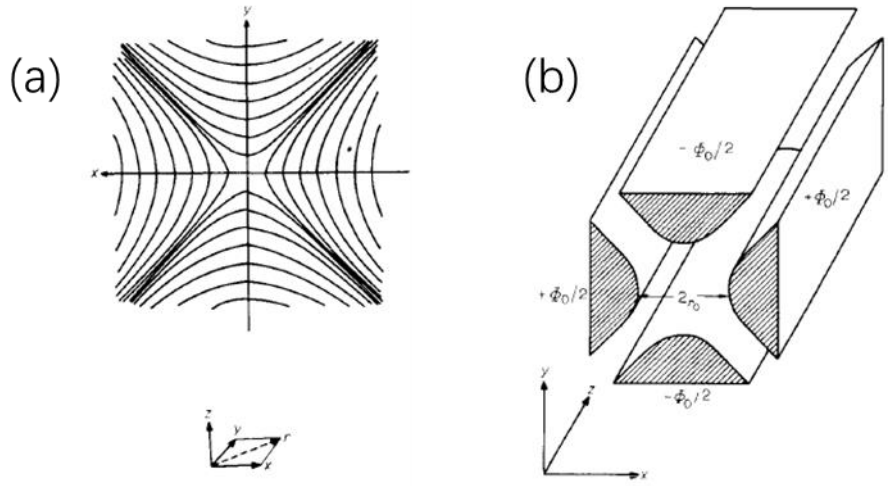

Figure 2-7. (a) Equipotential lines for a quadrupole field where $\Phi = -1/2\ E_0\lambda\ (x^2 - y^2)$; (b) The electrode structure required to generate the potential shown in (a). These are the ideal quadrupole mass filter electrodes having hyperbolic cross-sections.

2.3.2.2 Cold trap

In the analysis of products from LOB, the products are volatile to varying degrees due to the electrolyte properties of the organics. Therefore, in order to better target and quantify the products, a pre-concentration device was introduced to assist GC/MS by injecting the pre-concentrated analytes into the gas chromatograph for accurate mass spectrometry of all products.

Cold trap. As the carrier gas bubbles pass through the cell headspace, they carry volatile products into the trap system. Vapor-extracted volatile compounds are trapped in the cold trap, primarily in the capillary then cooled with liquid nitrogen or solid

carbon dioxide. This step can be performed in either open or closed loop[2]. In the open-loop configuration, untapped molecules are eliminated. In the closed-loop approach, all the gas phases flow passing through the closed-loop trap[3] are trapped. The captured compounds are desorbed by an electric heater (in most cases) into the GC-column to be analyzed. Thermal desorption has the advantages of (i)100% analysis of the trap content and (ii)no solvent contamination. Additionally, the three main advantages of cryogenic trapping over other trapping techniques, such as packed traps[4], solvent trapping[5], and multi-channel traps[6], are: (i)no artifacts from thermal desorption, (ii)no residues, and (iii)no capacity limitation problems.

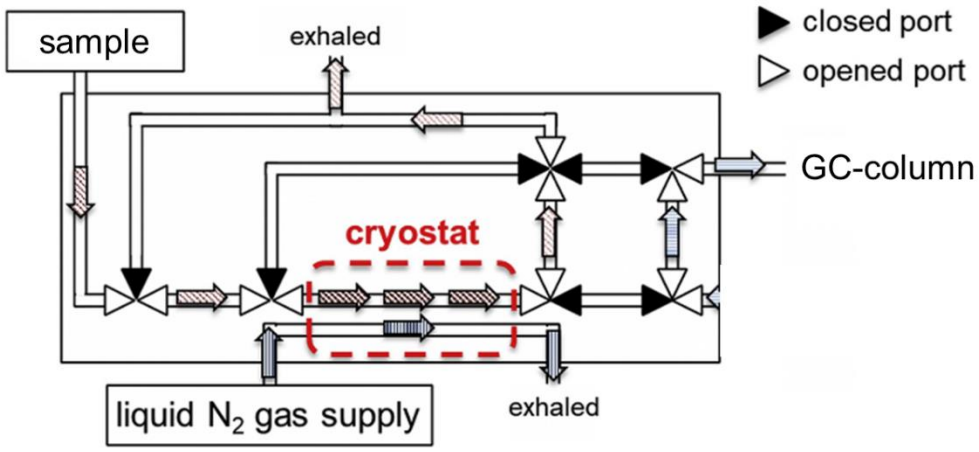

Figure 2-8. Internal structure of the normal gas pre-concentrator and the path during concentration.[7]

2.3.2.3 Mass spectrometry systems

2.3.2.3.1 On-line QMS & TSP-GC/MS system

Figure 2-9 shows the experimental set-up. The gas passes through the air-tight cell, which is electrically connected with a potentiostat, and will carry with products to the following mass chromatography. After 10 hr of discharge, the inlet gas will be switched from O_2 to He and purged at 20 cc/min for 1 hr 40 min to completely replace the O_2 inside cell with He. Then the He gas flow is reduced to 5 cc/min for the LSV measurement, and the outlet gas is introduced into the on-line QMS and 16 channel gas collectors.

On-line mass spectrometry was carried out with M-201GA-DM quadrupole mass spectrometer (QMS) by Canon Anelva Corp. The outlet gas was partially (approximately 1%) introduced into the on-line QMS chamber via a 4 m long capillary (inner diameter 0.05 mm). The mass numbers of 12-90 were monitored by the on-line QMS during a voltage sweep of 50 mV s^{-1}.

Ex-situ mass spectroscopy was carried out on an Agilent Technologies 5977A mass selective detector (MSD) gas chromatography (GC) System. During LSV, gas-

phase decomposition products were collected every 1 hr by seven Agilent J&W HP-PLOT Q columns (inner diameter 0.53 mm, length 2 cm) parallel packed inside a 1/8" stainless tube cartridge and then seven columns were transferred to a thermal separation probe (TSP) to desorb the collected gas into GC/MS under 250 ℃. GC/MS results were analyzed against the date base (NIST library).

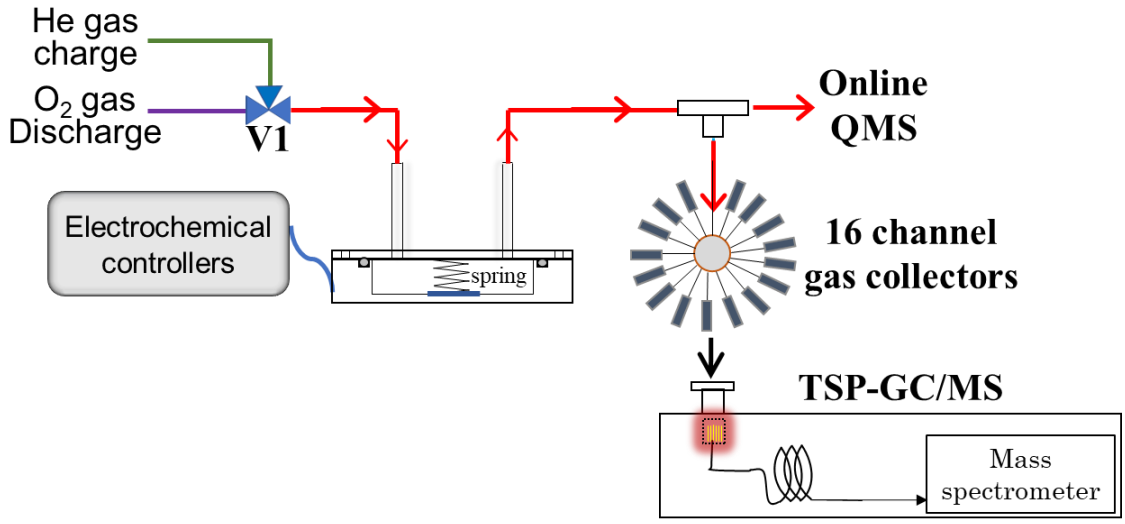

Figure 2-9. Schematic diagram of experimental set-up

2.3.3.3.2 On-line CPTC-GC/MS system

After assembly, the cell was connected to an O_2 line (1 atm), electrochemical controllers (charge/discharge system: HJ1020mSD8, Hokuto Denko and electrochemical measurement system: HZ-7000, Hokuto Denko), and to the cold trap pre-concentrator (CTPC) (NIT-P-3R: Pico-Device). **Figure 2-10(a)** shows a schematic

diagram of the on-line CTPC-GC/MS system constructed in this work for real-time detection of molecules generated in a cell during discharge/charge. The system consists of air-tight cell, CTPC, GC/MS, and their controllers.

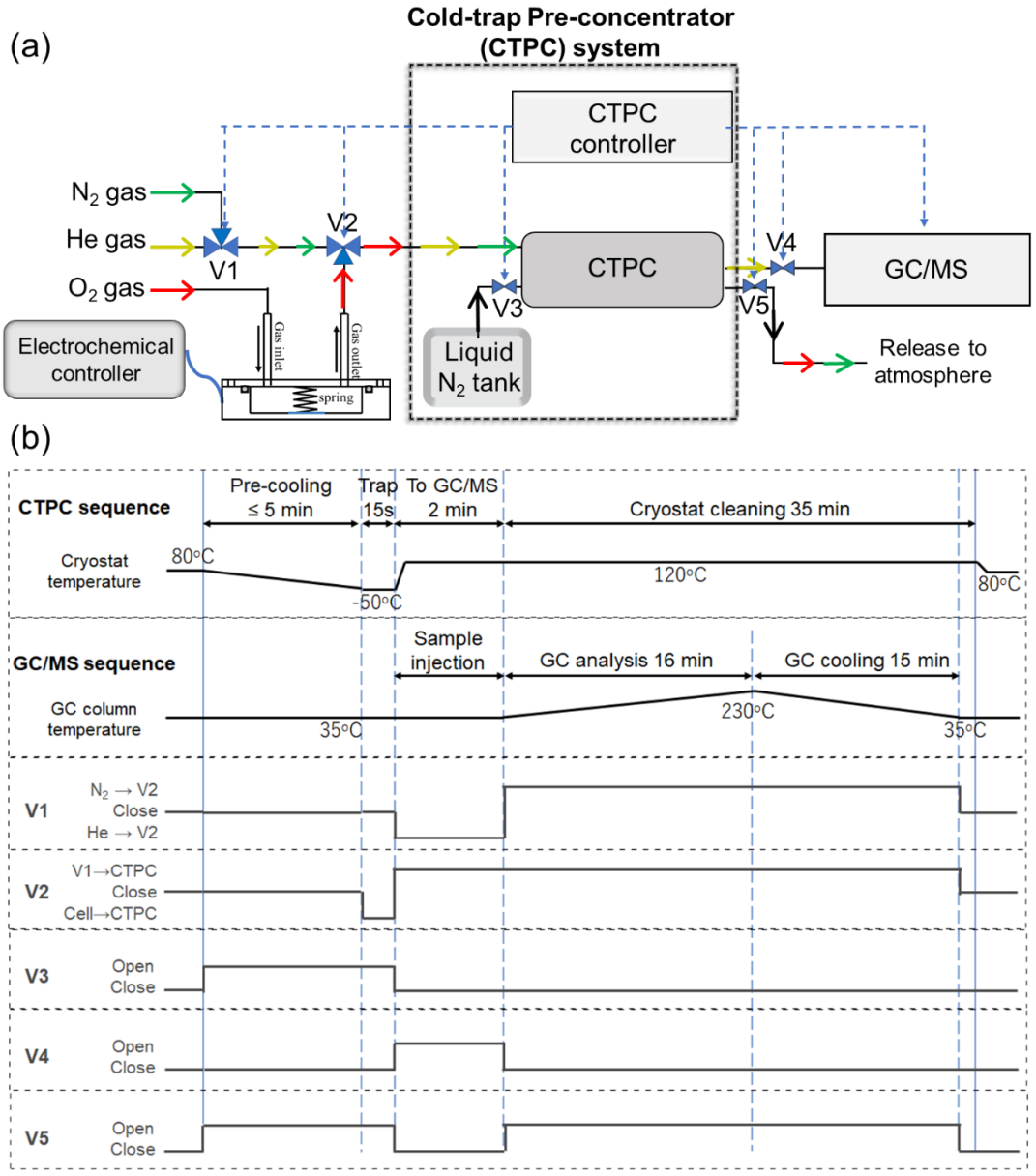

Figure 2-10. (a) Schematic diagram of on-line CTPC-GC/MS system. V1, V2, V3, V4, and V5 are solenoid valves controlled by the CTPC controller. **(b)** Sequences of CTPC–GC/MS operation.

Sampling was started immediately after the cell was connected to the charge/discharge system and filled with O_2 gas. After 2 hr at open circuit potential (OCP), constant-current (0.4 mA) discharge was performed for 10 hr followed by 2 hr at OCP, and then charging was performed with constant current by using the charge/discharge system or with voltage sweep (0.05 mV s^{-1}) by using the electrochemical measurement system.

Because organic molecules can be oxidized electrochemically, CTPC–GC/MS analysis was also performed during OCP and voltage sweep from OCP to 4.8 V but without discharge so that the degradation of TEGDME proceeded only via electrochemical oxidation. To separate the effects of time and discharge on the degradation process, the cell was kept at OCP before the voltage sweep for much longer (6 hr) than was the case with discharge (2 hr).

The CTPC, which was originally developed for the detection of organic vapor released from human skin,[7] was modified so that automatic samplings of the head space gas of the cell at preset intervals was possible. The core of the CTPC was a small cryostat, which was cooled with partly evaporated liquid nitrogen while being simultaneously heated by pulsed direct current to keep the temperature at a preset

value (-50℃ in this study). The head-space gas was introduced into the CTPC and trapped in the cryostat for a specified duration (usually 15 s in this study). Then, the cryostat was heated instantly to 120℃ using a direct current of 5 A to transfer the gas to the GC/MS (GCMS-QP2010 Ultra; Shimadzu), which was equipped with a 20 m VF-WAX column or 20 m DB17 column (Agilent Technologies). Column temperature was scanned from 25 to 230℃.

Figure 2-10(b) shows the sequence of the operation of CTPC-GC/MS system shown in **Figure 2-10(a)**. Gas flows are regulated by solenoids valves (V1 ~ V5), which are controlled by the CTPC controller. To initiate the sampling and GC/MS analysis, V3 1s open to transfer liquid nitrogen to pre-cool the cryostat. At the same time, V5 is open to release the evaporated nitrogen. After pre-set pre-cooling time (e.g., 5 min), V2 (three-way valve) is set to cell-CTPC flow for 15 s so that the head-space gas is transferred to the CTPC. To transfer the sample to GC/MS, 1. V3 and V5 is closed and the temperature of the cryostat is raised to 120℃ so that trapped molecules are evaporated, and 2. V1 is set to He-V2, V2 is set to V1-CTPC, and V4 is open so that He flows to the CTPC and carries the evaporated molecules to the GC/MS. After the completion of the sample transfer, the GC/MS analysis is initiated by a start signal from the CTPC controller. At the same time, V1 is set to N_2-V2, V4 is closed, and V5

is open so that N2 flows to the CTPC to clean the cryostat. The Column temperature of the GC is raised to 230℃ according to the pre-set program for the analysis. After the GC/MS analysis is completed, the column temperature is cooled down to 35℃ and V1, V2, and V5 are closed so that the system is ready for the next sampling.

References

1 Dettmer-Wilde, K.; Engewald, W., Practical gas chromatography. A Comprehensive Reference. Springer 2014, 902.

2 Núñ, A. J.; Gonza, L. F.; Jana, J., Pre-concentration of headspace volatiles for trace organic analysis by gas chromatography. Journal of Chromatography A 1984, 300, 127-162.

3 Grob, K., Organic substances in potable water and in its precursor: Part I. Methods for their determination by gas-liquid chromatography. Journal of Chromatography A 1973, 84 (2), 255-273.

4 Baltussen, E.; Janssen, H. G.; Sandra, P.; Cramers, C. A., A new method for sorptive enrichment of gaseous samples: application in air analysis and natural gas characterization. Journal of High Resolution Chromatography 1997, 20 (7), 385-393.

5 Jursík, T.; Stránský, K.; Ubik, K., Trapping system for trace organic volatiles. Journal of Chromatography A 1991, 586 (2), 315-322.

6 Ortner, E. K.; Rohwer, E. R., Trace analysis of semi-volatile organic air pollutants using thick film silicone rubber traps with capillary gas chromatography. Journal of High Resolution Chromatography 1996, 19 (6), 339-344.

7 Arakawa, T.; Aota, T.; Iitani, K.; Toma, K.; Iwasaki, Y.; Mitsubayashi, K., Skin ethanol gas measurement system with a biochemical gas sensor and gas concentrator toward monitoring of blood volatile compounds. Talanta 2020, 219, 121187.

Chapter 3: Real-time Monitoring of O_2, H_2O, and CO_2 Generation during Charge Process of Lithium-Oxygen Battery by On-line Mass Spectroscopy to Understand the Nature of Li_2O_2 and its Relation to the Generations of H_2O and CO_2

3.1 Introduction

Lithium-air battery (LAB) has attracted significant interests over the past decades because of its very high theoretical energy density and transition metal free cathode.[1-11] Oxygen from air and Li metal are the active materials for cathode and anode, respectively, for LAB with the cell reaction of $2Li + O_2 \rightleftarrows Li_2O_2$. Usually, porous carbon is used as the cathode (positive electrode) material to accommodate Li_2O_2 generated during discharge.[12-17] There are many critical problems to be solved before LAB can be used as a practical device. Many components of air such as water, CO_2, and even N_2, are harmful to LAB operation[18-22] and, therefore, most of the fundamental studies have been carried out for lithium oxygen battery (LOB), which uses pure dry O_2 instead of air.[19, 20, 23] Even LOB has a serious issue of low cyclability due to the degradation of positive electrode (carbon) and electrolyte solution, and the degradation/dendrite formation of negative Li metal electrode.[24-30] To improve the cyclability, it is essential to clarify the mechanism of LOB degradation.[31-32] The

degradations of positive electrode and electrolyte during the charging are considered to be more serious and many efforts have been made to investigate the degradation mechanism at positive electrode by various techniques such as surface enhanced Raman scattering,[33] electrochemical quartz crystal microbalance,[34] X-ray diffraction (XRD)[35] / X-ray photoelectron spectroscopy (XPS),[36-37] mass spectroscopy[38-43].

Reaction sites for the formation of Li_2O_2 have been discussed for a long time but still no agreement is reached. The previous work in my group [44] reported that very long (~80 μm) Li_2O_2 nanowire can be grown at gold electrode covered with single-layer graphene (SLG) and the reaction site is the defect sites of SLG on Au electrode/Li_2O_2 interface based on the Raman analysis with isotope $^{18}O_2$. On the other hand, Nakanishi[45] suggested that Li_2O_2 grew at electrolyte/Li_2O_2 interface at surface modified carbon paper cathode based on the results of nano-SIMS analysis that there exist two types of Li_2O_2; one is formed earlier part of discharge close to the electrode and is more difficult to be oxidized and the other is formed in latter part of discharge covering the Li_2O_2 formed earlier and is easier to be oxidized. More recently, Tan et al.[46-47] suggested that Li_2O_2 deposition takes place both at cathode/Li_2O_2 interface and at electrolyte/Li_2O_2 interface after the initial deposition of insulating Li_2O_2.

Origin of CO_2 is also a very important issue for understanding degradation mechanisms. McCoskey et al.[48] suggested that about 50% of CO_2 originated from carbonate generated by the oxidation of cathode carbon based on the results using carbon cathode made of ^{13}C. Many papers[49-51] mentioned that CO_2 originated from carbonate and carboxylate species formed by the attack of reduced oxygen species on electrolyte and/or carbon during discharge/charge process.

In this chapter, on-line mass spectrometry of quadrupole mass spectrometry (QMS) and thermal separation probe-gas chromatogram/mass spectrometry (TSP_GC/MS) were used for real-time monitoring high vapor and non-real-time detecting low vapor of generated gaseous products during charge of lithium-oxygen battery (LOB), which was operated with pure oxygen, not air, with 1 M lithium bis(trifluoromethanesulfonyl)imide (LiTFSI) tetraethylene glycol dimethyl ether (TEGDME) electrolyte solution. Linear sweep voltammetry (LSV) and voltage step modes were employed for charge instead of constant current charge so that the energy of the product formation during charge process can be understood quantitatively. The presence of two distinctly different types of Li_2O_2, one being decomposed in wide range of relatively low voltages (2.8 – 4.2 V) (l-Li_2O_2) and the other being decomposed at higher voltage of around 4.2 V (h-Li_2O_2), was confirmed by both LSV

and step experiments. H_2O generation started when O_2 generation reaches its peak and CO_2 generation took place accompanied by the decomposition of h-Li_2O_2. Based on the above results as well as the results of the effects of discharge time and isotope oxygen on the distribution of products during charging, the generation mechanism of O_2, H_2O, and CO_2 during charging is discussed in relation to the reactions during discharge.

3.2 Results and discussion

3.2.1 Constant current discharge/charge curves and mass signals as a function of charge during charging

Figure 3-1 shows a typical 1st discharge and charge curves (bottom panel) and ion currents of the Q-mass for m/z=18 (H_2O), 32 (O_2), and 44 (CO_2) as a function of charge for the present cell configuration obtained at a constant current of 0.2 mA cm^{-2}.

As already reported by many groups for various carbon cathodes, the discharge voltage was relatively constant with small overpotential up to 2 mAh cm^{-2} discharge, but during charging the voltage increased significantly with several inflection points, indicating several processes with different redox potentials were involved in the discharge process. The charge dependence of the mass signals for H_2O (18), O_2 (32),

and CO_2 (44) were essentially the same as those reported in previous papers, although the earlier results were for LOB with NO_3^-/Br^- dual mediators and Ketjenblack cathode. The charge dependence of the mass signal of O_2 (m/z=32) is not as simple as the mass signal of 32 increased sharply with the start of charging, reached a peak and decrease, but then increased and decreased again despite a constant current flow, indicating that the current efficiency of the oxidation of Li_2O_2, i.e., the formation of O_2, varied during the discharge in a complex manner. The increase and decrease of the mass signal of 32 appear to be related to the variations of mass signals of 18 and 44, suggesting that the variation in current efficiency for the oxidation of Li_2O_2 was affected by the generation of H_2O and CO_2.

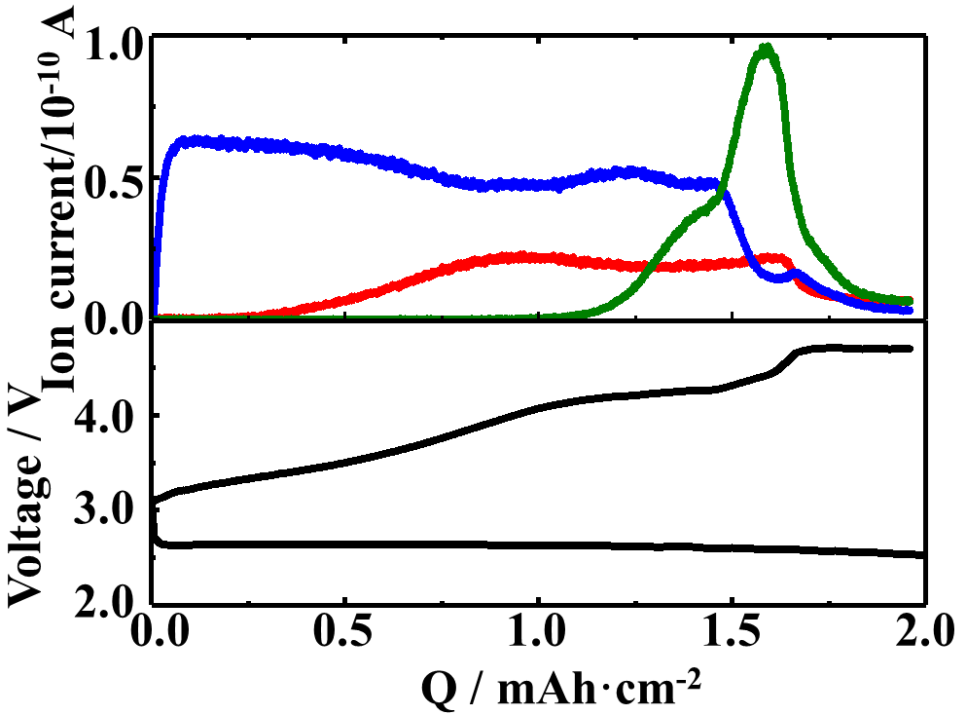

Figure 3-1. **(a)** Typical discharge/charge curves of a Li/TEGDME-1M LiTFSI/KJCNT cell (electrode area: 2 cm^2) obtained under constant current of 0.4 mA (0.2 mA cm^{-2}) for both discharge and charge. **(b)** Online mass spectra of m/z = 18 (red) / 32 (blue) / 44 (green).

3.2.2 Behaviors of current and mass signals during anodic voltage sweep

To understand the charging process more quantitatively, charging was performed under linear voltage sweep mode instead of constant current.[52-56]

After the constant current discharge (0.2 mA cm^{-2}) for 9.6 hr (cut off voltage was 2 V as shown in **Figure 3-2(a)**), the voltage of the KJCNT electrode relative to the Li electrode, i.e., the cell voltage, was scanned positively from OCP, i.e., 2.8 V, to 4.8 V at a scan rate of 0.05 mV s^{-1}, and current and the on-line Q-mass signals were recorded

simultaneously. **Fig. 3-2(b)** shows current (black line) as a function of the voltage. Current increased immediately as the voltage starts scanning positively from OCP and reached a maximum at 3.3 V. It gradually decreased after the 1st maximum, reached the 1st minimum at 4.15 V, increased again to reach the 2nd maximum at 4.45 V, decreased to reach the 2nd minimum at 4.65 V, and then increased again. The current – voltage relation obtained after discharge can be divided into four regions; **Region I**: up to the 1st maximum (~3.3 V), **Region II**: from the 1st maximum to the 1st minimum (3.3 V~4.15 V), **Region III**: from the 1st minimum to the 2nd minimum (4.15 V~4.65 V), and **Region IV**: from the 2nd minimum (4.65 V~: final current increase). **Fig. 3-2(b)** (red line) also show the current response of the same cell configuration but without discharge under a linear voltage scan at a scan rate of 0.05 mV s^{-1}. In this case, the current was very small compared with that observed in the discharged cell. The current started to increase from around 4.15 V, and gradually increased significantly in the voltage regions corresponding to **Region III** and **Region IV** of the discharged cell, respectively. This current should be due to the direct electrochemical anodic decomposition of the electrolyte solutions, TEGDME and LiTFSI. The current in the cell without discharge became larger than that in the discharged cell at voltages more positive than ca. 4.7 V. These results suggest that the current in the discharged cell in is

mainly due to the anodic oxidation of discharge products in **Region III** with slight contribution of the direct electrochemical decomposition of the electrolyte solutions and that in **Region IV** was almost due to the direct electrochemical decomposition of the electrolyte solutions.

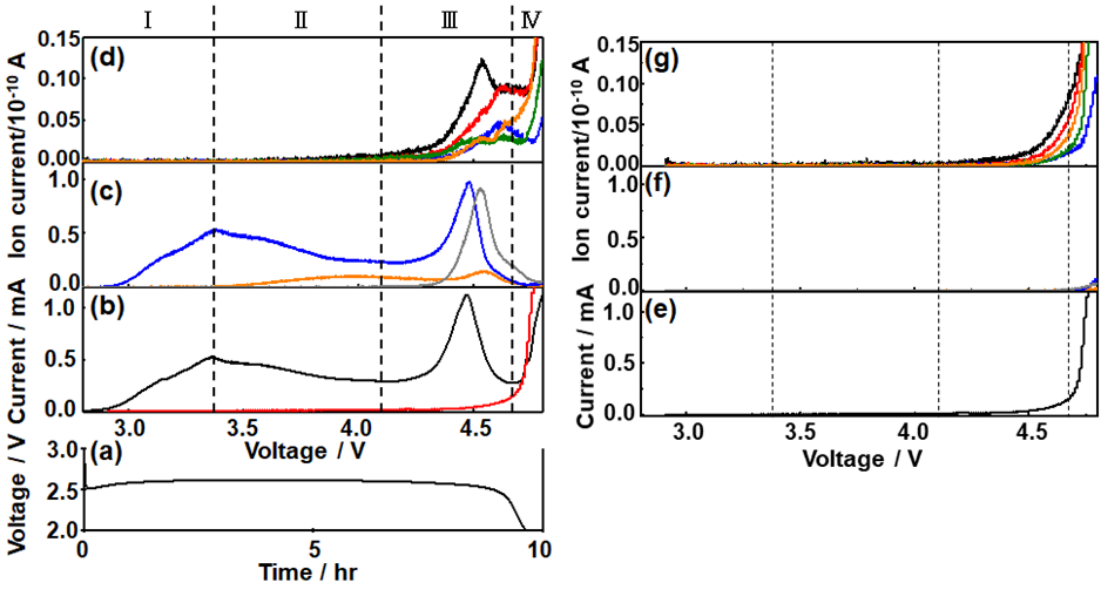

Figure 3-2. **(a)** Discharge curve of a Li/TEGDME-1M LiTFSI/KJCNT cell (electrode area: 2 cm^2) obtained under constant current of 0.4 mA (0.2 mA cm^{-2}). **(b, e)** Current, **(c, f)** mass signals of 18 (H_2O^+): orange, 32 (O_2^+): blue, and 44 (CO_2^+): gray (middle panel), and **(d, g)** mass signals of fragments related to organic molecules derived from TEGDME, i.e., 28 (CO^+): black, 29 (COH^+): red, 30 ($HCOH^+$): blue, 31 (CH_3O^+, CH_2OH^+): green, and 45 ($CH_3OCH_2^+$, $COOH^+$): orange, as a function of cell voltage during the voltage sweep with 0.05 mV s^{-1} after (**(b)-(d)**) and without the discharge (**(e)-(g)**). Current response without discharge **(e)** is also shown in **(b)** (red line) for a comparison. Note: The scales for y-axis of (**(c)**, **(f)**) are 8 times larger than those of (**(f)**, **(g)**).

The Q-mass signal of m/z=32 (O_2) behaved similarly to the current, and two

maxima were observed. It was detected even in **Region I** since the major reaction is $Li_2O_2 \rightarrow 2Li^+ + O_2 + 2e^-$. It increased immediately when voltage scan was started, as did current, reaching a maximum at 3.3 V (**Region I**). The Q-mass signals of m/z=18 (H_2O) and m/z=44 (CO_2) were not significant in **Region I**.

In **Region II**, the O_2 signal decreased gradually after the 1st maximum as did current but declined more rapidly than the current and reached a minimum at 4.1 V. The fact that the O^2 signal decreases more rapidly than the current means that the current efficiency for O_2 production is decreasing in this region. The H_2O signal started to increase just after the 1st current/O_2 maximum when the current efficiency for O_2 generation current efficiency started to decrease, suggesting that H_2O formation is related to the decrease of the current efficiency for oxygen generation, i.e., Li_2O_2 oxidation. The mass signal due to CO_2 was not significant in **Region II**.

In **Region III**, the O_2 signal increased again after a minimum at 4.1 V and reached a maximum at 4.4 V, which is 50 mV more negative than the voltage of the 2nd current peak, and decreased as did the current, but more rapidly. The H_2O signal decreased very slightly with voltage and started to increase at ca. 4.4 V to reach a maximum at ca. 4.5 V, which was more positive than the peak positions of current (4.45 V) and O_2

signal (4.4 V). The CO_2 signal became significant at 4.1 V where the current and O_2 signal started to increase again and reached a maximum at ca. 4.5 V, which was more positive than the peak positions of current (4.45 V) and O_2 signal (4.4 V) but was equal to that of H_2O peak (4.5 V).

Thus, Li_2O_2 was decomposed in **Region I**, **II**, and **III**, and the presence of two distinct O_2 generation peaks (3.3 V and 4.4 V) indicates that there existed at least two types of Li_2O_2 oxidation corresponding to the 2nd peak (**Region III**) being more difficult to be oxidized, as suggested by several previous reports.[43, 57-60]. While the 2nd peak was more or less symmetric and rather sharp (full width half maximum of ca. 0.14 V), the first peak (**Region I** and **II**) was very broad, indicating that both current and O_2 mass signals did not much decrease with about half of the peak remained at the minimum (4.15 V).

In **Region IV**, mass signals of O_2, H_2O and CO_2 declined monotonously, although current increased again rapidly at voltages more positive than 4.6 V. Instead, as shown in **Fig. 3-2(d)** signals related to organic molecules derived from TEGDME such as m/z = 29, 31, 45, and 60 became significant in this region. These results agreed with the suggestion that the current of the discharged cell in **Region IV** was mainly due to

direct electrochemical decomposition of the electrolyte solutions.

The contribution of direct electrochemical decomposition of the electrolyte solutions to the mass signals – voltage relations of a discharged cell can be evaluated by comparing with the mass signals of the same cell configuration without discharge, with linear voltage scan with the scan rate of 0.05 mV s^{-1} shown in **Fig. 3-2(f, g)**. At the cell without discharge, the current started to increase from around 4.15 V, and increased gradually and significantly in the voltage region corresponding to **Region III** and **Region IV**, respectively, of the discharged cell as already mentioned (**Fig. 3-2 (a, e)**). Mass signals related to organic molecules derived from TEGDME such as m/z = 29, 31, 45, and 60 (**Fig. 3-2(g)**) increased accordingly but those of 18, 32, and 44 were almost negligible compared with that of discharged cell in **Regions I – III** (**Fig. 3-2(f)**). These results confirm that the products detected in the discharged cell in **Region III** was mainly due to the anodic oxidation of discharged products, with slight contribution from direct electrochemical decomposition of the electrolyte solution. Those in **Region IV** was almost due to direct electrochemical decomposition of the electrolyte solutions as already suggested by the current-voltage relations.

3.2.3 Contribution of various oxidation reactions on current during anodic voltage

sweep of discharged cell

As mentioned above, after the 1st current peak, the O_2 mass signal decreases more steeply than the current with voltage due to the production of H_2O. In addition, CO_2, as one of the other main side products, also significantly contributes to the 2nd current peak.

In order to more clearly show the distribution of electrochemical current to each product, in other words, the products generation contribution to the electrochemical current, the voltage dependence of mass signals of main products (O_2) and main side products (H_2O and CO_2) were normalized to as a 'partial current' fitting the electrochemical current. In **Figure 3-3** the 'partial current' obtained from O_2 generation was plotted (blue line) along with current (black line) as a function of voltage utilizing the voltage dependence of O_2 mass signal normalized at the 1st peak as the current efficiency for O_2 generation was 1 at the maximum. Since it takes time for O_2 to be generated before mass is detected, there is a slight time delay in the 'partial current' corresponding to O_2 generation relative to the current, but the total current and the 'partial current' due to O_2 generation are found to be reasonably well matched.

After the 1st peak, the 'partial current' due to O_2 generation became less than the

total current. Since H_2O signal increased in this region as mentioned above, the voltage dependence of the H_2O mass signal was used to evaluate the 'partial current' due to H_2O generation and minimize the difference to the electrochemical current. Thus, the sum (green line) of the 'partial current' due to O_2 generation (blue line) and the 'partial current' due to H_2O generation (orange line) is in good agreement with the current measured in **Region II**. Thus, the decrease in O_2 generation efficiency after the 1st maximum (in **Region II**) is well explained by generation of H_2O.

In **Region III**, the difference between the measured current and the sum of the 'partial current' due to O_2 generation and H_2O generation became apparent. One of the reasons is the delay of mass detection, but even the peak height of the sum of 'partial currents' was smaller than the measured current. The discrepancy was minimized by taking into account the 'partial current' due to CO_2 generation (gray line) evaluated by utilizing the voltage dependence of H_2O mass signal as the sum (red line) of the 'partial currents' due to O_2 generation (blue line), H_2O generation (orange line), and CO_2 generation (gray line) is in reasonable agreement with the measured current in **Region III** up to 4.6 V.

At higher voltages (more positive voltages of KJCNT electrode), contributions of

O_2, H_2O, and CO_2 generation to the anodic current was minimal, and the current was dominated by direct anodic decomposition of electrolyte solution.

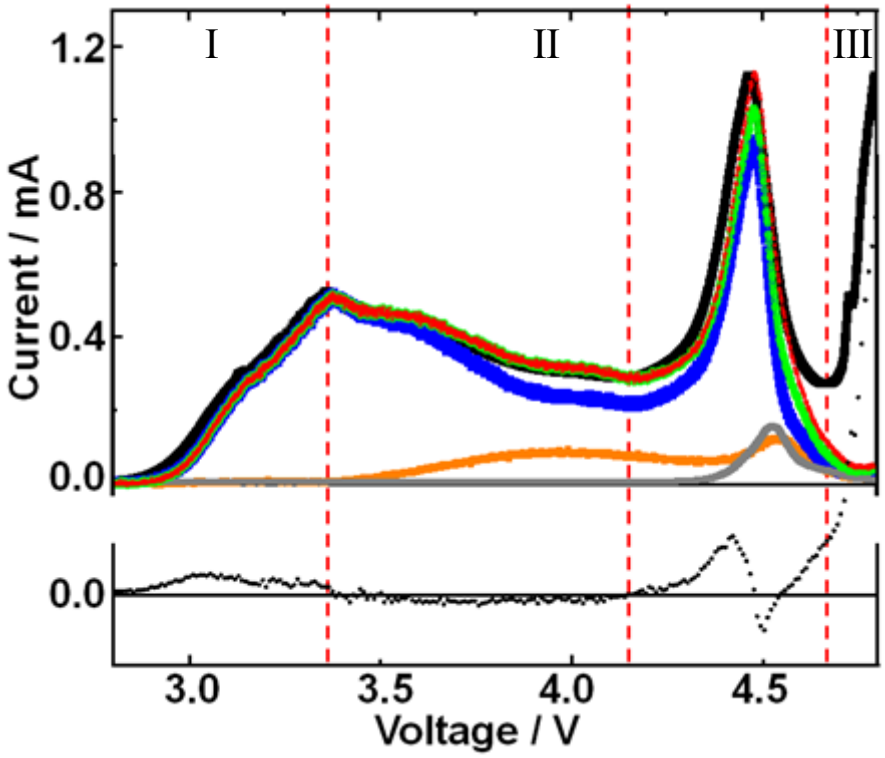

Figure 3-3. Top panel: Measured current (black), 'partial currents' due to O_2 generation (blue), H_2O generation (orange), and CO_2 generation (gray), and the sum of O_2 generation and H_2O generation currents (green), and the sum of O_2 generation, H_2O generation and CO_2 generation currents (red). Bottom panel: Difference between measured current and the sum of 'partial currents' due to O_2 generation, H_2O generation and CO_2 generation.

3.2.4 Charging by voltage steps

To see how the anodic generation of O_2, H_2O, and CO_2 proceeded, voltage step experiments were also performed.

Figure 3-4 shows the responses of current (middle panel) and mass signals of 18 (orange), 32 (blue), and 44 (gray) when voltage steps were applied in the sequence shown in the bottom panel (300 mV voltage step and 6000 s stay). Since the background signal of 18 (H_2O) was rather high (~ $1.5x10^{-11}$ A), the data shown in the figure are background corrected.

When the voltage was stepped from 2.9 to 3.2 V (within **Region I**), 3.2 to 3.5 V (**Region I** to **Region II**), 3.5 to 3.8 V (within **Region II**), and 3.8 to 4.1 V (within **Region II**) and kept at the given value for 6000 s, the current increased sharply and decreased monotonically with time. The time dependence of oxygen generation was similar to that of current in these cases, although there existed some delay in the rising portion of oxygen generation compared to the current rise. It is interesting to note that both current and O_2 signal became smaller after 6000 s, but they increased significantly again when the next voltage step was applied. This means that there existed Li_2O_2 which cannot be oxidized at a given voltage, for example at 3.8 V, but can be oxidized at more positive voltage, for example at 4.1 V. Thus, the deposited Li_2O_2 was energetically distributed very widely with required oxidation voltage varied from 2.8 V to 4.1 V. An increase in the H_2O signal was also observed when these voltage steps were applied, except for the voltage step from 2.9 to 3.2 V (within **Region I**), as

expected from the LSV (**Fig. 3-2**). The time dependence of the H_2O signal was, however, quite different from that of the current and O_2 signals. It increased very slowly with voltage steps and decreased very slightly after the peak. No significant change in the CO_2 signal was observed when these voltage steps were applied as expected from the LSV (**Fig. 3-2**).

When the voltage was pulsed from 4.1 to 4.4 V (**Region II** to **Region III**), the current-time relation was quite different from that of other voltage steps. After the current spike due to double layer charging, current increased and then decreased again but not monotonically, indicating that a rather complex processes is taking place. The O_2 signal is also quite different from those of other voltage steps. It increased upon voltage step as in the case of other voltage steps, but does not monotonically decrease, indicating a shoulder portion in the ion current signal – time dependent profile. This should be caused by the oxidation of Li_2O_2 corresponding to the 2nd peak in the LSV (**Fig. 3-2**). The behavior of the H_2O signal was similar to those observed in other voltage step cases, increasing very slowly upon voltage step and decreasing very slightly after a peak. The CO_2 signal increased corresponding to this voltage step, but rather complex way, it decreases after a peak.

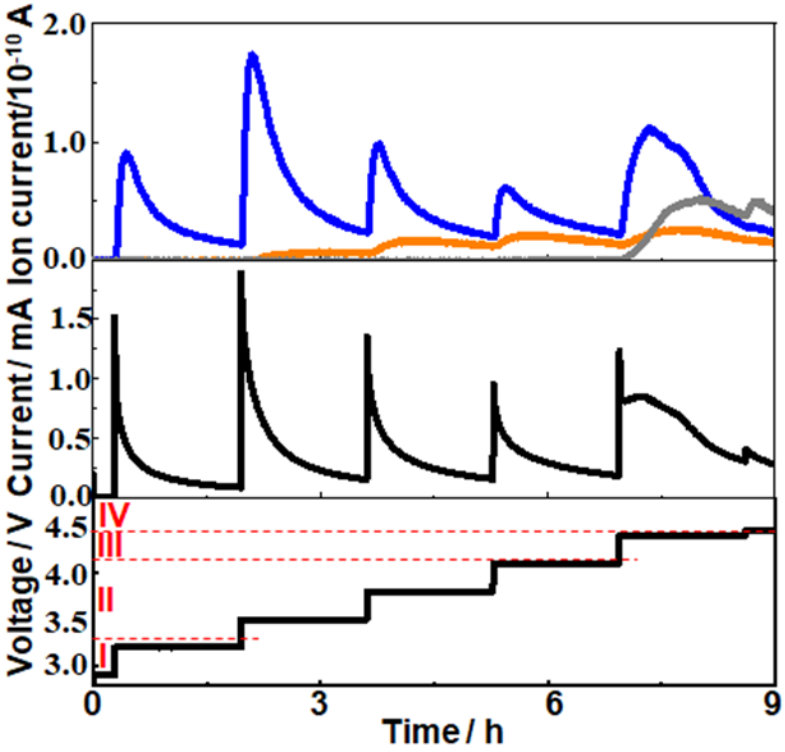

Figure 3-4. Time dependencies of current (middle panel) and mas signal of 18 (orange), 32 (blue), and 44 (gray) (top panel) when the sequences of the voltage step (300 mV step and 6000 s stay before the next step) were applied were applied as shown in the bottom panel.

As shown in **Figure 3-5**, the presence of two different types of Li_2O_2 can be clearly seen when the voltage was stepped from OCP (2.8 V) to 4.4 V, at which the 2nd maximum of the mass signal of m/z=32, i.e., oxygen, was observed in the LSV (**Fig. 3-2**).

Current increased sharply and decreased but then reached a plateau at ca. 0.9 hr, and then decreased again.

Oxygen (m/z = 32) signal increased upon voltage step but very slowly compared to current, reaching a maximum at ca. 0.2 hr, then decreased, reaching a plateau at ca. 1hr, and then decreased again. This behavior can be understood by considering the oxidation of Li_2O_2 corresponding to the 1st and 2nd peak in the LSV (**Fig. 3-2**). The time dependence of the oxygen signal can be deconvoluted into two peaks, the first peak being the one with a maximum at ca. 0.2 hr and the 2nd peak represented by a Gaussian curve with a maximum at ca. 1.2 hr as shown with the red dot line in **Fig. 3-5**. More accurate fitting requires the contribution of oxygen generation accompanied with H_2O (e.g., $LiOH \rightarrow Li^+ + 1/2H_2O + 1/4O_2 + e^-$) and CO_2 (e.g., $Li_2CO_3 \rightarrow 2Li^+ + CO_2 + 1/2O_2 + 2e^-$) generation. The integrated amount of the 2nd oxygen peak based on the fitting agreed well with that obtained from the LSV as shown in **Table 3-1**. Thus, it was confirmed that there are existed two types of Li_2O_2, one of which is more easily oxidized than the other. The first type of Li_2O_2 is oxidized at more negative voltages in the LSV (**Fig. 3-2**) and in the sequential step (**Fig. 3-4**) modes, but earlier when voltage was stepped to and kept at 4.4 V where both types of Li_2O_2 can be oxidized (**Fig. 3-5**). These results also show that in all charging modes, i.e., LSV and all step modes, Li_2O_2 corresponding to the 2nd oxygen peak was oxidized after the oxidation of Li_2O_2 corresponding to the 1st oxygen peak was completed.

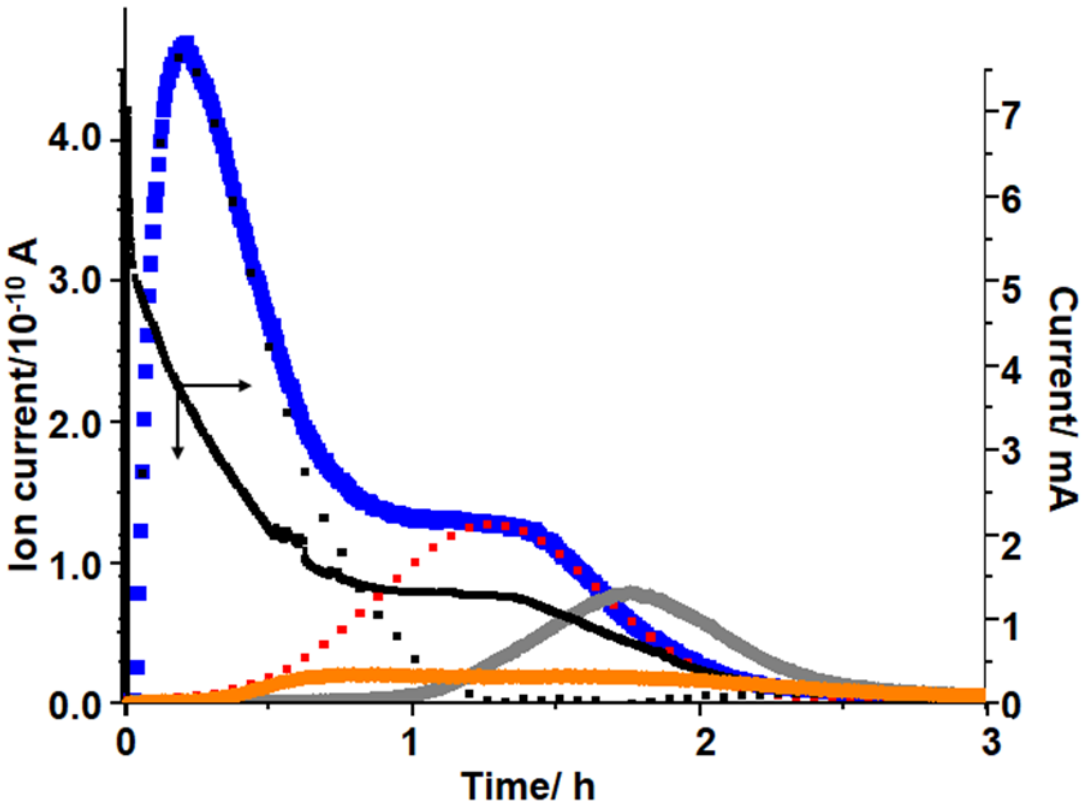

Figure 3-5. Time dependencies of current (black) and mas signals of 18 (orange), 32 (blue), and 44 (gray) when voltage was stepped from 2.8 to 4.4 V. Red dotted line shows Gaussian fitting for the 2nd oxygen generation and black dotted line is the residue for O_2 generation after the subtraction of red curve.

H_2O signal started to increase at around 0.2 hr, which was close to the position of the 1st oxygen peak, increased rather slowly, reached a broad maximum at ca. 0.75 hr. It then declined and increased slightly, reached the 2nd maximum at ca. 1.6 hr, and then decreased slowly. This behavior is similar to that of H_2O generation in the LSV and sequential step modes. The integrated amount of mass signal of H_2O was in reasonable agreement with that obtained from the LSV measurement as also shown in

Table 3-1.

CO_2 signal started to increase at around 1hr when the 1st oxygen generation was almost completed, reached a maximum at ca. 1.8 hr, and then decreased. The integrated amounts of mass signal of 44 was in good agreement with those obtained from the LSV measurements as shown in **Table 3-1**. It must be stressed that CO_2 generation was started when the oxidation of the first type of Li_2O_2, corresponding to the 1st oxygen peak in the LSV, was completed and the second type of Li_2O_2, corresponding to the 2nd oxygen peak in the LSV, was started as were the cases in the LSV (**Fig. 3-2**) and sequential step modes (**Fig. 3-4**).

Table 3-1 Integrated amounts of current (charge) and mass signals corresponding to O_2, H_2O, and CO_2 during the LSV (**Fig. 3-2**) and when voltage was stepped to 4.4 V.

	Integrated current (charge)/ mAh	Integrated mass signal (ion current)/ 10^{-10}Ah				
		O_2			H_2O	CO_2
		1st	2nd	Total		
LSV	3.88	2.08	1.17	3.25	0.524	0.761
Step to 4.4 V	3.73	2.15	1.12	3.27	0.406	0.702

3.2.5 Effect of discharge time on the behavior of charging by voltage sweep

To further understand the relation between O_2 generation (Li_2O_2 oxidation) and the generations of H_2O and CO_2, time (voltage) dependence of current (LSV) and

intensity of mass signals of 18 (H_2O), 32 (O_2), and 44 (CO_2) under voltage sweep (0.05 mV s^{-1}) were obtained after constant current (0.2 mA cm^{-2}) discharge of various time durations.

Figure 3-6 shows the results for the cells with discharge time of 2 (orange), 4 (blue), 6 (red), 8.8 (green), and 9.6 hr (black). It is clear that as discharge time increased, (1) both the current and mass signals increase, and (2) the voltage of the 2nd current peak, the 2nd peaks of mass signals of 18 and 32, and the peak of mass signal of 44 shifted to more positive voltages.

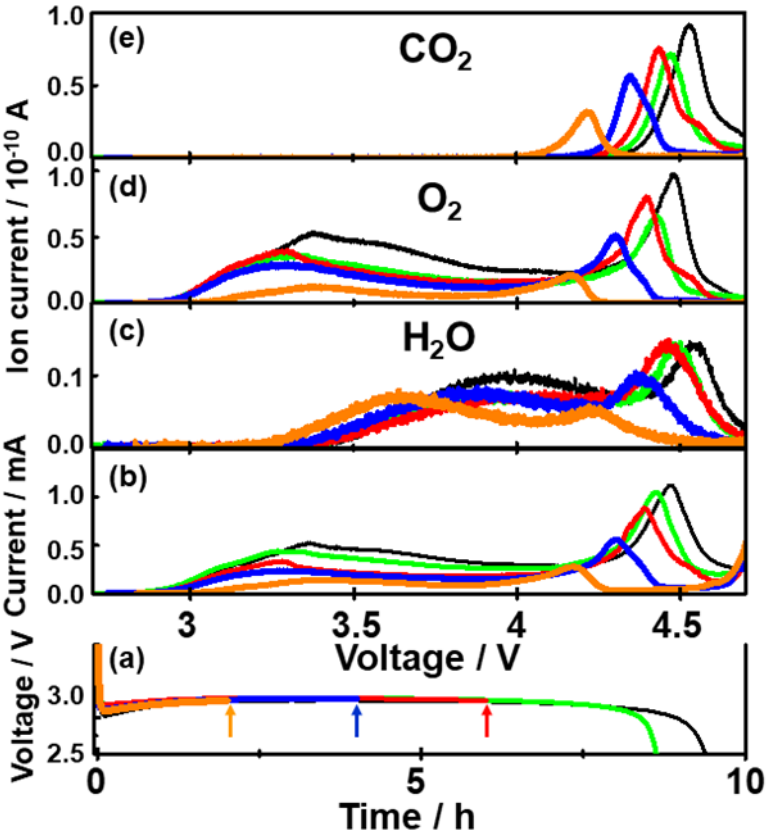

Figure 3-6. (a) Discharge curves of various cells of discharge times of 2 (orange), 4 (blue), 6 (red), 8.8 (green), and 9.6 hr (black). **(b)** ~ **(e)** Voltage dependencies of **(b)** current and the background corrected ion currents of Q-mass at **(c)** 18(H_2O), **(d)** 32 (O_2), and **(e)** 44 (CO_2) as a function of time for 2 (orange), 4 (blue), 6 (red), 8.8 (green) and 9.6 hr (black) discharged cells.

Figures 3-7 shows the integrated amounts of current (= charge: ▼) and mass signals of 18(▲), 32 (●), and 44 (■), which are normalized by the values of corresponding signals obtained for 9.6 hr discharge. Except for 18 (H_2O) signal, integrated amounts are linearly increased with the discharge time.

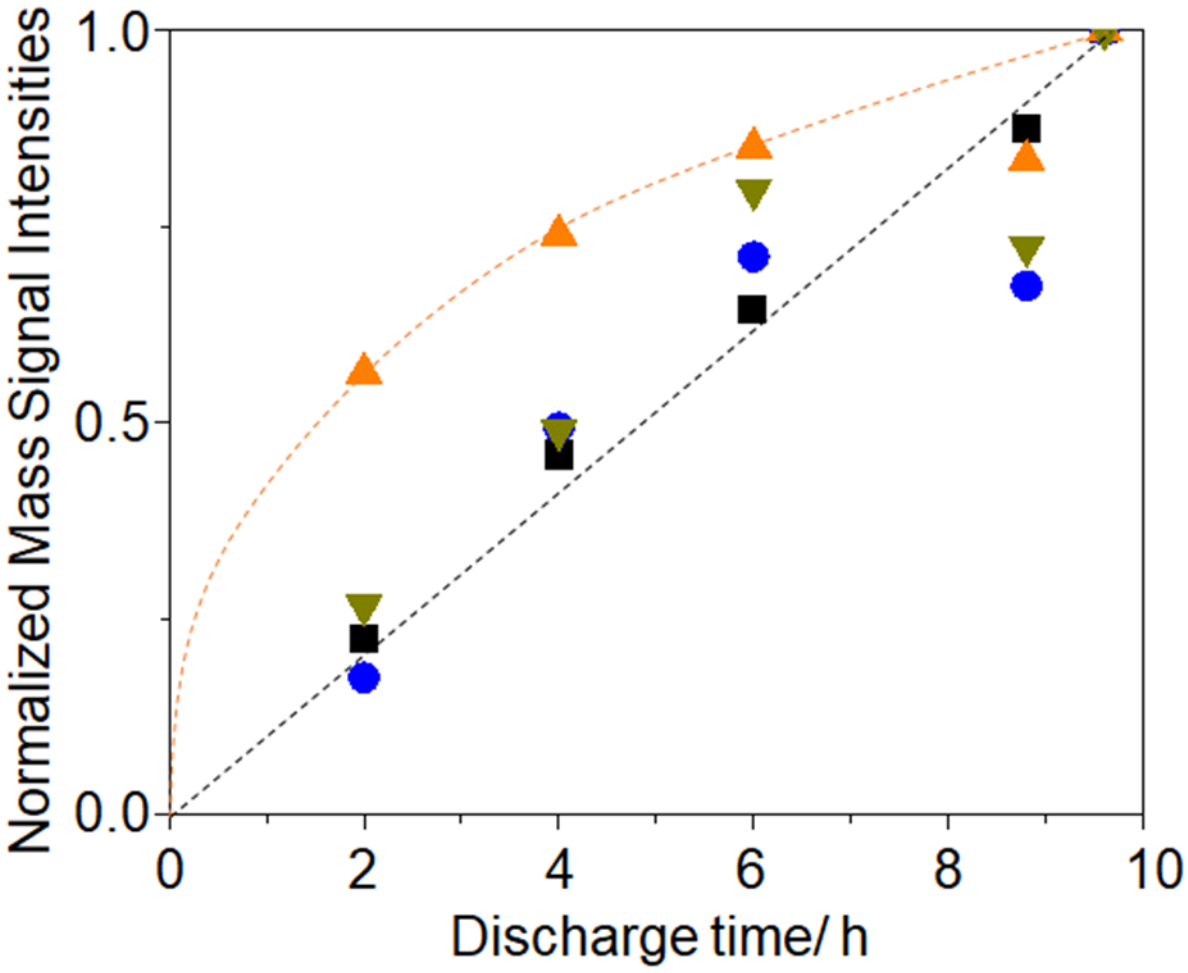

Figure 3-7. Discharge time dependencies of integrated signal intensities, i.e., current (▼), and ion current of 18 (▲), 32 (●), and 44 (■), normalized by those of 9.6 hr discharge.

Figure 3-8 shows the discharge time dependence of the positions of the second current peak (+), the second peak of 18 (■), the second peak of 32 (●), and the peak of 44 (▲). All peaks are positively shifted with discharge time as mentioned above. The positions of the peaks are all: the 2nd current peak ≈ the 2nd peak of 32 < the peak of 44 < the 2nd peak of 18. The voltages of the 2nd peak of 18 and 32, and the voltages

of 44 are linearly related with the voltages of the 2nd current peak for different discharge time (inset of **Fig. 3-8**), indicating the voltage differences of these peaks are constant regardless of discharge time, with ca. 63 mV and 46 mV differences between 32 and 18 and 32 and 44, respectively. These results suggest that CO_2 generation occurs not at a voltage more positive than the inherent redox potential of Li_2CO_3 oxidation, that is 3.8 V, but when the oxidation of Li_2O_2 corresponding to the 2nd oxygen peak progresses, and that the source of CO_2 (probably Li_2CO_3 generated during discharge) is thought to exist at the same site as Li_2O_2 corresponding to the 2nd oxygen peak.

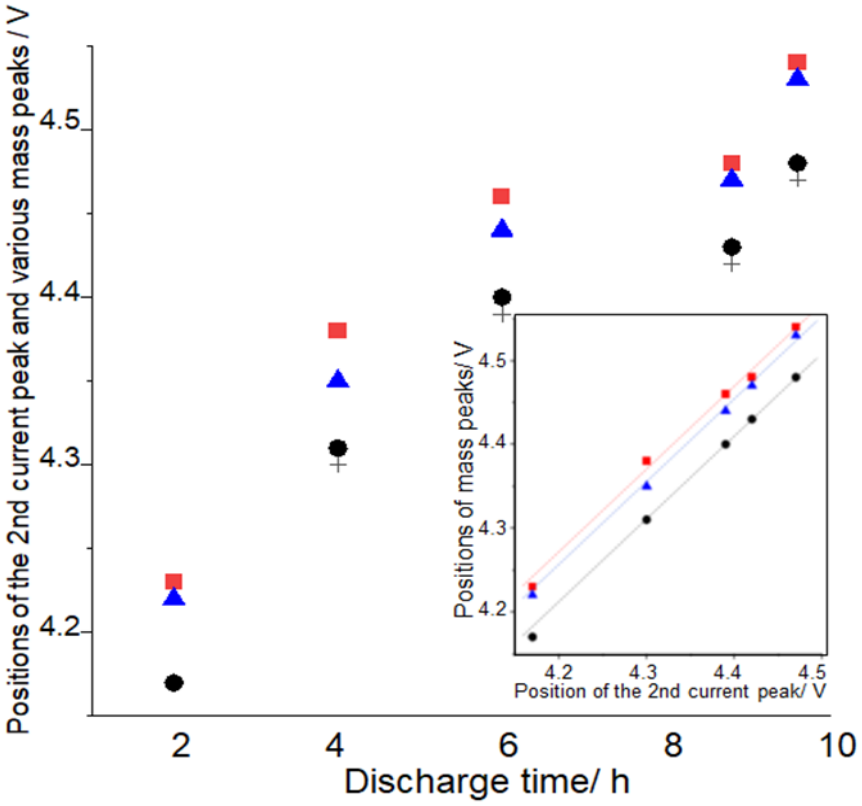

Figure 3-8. Discharge time dependencies of the positions of the second current peak (+), the second peak of 18 (■), the second peak of 32 (●), and the peak of 44 (▲). Inset: Positions of the second peak of 18 (■), the second peak of 32 (●), and the peak of 44 (▲:) as a function of the positions of the second current peak.

3.2.6 The use of two types of isotopic oxygen during discharging

Isotope oxygen has been used to obtain detailed information for the growth of Li_2O_2. Here we, however, used isotope oxygen to approach the mechanisms of not only Li_2O_2 growth but also the generation of H_2O and CO_2. **Figure 3-9** shows mass signals (ion currents) corresponding to (iii) O_2, (iv) H_2O, and (v) CO_2, and (ii) currents for various cells with constant current discharge of 0.4 mA (0.2 mA cm^{-2}) under various

isotope O_2 gas flow conditions as shown in the bottom panel (i). Red, blue, and black lines are of the ion currents (mass signals) related to ^{16}O, ^{18}O and $^{16}O + {}^{18}O$.

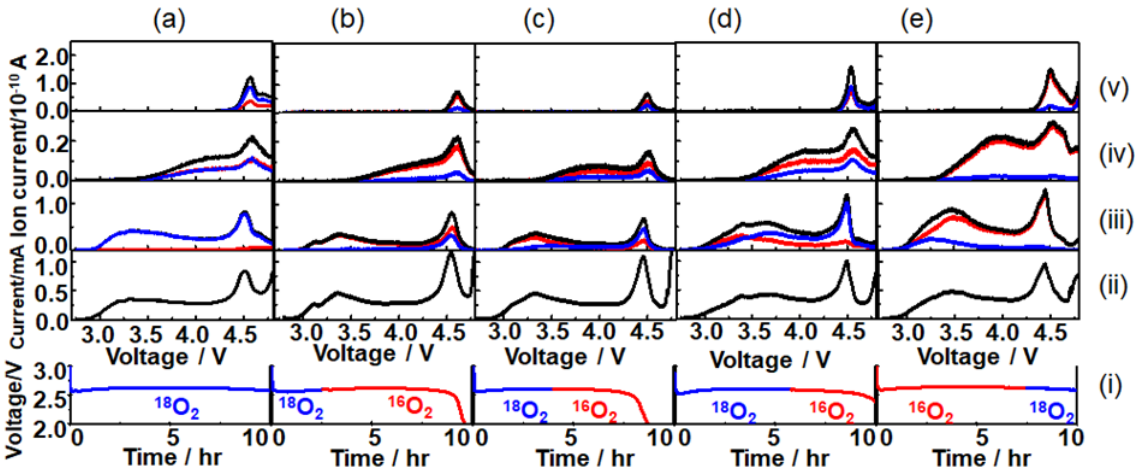

Figure 3-9. Mass signals (ion currents) for (iii) O_2, (iv) H_2O, and (v) CO_2, and (ii) currents for various cells with constant current discharge of 0.4 mA (0.2 mA cm^{-2}) under various isotope O_2 gas flow conditions as shown in the bottom panel (i). (a) 10 hr $^{18}O_2$ flow, (b) 2.5 hr $^{18}O_2$ flow followed by 7.1 hr $^{16}O_2$ flow, (c) 4 hr $^{18}O_2$ flow followed by 4.6 hr $^{16}O_2$ flow, (d) 5.8 hr $^{18}O_2$ flow followed by 4.2 hr $^{16}O_2$ flow, and (e) 7.5 hr $^{16}O_2$ flow followed by 2.5 hr $^{18}O_2$ flow. In (iii), (iv) and (v), red, blue, and black lines are of mass signals related to ^{16}O, ^{18}O and $^{16}O + {}^{18}O$ (see the details in the text).

In the case of O_2, the sum of the ion currents of 32 ($^{16}O^{16}O$) and half of the ion currents of 34 ($^{16}O^{18}O$) are taken as the ion currents due to O_2 with ^{16}O contribution (**Equation 3-1**) and the sum of half of the ion currents of 34 and the ion currents of 36 ($^{18}O^{18}O$) are taken as the ion currents due to O_2 with ^{18}O contribution (**Equation 3-2**). The natural abundance of ^{18}O in "^{16}"O_2 gas and the concentrations of ^{16}O impurities in "^{18}"O_2 were taken into account in the analysis.

$$^{16}O = 0.9989775 \times MS32 + 0.5 \times MS34 - 0.008175 \times MS36 \quad (3\text{-}1)$$

$$^{18}O = 0.996025 \times MS36 + 0.5 \times MS34 - 0.0010225 \times MS32 \quad (3\text{-}2)$$

The coefficients in the equations are based on the ionization chart in the **Appendix I**.

Although the features of time dependencies of total O_2 generations are essentially the same in all the cases, but for features of the individual O_2 ($^{16}O_2$ and $^{18}O_2$) show that the initially introduced O_2 during discharge is more difficult to regenerate during charging. Most notably in **Fig. 3-9(b)** and (e). **Fig. 3-9(b)-i** shows that 2.5 hr of $^{18}O_2$ flow is introduced first during discharge followed by 7.5 hr of $^{16}O_2$ flow. However, during charging (**Fig. 3-9(b)-iii**), $^{18}O_2$ appears only at the 2nd oxygen/current peak and does not contribute to the 1st oxygen peak. Similarly, **Fig. 3-9(e)-i** that $^{16}O_2$ flowed for 7.5 hr during discharge, followed by $^{18}O_2$ for 2.5 hr, but $^{18}O_2$ introduced late in the discharge mainly contributes to the first oxygen peak during the charging process (**Fig. 3-9(e)-iii**).

In the case of H_2O, while the ion currents of 20 were taken as the ion currents due to ^{18}O ($H_2{}^{18}O$) (**Equation 3-5**), and the ion currents due to ^{16}O ($H_2{}^{16}O$) were obtained using the ion currents of 18 (**Equation 3-3**), but after the contribution of ^{18}O was corrected by considering the fragmentation of $H_2{}^{18}O$ (m/z = 20) to ^{18}O (m/z = 18) (**Equation 3-4**). Natural abundance of ^{18}O in $^{\text{“16”}}O_2$ gas and the concentrations of ^{16}O impurities in $^{\text{“18”}}O_2$ were taken into account in the analysis.

$$H_2{}^{16}O = corrMS18 = MS18 - {}^{18}O \quad (3\text{-}3)$$

$${}^{18}O = 0.0466\times{}^{18}O_2+0.0235\times{}^{16}O^{18}O+0.099\times C^{18}O_2+0.05\times C^{16}O^{18}O+0.009\times H_2{}^{18}O$$

$$= 0.045\times MS36 + 0.0235\times MS34 + 0.99\times MS48+0.05\times MS46+0.009\times MS20 \quad (3\text{-}4)$$

$$H_2{}^{18}O = M20 \quad (3\text{-}5)$$

The coefficients in the equations are based on the ionization chart in the **Appendix I**.

In the case of CO_2, the sum of the ion currents of 44 ($C^{16}O^{16}O$) and half of the ion currents of 46 ($C^{16}O^{18}O$) are taken as the ion currents due to CO_2 with ^{16}O contribution (**Equation 3-6**) and the sum of the half of the ion currents of 46 and the ion currents of 48 ($C^{18}O^{18}O$) are taken as the ion currents due to CO_2 with ^{18}O contribution (**Equation 3-7**). The natural abundances of not only ^{18}O in $^{\text{“16”}}O_2$ but also ^{13}C and the concentrations of ^{16}O impurities in $^{\text{“18”}}O_2$ were taken into account in the analysis.

$${}^{16}O = 0.995\times MS44 + 0.5\times MS46 - 0.01215\times MS48 \quad (3\text{-}6)$$

$${}^{18}O = 0.99205\times MS48 + 0.5\times MS46 - 0.0008\times MS44 \quad (3\text{-}7)$$

The coefficients in the equations are based on the ionization chart in the **Appendix I**.

Figure 3-10 shows the ratio of ^{18}O to the total amounts of O_2、H_2O, and CO_2 generated during charging as a function of the ratio of ^{18}O in O_2 gas flown during discharge.

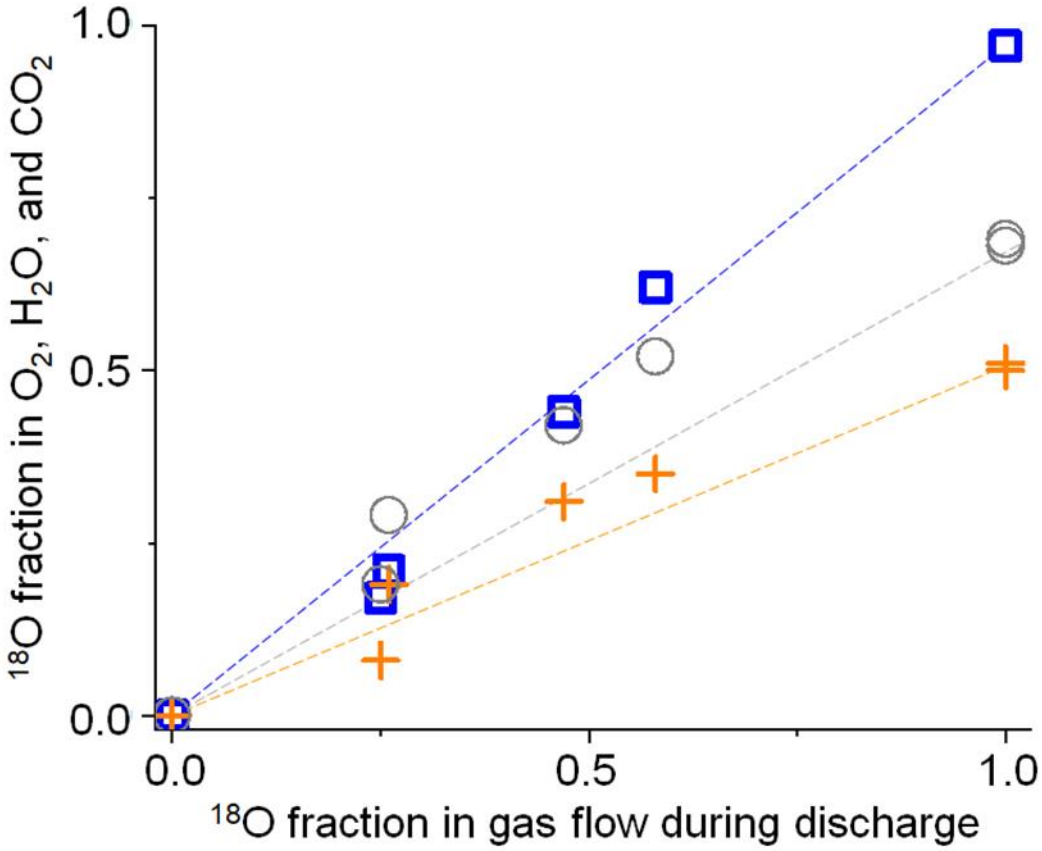

Figure 3-10. Fractions of ^{18}O in O_2 (□)、H_2O (+), and CO_2 (○) generated during charging as a function of the fraction of ^{18}O in O_2 gas flown during discharge.

They are linearly correlated, but with different slopes. While the fraction of ^{18}O in O_2 generated during charging is as same as that in O_2 gas flown during discharge, those in H_2O, and CO_2 generated during charging is less than those in O_2 gas flown during discharge. Only 50% and 70% of O in H_2O, and the CO_2 generated during charging were ^{18}O even $^{18}O_2$ was flown throughout the discharge.

Even in $^{18}O_2$ full flow experiment, significant amount (ca. 50%) of $H_2{}^{16}O$ was

also detected. That means around 50% of the O atom in H_2O generated from the electrolyte/solvent decomposition were detected. Possible mechanism of electrolyte/solvent decomposition into water is shown in **Scheme 3-1**.

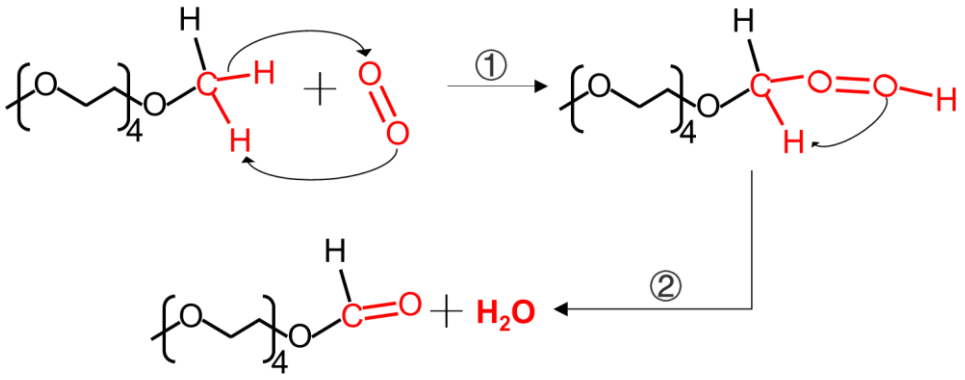

Scheme 3-1. Possible mechanism of electrolyte/solvent decomposition to water.

Figure 3-11 shows the integrated mass signals (ion currents) corresponding to O_2 (**Fig. 3-9(iii)**) with ^{16}O (red) or ^{18}O (blue) contributions during charging with the voltage sweep of 0.05 mV s^{-1} as a function of charge passed during discharge under corresponding isotope O_2 gas flow for various cells. Black (●) and red (●) closed circles are for the cells discharged with single isotope $^{16}O_2$ or $^{18}O_2$ gas flow, respectively, throughout the discharge. Data on the discharge time dependence with $^{16}O_2$ gas flow (**Fig. 3-7 and 3-8**) and $^{18}O_2$ (**Fig. 3-9**) gas flow are also included. Half-closed circles correspond to the cells discharged in sequence with two isotopic O_2 gases, and filled half for the order of gas flow. Thus, ◐ and ◑ are the integrated

amounts of O_2 based on ^{16}O and ^{18}O, respectively, when charging a cell with initial $^{16}O_2$ gas flow followed by $^{18}O_2$ gas flow during discharge, and ◐ and ◑ are the integrated amount of O_2 based on ^{18}O and ^{16}O, respectively, when charging a cell with initial $^{18}O_2$ gas flow followed by $^{16}O_2$ gas flow during discharge. Although the data are scattered, the amount of O_2 based on ^{16}O and ^{18}O has a linear relationship with the charge passed during discharge under $^{16}O_2$ and $^{18}O_2$ gas flow, respectively, regardless of the order of the gas flow. Thus, Li_2O_2 is formed with O_2, that flowed during Li_2O_2 formation.

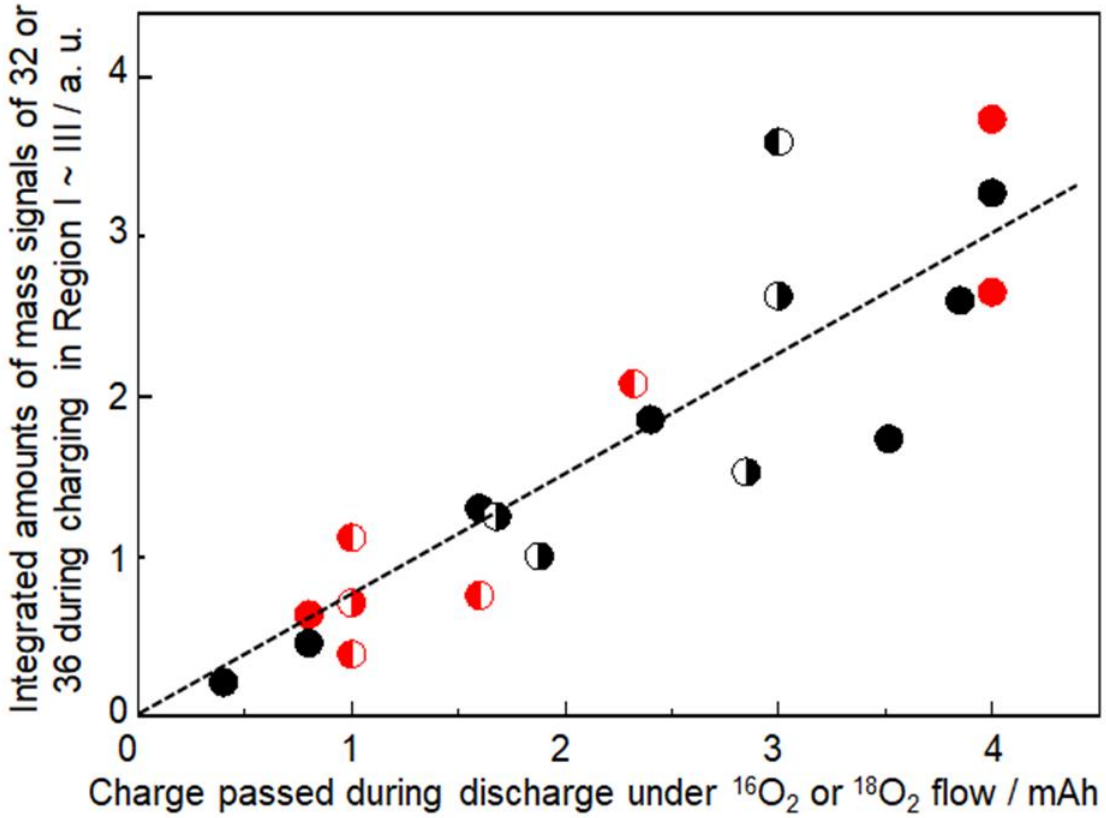

Figure 3-11. Integrated mass signals (ion currents) for 32 or 36 during charging with the voltage sweep of 0.05 mV s^{-1} for various cells as a function of charge passed during discharge under corresponding isotope O_2 gas flow. Black (●) and red (●) closed circles correspond to the cells discharged under single isotope of $^{16}O_2$ gas and $^{18}O_2$ gas flow, respectively, throughout the discharge. Half-closed circles correspond to the cells discharged under two isotopes of O_2 gas in sequence with filled half for the order of gas flow. ◐ and ◑ are the integrated amounts of O_2 based on ^{16}O and ^{18}O, respectively, during charging for the cells with initial $^{16}O_2$ gas flow followed by $^{18}O_2$ gas flow during discharge. ◐ and ◑ are the integrated amounts of O_2 based on ^{18}O and ^{16}O, respectively, during charging for the cells with initial $^{18}O_2$ gas flow followed by $^{16}O_2$ gas flow during discharge.

3.3 Conclusion

In conclusion, based on the above results as well as the results of the effects of discharge time and of isotope oxygen during discharge on product distribution during charge, generation mechanism of O_2, H_2O, and CO_2 during charge is discussed in relation to the reactions during discharge. By introducing and combining LSV and step research methods, the nature of Li_2O_2, as well as the generation of H_2O and CO_2, was clarified. There are two different types of Li_2O_2: Li_2O_2 (l-Li_2O_2), which decomposes over a wide voltage range of relatively low voltages (2.8 – 4.2 V) and Li_2O_2 (h-Li_2O_2), which decomposed at higher voltage of around 4.2 V. H_2O generation started when O_2 generation reached a peak, and around 50% O atom in H_2O originated from the discharge gas, the other 50% O atom in H_2O originated from the solvent decomposition or the initial water amount in the electrolyte. CO_2 generation took place accompanied with the decomposition of h-Li_2O_2, and around 70% O atom in CO_2 originated from the discharge gas, the 30% originated from the solvent decomposition.

References

1 Imanishi, N.; Luntz, A. C.; Bruce, P. The Lithium Air Battery: Fundamentals; Springer, 2014, pp 1-21.

2 Abraham, K.; Jiang, Z., A polymer electrolyte-based rechargeable lithium/oxygen battery. Journal of the Electrochemical Society 1996, 143 (1), 1.

3 Matsuda, S.; Ono, M.; Yamaguchi, S.; Uosaki, K., Criteria for evaluating lithium–air batteries in academia to correctly predict their practical performance in industry. Materials Horizons 2022, 9 (3), 856-863.

4 Aetukuri, N. B.; McCloskey, B. D.; García, J. M.; Krupp, L. E.; Viswanathan, V.; Luntz, A. C., Solvating additives drive solution-mediated electrochemistry and enhance toroid growth in non-aqueous Li–O2 batteries. Nature chemistry 2015, 7 (1), 50-56.

5 Kwak, W.-J.; Rosy; Sharon, D.; Xia, C.; Kim, H.; Johnson, L. R.; Bruce, P. G.; Nazar, L. F.; Sun, Y.-K.; Frimer, A. A., Lithium–oxygen batteries and related systems: potential, status, and future. Chemical Reviews 2020, 120 (14), 6626-6683.

6 Wu, Z.; Tian, Y.; Chen, H.; Wang, L.; Qian, S.; Wu, T.; Zhang, S.; Lu, J., Evolving aprotic Li–air batteries. Chemical Society Reviews 2022.

7 Girishkumar, G.; McCloskey, B.; Luntz, A. C.; Swanson, S.; Wilcke, W., Lithium−Air Battery: Promise and Challenges. The Journal of Physical

Chemistry Letters 2010, 1 (14), 2193-2203.

8 Zheng, J. P.; Liang, R. Y.; Hendrickson, M.; Plichta, E. J., Theoretical Energy Density of Li–Air Batteries. Journal of The Electrochemical Society 2008, 155 (6), A432.

9 Liang, Z.; Wang, W.; Lu, Y.-C., The path toward practical Li-air batteries. Joule 2022, 6 (11), 2458-2473.

10 Luntz, A. C.; McCloskey, B. D., Nonaqueous Li–Air Batteries: A Status Report. Chemical Reviews 2014, 114 (23), 11721-11750.

11 Jung, H.-G.; Hassoun, J.; Park, J.-B.; Sun, Y.-K.; Scrosati, B., An improved high-performance lithium–air battery. Nature Chemistry 2012, 4 (7), 579-585.

12 Woo, H.; Kang, J.; Kim, J.; Kim, C.; Nam, S.; Park, B., Development of carbon-based cathodes for Li-air batteries: Present and future. Electronic Materials Letters 2016, 12 (5), 551-567.

13 Ma, S. B.; Lee, D. J.; Roev, V.; Im, D.; Doo, S.-G., Effect of porosity on electrochemical properties of carbon materials as cathode for lithium-oxygen battery. Journal of power sources 2013, 244, 494-498.

14 Qu, D. In Fundamental principals of battery design: porous electrodes, AIP Conference Proceedings, American Institute of Physics: 2014; pp 14-25.

15 Xiao, J.; Mei, D.; Li, X.; Xu, W.; Wang, D.; Graff, G. L.; Bennett, W. D.; Nie, Z.; Saraf, L. V.; Aksay, I. A., Hierarchically porous graphene as a lithium–air battery electrode. Nano letters 2011, 11 (11), 5071-5078.

16 Liu, L.; Liu, Y.; Wang, C.; Peng, X.; Fang, W.; Hou, Y.; Wang, J.; Ye, J.; Wu, Y.,

Li2O2 Formation Electrochemistry and Its Influence on Oxygen Reduction/Evolution Reaction Kinetics in Aprotic Li–O2 Batteries. Small Methods 2022, 6 (1), 2101280.

17 Wang, F.; Li, X.; Xie, Y.; Lai, Q.; Tan, J., Effects of Porous Structure on Oxygen Mass Transfer in Air Cathodes of Nonaqueous Metal–Air Batteries: A Mini-review. ACS Applied Energy Materials 2022, 5 (5), 5473-5483.

18 Tran, C.; Yang, X.-Q.; Qu, D., Investigation of the gas-diffusion-electrode used as lithium/air cathode in non-aqueous electrolyte and the importance of carbon material porosity. Journal of Power Sources 2010, 195 (7), 2057-2063.

19 Imanishi, N.; Luntz, A. C.; Bruce, P. The Lithium Air Battery: Fundamentals; Springer, 2014, pp 306-308

20 Kang, J.-H.; Lee, J.; Jung, J.-W.; Park, J.; Jang, T.; Kim, H.-S.; Nam, J.-S.; Lim, H.; Yoon, K. R.; Ryu, W.-H.; Kim, I.-D.; Byon, H. R., Lithium–Air Batteries: Air-Breathing Challenges and Perspective. ACS Nano 2020, 14 (11), 14549-14578.

21 Geng, D.; Ding, N.; Hor, T. S. A.; Chien, S. W.; Liu, Z.; Wuu, D.; Sun, X.; Zong, Y., From Lithium-Oxygen to Lithium-Air Batteries: Challenges and Opportunities. Advanced Energy Materials 2016, 6 (9), 1502164.

22 Imanishi, N.; Yamamoto, O., Rechargeable lithium–air batteries: characteristics and prospects. Materials Today 2014, 17 (1), 24-30.

23 Zhang, J.-G.; Wang, D.; Xu, W.; Xiao, J.; Williford, R. E., Ambient operation of Li/Air batteries. Journal of Power Sources 2010, 195 (13), 4332-4337.

24 Black, R.; Adams, B.; Nazar, L., Non-aqueous and hybrid Li-O2 batteries. Advanced Energy Materials 2012, 2 (7), 801-815.

25 McCloskey, B. D.; Bethune, D.; Shelby, R.; Mori, T.; Scheffler, R.; Speidel, A.; Sherwood, M.; Luntz, A., Limitations in rechargeability of Li-O2 batteries and possible origins. The journal of physical chemistry letters 2012, 3 (20), 3043-3047.

26 Shao, Y.; Ding, F.; Xiao, J.; Zhang, J.; Xu, W.; Park, S.; Zhang, J. G.; Wang, Y.; Liu, J., Making Li-air batteries rechargeable: Material challenges. Advanced Functional Materials 2013, 23 (8), 987-1004.

27 Yao, X.; Dong, Q.; Cheng, Q.; Wang, D., Why do lithium–oxygen batteries fail: parasitic chemical reactions and their synergistic effect. Angewandte Chemie International Edition 2016, 55 (38), 11344-11353.

28 Laoire, C. O.; Mukerjee, S.; Abraham, K.; Plichta, E. J.; Hendrickson, M. A., Influence of nonaqueous solvents on the electrochemistry of oxygen in the rechargeable lithium− air battery. The Journal of Physical Chemistry C 2010, 114 (19), 9178-9186.

29 Liu, T.; Vivek, J. P.; Zhao, E. W.; Lei, J.; Garcia-Araez, N.; Grey, C. P., Current challenges and routes forward for nonaqueous lithium–air batteries. Chemical reviews 2020, 120 (14), 6558-6625.

30 Ue, M.; Uosaki, K., Recent progress in liquid electrolytes for lithium metal batteries. Current Opinion in Electrochemistry 2019, 17, 106-113.

31 Li, F.; Zhang, T.; Zhou, H., Challenges of non-aqueous Li–O2 batteries: electrolytes, catalysts, and anodes. Energy & Environmental Science 2013, 6 (4), 1125-1141.

32 Xu, W.; Xu, K.; Viswanathan, V. V.; Towne, S. A.; Hardy, J. S.; Xiao, J.; Nie, Z.; Hu, D.; Wang, D.; Zhang, J.-G., Reaction mechanisms for the limited reversibility of Li–O2 chemistry in organic carbonate electrolytes. Journal of Power Sources 2011, 196 (22), 9631-9639.

33 Lu, Y.-C.; Gallant, B. M.; Kwabi, D. G.; Harding, J. R.; Mitchell, R. R.; Whittingham, M. S.; Shao-Horn, Y., Lithium–oxygen batteries: bridging mechanistic understanding and battery performance. Energy & Environmental Science 2013, 6 (3), 750-768.

34 Gittleson, F. S.; Yao, K. P.; Kwabi, D. G.; Sayed, S. Y.; Ryu, W. H.; Shao-Horn, Y.; Taylor, A. D., Raman spectroscopy in lithium–oxygen battery systems. ChemElectroChem 2015, 2 (10), 1446-1457.

35 Tomita, K.; Noguchi, H.; Uosaki, K., Effect of Water and HF on the Distribution of Discharge Products at Li–O2 Battery Cathode. ACS Applied Energy Materials 2018, 1 (7), 3434-3442.

36 Song, C.; Ito, K.; Sakata, O.; Kubo, Y., Operando structural study of non-aqueous Li–air batteries using synchrotron-based X-ray diffraction. RSC advances 2018, 8 (46), 26293-26299.

37 Marchini, F.; Herrera, S.; Torres, W.; Tesio, A. Y.; Williams, F. J.; Calvo, E. J. Surface Study of Lithium–air Battery Oxygen Cathodes in Different Solvent–electrolyte Pairs. Langmuir. 2015, 31 (33), 9236-9245.

38 Yao, K. P.; Kwabi, D. G.; Quinlan, R. A.; Mansour, A. N.; Grimaud, A.; Lee, Y.-L.; Lu, Y.-C.; Shao-Horn, Y., Thermal stability of Li2O2 and Li2O for Li-air batteries: in situ XRD and XPS studies. Journal of The Electrochemical Society 2013, 160 (6), A824.

39 McCloskey, B. D.; Bethune, D. S.; Shelby, R. M.; Girishkumar, G.; Luntz, A. C., Solvents' critical role in nonaqueous lithium–oxygen battery electrochemistry. The Journal of Physical Chemistry Letters 2011, 2 (10), 1161-1166.

40 Ue, M.; Asahina, H.; Matsuda, S.; Uosaki, K., Material balance in the O 2 electrode of Li–O 2 cells with a porous carbon electrode and TEGDME-based electrolytes. RSC advances 2020, 10 (70), 42971-42982.

41 McCloskey, B. D.; Scheffler, R.; Speidel, A.; Bethune, D. S.; Shelby, R. M.; Luntz, A. C., On the efficacy of electrocatalysis in nonaqueous Li–O2 batteries. Journal of the American Chemical Society 2011, 133 (45), 18038-18041.

42 Herl, T.; Matysik, F. M., Recent developments in electrochemistry–mass spectrometry. ChemElectroChem 2020, 7 (12), 2498-2512.

43 Xin, X.; Ito, K.; Kubo, Y., Highly Efficient Br–/NO3– Dual-Anion Electrolyte for Suppressing Charging Instabilities of Li–O2 Batteries. ACS Applied Materials & Interfaces 2017, 9 (31), 25976-25984.

44 Tomita, K.; Noguchi, H.; Uosaki, K., Electrochemical Growth of Very Long (~ 80 μm) Crystalline Li2O2 Nanowires on Single-Layer Graphene Covered Gold and Their Growth Mechanism. Journal of the American Chemical Society 2020, 142 (46), 19502-19509.

45 Nishioka, K.; Tanaka, M.; Fujimoto, H.; Amaya, T.; Ogoshi, S.; Tobisu, M.; Nakanishi, S., Overlooked Factors Required for Electrolyte Solvents in Li–O2 Batteries: Capabilities of Quenching 1O2 and Forming Highly-Decomposable Li2O2. Angewandte Chemie International Edition 2022, 61 (12), e202112769.

46 Zhang, Z.; Xiao, X.; Yu, W.; Zhao, Z.; Tan, P., Reacquainting the Sudden-Death and Reaction Routes of Li–O2 Batteries by Ex Situ Observation of Li2O2 Distribution Inside a Highly Ordered Air Electrode. Nano Letters 2022, 22 (18), 7527-7534.

47 Tan, C.; Cao, D.; Zheng, L.; Shen, Y.; Chen, L.; Chen, Y., True Reaction Sites on Discharge in Li–O2 Batteries. Journal of the American Chemical Society 2022, 144 (2), 807-815.

48 McCloskey, B. D.; Speidel, A.; Scheffler, R.; Miller, D.; Viswanathan, V.; Hummelshøj, J.; Nørskov, J.; Luntz, A., Twin problems of interfacial carbonate formation in nonaqueous Li–O2 batteries. The journal of physical chemistry letters 2012, 3 (8), 997-1001.

49 Zhao, Z.; Huang, J.; Peng, Z., Achilles' Heel of Lithium–Air Batteries: Lithium Carbonate. Angewandte Chemie International Edition 2018, 57 (15), 3874-3886.

50 Ottakam Thotiyl, M. M.; Freunberger, S. A.; Peng, Z.; Bruce, P. G., The Carbon Electrode in Nonaqueous Li–O2 Cells. Journal of the American Chemical

Society 2013, 135 (1), 494-500.

51 Chen, K.; Huang, G.; Ma, J. L.; Wang, J.; Yang, D. Y.; Yang, X. Y.; Yu, Y.; Zhang, X. B., The stabilization effect of CO2 in lithium–oxygen/CO2 batteries. Angewandte Chemie International Edition 2020, 59 (38), 16661-16667.

52 Peng, Z.; Freunberger, S. A.; Chen, Y.; Bruce, P. G., A reversible and higher-rate Li-O2 battery. Science 2012, 337 (6094), 563-566.

53 McCloskey, B. D.; Speidel, A.; Scheffler, R.; Miller, D.; Viswanathan, V.; Hummelshøj, J.; Nørskov, J.; Luntz, A., Twin problems of interfacial carbonate formation in nonaqueous Li–O2 batteries. The journal of physical chemistry letters 2012, 3 (8), 997-1001.

54 McCloskey, B. D.; Bethune, D. S.; Shelby, R. M.; Girishkumar, G.; Luntz, A. C., Solvents' critical role in nonaqueous lithium–oxygen battery electrochemistry. The Journal of Physical Chemistry Letters 2011, 2 (10), 1161-1166.

55 McCloskey, B. D.; Scheffler, R.; Speidel, A.; Bethune, D. S.; Shelby, R. M.; Luntz, A. C., On the efficacy of electrocatalysis in nonaqueous Li–O2 batteries. Journal of the American Chemical Society 2011, 133 (45), 18038-18041.

56 Kim, D. W.; Ahn, S. M.; Kang, J.; Suk, J.; Kim, H. K.; Kang, Y., In situ real-time and quantitative investigation on the stability of non-aqueous lithium oxygen battery electrolytes. Journal of Materials Chemistry A 2016, 4 (17), 6332-6341.

57 Nishioka, K.; Morimoto, K.; Kusumoto, T.; Harada, T.; Kamiya, K.;

Mukouyama, Y.; Nakanishi, S., Isotopic Depth Profiling of Discharge Products Identifies Reactive Interfaces in an Aprotic Li–O2 Battery with a Redox Mediator. Journal of the American Chemical Society 2021, 143 (19), 7394-7401.

58 Wang, Y.; Lu, Y. C., Isotopic labeling reveals active reaction interfaces for electrochemical oxidation of lithium peroxide. Angewandte Chemie 2019, 131 (21), 7036-7040.

59 Wang, J.; Zhang, Y.; Guo, L.; Wang, E.; Peng, Z., Identifying reactive sites and transport limitations of oxygen reactions in aprotic lithium-O2 batteries at the stage of sudden death. Angewandte Chemie International Edition 2016, 55 (17), 5201-5205.

60 Ganapathy, S.; Adams, B. D.; Stenou, G.; Anastasaki, M. S.; Goubitz, K.; Miao, X.-F.; Nazar, L. F.; Wagemaker, M., Nature of Li2O2 oxidation in a Li–O2 battery revealed by operando X-ray diffraction. Journal of the American Chemical Society 2014, 136 (46), 16335-16344.

Chapter 4: Accurate On-Line Mass Spectroscopy Evaluation of Real-time Products of Lithium-air Battery Based on Isotope exchanged solvents and discharge gases

4.1 Introduction

Over the past decades, the massive use of fossil fuels and electricity has greatly improved our standard of living[1-10]. Energy, especially electricity, is at the heart of modern society. Today, more than 80% of the world's domestic and industrial electricity consumption comes from fossil fuels such as coal, petroleum, and natural gas. However, the massive consumption of fossil fuels will lead to the depletion of natural resources and the production of large amounts of greenhouse gases (e.g., CO_2), leading to the ecological degradation of our environment. As a result, the electrochemical energy and energy storage systems will play an important role in shifting the future energy networks to clean and renewable energy sources. Which can be applied to electric vehicles (EVs), hybrid electric vehicles (HEVs), portable electronic devices and even large energy stations[11-20].

Lithium-ion batteries (LIBs) are currently the most popular type of electrochemical energy storage and have been commercialized by Sony since 1991. Due to their relatively high energy density, the LIBs will continue to evolve to provide much higher energy density[21-30]. It is well known that LIBs have penetrated everywhere in our daily lives, such as computers, telecommunication devices, etc. Although LIBs have been a great success in the clean energy field so far, there have been constant demands to improve the capacity and performance of LIBs as they have not been able to meet the emerging needs of society.

Rechargeable lithium-air batteries (LABs) are considered the most promising energy storage devices because of their large theoretical energy density of 3860 Ah kg^{-1}. Despite significant efforts by many research groups, LABs are still far from practical use and many problems must be overcome[31-40]. The paramount problem is the use of air. Air contains many components other than oxygen, including N_2, water, and CO_2, which interfere battery reactions. Thus, most of the fundamental studies are research has focused on lithium oxygen batteries (LOBs), which uses pure oxygen as an active material. However, LOBs have many serious problems, including low cyclability caused by (1)high charging overpotential, which induces degradation of positive electrode (carbon) and electrolyte solution, and (2)degradation/dendrite formation of

negative Li metal electrode[41-45]. To improve the cyclability, it is essential to clarify the degradation mechanism of electrodes and electrolyte.

In this chapter, on-line quadrupole mass spectroscopy (QMS) was employed, combining with isotope experiments, $^{12}CD_3$_TEGDME and $^{13}CH_3$_TEGDME as exchange of solvent TEGDME, and $^{18}O_2$ as exchange of discharge gas $^{16}O_2$, to follow and analyze products during charging, accordingly, to clarify the degradation mechanisms of electrodes and electrolyte. As far the main reaction in battery is that lithium reacts with oxygen to produce lithium peroxide. Side reactions will together with this main reaction to generate CO_2, H_2O, and organic compounds etc. To well clarify the decomposition mechanism, mass spectrometry was introduced to detect products generated from the main and side reactions in the battery, and combine them with the isotopic experimental results, all the measured mass numbers can be assigned to the corresponding products. Thus, the reaction mechanism of battery degradation can be deduced.

4.2 Results and discussion

4.2.1 Mass behaviors

Figure 4-1 shows the current and mass behaviors during voltage sweep of with (left side) and without (right side) Li_2O_2 pre-decompose. The cell is constant current 0.4 mA discharged for 10 hr, then linear sweep of voltage with 0.05 mV s^{-1} from OCP (around 2.8 V) to 4.8 V. **Fig. 4-1(a)** shows the discharge curve, **Figs. 4-1(b)~(e)** present the current and mass behaviors of several mass numbers as voltage increases linearly. The mass signals of mass numbers in range of m/z = 12 to 90 present three types of behaviors, that are shown in **Figs.4-1(c)~(e)**. **Fig. 4-1**(**c**) shows mass signals of m/z = 32, the main charge product of O_2, and m/z = 18/44, the main side reaction products H_2O and CO_2, that generate large amount during charging but at relatively low overpotential. **Fig. 4-1**(**d**) shows mass behaviors of m/z = 29/30/45, et al. that increase/generate with the 2nd current peak. **Fig. 4-1**(**e**) shows mass behaviors of m/z = 58/75/88, et al., that increase/generate after the 2nd current peak. Mass signals of those increase before the 2nd current peak are related to compounds produced due to degradation of electrodes and electrolyte due to attack by the reactive species such as super oxide and singlet oxygen etc. that generated in the process of battery main reactions. While those increase at high overpotential where after the second current peak are related to compounds produced by electrode and electrolyte degradation due to high overpotentials.

The red line in **Fig. 4-1(c)** is the mass signal of m/z = 32, which is attributed to O_2 that generated from the decomposition of the discharge products Li_2O_2, indicating that the O_2 behavior is identical to that of the current. It has been proven that during discharge two types of Li_2O_2 will be generated,[46-48] which corresponding to that two types of O_2 will be released from two types of Li_2O_2 decomposition during charging. **In chapter 3**, the two O_2 peaks during LSV are assigned to two types of O_2 generation. Mass signal of m/z = 18 (black line in **Fig. 4-1(c)**), which is attributed to H_2O, increases after both two peaks of O_2. This indicates that significant formation of any type of O_2 promotes the generation of H_2O. Mass signal of m/z = 44 ((blue line in **Fig. 4-2(c)**), which is attributed to CO_2, increases simultaneously with the 2nd O_2 peak, indicating that CO_2 generation is associated with the second type of O_2. The black, red, and blue lines in **Fig. 4-1(d)** are the mass behaviors of m/z = 29, 30, and 45, defined as fragments of COH^+, $HCOH^+$, and $CH_3OCH_2^+$ and/or $COOH^+$. These fragments appear only when the second O_2 peak occurs, suggesting that with the second oxygen generation, a large amount of generated reactants attack the electrolyte and electrodes, leading to the generation of these organic components. The black, red, and blue lines in **Fig. 4-1(e)** are mass behaviors of m/z = 58, 75, and 88, defined as fragments of $CH_3OCHCH_2^+$, $CH_3OCHOCH_3^+$, and $(CH_2CH_2O)_2^+$. It is evident that these

components possess larger molecular weights and longer molecular chains and appear at higher overpotentials that after the second O_2 peak. This suggests that the presence of these components is not related to the battery reaction, in which, Li_2O_2 is decomposed to O_2, but only to the overpotential.

Figs. 4-1(f)~(i) show the results of comparative experiments that LSV without discharge performed beforehand. In this case the current in **Fig. 4-1(f)** shows no peak but an eventually increase at high overpotential (> 4.5 V), accordingly no m/z = 32 (O_2; red line), negligible m/z =18 (H_2O; black line) and m/z = 44 (CO_2; blue line) were obtained in **Fig. 4-1(g)**. And also, no compounds are observed in **Fig. 4-1(h)** at voltage lower than 4.5 V, while the compounds in **Fig. 4-1(h)** and **Fig. 4-1(i)** both rise at high overpotential (> 4.5 V). This indicates that last sharp increase in both current and mass are due to the high overpotential. This suggests that the current and mass increase at < 4.5 V in **Figs. 4-1(b)~(e)** are associated with the production of reactive oxygen species.

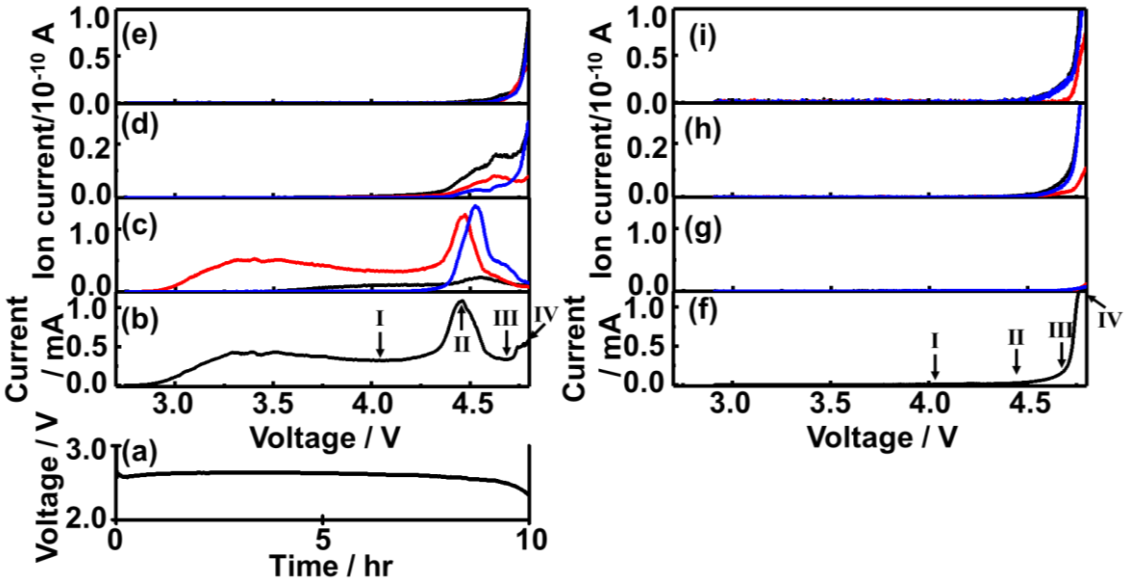

Figure 4-1. **(a)** Discharge curve of a Li/TEGDME-1M LiTFSI/KJCNT cell (electrode area: 2 cm^2) obtained under constant current of 0.4 mA (0.2 mA/cm^2). **(b, f)** Current, **(c, g)** mass signals of 18 (H_2O^+): black, 32 (O_2^+): red, and 44 (CO_2^+): blue, and **(d, h)** mass signals of fragments related to organic molecules derived from TEGDME, i.e., 29 (COH^+): black, 30 ($HCOH^+$): red, and 45 ($CH_3OCH_2^+$, $COOH^+$): blue, and **(e, i)** 58 ($CH_3OCHCH_2^+$): black, 75 ($CH_3OCHOCH_3^+$): red, and 88 ($(CH_2CH_2O)_2^+$): blue, as a function of cell voltage during the voltage sweep with 0.05 mV s^{-1}.

Mass spectra of m/z =12~90 at four typical voltage sweeping stages in **Fig. 4-1(b)**, the first current minimum (I; 4.06 V), the second current peak (II; 4.45 V), the second current minimum (III; 4.68 V), and the final (IV; 4.8 V) are shown in the upper panels in **Figure 4-2**. As a comparison, mass spectra of m/z =12~90 at same voltage in **Fig. 4-1(f)** are shown in the bottom panels in **Fig. 4-2**. At 4.06 V (**Fig. 4-2I**), the upper panel shows four mass peaks at m/z = 16 (O^+), 17 (OH^+), 18 (H_2O^+), and 32 (O_2^+), which are ionized from O_2 and H_2O. The bottom panel shows no mass peak. Indicating that in

addition to the main battery reaction that $Li_2O_2 \rightarrow 2Li + O_2$, the generated reactive oxygen species seized the H^+ from electrolyte solution to produce H_2O.

At 4.45 V (**Fig. 4-2II**), in the upper panel additional peaks of m/z = 28 (CO^+), 29 (COH^+), 30 ($HCOH^+$), 31 ($HCHOH^+$) and 44 (CO_2^+) appear, which are definitely ionized from CO_2, *Alcohols* and/or *Aldehydes*. The amounts of m/z = 29~31 are quite small compared to m/z = 32 and 44. But their volumes are actually a lot, just compressed, because of the large scale of the y-axis. In the bottom panel, still nothing appears. Suggesting that as charging proceeds, more reactive oxygen species are formed, which are not only seize H^+ but also attack the electrolyte (TEGDME) and cathode. Leading to battery degradation.

At 4.68 V (**Fig. 4-2III**), furthermore peaks at m/z = 15 (CH_3^+), 29 (COH^+), 30 ($HCOH^+$), 31 ($HCHOH^+$), and 45 ($CH_3OCH_2^+$, $COOH^+$) appear in the upper panel, and peaks at m/z = 15 (CH_3^+), 28 (CO^+), 29 (COH^+), and 45 ($CH_3OCH_2^+$, $COOH^+$) appear in the bottom panel. Which shows that *Alcohol*s and/or *Aldehyde*s are generated with and without discharge voltage sweep. This means that in addition to reactive oxygen, electrolyte (TEGDME) and cathode decomposition are also caused by high overpotential.

At 4.8 V (**Fig. 4-2IV**), more peaks with larger mass of m/z = 58 ($CH_3OCHCH_2^+$), 75 ($CH_3OCHOCH_3^+$), and 88 ($(CH_2CH_2O)_2^+$) appear in the upper panel, while more and higher peaks appear in the bottom panel. **Fig. 4-1(f)** shows a much higher current value at 4.8 V than **Fig. 4-1(b)**, that means the degradation of electrolyte is also much significant. Since oxygen is no longer produced (**Fig. 4-1(c)**), the high overpotential becomes the main cause of battery degradation.

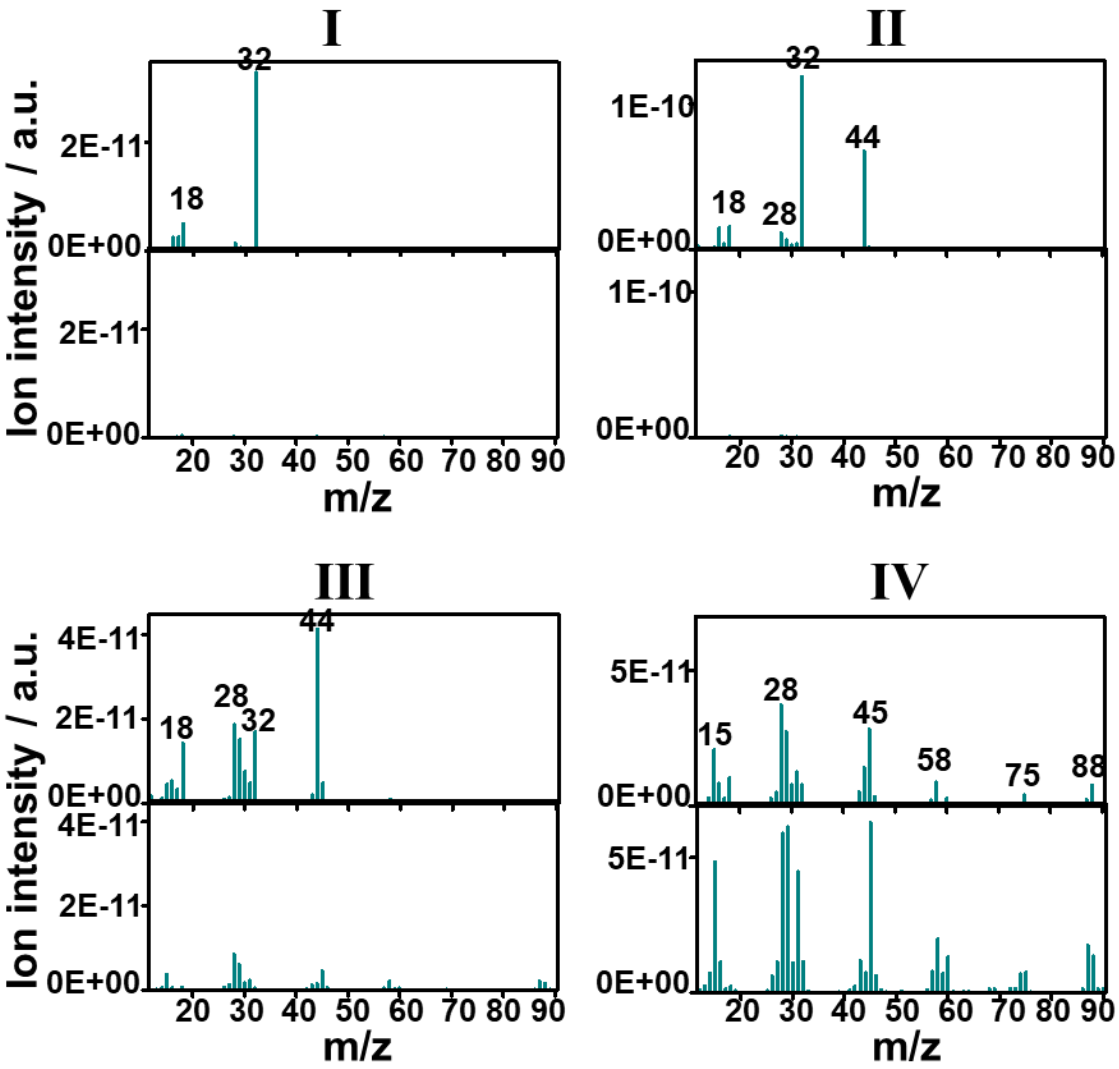

Figure 4-2. Mass peaks of m/z = 12 to 90 at voltage of 4.06 V; **I**, 4.45 V; **II**, 4.68 V; **III**, and 4.8 V; **IV** of with (the top panel) and without (the bottom panel) discharge experiments.

According to the above results, at high overpotential, both high overpotential and reactive oxygen species affect the decomposition of electrolyte (TEGDME) and cathode. To further distinguish the role of both in battery degradation, discharge time dependent experiments were proposed. As shown in **Figure 4-3, (a)** shows discharge

curves of 2 (orange), 4 (blue), 6 (red), 8.8 (green), and 9.6 hr (black) discharge. **(b)** shows the current behaviors as the voltage was swept from OCP (~ 2.8 V) to 4.7 V, when the current of 9.6 hr discharge (black) case reaches the minimum value before the eventual increase. For the first current peak, only the peak intensities increase with discharge time. For the second current peak, in addition to the peak intensities increase with discharge time, the peak positions also show a shift to the more positive voltage. **(c)** Shows voltage dependence of m/z = 75 ($CH_3OCHOCH_3^+$), obviously, the mass behavior is not affected at all by discharge time. This implies that the production of $CH_3OCHOCH_3^+$ is entirely due to the high overpotential, independent of the battery reaction. **(d)** Shows voltage dependence of m/z = 45 ($CH_3OCH_2^+$, $COOH^+$), interestingly, the mass behavior is similar to that of the current that intensity increases with discharge time and peak shifts positively. This indicates that the formation of $CH_3OCH_2^+$ and /or $COOH^+$ is critically related to the formation of O_2. Furthermore, the sharp increase at the final stage of charge (**Fig. 4-3(c)**) is independent to the discharge time, which indicates that the sharp increase is induced by the high overpotential.

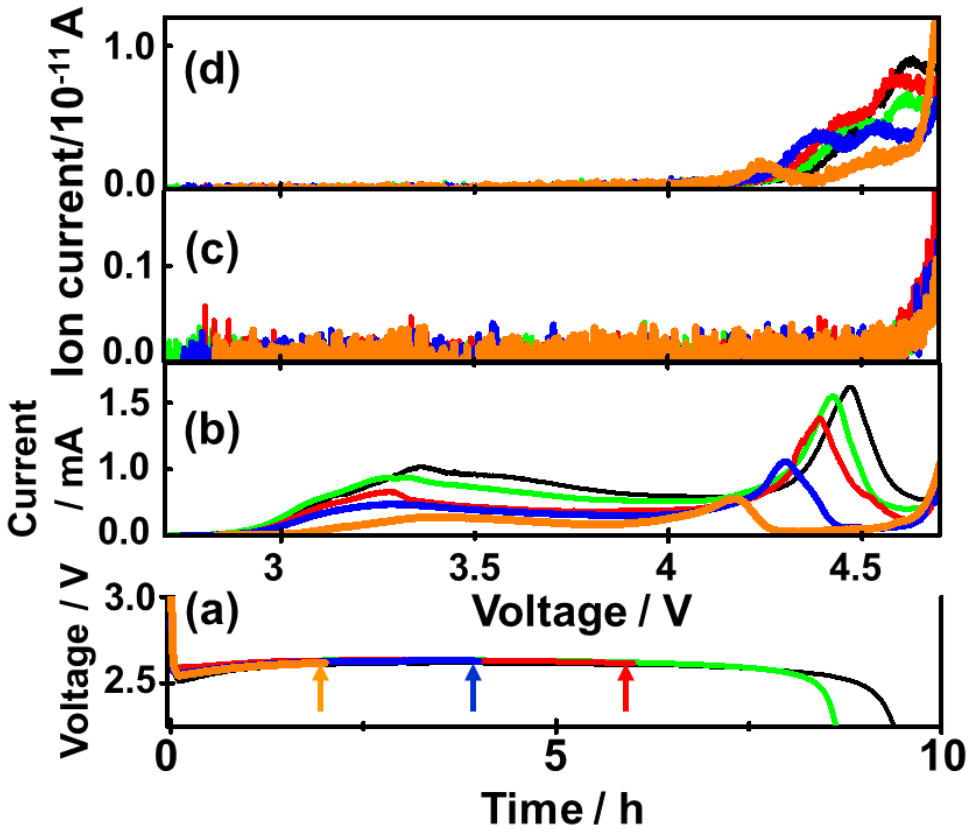

Figure 4-3. **(a)** Discharge curves of various cells of discharge times of 2 (orange), 4 (blue), 6 (red), 8.8 (green), and 9.6 hr (black). **(b)** ~ **(d)** Voltage dependencies of **(b)** current and the background corrected ion currents of Q-mass of m/z = **(c)** 75, **(d)** 45.

4.2.2 Correlation analysis of m/z using Python

Since the on-line QMS monitors mass numbers from 12 to 120 at once, it's difficult to understand the relationships among these mass numbers, so Python was introduced to better analyze the correlation among these mass numbers. The linear relationship among mass numbers (in the lower left corner) and the correlation coefficient (in the upper right corner) can be output simultaneously by a python

calculation. The color shades of the correlation coefficients indicate the degree of correlation between parameters, from blue (negative correlation) to red (positive correlation), which gives a more visual representation of the correlation.

Main code for creating the linear relationships is shown as below.

```
if __name__ == '__main__':
    var1 = int(sys.argv[1]) #x
    var2 = int(sys.argv[2]) #y
    var3 = sys.argv[3] #csv data file
    var4 = int(sys.argv[4]) # starting data row index
    var5 = int(sys.argv[5]) # ending data row index
    df1 = pd.read_csv(var3)
    cols = df1.columns.values #variable names
    #tcol = cols[4:]
    #for elm in cols:
    #    if elm in tcol:
    #        df1[elm] = df1[elm]*1E13
    #df1[cols[0]] = df1[cols[0]]/10000
    df1 = df1.iloc[var4:var5]
```

Main code for creating the correlations is shown as below.

```
if __name__ == '__main__':
    var1 = int(sys.argv[1]) #x
    var2 = int(sys.argv[2]) #y
    var3 = sys.argv[3] #csv data file
    var4 = int(sys.argv[4]) #starting data row index
    var5 = int(sys.argv[5]) #ending data row index
    df1 = pd.read_csv(var3)
    cols = df1.columns.values
    #tcol = cols[4:]
    #for elm in cols:
```

```
    #    if elm in tcol:
    #        df1[elm] = df1[elm]*1E13
    #df1[cols[0]] = df1[cols[0]]/10000
    df1 = df1.iloc[var4:var5]
    plt.rcParams["figure.figsize"] = [4,4]
    plt.figure(dpi=600)
    plt.rcParams['savefig.dpi'] = 60
    plt.rcParams["figure.dpi"] = 10
    plt.rcParams.update({'font.size': 8})
    corr1 = pearsonr(df1[cols[var2]],df1[cols[var1]])
    ax = plt.gca()
    ax.set_axis_off()
    marker_size = 40000
    ax.scatter([.5], [.5], marker_size, c = [corr1[0]], alpha=1,
cmap="seismic",vmin=-2.4, vmax=2.4, transform=ax.transAxes,marker='s')
    font_size = abs(corr1[0]) * 80 + 5
    corr2 = round(corr1[0],2)
    ax.annotate(str(corr2), [.5, .5,],  xycoords="axes fraction", ha='center',
va='center', fontsize=font_size)
    ax.get_figure().savefig('subplots_corr/corr_y-'+cols[var1]+'_x-
'+cols[var2]+'.jpg')
```

The output of linear relationships and correlations are images, and the images combination code is as the follow,

```
def combine_images(img_2d):
    return cv2.vconcat([cv2.hconcat(listh) for listh in img_2d])
if __name__ == '__main__':
    var1 = sys.argv[1]
    df1 = pd.read_csv(var1)
    cols = df1.columns.values
    imgtile = []
    i = 0
    while i < len(cols):
        holder = []
        j = 0
```

```
        while j < len(cols):
            holder.append(0)
            j += 1
        imgtile.append(holder)
        i += 1
    i = 0
    while i < len(cols):
        j = i
        while j < len(cols):
            imgtile[j][i] = cv2.imread('subplots_scatter/scatter_y-'+cols[j]+'_x-
'+cols[i]+'.jpg')
            j += 1

        i += 1
    print('SCATTER PLOTS COLLECTED.')
    i = 0
    while i < len(cols):
        j = i
        while j < len(cols):
            if i == j:
                pass
            else:
                imgtile[i][j] = cv2.imread('subplots_corr/corr_y-'+cols[j]+'_x-
'+cols[i]+'.jpg')
            j += 1
        i += 1
    print('CORRELATION PLOTS COLLECTED.')
```

An output diagram (correlation_matrix) of correlations between parameters of time, voltage, current, charge, and m/z = 12~120 is shown in **Figure 4-4**. Parameters are output on the diagonal, correlation coefficients with color are output on the upper right corner, and linear relationships are output on the lower left corner. Due to the

space limitation, only a low-resolution output diagram can be seen. However, the overall layout of the output combine diagram is still clear. The correlations of the parameters of time, voltage, current, charge, and m/z = 12~90 are shown in the dashed box in **Fig. 4-4**. The correlations between m/z = 91 and 120 and with other parameters are very low. This is evident from the fact that the correlation in the upper right corner is almost white. Thus, the subsequent mass spectra were analyzed up to m/z = 90.

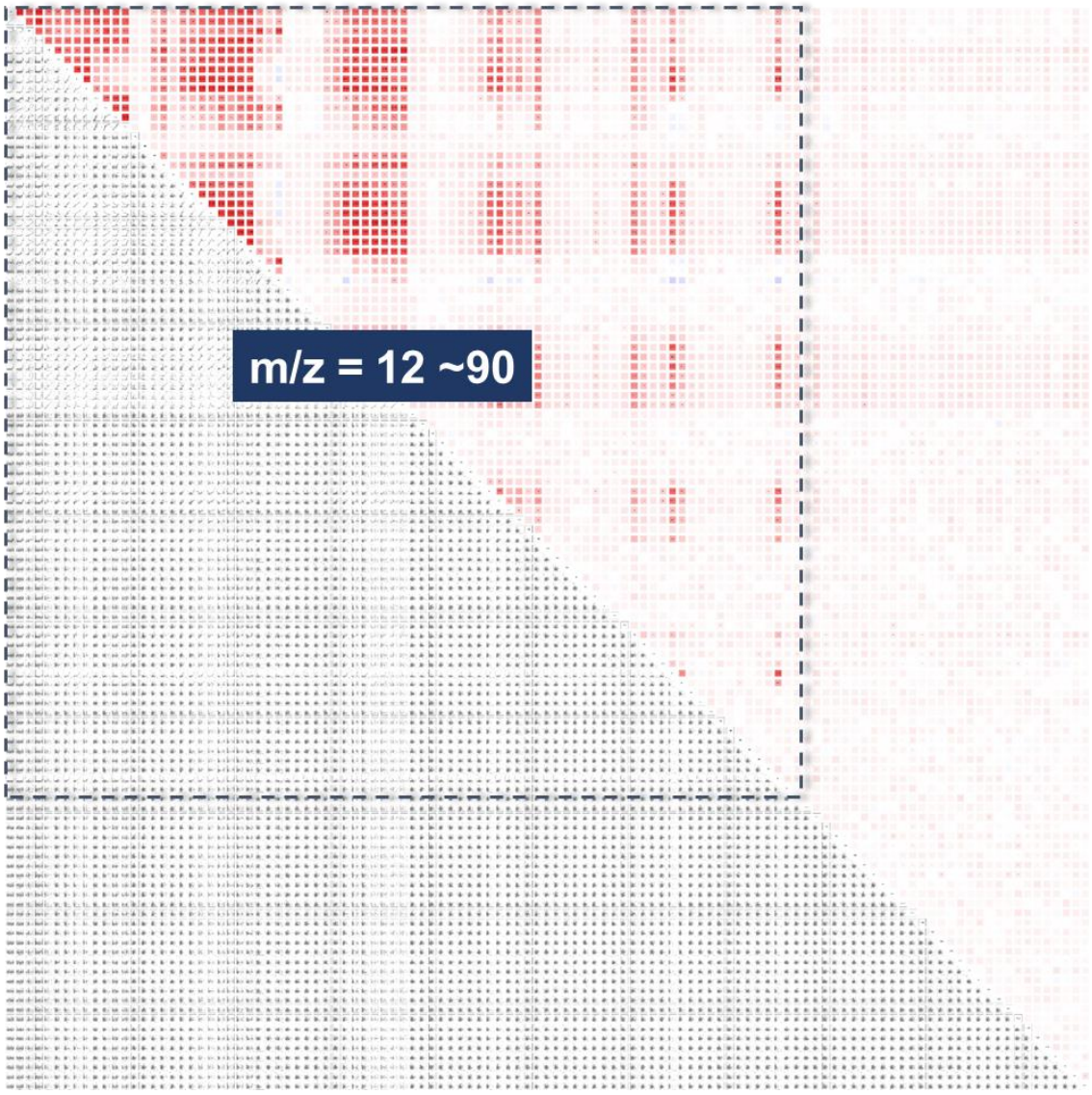

Figure 4-4. Python calculated correlation of mass numbers at voltage sweep from OCP (~2.8 V) to 4.8 V.

To show the python results more clearly, the correlation_matrix between time, voltage, current, charge H_2O (MS18), O_2 (MS32) and CO_2 (MS44) in the four partitions (I; OCP~4.06 V, II; 4.06~4.45 V, III; 4.45~4.68 V, IV; 4.68~4.8 V) of **Fig. 4-1(b)** is shown in **Figures 4-5/6/7/8**.

Fig. 4-5 shows the correlation_matrix between the parameters of time, voltage, current, charge, and mass number 18 (H_2O) and 32 (O_2) in voltage range of OCP~4.06 V. (Since no CO_2 (MS44) was detected in this region, MS44 is not shown here for clarity.) It is obvious that the linear relationships and correlations between parameters are presented visually. For clarity, the correlation and linearity of current vs. MS32 are marked with red and black arrows, respectively, in **Fig. 4-5**. Since this is voltage sweep, there is a linear correlation between time and voltage, with correlation coefficient showing the reddest color. As the voltage increases linearly, the current flow becomes nonlinear, so the correlation coefficient between time and voltage is less than 1, which is 0.72, a light red color. Since charge is a time aggregation of current, it has an almost linear relationship with time and voltage, with a correlation coefficient of 0.99, which is bright red color. The generation of H_2O (MS18) starts with the first current peak and then increases linearly, and its behavior is very similar to that of charge that the correlation coefficient with charge is 0.92, which is bright red color. In the early stage of charging, since the main product is O_2 (MS32), O_2 behaves in the same way as the current, as indicated by the black and red arrows, which showing a linear relationship and a correlation coefficient of 0.99, which is bright red color.

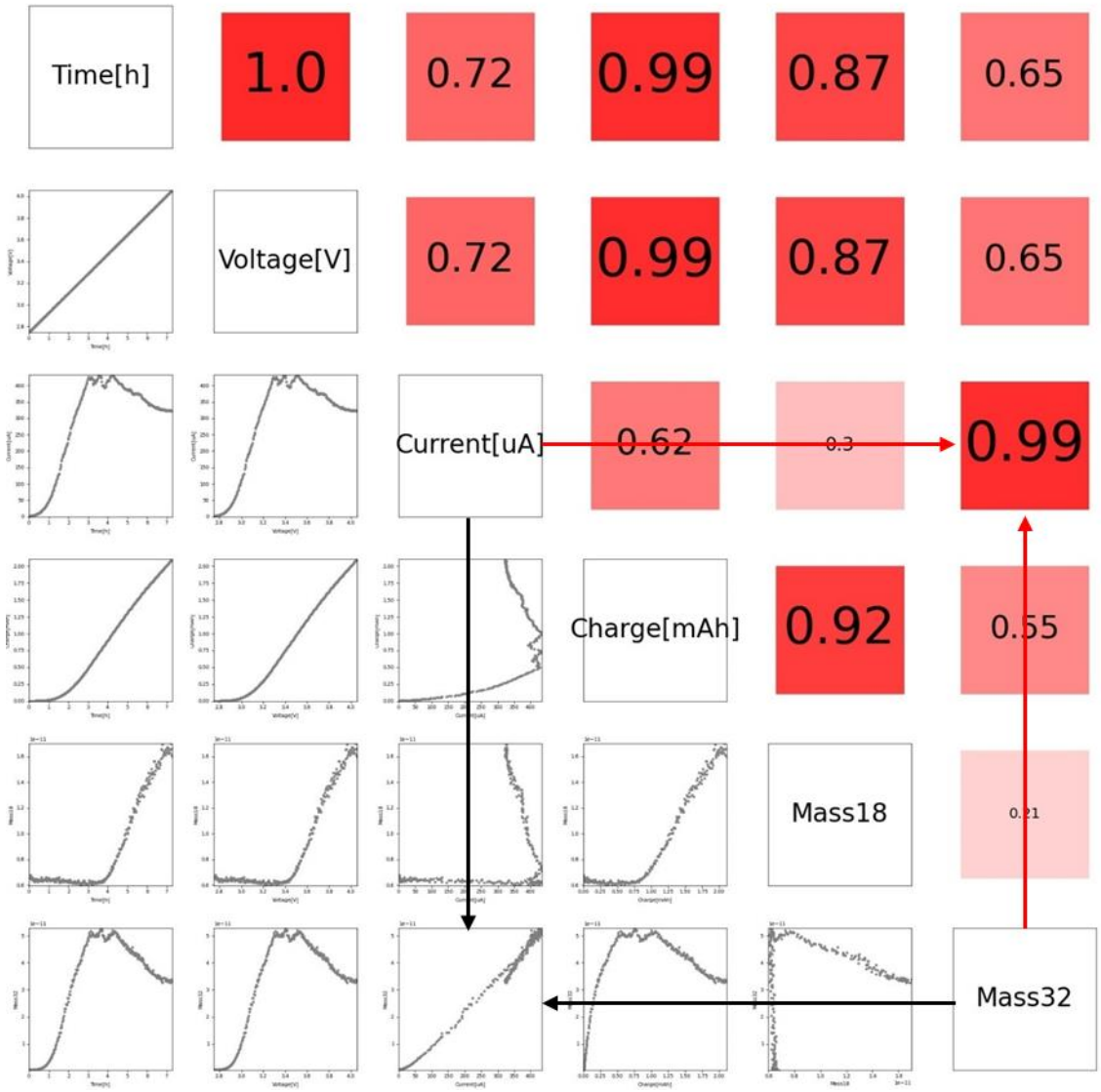

Figure 4-5. Python calculated correlation of mass numbers at voltage sweep from OCP (~2.8 V) to 4.06 V which is the first current minimum in **Fig. 4-1(b)**.

Fig. 4-6 shows the correlation_matrix between the parameters of time, voltage, current, charge, and mass numbers 18 (H_2O), 32 (O_2) and 44 (CO_2) in the voltage range of 4.06~4.45 V. In this region, CO_2 (MS44) occurs together with the second peak of current/O_2 (**Figs. 4-1(b/c)**), so a high correlation between MS44 and current/O_2 is

indicated by the black arrows and a correlation coefficient of 0.94/0.98 with bright red color which indicated by the red arrows.

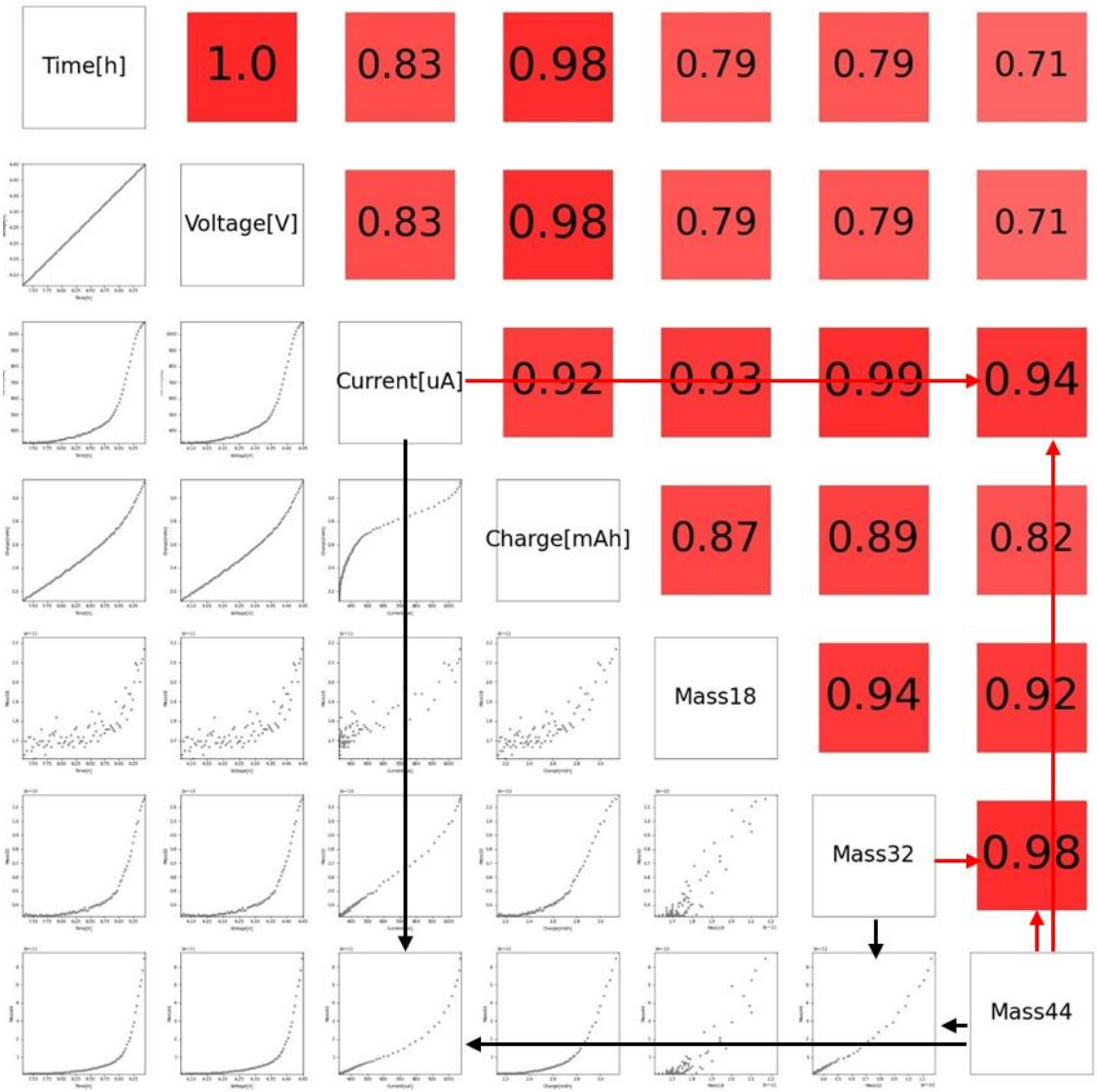

Figure 4-6. Python calculated correlation of mass numbers at voltage sweep from 4.06 to 4.45 V which is the second current peak in **Fig. 4-1(b)**.

Fig. 4-7 shows the correlation_matrix between the parameters of time, voltage, current, charge, and mass numbers 18 (H_2O), 32 (O_2) and 44 (CO_2) in the voltage

range of 4.45~4.68 V. In this region, the current and O_2 (MS32) generation decrease and a negative correlation appears, as marked with black arrows. The correlation coefficients are -0.95 and -0.93 (the correlation coefficient between charge and MS32 is -0.98), as indicated by the blue arrows, which are bright blue color.

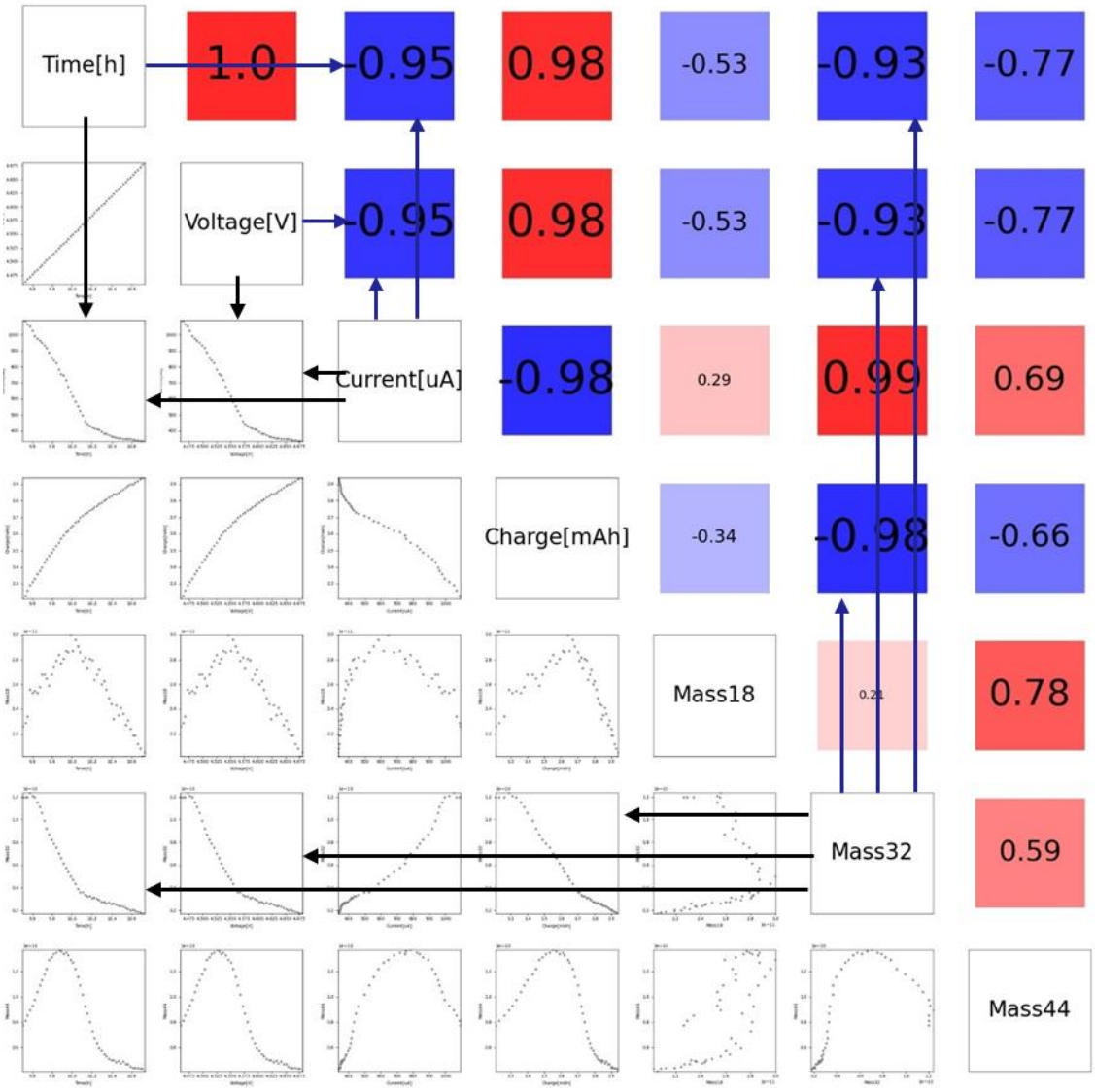

Figure 4-7. Python calculated correlation of mass numbers at voltage sweep from 4.45 to 4.68 V which is the second current minimum in **Fig. 4-1(b)**.

Fig. 4-8 shows the correlation_matrix between the parameters of time, voltage, current, charge, and mass numbers 18 (H_2O), 32 (O_2) and 44 (CO_2) in the voltage range of 4.68~4.8 V. In this region, the main products are organic products instead of H_2O, O_2 and CO_2. Therefore, MS18/32/44 are negatively correlated with time, voltage, current and power, as indicated in the dash blue square.

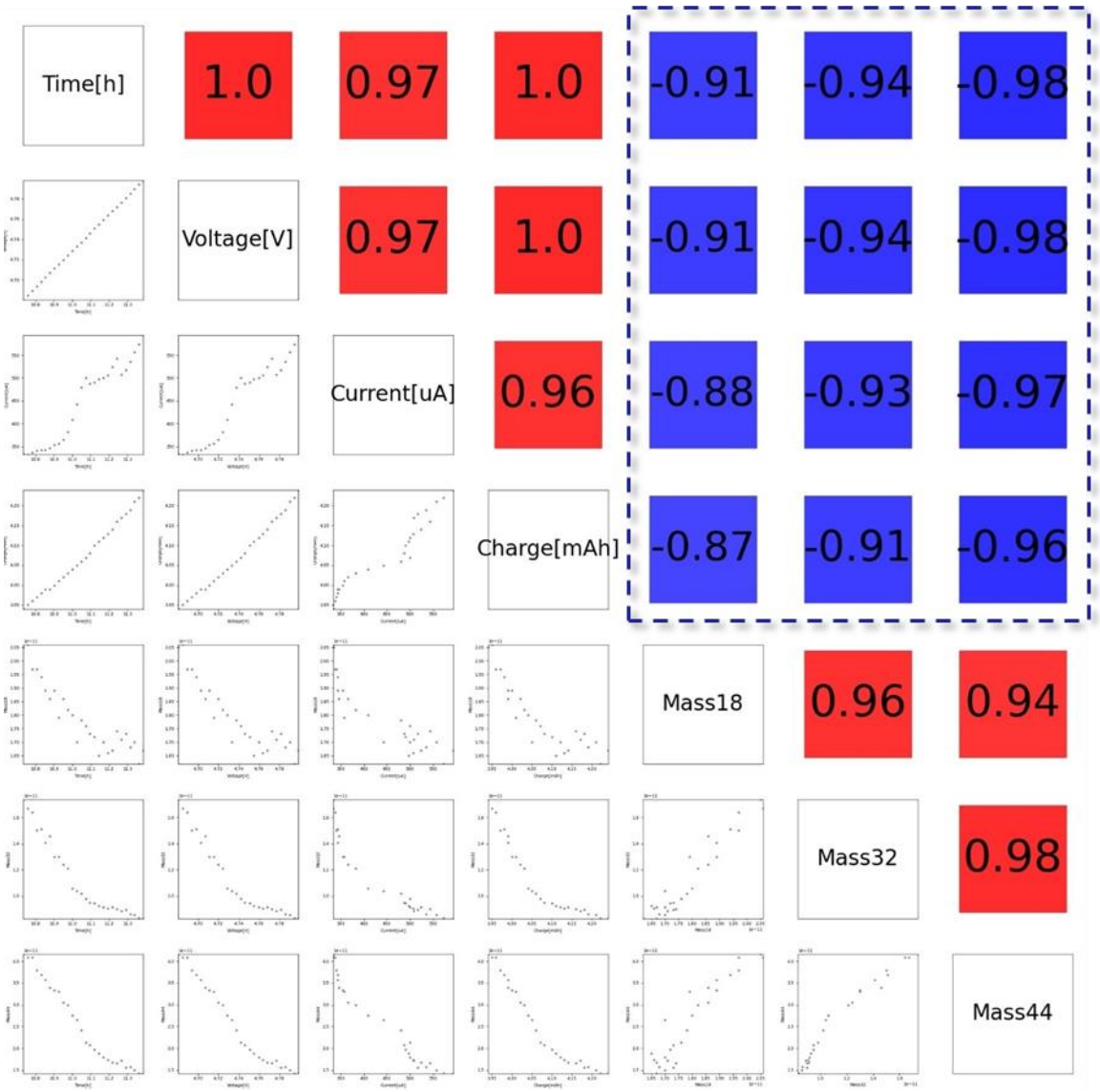

Figure 4-8. Python calculated correlation of mass numbers at voltage sweep from 4.68 to 4.8 V which is the first current minimum in **Fig. 4-1(b)**.

Figure 4-9 shows the correlation_matrix between the parameters of time, voltage, current, charge, and mass number 18 (H_2O), 32 (O_2) and 44 (CO_2) for the full voltage sweep process (OCP to 4.8 V). The region-wide correlation matrix visualizes the linearity and correlation degree/ coefficients between parameters for the entire process.

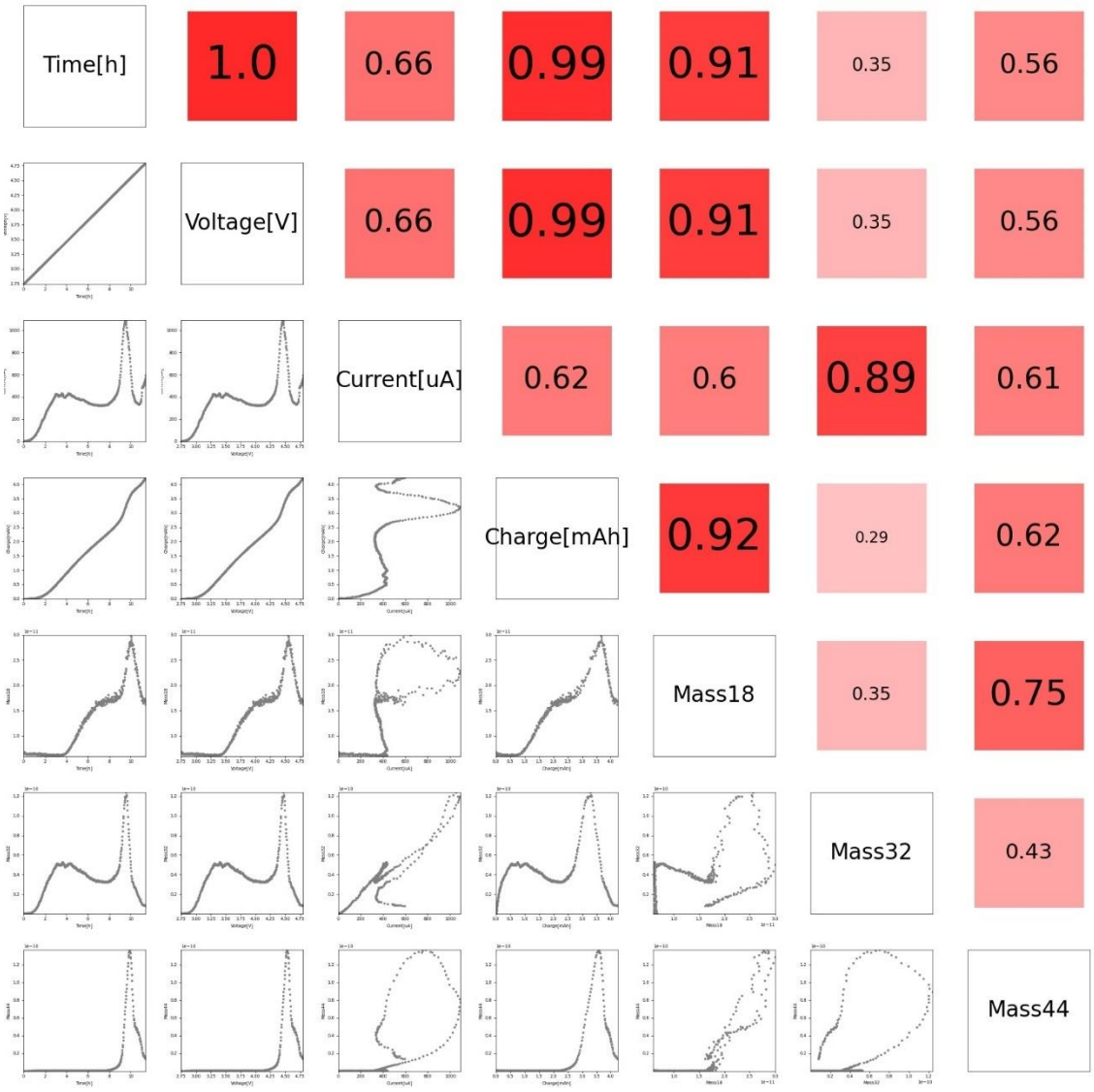

Figure 4-9. Python calculated correlation of mass numbers at voltage sweep from OCP (~2.8 V) to 4.8 V that is the full voltage sweep process in **Fig. 4-1(b)**.

4.2.3 Isotope effect in TEGDME degradation mechanism study

Figure 4-1(f) shows the LSV curve that without discharge beforehand, which means there is no Li_2O_2 pre-deposition. It only shows an eventual rise in current at the high overpotential/final voltage sweep, implying that the decomposition of electrolyte

and cathode at high overpotential is not related to the main battery reaction, $Li_2O_2 \leftrightarrow 2Li + O_2$. Furthermore, the mass spectrum at the minimum value of the current before the final rise (**Fig. 4-2IV** bottom panel) indicates that there is already electrolyte and/or cathode decomposition products due to the high overpotential. Therefore, the analysis of the battery degradation mechanism will be studied up to the voltage of the minimum current before the final rise. To further investigate the product formation mechanism, isotope experiments were introduced, as seen in **Figure 4-10**. **Panel i** shows the discharge curves of all isotope experiments, and panel **ii** shows the current behaviors when the voltage is swept from OCP to the value of the minimum current before the final rise in the isotope experiments. Panels **iii**, **iv**, **v**, and **vi** show the four typical mass behaviors in the isotope experimental analysis with m/z = 88/35/36/13.

Apparently, the discharge curves (**panel i**) in all isotope experiments are last for 10 hr, and the LSV currents (**panel ii**) all show similar behavior with two clear peaks. This suggests that the results of these six isotope experiments are comparable.

Panel iii shows the behavior of m/z = 88 as a function of voltage, indicating that the behavior does not change when changing the solvent ($^{12}CH_3$_TEGDME, $^{13}CH_3$_TEGDME, $^{12}CD_3$_TEGDME) or the discharge gas ($^{16}O_2$, $^{18}O_2$) introduced

during the discharge. This indicates that the O atom in the compound ($(CH_2CH_2O)_2^+$) corresponding to m/z = 88 does not originate from the discharge gas and the H atom does not originate from the methyl group at the terminal of the TEGDME.

Panel iv shows the behavior of m/z = 35 as a function of voltage. Since the routine experiment uses $^{12}CH_3$_TEGDME as solvent and $^{16}O_2$ as discharge gas, the mass numbers of CH_3OH^+ and O_2^+ are both equal to 32. Since O_2 is the main charge product of the battery reaction, $Li_2O_2 \rightarrow 2Li + O_2$, the amount of CH_3OH^+ is negligible compared to O_2^+ although the amount of CH_3OH^+ is large. By introducing $^{12}CD_3$_TEGDME as a solvent, CH3OH$^+$ becomes $^{12}CD_3OH^+$ with a mass number of 35, which is easily separated from the masses of O_2^+ and other compounds. Based on experiments using $^{12}CD_3$_TEGDME as a solvent, further analysis can be performed to determine the formation behavior and yield of the CH_3OH compound, and the analysis process is detailed in the **Section 4.2.4**.

Panel v shows the behavior of m/z = 36 as a function of voltage. In $^{18}O_2$ flow discharge cases, mass behavior is similar to that of the current. Because comparing with normal experiments, $^{16}O_2$ is replaced by $^{18}O_2$ as the discharge gas and the mass

number of oxygen produced by the decomposition of lithium peroxide during charging, $Li_2{}^{18}O_2 \rightarrow 2Li + {}^{18}O_2$, is 36.

Panel vi shows the behavior of m/z = 13 as a function of voltage. Only the $^{13}CH_3$_TEGDME experiment shows a peak in the same position as the CO_2 peak in **Fig. 4-1(c)** (blue). This means that this peak is mainly a $^{13}C^+$ peak from the ionization of $^{13}CO_2$. Source of C for CO_2 include carbon cathode, as well as methyl and methylene fractions of TEGDME. By using $^{13}CH_3$_TEGDME as the solvent, the methyl fraction from $^{13}CH_3$_TEGDME forms $^{13}CO_2$, which ionizes to $^{13}C^+$, i.e., m/z = 13.

The detailed attribution analysis of degradation products based on isotopic experiments is presented in the **Section 4.2.4**. Detailed isotope experiments table mass spectra are shown in **Appendix II**.

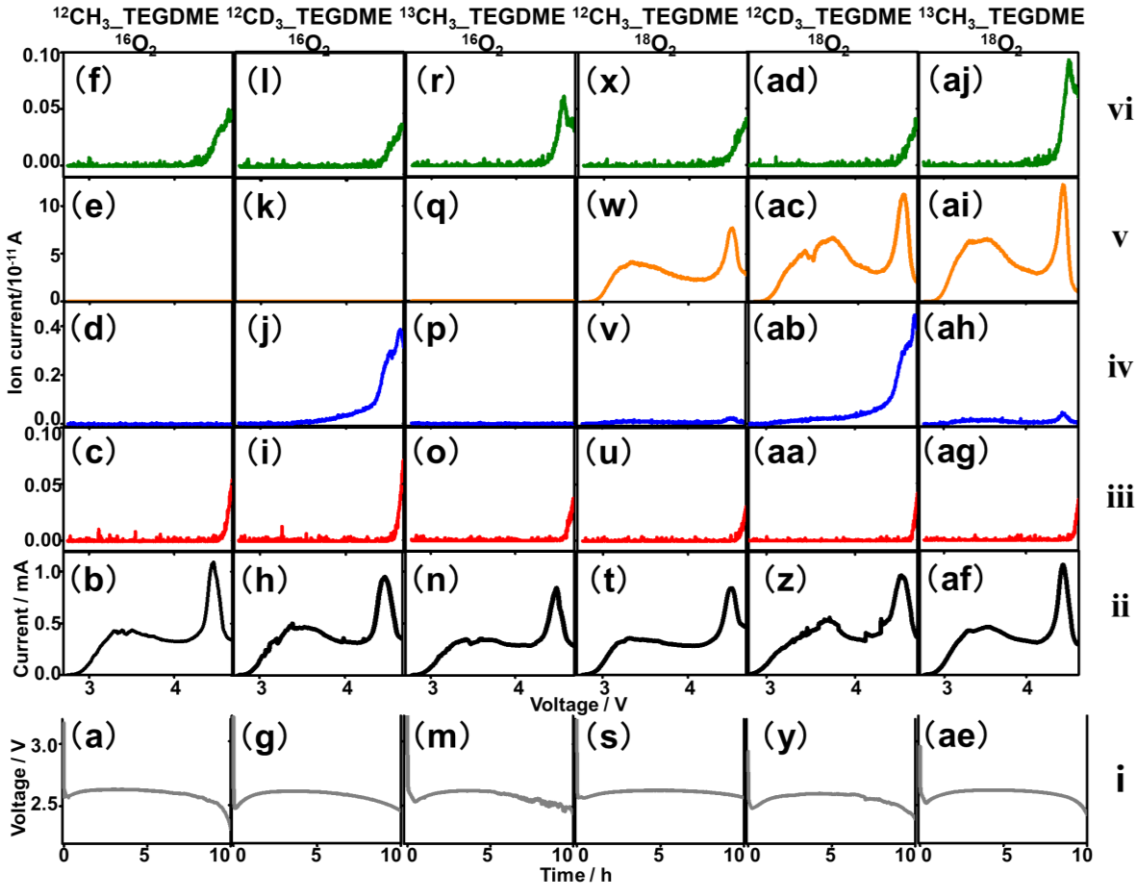

Figure 4-10. Isotope experiments of **(a)**, **(g)**, **(m)**, **(s)**, **(y)**, and (ae) discharge as a function of time, and **(b)~(f)**, **(h)~(l)**, **(n)~(r)**, **(t)~(x)**, **(z)~(ad)**, and **(af)~(aj)** current and m/z = 88/35/36/13 as a function of voltage in $^{12}CH_3$_TEGDME electrolyte under $^{16}O_2$ flow discharge, $^{12}CD_3$_TEGDME electrolyte under $^{16}O_2$ flow discharge, $^{13}CH_3$_TEGDME electrolyte under $^{16}O_2$ flow discharge, $^{12}CH_3$_TEGDME electrolyte under $^{18}O_2$ flow discharge, $^{12}CD_3$_TEGDME electrolyte under $^{18}O_2$ flow discharge, and $^{13}CH_3$_TEGDME electrolyte under $^{18}O_2$ flow discharge.

4.2.4 Precise analytical procedures for battery degradation products

The following analyze are all based on the voltage sweep up to 4.68 V, which is proved enough for charging of battery as or less than 4.5 V was used as the usual battery cut off potential.[51-53] According to the results, all mass signals can be divided into two types: appearance only due to the high overpotential and generation related to

the battery process, that is $Li_2O_2 \leftrightarrow Li^+ + O_2$ (2.96 V vs Li/Li^+).

The following analysis is performed based on the voltage sweep to 4.68V, which is before the final current increase (**Fig. 4-1(b)**). Based on the above analysis (**Fig. 4-2 IV**), many products are generated at high overpotential. And based on the analysis of **Fig. 4-3(c)**, it can be concluded that some mass numbers, e.g., m/z = 88, 75, 58, that appear only depending on the high overpotential. these are electrochemical degradation products, i.e., **Type 1** (**Figure 4-11**). But the point is that the cut off potential is or less than 4.5 V in a typical cell. This means the degradation of a typical cell is mainly caused by the active material during the charging/discharging processes. The corresponding products are chemical degradation products, i.e., **Type 2** (**Figure 4-11**).

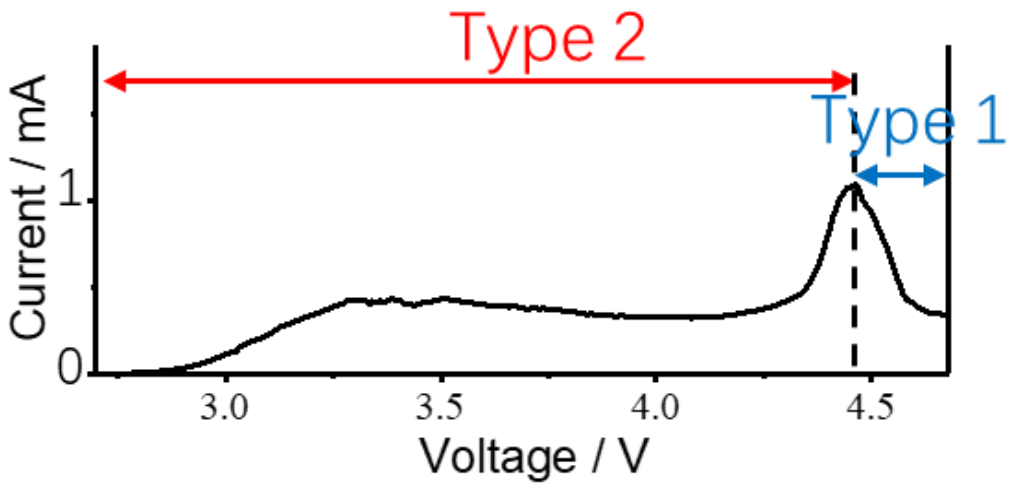

Figure 4-11. The voltage range of the degradation that **Type 1** is from OCP (~2.8 V) to the voltage (4.45 V) of the second current peak, **Type 2** is higher than the voltage (4.45 V) at the second current peak.

4.2.4.1 Electrochemical degradation products

For the first type, **Figure 4-12** shows on-line QMS results of m/z = 88, 75, and 58 that under 10/6/4/2/0 hr discharge. The mass behaviors of m/z = 88, 75, and 58 are not affect by discharge time, but all mass signals simply show an increase due to high overpotential. This means that the generation of the fragments corresponding to m/z = 88, 75, and 58 is not affect by the amount of Li_2O_2, the main discharge product deposited during the discharge.

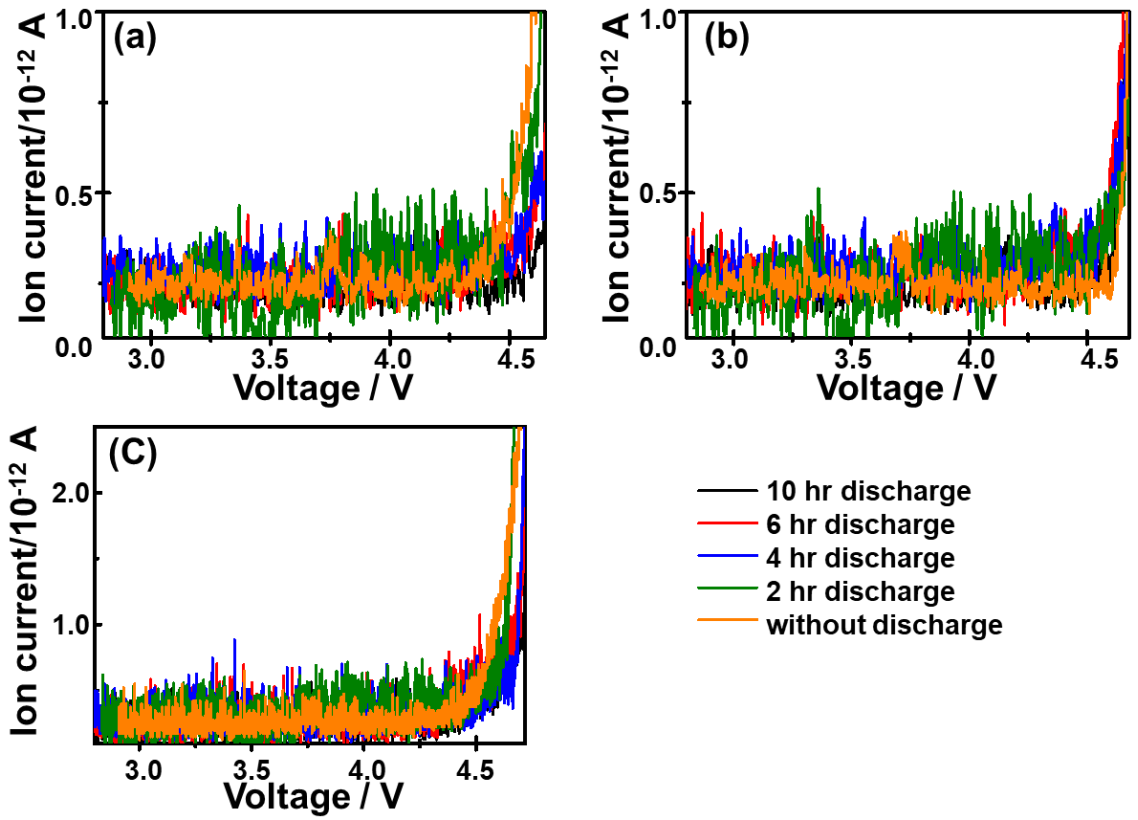

Figure 4-12. Discharge time dependent mass signals for m/z = 88**(a)**, 75**(b)**, and 58**(c)** as a function of voltage.

4.2.4.1.1 Assignment of *1,4-Dioxane* (m/z = 88/87)

Figure 4-13 shows the on-line QMS of m/z = 88/87/58 in the isotope experiments. It is clear that the mass behaviors of m/z = 88 are the same in all isotope experiments. Thus, considering the molecular structure of the isotope TEGDME (**Figure 4-14**), it can be deduced that MS88 should be derived from the middle part of TGEDME. The possible fragment/molecule could then be *1,4-Dioxane* (b.p.~101°C, v.p.~5.08 kPa; b.p. means boiling point, v.p. means vapor pressure). To further confirm the presence of

1,4-Dioxane in the decomposition products, The mass spectrum of *1,4-Dioxane* was checked from the NIST (National Institute of Standards and Technology) database (DB), it shows *1,4-Dioxane* is not only contributes to m/z = 88 but also m/z = 87/58/…. The coefficients are 52.08, 6.1, 40.8, …, respectively. Thus, as shown in **Fig. 4-13**, when multiplied by 8, m/z = 87 behaves very similarly to m/z = 88. Additionally, the on-line QMS of m/z=87 and m/z=58 in **Fig. 4-13** also shows no isotopic influence. So, it is true that *1,4-Dioxane* presents in the decomposition products. The Mass behavior of *1,4-Dioxane* = (100/52.08) × MS88 is shown in **Figure 4-15**.

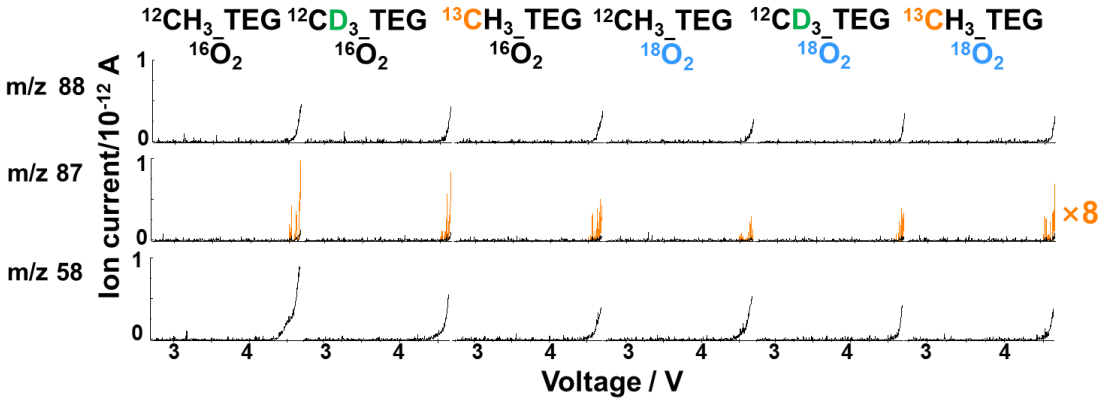

Figure 4-13. On-line QMS of m/z=88/87/58 in isotope experiments.

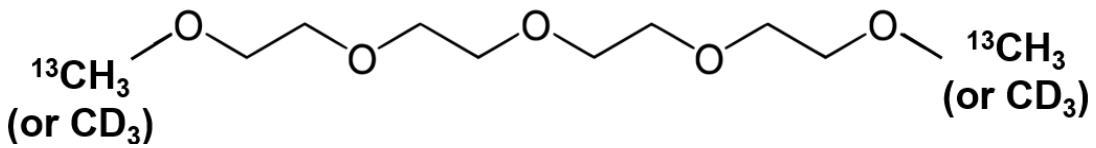

Figure 4-14. The isotope molecular structure of $^{13}CH_3$_TEGDME, and $^{12}CD_3$_TEGDME.

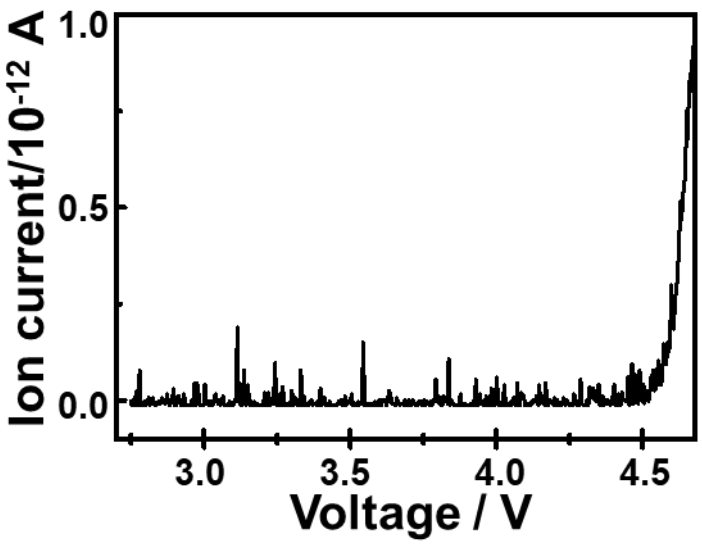

Figure 4-15. Mass signal of *1,4-Dioxane* as a function of voltage.

4.2.4.1.2 Assignment of *Methylal* (m/z = 75)

Figure 4-16 shows the on-line QMS of m/z = 75/77/81 in the isotope experiments. Where m/z = 75 will plus 2 to become m/z = 77 in the $^{13}CH_3$_TEG $^{16}O_2/^{18}O_2$ experiments, and plus 6 to become m/z=81 in $^{12}CD_3$_TEG $^{16}O_2/^{18}O_2$ experiments. That means there exist two methyl groups from the terminal portion of TEGDME in the fragment of m/z = 75, so two ^{12}C will become ^{13}C which plus 2 mass in $^{13}CH_3$_TEG experiments, and H will become D which plus 6 mass in $^{12}CD_3$_TEG experiments.

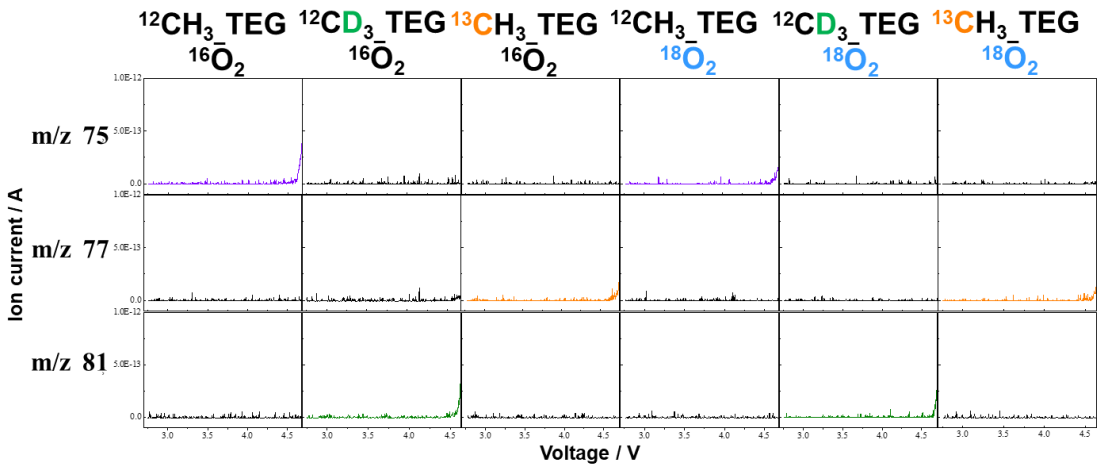

Figure 4-16. On-line QMS of m/z = 75/77/81 in isotope experiments.

Thus, the fragment with m/z = 75 should be $CH_3OCHOCH_3^+$, which will become $^{13}CH_3OCHO^{13}CH_3^+$ in the isotope $^{13}CH_3$_TEG experiments, and $CD_3OCHOCD_3^+$ in the isotope $^{12}CD_3$_TEG experiments. So, the possible initial molecule should be *Methylal* (b.p.~41.6°C, v.p.~53.3 kPa). As the main contributions of methylal to mass numbers (coefficients) are 29(43.84), 31(11.71), 45(100), 75(43.74). The mass signal of *Methylal* = (100/43.74) × MS75, is shown in **Figure 4-17**.

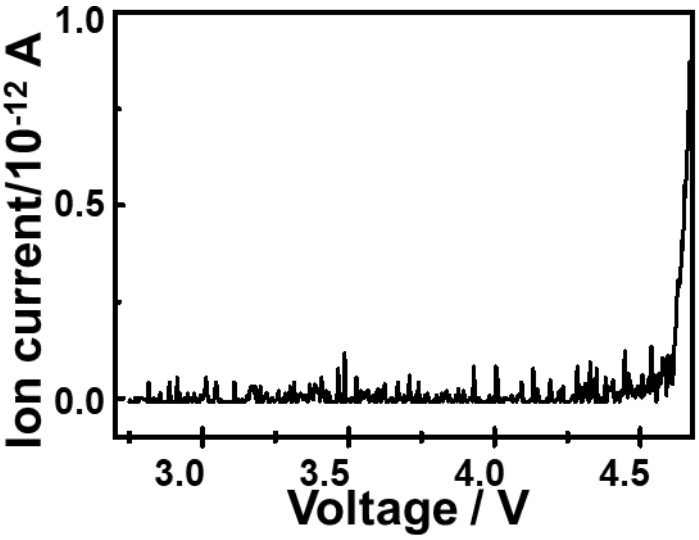

Figure 4-17. Mass signal of *Methylal* as a function of voltage.

4.2.4.1.3 Assignment of *Methoxyethene* (m/z = 58)

The top three panels of **Figure 4-18** show on-line QMS of m/z = 58/59/61. It seems that m/z = 58 in both $^{16}O_2$ and $^{18}O_2$ flowing discharge cases will remain m/z = 58 and plus 3 mass to become m/z = 61 in $^{12}CD_3$_TEG experiments, remain m/z = 58 and plus 1 mass to become m/z = 59 in $^{13}CH_3$_TEG experiments. This means that both methyl and methylene group of TEGDME are presented in the fragment with m/z = 58 and no O atom derived from the discharge gas. DB sugesst that the possible fragment of m/z = 58 should be $CH_3OC_2H_3^+$ (*Methoxyethene*). To further confirm, the bottom panel of **Fig. 4-18** shows the total on-line QMS of m/z = 58/58+61/58+59 or *Methoxyethene* in normal_TEG/$^{12}CD_3$_TEG/$^{13}CH_3$_TEG based electrolyte that under

both $^{16}O_2$ and $^{18}O_2$ flow during discharge. It's clear that the on-line QMS behaviors of *Methoxyethene* in all isotope experiments are very similar. Thus, it's true that two types of *Methoxyethene* were generated.

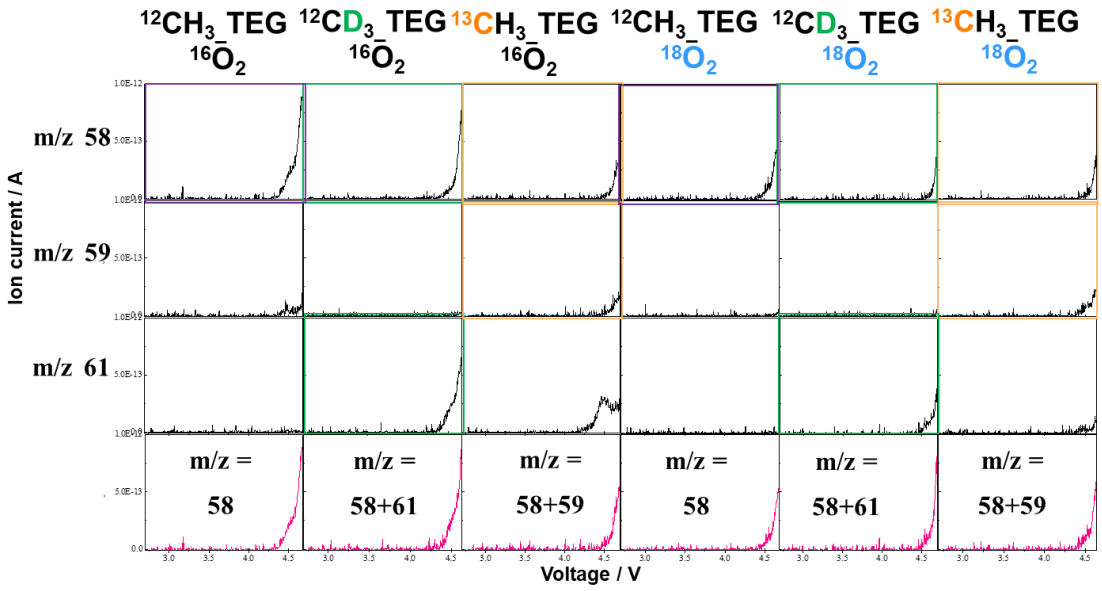

Figure 4-18. On-line QMS of m/z = 58/59/61 and fragment related to $CH_3OC_2H_3^+$ in isotope experiments.

Figure 4-19 shows two different *Methoxyethene* generation schemes. One (terminal carbon (T_C) *Methoxyethene*) is generate from the methyl portion of TEG, where m/z = 58 will become to m/z = 61 in the $^{12}CD_3$_TEG experiment and m/z = 59 in the $^{13}CH_3$_TEG experiment. The other (middle carbon (M_C) *Methoxyethene*) is generate from methylene portion of TEG, which is remain m/z = 58 in the $^{12}CD_3$_TEG and $^{13}CH_3$_TEG experiments.

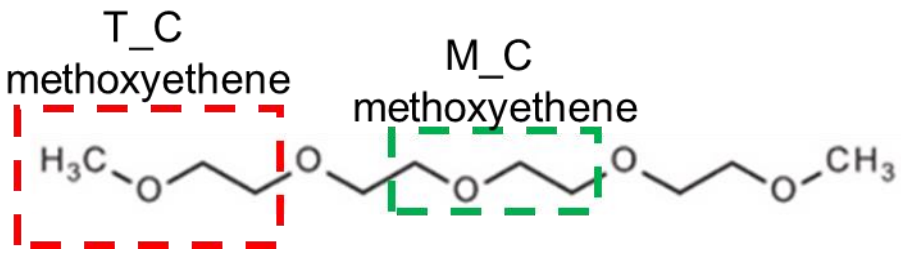

Figure 4-19. Generation scheme of two different kinds of *Methoxyethene*.

As in the DB, the contributions of *Methoxyethene* to the mass numbers (coefficients) are 14(24.62), 15(100), 26(28.93), 27(60.26), 28(65.97), 29(62.87), 31(40.34), 42(19.92), 43(68.57), 58(77.58). The mass signal of *Methoxyethene* = (100/77.58) × MS58 (**Figure 4-20**)

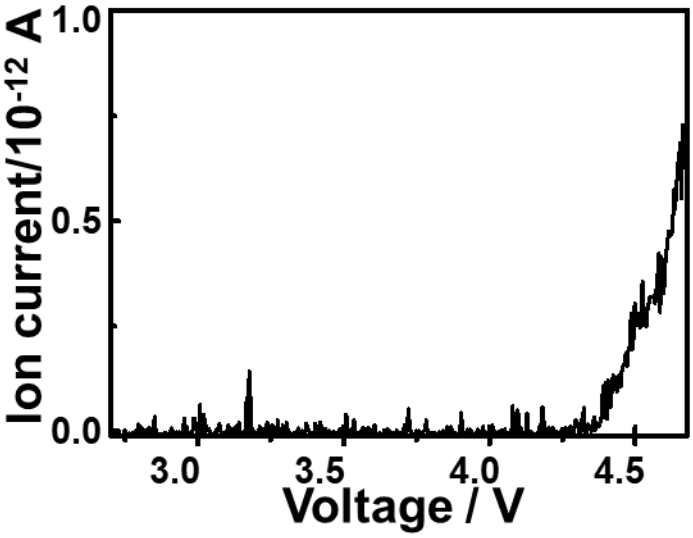

Figure 4-20. Mass signal of *Methoxyethene* as a function of voltage.

4.2.4.2 Chemical degradation products

The second type refers to the mass signal contributed from chemically generated molecules. This section is explained from large mass numbers to small mass numbers in order to eliminate the influence of large mass numbers on small mass numbers.

4.2.4.2.1 Assignment of *1,3-Dioxolane* (m/z = 74/73)

From the discharge time dependent experiments (**Figure 4-21**), the mass signals of the experiments without discharge show no overall change, the mass signals with different discharge time exhibit an insignificant peak around 4.63 V, and the peak intensity increases with discharge time, which means that the amount of m/z = 73 is associated with the amount of Li_2O_2 decomposed during charging.

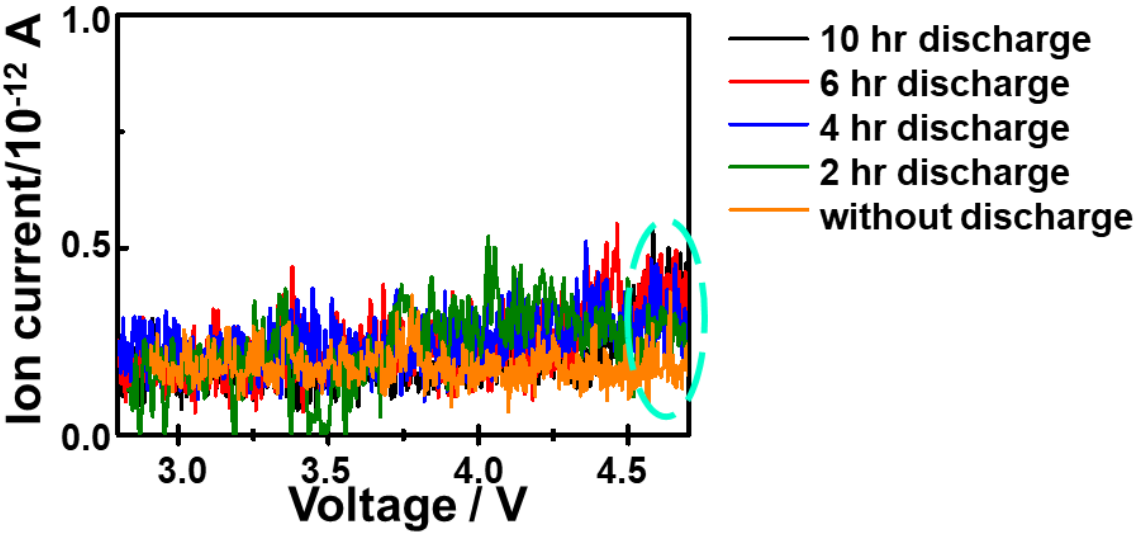

Figure 4-21. Mass signals of m/z = 73 with different discharge time, as a function of voltage.

Figure 4-22 shows on-line QMS of m/z = 73 and 74, indicating that mass behaviors are not affected by the isotope TEGDMEs and oxygens, which means that the corresponding fragment is generated from the middle portion of TEGDME. The possible fragment should be $C_3H_5O_2^+$ that is ionized from *1,3-Dioxolane* (boiling point is 78°C, vapor pressure is 10.53 kPa). To further confirm this, mass spectrum of *1,3-Dioxolane* was checked in DB and the main contributions to mass numbers (coefficients) were 15(21.49), 27(11.19), 29(43.89), 31(7.29), 43(21.39), 44(63.7), 45(29.79), 73(100), 74(5.69). It is well known the intensity ratio of 74/73 is 0.057, which was close to the experimental result. Thus, dioxolane is exist in the

decomposition products. The ionized contribution to m/z = 73 is 100, thus, the mass behavior of 1,3-dioxolane is the same as m/z = 73 (**Figure 4-23**).

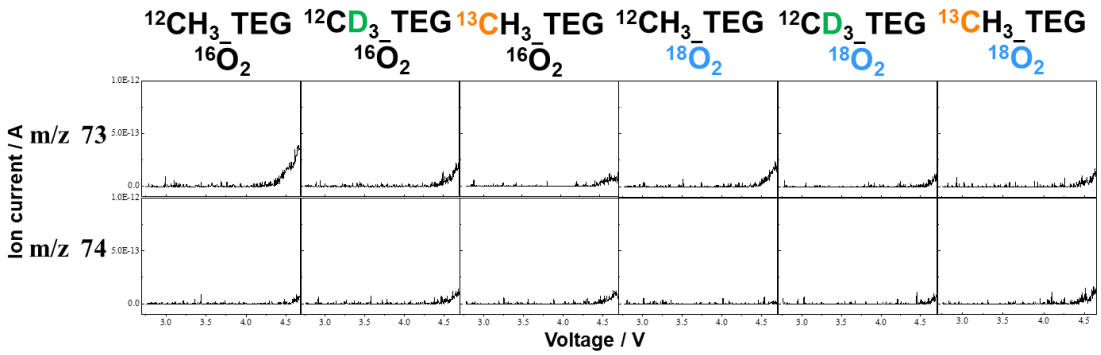

Figure 4-22. On-line QMS of m/z = 73/74 in isotope experiments as a function of voltage.

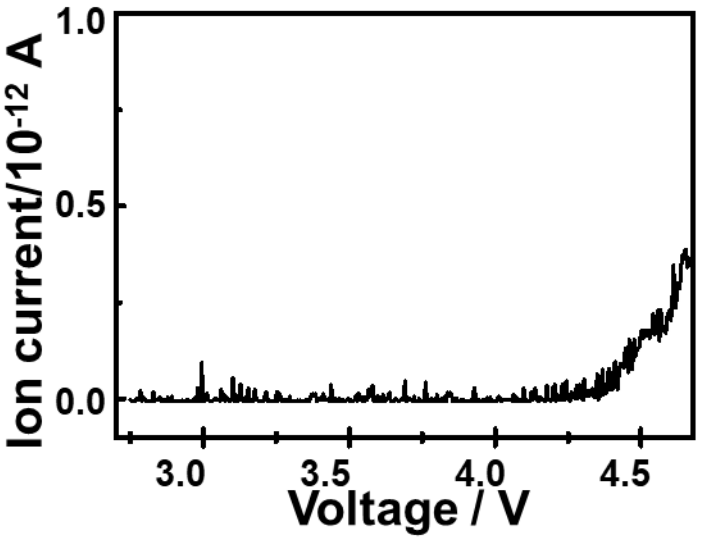

Figure 4-23. Mass signal of *1,3-Dioxolane* as a function of voltage.

4.2.4.2.2 Assignment of *Methyl formate* (m/z = 60)

In the discharge time dependence plots (**Figure 4-24**), the mass signals for the 10, 6, and 4 hr discharge show a peak and then increase, with the peak showing a positive shift as the discharge time increases. For the 2 and 0 hr discharge, the mass signals only show an increase at the final. Moreover, the increased behaviors at the final high overpotential are all same for all experiments. This indicates that two types of fragments that related to m/z = 60 were generated. One corresponds to the positively shifted peak that are produced chemically due to the reactive oxygen species, and the other is corresponds to the increase that generated electrochemically because of the high overpotential.

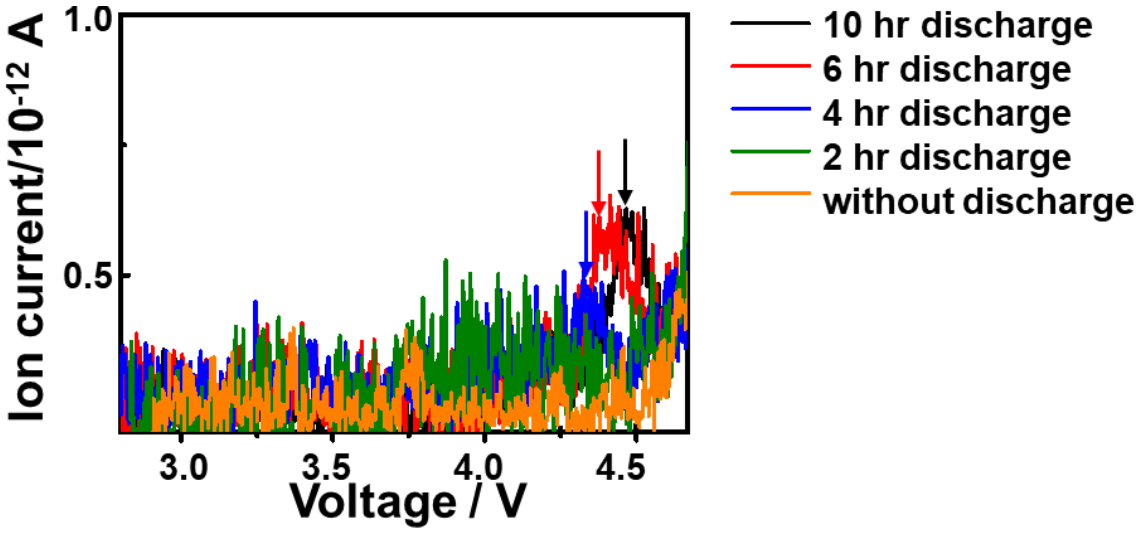

Figure 4-24. Mass signals of m/z = 60 with different discharge time, as a function of voltage.

Figure 4-25 shows the on-line QMS of m/z = 60~65. It is clear that m/z = 60 is plus 3 mass to m/z = 63 in the $^{12}CD_3$_TEG $^{16}O_2$ experiment, plus 1 mass to m/z = 61 in the $^{13}CH_3$_TEG $^{16}O_2$ experiment, plus 2 mass to m/z = 62 in the $^{12}CH_3$_TEG $^{18}O_2$ experiment, plus 5 mass to m/z = 65 in the $^{12}CD_3$_TEG $^{18}O_2$ experiment, and plus 3 mass to m/z = 63 in the $^{13}CH_3$_TEG $^{18}O_2$ experiment. As suggested by DB, possible fragments for m/z = 60 are *Acetic acid* (b.p.~117.77°C, v.p.~2.09 kPa), *Methoxyethane* (b.p.~7.4°C, v.p.~199.05 kPa), and *Methyl formate* (b.p.~31.5°C, v.p.~78.09 kPa).

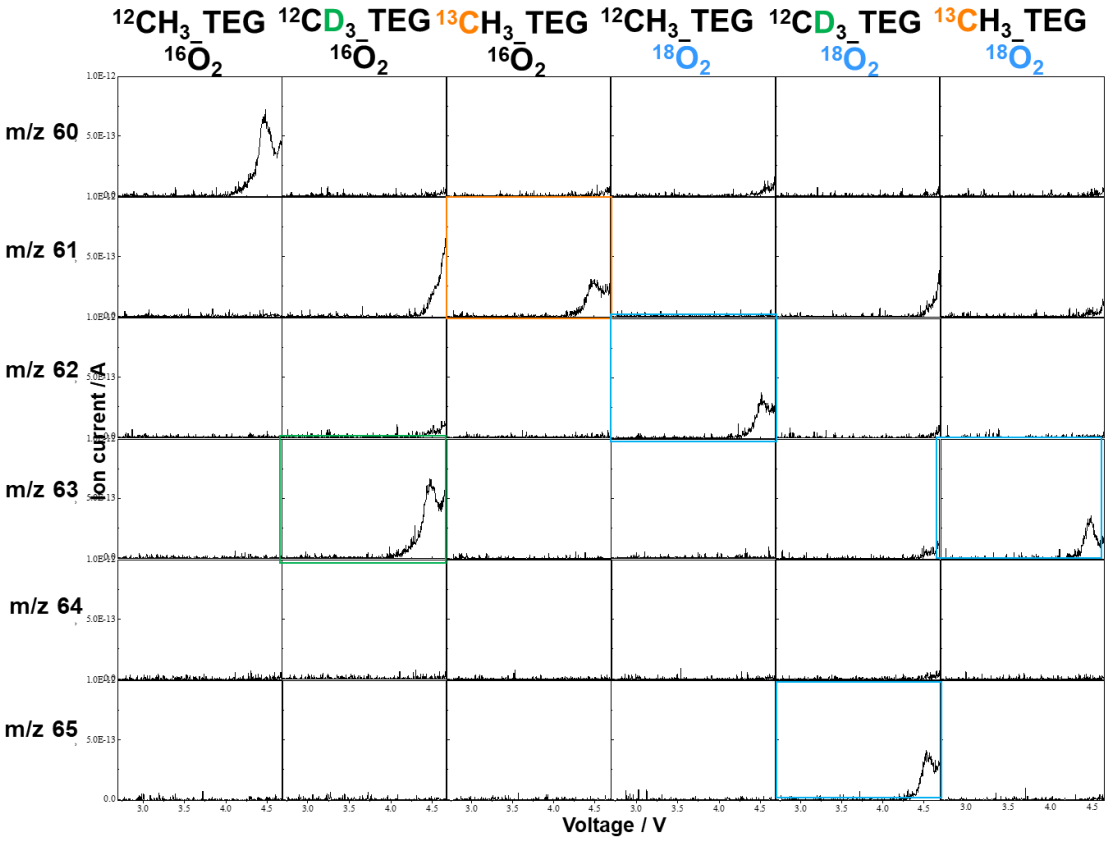

Figure 4-25. On-line QMS of m/z = 60/61/62/63/64/65 in isotope experiments as a function of voltage.

According to **Fig. 4-25**, the existence of *Acetic acid* and *Methoxyethane* can be excluded by the following analysis:

By using $^{12}CD_3$_TEG, m/z = 60 becomes m/z = 63, which means that the methyl part (CH_3O^-) of fragment should be plus 3 mass to CD_3O^-, but *Acetic acid* (CH_3COOH) is generated from the middle/methylene portion (-CH_2CH_2O-) of TGEDME, accordingly m/z = 60 is still m/z = 60 in the $^{12}CD_3$_TEG experiment, so the existence of *Acetic acid* is excluded. And this can be further confirmed by using $^{13}CH_3$_TEG, m/z = 60 *Acetic acid* (CH_3COOH) remains m/z = 60. By introducing $^{18}O_2$ as the discharge gas, m/z = 60 becomes m/z = 62, that means one of the O atoms in the fragment should be derived from the discharge gas, but *Methoxyethane* is generated by simply cleaving the terminal portion of TEGDME ($CH_3OCH_2CH_2$-), so the O atoms in *Methoxyethane* are from TEGDME not discharge gas, thus m/z = 60 remains m/z = 60 in *Methoxyethane*, which can be confirmed in both $^{13}CH_3$_TEG and $^{12}CD_3$_TEG under $^{18}O_2$ discharge experiments.

The existence of *Methoxyethane* is also excluded. However, in *Methyl formate* (CH_3OCHO), the fragment of CH_3O^- is generate from the methyl group of TEGDME, so in the $^{12}CD_3$_TEG experiment CH_3OCHO will plus 3 mass to CD_3OCHO, and in

the $^{13}CH_3$_TEG experiment $^{12}CH_3OCHO$ will plus 1 mass to $^{13}CH_3OCHO$. In addition, O atom of the fragment -CHO is derived from the discharge gas, so in the $^{18}O_2$ discharge experiments, $CH_3{}^{16}OCH^{16}O$ will plus 2 mass to become $CH_3{}^{16}OCH^{18}O$. Thus, the molecule contributing to m/z = 60 should be *Methyl formate*. As in the DB, the main contributions of *Methyl formate* to mass numbers (coefficients) are 15(18.79), 29(45.49), 31(100), 32(45.79), 60(37.99)). The mass spectrum of *Methyl formate* = (100/37.99) × MS60 isshown in **Figure 4-26**. The black line shows total *Methyl formate*, the red line shows *Methyl formate* that generated chemically due to the reactive oxygen species, and the blue line shows *Methyl formate* that generated electrochemically as the result of the high overpotential.

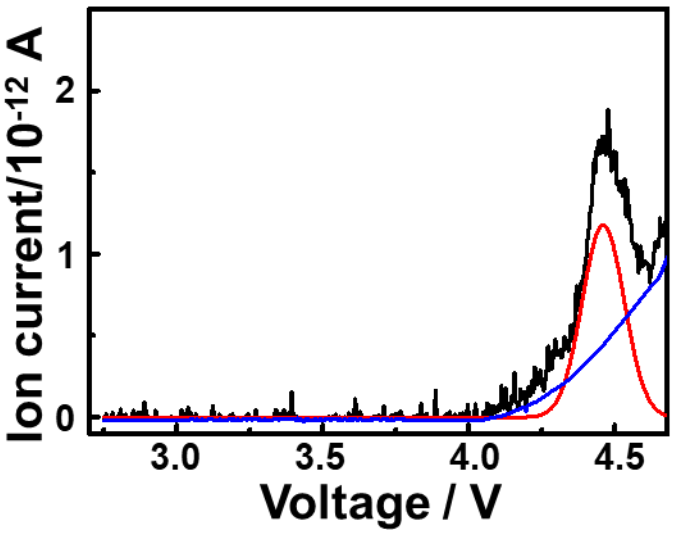

Figure 4-26. Mass signal of total (black)/chemically generated (red)/ electrochemically generated (blue) *Methyl formate* as a function of voltage).

4.2.4.2.3 Assignment of *Ethnol*/*Acetic acid*/*Dimethyl ether* and *Methoxyethane* (m/z = 45/46)

The mass signal from the discharge time dependent experiments (**Figure 4-27**) shows two peaks at 2/4/6/10 hr of discharge, and an increase at the final high overpotential that overlap with the no discharge case. This means that the final increase is related to the electrochemical reaction as a result of the high voltage. Additionally, the two peaks in the 2/4/6/10 hr discharge experiments increase with discharge time and show a positive shift, indicating that the amount of m/z = 45 is proportional to the amount of deposited Li_2O_2.

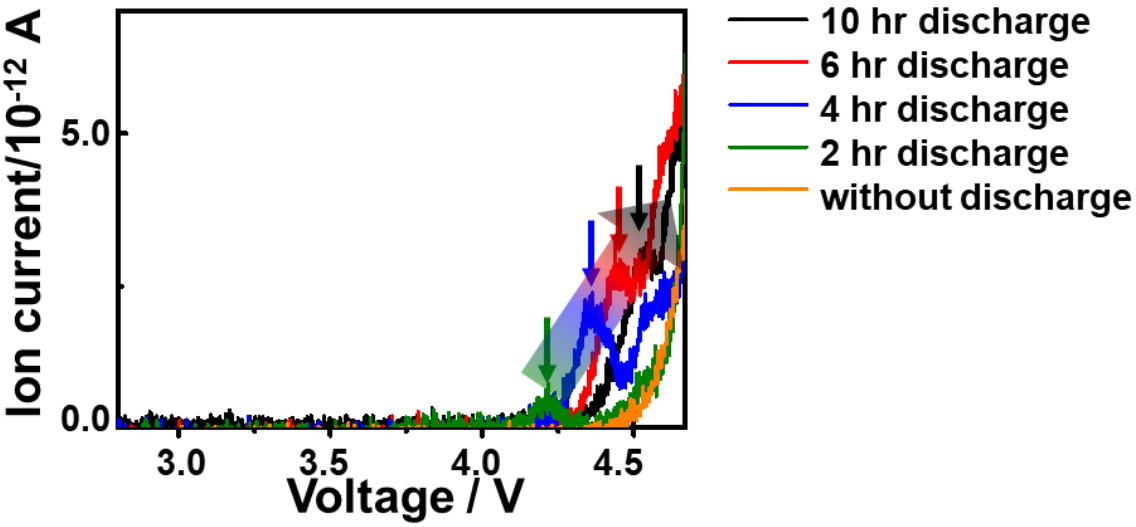

Figure 4-27. Mass signals of m/z = 45 with different discharge time, as a function of voltage.

On-line QMS results indicate that the main charing products are O_2, H_2O, and

CO_2 (**Figure 4-28**). DB shows that ionized CO_2 contribute to m/z = 45 by a coefficient of 1.2. By removing this CO_2 contribution, the on-line QMS of m/z = 45 is plotted in black color in **Fig. 4-28** (gray color is the total on-line QMS of m/z = 45).

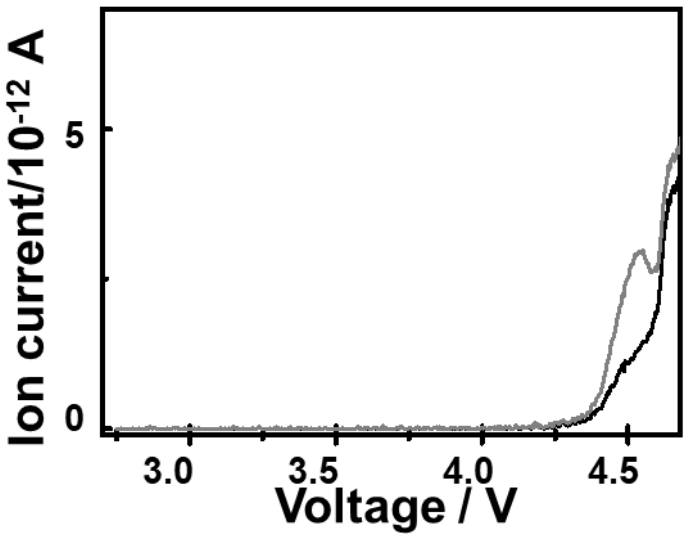

Figure 4-28. Online QMS of m/z = 45 as a function of voltage; grey color shows the total mass signal of m/z = 45, black color indicates mass signal of m/z = 45 after remove the CO_2 contribution.

✓ Define the fragements related to m/z = 45 by the isotope $^{12}CD_3\_TEG\_^{16}O_2$ experiment.

Since the elemental compositions for MS45 are C_2H_5O or CHO_2, three fragments may be present; $CH_3OCH_2^+$, $CH_3CH_2O^+$, and $COOH^+$. If all fragments were existed and contributed to m/z = 45, the fragment of $CH_3OCH_2^+$ would be $CD_3OCH_2^+$ for $CD_3\_TEG\_^{16}O_2$ and contribute to m/z = 48, and become $^{13}CH_3OCH_2^+$ for

$^{13}CH_3$_TEG_$^{16}O_2$ and contribute to m/z = 46. The fragment of $CH_3CH_2O^+$ will keep $CH_3CH_2O^+$ and contributes to m/z = 45, while $COOH^+$ becomes $COOH^+$/$COOD^+$ and contributes to m/z = 45/46. The on-line QMS for m/z = 45/46/48 (after removing the contribution of CO_2 and other big molecules with mass numbers higher than 45) are shown in **Figure 4-29**. It is clear that what was m/z = 45 in the normal experiment are now m/z = 45, 46 , and 48 for CD_3_TEG_$^{16}O_2$, and m/z = 46 for $^{13}CH_3$_TEG_$^{16}O_2$. Thus, all three fragments exist, and the amount of fragments $CH_3CH_2O^+$, $COOH^+$, and $CH_3OCH_2^+$, can be defined by m/z = 45 ($CH_3CH_2O^+$), 46 ($COOD^+$), and 48 ($CD_3OCH_2^+$) in the CD_3_TEG_$^{16}O_2$ case by the ratio of MS45/(MS48+MS45+MS46), MS46/(MS48+MS45+MS46), and MS48/(MS48+MS45+MS46).

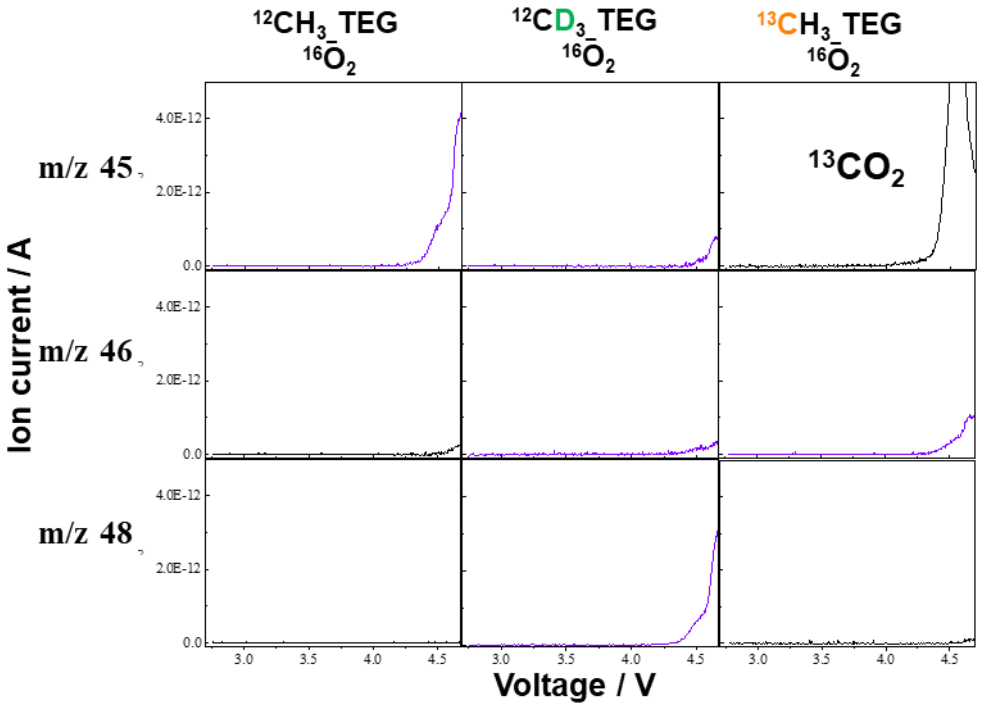

Figure 4-29. Online QMS of m/z = 45/46/48 in isotope experiments as a function of voltage.

Figure 4-30 shows the on-line QMS of m/z = 45 (blue line)/46 (black line)/48 (red line) in the CD_3_TEG experiment. It is clear that m/z = 48 ($CD_3OCH_2^+$) (red line) is much higher compared to m/z=45 ($CH_3CH_2O^+$) (blue line) and 46 ($COOD^+$) (black line). The ratios of MS45/(MS45+MS46+M48), MS46/(MS45+MS46+M48), and MS48/(MS45+MS46+M48), i.e., $CH_3CH_2O^+$/total ~ a (blue line), $COOD^+$/total ~ b (black line), and $CD_3OCH_2^+$/total ~ c (red line) are shown in **Figure 4-31** (a, b, and c represent variable values not a certain value).

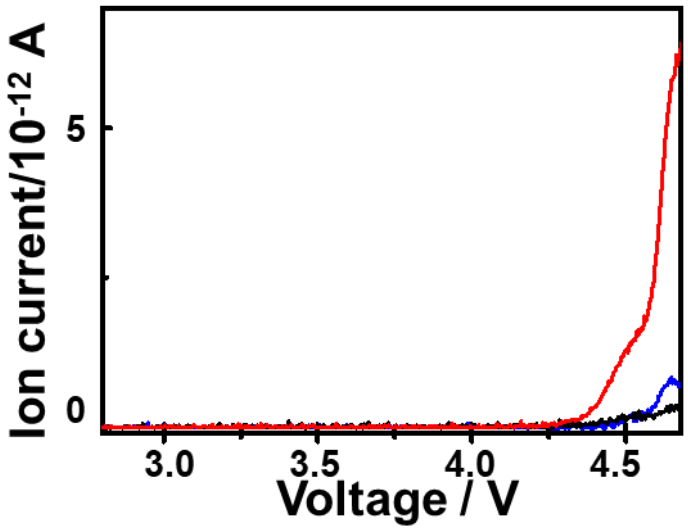

Figure 4-30. Online QMS of m/z = 45 (blue line) /46 (black line) /48 (red line) in CD_3_TEG experiment as a function of voltage.

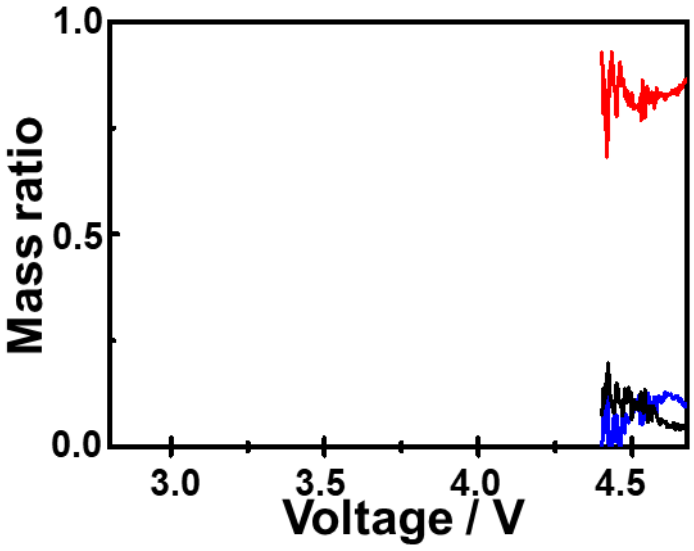

Figure 4-31. The ratio of MS45/(MS45+MS46+M48), MS46/(MS45+MS46+M48), and MS48/(MS45+MS46+M48) in CD_3_TEG case as a function of voltage.

Thus, under normal circumstances, the mass signals of the three fragments are CH_3OCH_2 = c × MS45, CH_3CH_2O = a × MS45, COOH = b × MS45. The voltage responses of total MS45 (gray line), $CH_3OCH_2^+$ (red line), $CH_3CH_2O^+$ (blue line), and $COOH^+$ (black line) are shown in **Figure 4-32**.

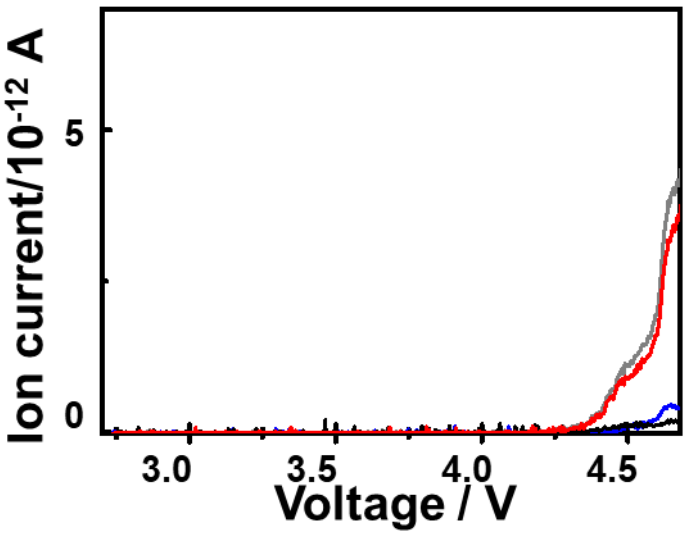

Figure 4-32. Mass signal of m/z = 45, and fragments $CH_3CH_2O^+$, $COOH^+$, and $CH_3OCH_2^+$ as a function of voltage in normal case.

✓ Define the molecules corresponding to $CH_3CH_2O^+$, $COOH^+$, and $CH_3OCH_2^+$.

We can see that the tendencies of these three fragments are different: $CH_3CH_2O^+$ shows a small peak at the 2nd peak of MS45, $COOH^+$ shows a simple and weak increase, and $CH_3OCH_2^+$ shows very similar behavior to MS45.

4.2.4.2.3.1 Assignment of *Ethanol* (fragment of $CH_3CH_2O^+$)

DB suggested that three are three possible molecules, i.e., CH_3CH_2OH (b.p.~78.2°C, v.p.~7.91 kPa), $HOCH_2CH_2OH$ (b.p.~197.6°C, v.p.~0.01 kPa), and $CH_3OCH_2CH_2OCH_3$ (b.p.~85°C, v.p.~10.19 kPa), which can contribute to the fragment $CH_3CH_2O^+$. But the main mass contributions (coefficients) of $HOCH_2CH_2OH$ are 27(5.1), 29(18.92), 31(100), 32(10.11), 33(36.23), 42(5.5), 43(14.21), 62(5.4). There is

no contribution to MS45, and $HOCH_2CH_2OH$ is easier to break at the middle C-C bond, i.e., it is not easy to generate fragment $CH_3CH_2O^+$. So $HOCH_2CH_2OH$ is excluded. $CH_3OCH_2CH_2OCH_3$ shows contributions to mass numbers 28(6.49), 29(20.17), 43(7.45), 45(100), 58(10.49), 60(18.49), 90(9.24). As there is no mass signal of m/z = 90 in the experimental result, and $CH_3OCH_2CH_2OCH_3$ is easier to break at the middle C-C bond that will form the fragment $CH_3OCH_2^+$, not $CH_3CH_2O^+$. The existence of the molecule $CH_3OCH_2CH_2OCH_3$ is also excluded. Thus, the fragment of $CH_3CH_2O^+$ is only from molecule CH_3CH_2OH, with main mass contributions to 27(22.41), 29(29.85), 31(100), 43(11.44), 45(51.5), 46(21.63). That is, ion current behavior of the molecule CH_3CH_2OH = (100/51.5) × fragment $CH_3CH_2O^+$ (**Figure 4-33**).

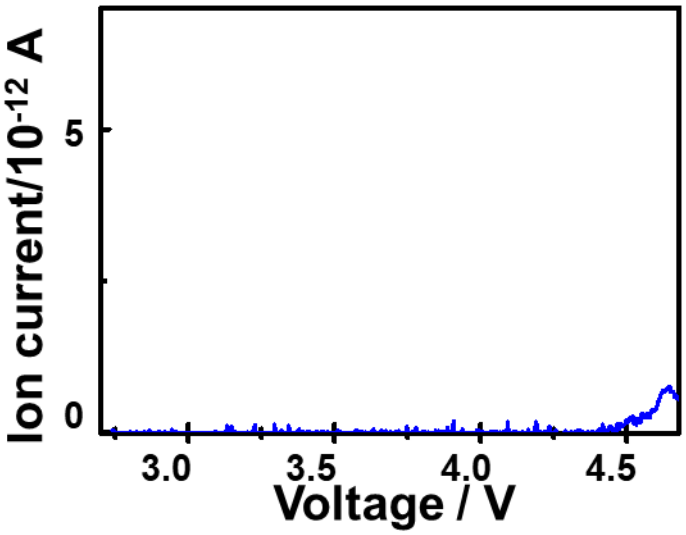

Figure 4-33. Mass signal of *Ethanol* as a function of voltage.

4.2.4.2.3.2 Assignment of *Acetic acid* (fragment of $COOH^+$)

DB suggested that there are four possible molecules (HCOOH (b.p.~100.72ºC,

v.p.~5.68 kPa), CH_3COOH (b.p.~117.77°C, v.p.~2.09 kPa), CH_3OCH_2COOH (b.p.~203.5°C, v.p.~0.02 kPa), and CH_3COOCH_3 (b.p.~56.8°C, v.p.~28.8 kPa)) that can contribute to fragment $COOH^+$. But for the molecule CH_3OCH_2COOH, the vapor pressure at 25°C is 0.02 kPa, and the boiling point is 203.5°C. Thus, it is impossible to be detected by on-line QMS. In other words, CH_3OCH_2COOH does not exist. The main mass contributions(coefficients) of CH_3COOCH_3 are 15(6.5), 29(6.8), 42(12.5), 43(100), 59(11.2), 74(25.3), there is no contribution to MS45 as CH_3COOCH_3 is easier to break at CO-O bond that forms fragment $CH3CO^+$, not $COOH^+$. Thus, CH_3COOCH_3 also does not exist.

The molecule HCOOH can also be excluded by comparing it with m/z = 46. **Figure 4-34** shows the ionic current of the fragment $COOH^+$ (black line) and the remaining m/z = 46 (dark yellow line) that after corrected by molecules (coefficients) CO_2 (0.4), $CH_3OCH_2OCH_3$ (2.2), and C_2H_5OH (21.63). The intensity of m/z = 46 is much lower than the fragment $COOH^+$. However, from DB, the main mass contributions of the molecule HCOOH are 17(17.12), 28(17.22), 29(100), 44(10.01), 45(47.64), i.e., fragment $COOH^+$, 46(60.96), and the ion current of m/z = 46 should be little higher than fragment $COOH^+$. Thus, there is no molecule HCOOH. So, fragment of $COOH^+$ should come from CH_3COOH, and the ion current behavior of CH_3COOH

= (100/47.64) × fragment $COOH^+$ (**Figure 4-35**).

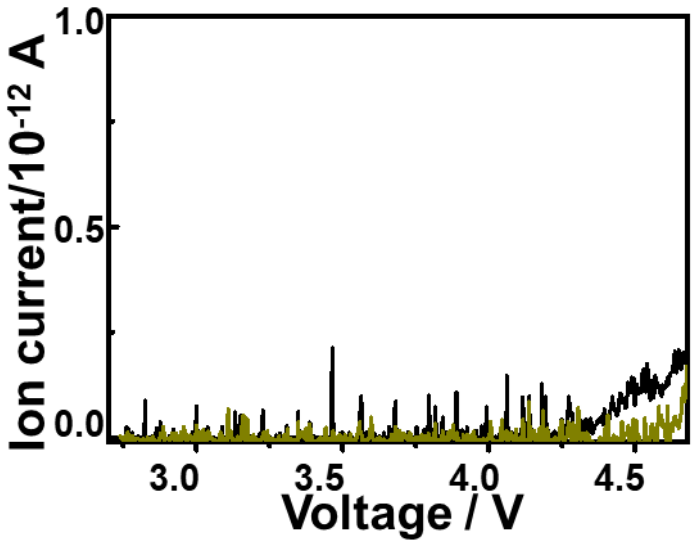

Figure 4-34. On-line QMS of real m/z = 46 (dark yellow line) and fragment $COOH^+$ (black line) as a function of voltage.

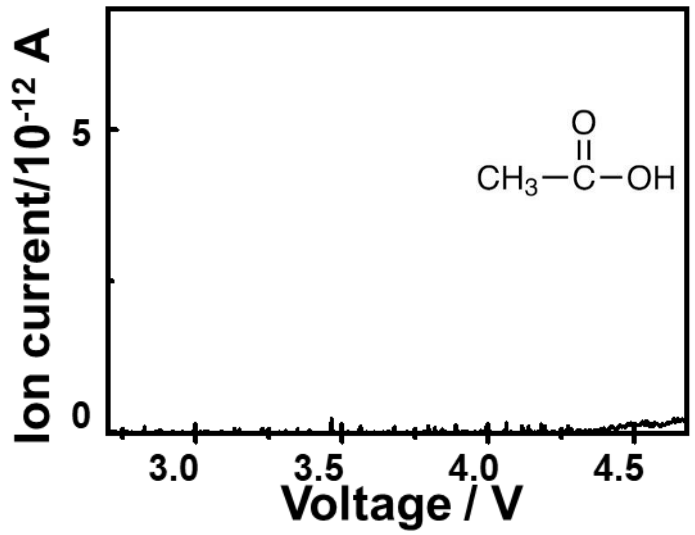

Figure 4-35. Mass signal of *Acetic acid* as a function of voltage.

4.2.4.2.3.3 Assignment of *Dimethyl ether* and *Methoxyethane* (fragment of $CH_3OCH_2^+$)

DB suggested that two possible molecules, i.e., CH_3OCH_3 (b.p.~ -24.8°C, v.p.~593.28 kPa), and CH_3OC2H_5 (b.p.~7.4°C, v.p.~199.05 kPa), can contribute to fragment $CH_3OCH_2^+$. The main mass contributions (coefficients) of CH_3OCH_3 are 15(24.12), 29(38.73), 45(100), 46(60.76). CH_3OC2H_5 has mass contributions of 14(6.81), 15(25.02), 26(8.01), 27(20.42), 28(7.91), 29(49.04), 31(19.92), 43(6.91), 45(100), 59(10.81), 60(25.82). The significant difference between these two molecules is mass number of 46, so the mass signal of molecule CH_3OCH_3 can be determined by m/z = 46 that CH_3OCH_3 = 1.65 × the remaining MS46, then mass signal of molecule $CH_3OC_2H_5$ = fragment $CH_3OCH_2^+$ – molecule CH_3OCH_3. The result was shown in **Figure 4-36** that the mass signal of fragment $CH_3OCH_2^+$ was plotted in red color, molecule CH_3OCH_3 (*Dimethyl ether*) was plotted in orange color, and molecule $CH_3OC_2H_5$ (*Methoxyethane*) was plotted in green color.

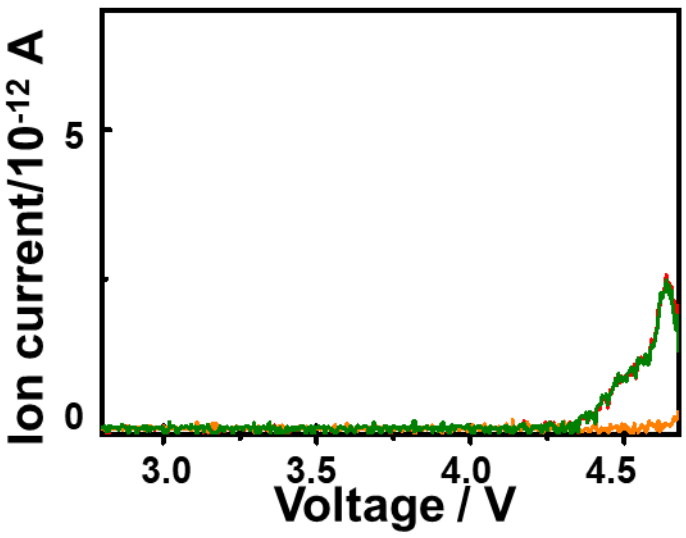

Figure 4-36. Mass signal of fragment $CH_3OCH_2^+$ (red line), *Dimethyl ether* (orange line), and *Methoxyethane* (green line) as a function of voltage.

4.2.4.2.4 Assignment of *Methanol* (m/z = 31)

The discharge time dependent mass signals of m/z = 31 (**Figure 4-37**) show that for 2/4/6/10 hr discharge, two obvious peaks appear, which increase and positive shift with discharge time, indicating that the corresponding fragment(s) of m/z = 31 generated in this part is related to the amount of Li_2O_2 decomposition. Moreover, an increasing trend in the case of 2/4/6/10 hr discharge, which overlaps with the case of no discharge at voltage higher than 4.5 V, indicating that the corresponding fragment(s) of m/z = 31 generated at this part is only related to decomposition due to high overpotential.

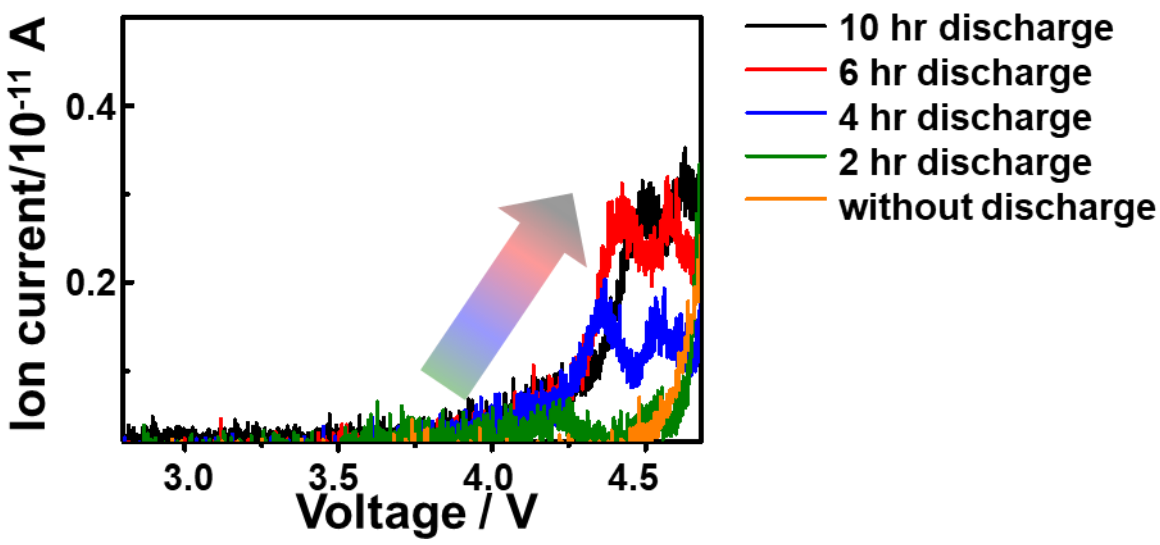

Figure 4-37. Mass signals of m/z = 31 with different discharge time, as a function of voltage.

Empirically, m/z = 31 should be composed of one 'C' atom, one 'O' atom, and three 'H' atoms. The corresponding fragment(s) should be CH_2OH^+ or/and CH_3O^+. Fragment CH_2OH^+ should originated from the molecule CH_3OH and fragment CH_3O^+ should be ionized from molecules generated by the decomposition of the electrolyte (TEGDME). If the fragment CH_2OH^- exists, the mass number of the molecule CH_3OH in normal TEG $^{16}O_2/^{18}O_2$ discharge experiments is 32. In the case of $^{16}O_2$ flow discharge m/z = 32 is mainly related to the O_2 molecule but in the case of $^{18}O_2$ flow discharge m/z = 32 is related only to CH_3OH. **Figure 4-38** shows that even in the cases of $^{18}O_2$ flow discharge, a very strong signal of m/z = 32 still remains. Thus, it is true that fragment of CH_2OH^+ exists. Furthermore, m/z = 31 (CH_2OH^-), and m/z = 32

(CH_3OH) for normal TEG under $^{16}O_2/^{18}O_2$ flow, will become m/z = 33 (CD_2OH^-), and m/z = 35 (CD_3OH) in CD_3_TEG under $^{16}O_2/^{18}O_2$ flow. Also, m/z = 32 ($^{13}CH_2OH^-$), and m/z = 33 ($^{13}CH_3OH$) for $^{13}CH_3$_TEG under $^{16}O_2/^{18}O_2$ flow. All of this is confirmed in **Fig. 4-38**, which further confirms the existence of the fragment CH_2OH^- ionized from the molecule CH_3OH in the decomposition products. However, the m/z = 34 for the CD_3_TEG $^{16}O_2/^{18}O_2$ discharge cases still can't be explained. If suppose the fragment CH_3O^- exists, the m/z = 31 (CH_3O^-) for normal TEG under $^{16}O_2/^{18}O_2$ flow will become to m/z = 34 (CD_3O^-) for CD_3_TEG under $^{16}O_2/^{18}O_2$ flow. That is m/z = 31 is related to both CH_2OH^+ and CH_3O^+ fragments.

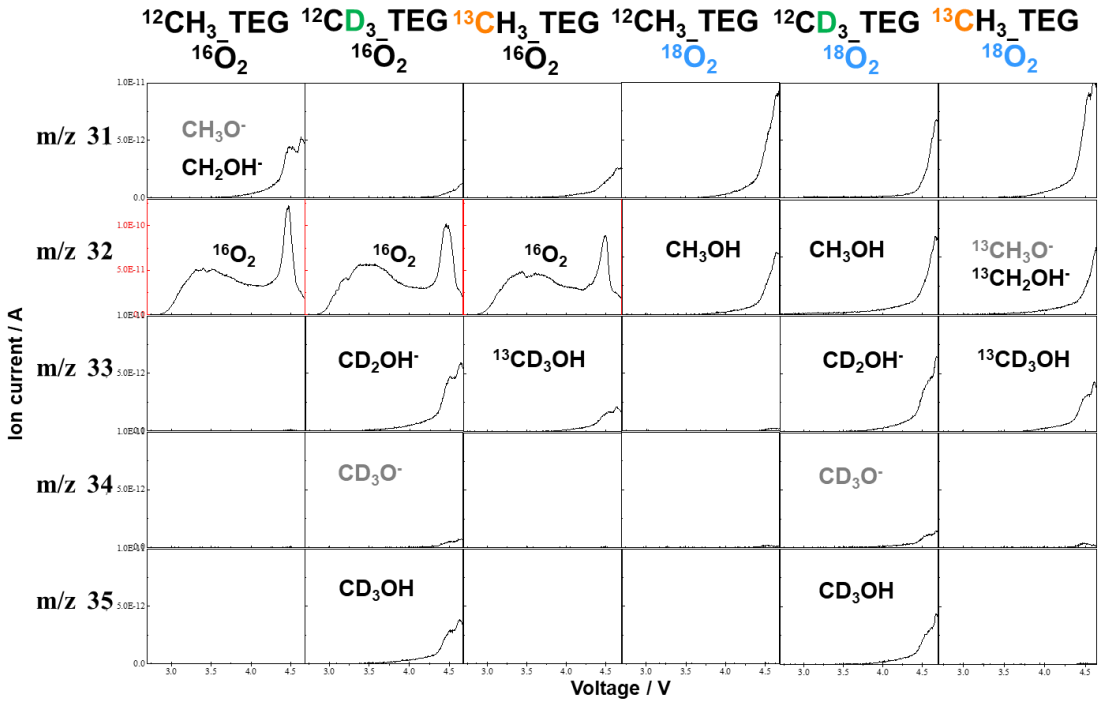

Figure 4-38. On-line QMS of m/z = 31/32/33/34/35 in isotope experiments as a function of voltage.

To determine the contribution of the fragments of CH_2OH^+ and CH_3O^+ to m/z = 31, the ratios of MS33/(MS33+MS34) (referred to 'a') and MS34/(MS33+MS34) (referred to 'b') were calculated for CD_3_TEG, as shown in **Figure 4-39**. Accordingly for normal TEG, the contributions of CH_2OH^+ and CH_3O^+ to m/z = 31 (black line in **Figure 4-40**) should be CH_3O^+ = MS31 × a (red line in figure 38); CH_2OH^+ = MS31 × b (blue line in **Fig. 4-40**). The main mass contributions of CH_3OH are 15(12.39), 29(44.59), 31(100), 32(74.4). That is the mass spectrum of molecule CH_3OH = fragment of CH_2OH^+ which was plotted in blue color in **Fig. 4-40**. Fragments of

CH_3O^+ were attributed to molecules such as *1,4-Dioxane*, *Methylal*, and *3-Dioxolane*, et al. which were confirmed ionized from TEGDME.

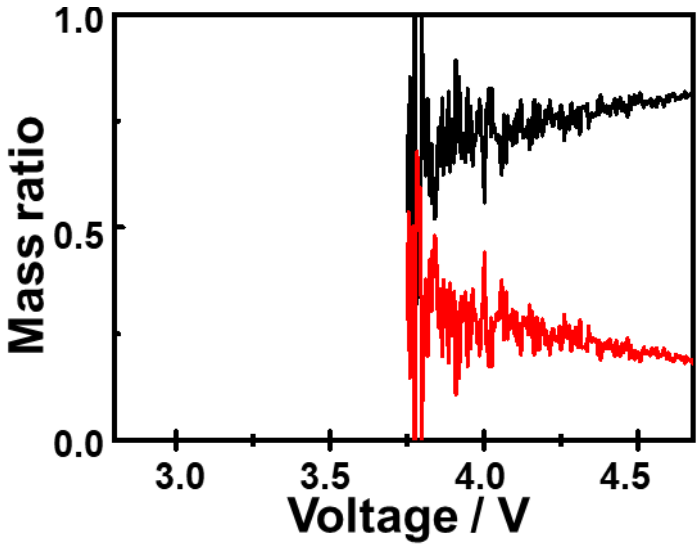

Figure 4-39. The ratio of MS33/(MS33+MS34) (black line), MS34/(MS33+MS34) (red line) in CD_3_TEG case as a function of voltage.

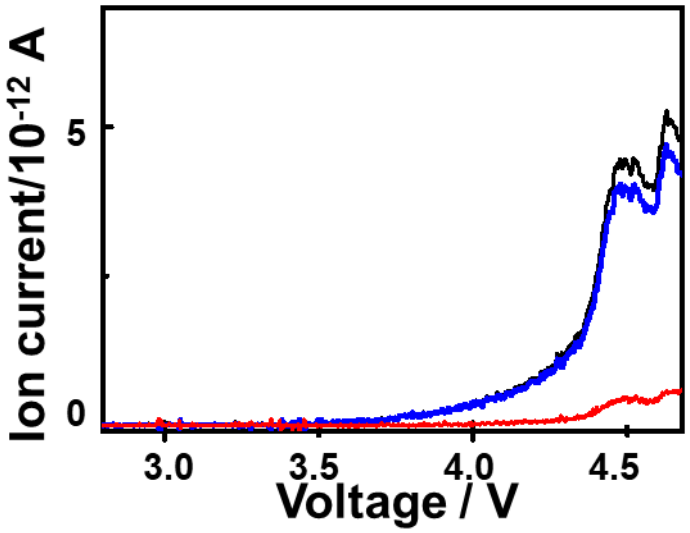

Figure 4-40. Mass signal of fragment m/z = 31/*Methanol*(black line), CH_3O^+ (red line), CH_2OH^+ (blue line) as a function of voltage.

4.2.4.2.5 Assignment of *Ethane* (C_2H_6), *Formaldehyde* (HCHO), and *Carbon monoxide* (CO) (m/z = 30/29/28)

Figure 4-41 shows the discharge time dependence of m/z = 30 (a) /29 (b) /28 (c) as a function of voltage, and clearly these three show that peaks at 2/4/6/10 hr discharge increase and positive shift with discharge time, and the corresponding fragment(s) generated in this part is related to the amount of Li_2O_2 decomposition. Additionally, the increasing trend of 2/4/6/10 hr discharge overlap with the no discharge experiment at high overpotential, suggesting that the corresponding fragment(s) generated in this part is only related to the decomposition caused by high overpotential.

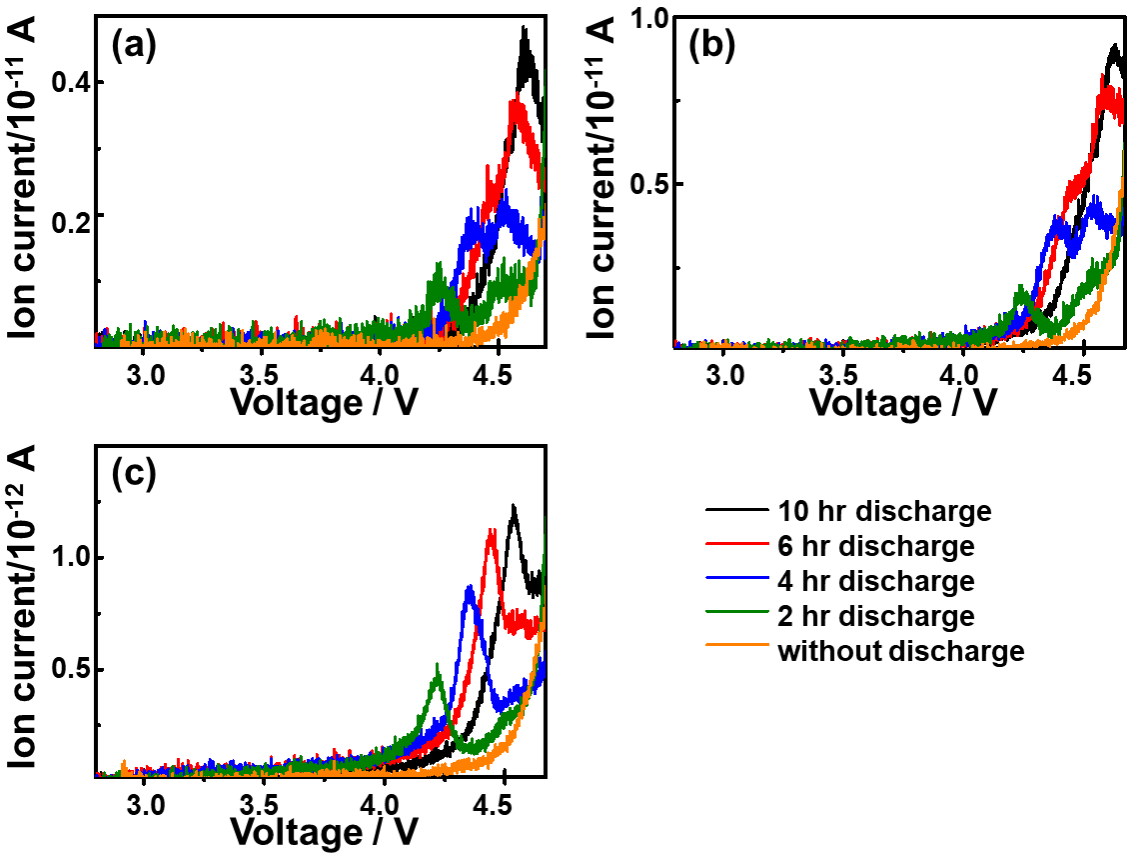

Figure 4-41. Mass signals of m/z = 30 (a) /29 (b) /28 (c) with different discharge time, as a function of voltage.

MS30 can be from fragment components of CH_2O and C_2H_6, MS29 is from fragment components of CHO and C_2H_5, MS28 is from fragment components of CO and C_2H_4. In other words, these fragments are related to molecules C_2H_6 and HCHO. **Table 4-1** shows the ionization table (from DB) for the molecules $C_2H_6^+$, $HCHO^+$, and CO^+.

Table 4-2. Ionization table of molecules $C_2H_6^+$ and $HCHO^+$.

molecule	MW	b.p./°C	vapor pressure(25° C)/kPa	m/z =										
				12	13	14	15	16	25	26	27	28	29	30
C_2H_6	30	-88.6	4194.18	0.40	1.00	3.00	4.40		3.50	23.22	33.23	100.00	21.52	26.22
HCHO	30	-21.11	518.62	1.00	1.00	1.00	2.00					24.00	100.00	58.01
CO	28	-191.5	20664970	4.7				1.7				100	1.2001	

Figure 4-42(a) shows the ion current of m/z = 28/29/30 and 32(b) shows the mass ratio of 30/29, 28/29, and 30/28, 29/28. It is clear that the fact m/z = 28 and m/z = 29 show almost the same ion current intensities and the mass ratios are not constant or similar to the ratio in **Table 4-1**, indicates that both molecules C_2H_6 and HCHO all exist. From **table 4-1** the main mass contribution of molecule C_2H_6 is 28(100), and the ion current behavior of molecule C_2H_6 can be defined by m/z = 26, i.e., molecule C_2H_6/MS28 = (100/23.22) × M26, thereby molecule HCHO, whose mass contribution is 29(100), is deduced by the remaining MS30 (R_MS30 = MS30 – (26.22/100) × molecule C_2H_6), i.e. molecule HCHO/R_MS29 = (100/58.01) × R_MS30 can be deduced. However, after removing the contribution of the molecules C_2H_6 and HCHO to MS28 i.e., R_MS28 = MS28 - (100/23.22) × MS26 – 0.24 × R_MS29, the excess MS28 (E_MS28) ion current is still very strong as shown in **Figure 4-43**, suggesting that there should be another possible molecule/fragment that contribute to m/z = 28. Since there are no mass numbers higher than 28 and no strong mass signal like 28, the corresponding molecule should only contribute to mass numbers up to 28 and mainly

28. By checking against DB, CO molecule is the most suitable candidate to explain the E_MS28(100) well, as shown in **Table 1**.

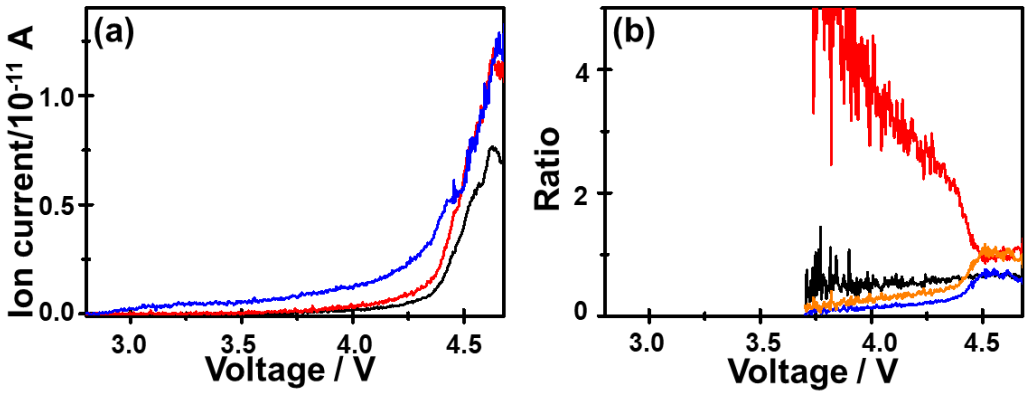

Figure 4-42. (a) Ion current of m/z = 30/29/28 as a function of voltage; **(b)** Ratio of MS30/MS29 (black line), MS28/MS29 (red line), MS30/28 (blue line), and MS29/28 (orange line) as a function of voltage.

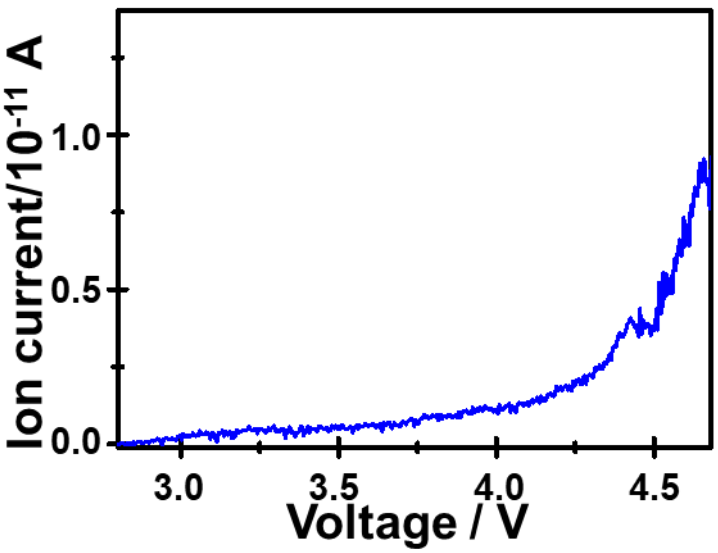

Figure 4-43. Ion current of excess m/z = 28 as a function of voltage.

Therefore, the mass signals of molecules *Formaldehyde*, *Ethane*, and *Carbon monoxide* should be C_2H_6 = MS28 = (100/23.22) × MS26, HCHO = R_MS29 =

(100/58.01) × R_MS30, CO = E_MS28 = M28^{-} (100/23.22) × M26 - (100/58.01) × R_MS30; R_MS30 = MS30 – (26.22/100) × molecule C_2H_6. The ion current as a function of voltage for the molecules *Ethane* (C_2H_6), *Formaldehyde* (HCHO), and *Carbon monoxide* (CO) are shown in **Figure 4-44**.

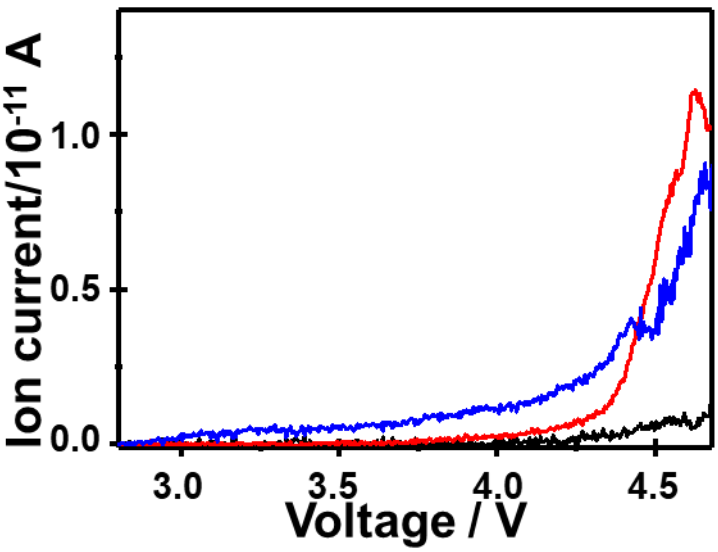

Figure 4-44. Ion current of molecules *Ethane* (C_2H_6) (black line), *Formaldehyde* (HCHO) (red line), and *Carbon monoxide* (CO) (blue line) as a function of voltage.

4.2.4.2.6 Assignment of *Methane* (CH_4) (m/z = 15/14/13/12)

Figure 4-45 shows the discharge time dependent mass signal of m/z = 15 as a function of voltage. Similarly, the peaks for 2/4/6/10 hr discharge increase and positive shift with discharge time, and the final increase overlap with no discharge case,

suggesting that the generation of corresponding fragment(s) is related to the amount of Li_2O_2 decomposition and high overpotential.

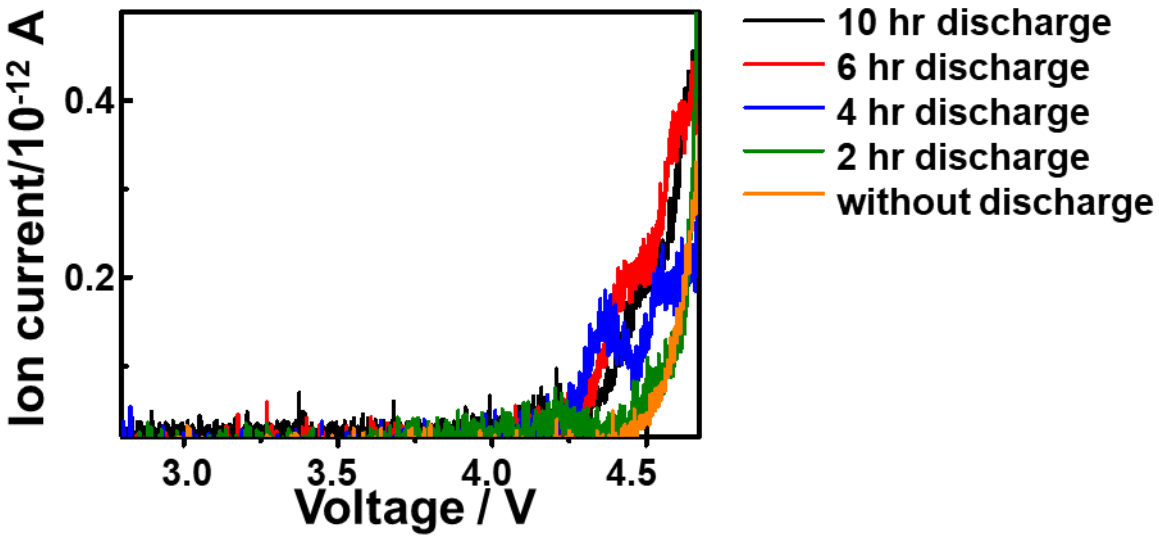

Figure 4-45. Mass signals of m/z = 15 with different discharge time, as a function of voltage.

By now, the remaining mass numbers are m/z = 16/15/14/13. **Figure 4-46(a)** shows ion currents of m/z = 15/14/13, which exhibit similar behavior except for intensity, **(b)** shows that ratios of MS14/MS15 and MS13/MS15 are relatively constant and consistent. The DB suggested that the possible molecule was CH_4. **Table 4-3** shows the main contribution of CH_4 to the mass numbers, the mass ratios of MS14/MS15, and MS13/MS15 are very close to the ratios in **Fig. 4-46 (b)**. This indicates that CH_4 exists in the decomposition products. Ion current for the molecule

CH_4 = (88.8/100) × MS15 is shown in **Figure 4-47**.

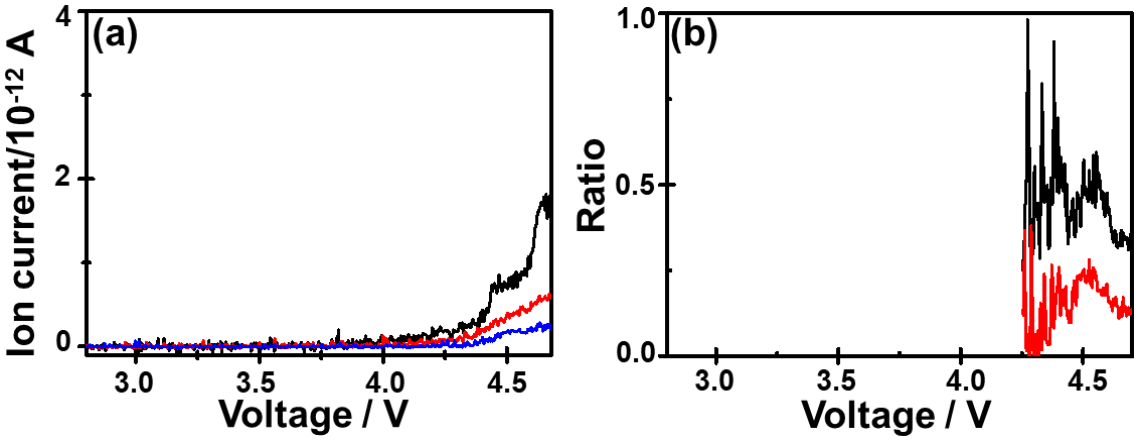

Figure 4-46 (a). Ion current of m/z = 15 (black line)/14 (red line)/13 (blue line) as a function of voltage. **(b)** Ratios of MS14/MS15 (black line), and MS13/MS15 (red line) as a function of voltage.

Table 4-3. Ionization table of molecules CH_4.

molecule	MW	b.p./°C	vapor pressure(25° C)/kPa	m/z =					
				12	13	14	15	16	17
CH_4	16	-161.5	62128.23	3.8	10.69	20.42	88.8	100	1.64

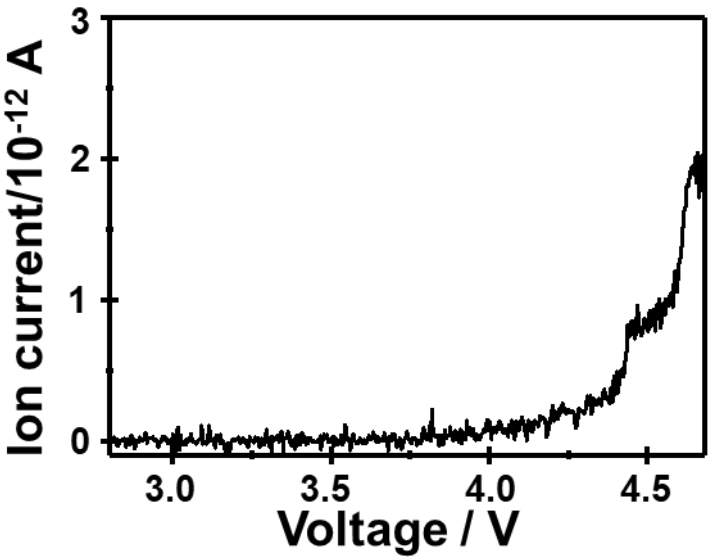

Figure 4-47. Ion current of molecules *Methane* (CH_4) as a function of voltage.

The mass signals of assignment process is attached in **Appendix III**. The calculation coefficients of mass number to molecule can be found in **Appendix I**.

4.2.5 Degradation mechanism of TEGDME

The process of molecular assignment of mass numbers is shown in **Table 4-4**. Combining the no-discharge and isotope exchange experiments, 17 molecules were identified. (See **Table 4-5**.)

Table 4-5. The assigned molecules and the corresponding main mass numbers.

Main mass number m/z =	molecule		Main mass number m/z =	molecule	
	name	structure		name	structure
32	Oxygen		45	Ethanol	
44	Carbon dioxide			Acetic acid	
18	Water			Dimethyl ether	
88	1,4-Dioxan			Methoxyethane	
75	Methylal		31	Methanol	
58	Methoxyethene	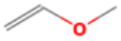	30	Formaldehyde	
73	1,3-dioxolane		28	Carbon monoxide	
60	Methyl formate		26	Ethane	
			15	Methane	

The above analysis shows that cell degradation starts after the first current/O_2 peak, indicating that reactive oxygen species trigger the degradation of TEGDME. Subsequently, when the voltage exceeds 4.45 V, i.e., the second current/O_2 peak, the overpotential gradually affects the degradation of TEGDME to a greater extent. **Scheme 4-1** illustrates the degradation process of TEGDME, where reactive oxygen species, either singlet oxygen or superoxide, attack the long-chain TEGDME and the molecule will be generated by cleavage, H or O extraction and recombination.

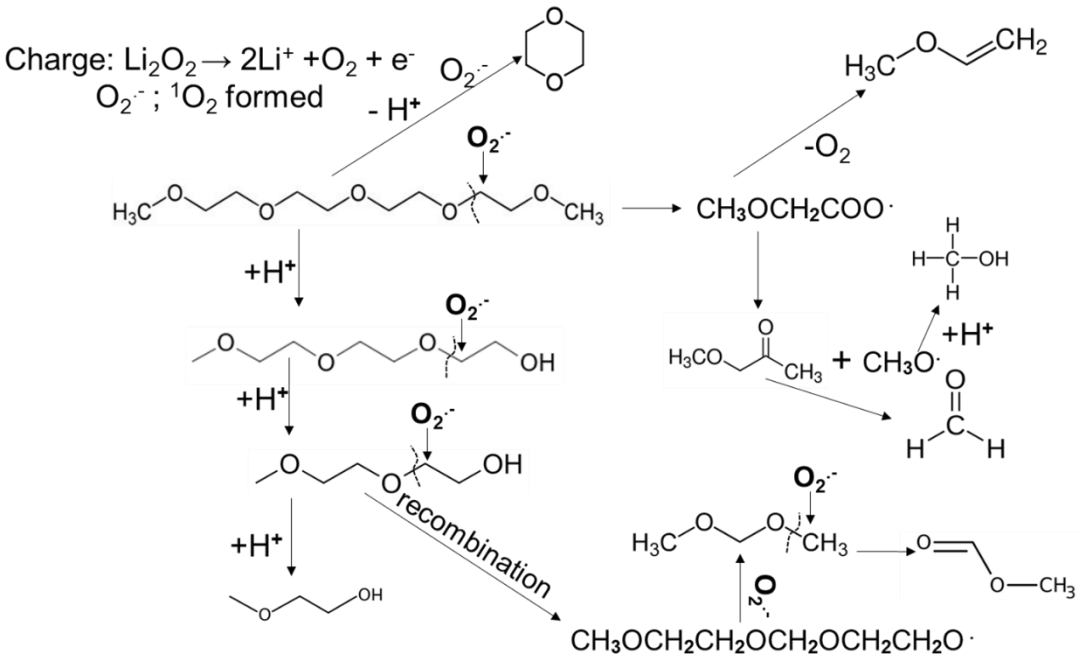

Scheme 4-1. Degradation mechanism occurs during charge with TEGDME-based electrolyte[4].

4.3 Conclusion

In conclusion, the degradation products of LOB based on 1M LiTFSI_TEGDME electrolyte can be detected by high sensitivity real-time QMS and well attributed by introducing isotope analysis, $^{12}CD_3$_TEGDME and $^{13}CH_3$_TEGDME as exchange of solvent TEGDME, and $^{18}O_2$ as exchange of discharge gas $^{16}O_2$. A total of 17 compounds were identified as the battery reaction products by mass spectrometry. From the detected products, battery degradation products can be divided into two types: generates from high overpotential induced degradation reactions (electrochemical reactions), such as *1,4-Dioxane*, *Methylal*, and *Methoxyethene*, and active species

triggered decomposition reactions (chemical reactions), such as *Methanol*, *Ethanol*, etc. Notably, some of degradation products are generated by both of the two reactions, such as *Methyl format*. A further study of the battery degradation mechanism has also been initiated by combining a cold trap and a mass spectrometry system.

References

1. Mudakkar, S. R.; Zaman, K.; Khan, M. M.; Ahmad, M., Energy for economic growth, industrialization, environment and natural resources: living with just enough. Renewable and Sustainable Energy Reviews 2013, 25, 580-595.

2. Lam, N.; Wallach, E.; Hsu, C.-W.; Jacobson, A.; Alstone, P.; Purohit, P.; Klimont, Z., The dirty footprint of the broken grid: the impacts of fossil fuel back-up generators in developing countries. 2019.

3. Azni, M. A.; Md Khalid, R.; Hasran, U. A.; Kamarudin, S. K., Review of the Effects of Fossil Fuels and the Need for a Hydrogen Fuel Cell Policy in Malaysia. Sustainability 2023, 15 (5), 4033.

4. Markandya, A.; Wilkinson, P., Electricity generation and health. The lancet 2007, 370 (9591), 979-990.

5. Ayres, R. U.; Ayres, E. H., Crossing the energy divide: moving from fossil fuel dependence to a clean-energy future. Pearson Prentice Hall: 2009.

6. Liu, L.; Cheng, S.; Li, J.; Huang, Y., Mitigating environmental pollution and impacts from fossil fuels: The role of alternative fuels. Energy Sources, Part A 2007, 29 (12), 1069-1080.

7. Hubbert, M. K., Energy from fossil fuels. Science 1949, 109 (2823), 103-109.

8. Dorian, J. P.; Franssen, H. T.; Simbeck, D. R., Global challenges in energy. Energy policy 2006, 34 (15), 1984-1991.

9. Pirani, S., Burning up: A global history of fossil fuel consumption. Pluto Press: 2018.

10. Jaccard, M., Sustainable fossil fuels: the unusual suspect in the quest for clean and enduring energy. Cambridge University Press: 2006.

11. Fathabadi, H., Plug-in hybrid electric vehicles: Replacing internal combustion engine with clean and renewable energy based auxiliary power sources. IEEE Transactions on Power Electronics 2018, 33 (11), 9611-9618.

12. Behera, B.; Ali, A., Factors determining household use of clean and renewable energy sources for lighting in Sub-Saharan Africa. Renewable and Sustainable Energy Reviews 2017, 72, 661-672.

13. Fathabadi, H., Utilizing solar and wind energy in plug-in hybrid electric vehicles. Energy conversion and management 2018, 156, 317-328.

14. Fathabadi, H., Novel battery/photovoltaic hybrid power source for plug-in hybrid electric vehicles. Solar Energy 2018, 159, 243-250.

15. Sabri, M. F. M.; Danapalasingam, K. A.; Rahmat, M. F., A review on hybrid electric vehicles architecture and energy management strategies. Renewable and Sustainable Energy Reviews 2016, 53, 1433-1442.

16. Chellaswamy, C.; Ramesh, R., Future renewable energy option for recharging full electric vehicles. Renewable and Sustainable Energy Reviews 2017, 76, 824-838.

17. Andersen, P. H.; Mathews, J. A.; Rask, M., Integrating private transport into renewable energy policy: The strategy of creating intelligent recharging grids for electric vehicles. Energy policy 2009, 37 (7), 2481-2486.

18. Longo, M.; Foiadelli, F.; Yaïci, W., Electric vehicles integrated with renewable energy sources for sustainable mobility. New trends in electrical vehicle powertrains

2018, 10, 203-223.

19. Poullikkas, A., Sustainable options for electric vehicle technologies. Renewable and Sustainable Energy Reviews 2015, 41, 1277-1287.

20. Farrington, R. B.; Anderson, R.; Blake, D. M.; Burch, S. D.; Cuddy, M. R.; Keyser, M. A.; Rugh, J. P., Challenges and potential solutions for reducing climate control loads in conventional and hybrid electric vehicles. National Renewable Energy Laboratory, Golden, CO, USA, Download from: www. ott. doe. gov/coolcar/pubs. html 1999.

21. Nishi, Y., Lithium ion secondary batteries; past 10 years and the future. Journal of Power Sources 2001, 100 (1-2), 101-106.

22. Reddy, M. V.; Mauger, A.; Julien, C. M.; Paolella, A.; Zaghib, K., Brief history of early lithium-battery developmen t. Materials 2020, 13 (8), 1884.

23. Zhang, D.; Haran, B.; Durairajan, A.; White, R. E.; Podrazhansky, Y.; Popov, B. N., Studies on capacity fade of lithium-ion batteries. Journal of Power Sources 2000, 91 (2), 122-129.

24. Jow, T. R.; Xu, K.; Borodin, O.; Ue, M., Electrolytes for lithium and lithium-ion batteries. Springer: 2014; Vol. 58.

25. Crabtree, G.; Kócs, E.; Trahey, L., The energy-storage frontier: Lithium-ion batteries and beyond. Mrs Bulletin 2015, 40 (12), 1067-1078.

26. Nishi, Y. In Lithium ion secondary battery technologies, present and future, Macromolecular Symposia, Wiley Online Library: 2000; pp 187-194.

27. Nishi, Y., The dawn of lithium-ion batteries. The Electrochemical Society Interface

2016, 25 (3), 71.

28. Nishi, Y., The development of lithium ion secondary batteries. The Chemical Record 2001, 1 (5), 406-413.

29. Blomgren, G. E., The development and future of lithium ion batteries. Journal of The Electrochemical Society 2016, 164 (1), A5019.

30. Sick, N.; Krätzig, O.; Eshetu, G. G.; Figgemeier, E., A review of the publication and patent landscape of anode materials for lithium ion batteries. Journal of Energy Storage 2021, 43, 103231.

31. Aurbach, D.; McCloskey, B. D.; Nazar, L. F.; Bruce, P. G., Advances in understanding mechanisms underpinning lithium–air batteries. Nature Energy 2016, 1 (9), 1-11.

32. Rahman, M. A.; Wang, X.; Wen, C., A review of high energy density lithium–air battery technology. Journal of Applied Electrochemistry 2014, 44, 5-22.

33. Imanishi, N.; Yamamoto, O., Rechargeable lithium–air batteries: characteristics and prospects. Materials today 2014, 17 (1), 24-30.

34. Liu, T.; Vivek, J. P.; Zhao, E. W.; Lei, J.; Garcia-Araez, N.; Grey, C. P., Current challenges and routes forward for nonaqueous lithium–air batteries. Chemical reviews 2020, 120 (14), 6558-6625.

35. Wang, J.; Li, Y.; Sun, X., Challenges and opportunities of nanostructured materials for aprotic rechargeable lithium–air batteries. Nano Energy 2013, 2 (4), 443-467.

36. Tan, P.; Jiang, H.; Zhu, X.; An, L.; Jung, C.; Wu, M.; Shi, L.; Shyy, W.; Zhao, T., Advances and challenges in lithium-air batteries. Applied energy 2017, 204, 780-

806.

37. Akhtar, N.; Akhtar, W., Prospects, challenges, and latest developments in lithium–air batteries. International Journal of Energy Research 2015, 39 (3), 303-316.

38. Song, M.-K.; Park, S.; Alamgir, F. M.; Cho, J.; Liu, M., Nanostructured electrodes for lithium-ion and lithium-air batteries: the latest developments, challenges, and perspectives. Materials Science and Engineering: R: Reports 2011, 72 (11), 203-252.

39. Balaish, M.; Kraytsberg, A.; Ein-Eli, Y., A critical review on lithium–air battery electrolytes. Physical Chemistry Chemical Physics 2014, 16 (7), 2801-2822.

40. Matsuda, S.; Ono, M.; Yamaguchi, S.; Uosaki, K., Criteria for evaluating lithium–air batteries in academia to correctly predict their practical performance in industry. Materials Horizons 2022, 9 (3), 856-863.

41. Shao, Y.; Park, S.; Xiao, J.; Zhang, J.-G.; Wang, Y.; Liu, J., Electrocatalysts for nonaqueous lithium–air batteries: status, challenges, and perspective. Acs Catalysis 2012, 2 (5), 844-857.

42. Bai, T.; Li, D.; Xiao, S.; Ji, F.; Zhang, S.; Wang, C.; Lu, J.; Gao, Q.; Ci, L., Recent Progress on Single Atom Catalysts for Lithium-air Battery Applications. Energy & Environmental Science 2023.

43. Kang, J.-H.; Lee, J.; Jung, J.-W.; Park, J.; Jang, T.; Kim, H.-S.; Nam, J.-S.; Lim, H.; Yoon, K. R.; Ryu, W.-H., Lithium–air batteries: air-breathing challenges and perspective. ACS nano 2020, 14 (11), 14549-14578.

44. Jung, K.-N.; Kim, J.; Yamauchi, Y.; Park, M.-S.; Lee, J.-W.; Kim, J. H., Rechargeable lithium–air batteries: a perspective on the development of oxygen

electrodes. Journal of materials chemistry A 2016, 4 (37), 14050-14068.

45. Grande, L.; Paillard, E.; Hassoun, J.; Park, J. B.; Lee, Y. J.; Sun, Y. K.; Passerini, S.; Scrosati, B., The lithium/air battery: still an emerging system or a practical reality? Advanced materials 2015, 27 (5), 784-800.

46. Nishioka, K.; Morimoto, K.; Kusumoto, T.; Harada, T.; Kamiya, K.; Mukouyama, Y.; Nakanishi, S., Isotopic Depth Profiling of Discharge Products Identifies Reactive Interfaces in an Aprotic Li–O2 Battery with a Redox Mediator. Journal of the American Chemical Society 2021, 143 (19), 7394-7401.

47. Wang, Y.; Lu, Y. C., Isotopic labeling reveals active reaction interfaces for electrochemical oxidation of lithium peroxide. Angewandte Chemie 2019, 131 (21), 7036-7040.

48. Wang, J.; Zhang, Y.; Guo, L.; Wang, E.; Peng, Z., Identifying reactive sites and transport limitations of oxygen reactions in aprotic lithium-O2 batteries at the stage of sudden death. Angewandte Chemie International Edition 2016, 55 (17), 5201-5205.

49. Tan, C.; Cao, D.; Zheng, L.; Shen, Y.; Chen, L.; Chen, Y., True Reaction Sites on Discharge in Li–O2 Batteries. Journal of the American Chemical Society 2022, 144 (2), 807-815.

50. Ganapathy, S.; Adams, B. D.; Stenou, G.; Anastasaki, M. S.; Goubitz, K.; Miao, X.-F.; Nazar, L. F.; Wagemaker, M., Nature of Li2O2 oxidation in a Li–O2 battery revealed by operando X-ray diffraction. Journal of the American Chemical Society 2014, 136 (46), 16335-16344.

51. Liu, J.; Chen, W.; Xing, A.; Wei, X.; Xue, D., Lithium cell-assisted low-

overpotential Li–O 2 batteries by in situ discharge activation. Chemical Communications 2017, 53 (76), 10568-10571.

52. Luo, Y.; Jin, C.; Wang, Z.; Wei, M.; Yang, C.; Yang, R.; Chen, Y.; Liu, M., A high-performance oxygen electrode for Li–O 2 batteries: Mo 2 C nanoparticles grown on carbon fibers. Journal of Materials Chemistry A 2017, 5 (12), 5690-5695.

53. Lobe, S.; Bauer, A.; Uhlenbruck, S.; Fattakhova-Rohlfing, D., Physical vapor deposition in solid-state battery development: from materials to devices. Advanced Science 2021, 8 (11), 2002044.

Chapter 5: On-line Real-time Detection of Degradation Products of Lithium Oxygen Battery by a Cold Trap Pre-concentrator-Gas Chromatography/Mass Spectroscopy System

5.1 Introduction

Lithium-air battery (LAB) has attracted much interest over the past several decades because of its very high theoretical energy density and transition-metal-free cathode.[5-12] Although a LAB with high specific energy density has been experimentally demonstrated, it is still far from practical due to many problems such as its low cyclability and low stability resulting from various side-reactions such as the decomposition of electrolyte solution mainly at the O_2-cathode.[12-22] To overcome these difficulties, it is essential to clarify the degradation mechanism by analyzing the reaction products and intermediates produced during the discharge/charge processes. Many techniques have been used to examine these reaction products and intermediates, including X-ray diffraction,[23,24] Raman spectroscopy,[25,26] X-ray photoelectron spectroscopy,[24] and mass spectroscopy (MS).[27-29] Among these methods, MS is particularly useful because it allows for direct determination of the products and intermediates. An on-line quadrupole mass spectrometer has been using to continuously monitor the generation of inorganic gaseous products such as O_2 (major product), and H_2O and CO (byproducts) during charging. In addition, organic compounds, which are

generated mainly by decomposition of the organic electrolyte, were collected in small columns during the discharge and charging processes and analyzed by thermal separation probe (TSP)-gas chromatography (GC)/MS. However, because the discharge and charging processes were conducted under continuous O_2 and He flow, respectively, some of the decomposition products were removed from the cell and the discharge/charge behavior should be different from the cell operated under passive gas exchange. Also, since the samples were collected in columns by adsorption, collected amount of each component was determined by the adsorption/desorption equilibrium and use of a rather long adsorption time (1 hr) led the molecules with low adsorption equilibrium constants to be replaced by molecules with high adsorption equilibrium constants. Furthermore, the TSP-GC/MS analysis was performed ex-situ after all sample collections were completed, some of the collected molecules may go through structural changes during the storage, resulting in the reduction of the accuracy.

In this chapter, on-line cold trap pre-concentrator (CTPC)-GC/MS system was constructed to detect reaction products of LABs during discharge and charging in real-time with high accuracy. By installing the cold trap between the cell and the GC/MS and adjusting the cold trapping temperature, all the volatile products generated during the cell reaction processes could be collected and analyzed by GC/MS without exposure to the ambient atmosphere. The generations of organic molecules were followed over time by repeatedly sampling the head-space gas of the cell for a very short time, e.g., 15s, for

a fixed period of time, e.g., 40 min, during the cell operation. By controlling the sampling time and period, loss of generated molecules by gas flow can be minimized. The CTPC-GC/MS system was applied to the LAB with 1 M lithium bis(trifluoromethanesulfonyl)imide (LiTFSI) tetraethylene glycol dimethyl ether (TEGDME) electrolyte solution operated under constant-current discharge and constant-current or voltage-sweep charging. A total of 37 peaks were detected and 27 of them were assigned to specific molecules. Several molecules were present as impurities in TEGDME even before discharge and a few molecules were generated during discharge but most of the molecules were generated during charging. The results obtained under voltage scan without discharge showed that some of the molecules generated at the end of charging were also generated without discharge, indicating these molecules were formed by direct electrochemical oxidation without involvement of active oxygen.

5.2 Results and discussion

5.2.1 CTPC-GC/MS analysis during the constant current discharge and LSV

Figure 5-1(a) and **(b)** shows the gas chromatograms (GCs)[31] obtained every 40 min during OCP, constant-current discharge, OCP, and voltage-sweep charge of cells with battery grade (BG-)TEGDME and high purity (HP-)TEGDME, respectively. At least 37 peaks were detected as summarized in **Table 5-1**. The former contains more impurities as shown in **Figure 5-2** and there are clear differences between the two, particularly in the earlier stage of experiments. Results obtained under the voltage-sweep and constant-

current charging modes were essentially the same with 37 peaks observed at the same positions in both cases, although the time dependencies of the peak intensities were different, reflecting the differences in the time dependencies of the voltage and the current. Results obtained for the cell without discharge carried out for Ar and O_2 filled cells are shown in **Fig. 5-1(c)** and **(d)**, respectively.

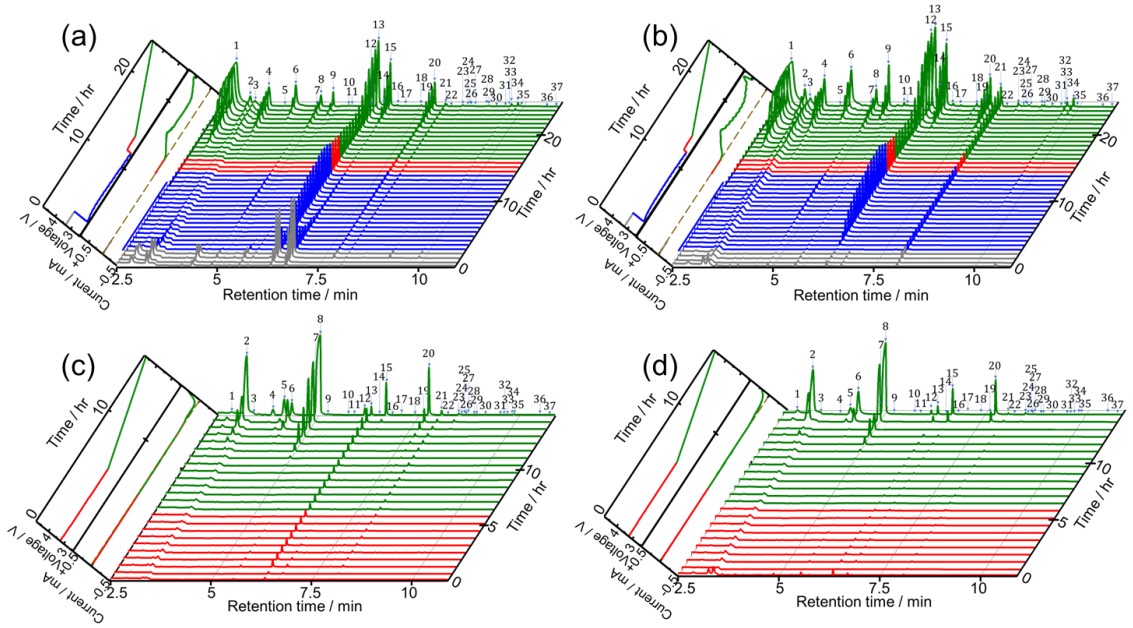

Figure 5-1. Gas chromatograms of head space gas sampled by CTPC-GC/MS every 40 min (**a, b**) during OCP (2 hr: gray), constant-current discharge (0.4 mA, 10 hr: blue), OCP (ca. 2.82 V, 2 hr: red), and charge by voltage sweep (0.05 mV s^{-1} from OCP (~2.82 V) to 4.7 V: green) of the cells prepared using (**a**) BG- and (**b**) HP-TEGDME and (**c, d**) OCP (3.27 V to 3.25 V, 6 hr: red lines) and voltage sweep (0.05 mV s^{-1} from 3.2 V to 4.7 V: green lines) without discharge of the cells prepared using HP-TEGDME filled with (**c**) Ar and (**d**) O_2. Left panel: voltage and current as a function of time. Color coding is as of gas chromatograms.

The full results for peak intensities as a function of time during OCP, discharge, and OCP, and of voltage during voltage scan (**Fig. 5-1(a, b)**), and those as a function of time

during OCP and of voltage during voltage scan (**Fig. 5-1(c, d)**) for all 37 peaks are shown in **Figure 5-2** and **5-3**, respectively. Comparison plots for all 37 peaks between with (**Fig. 5-1(b)**) and without (**Fig. 5-1(d)**) discharge are shown in **Figure 5-4**.

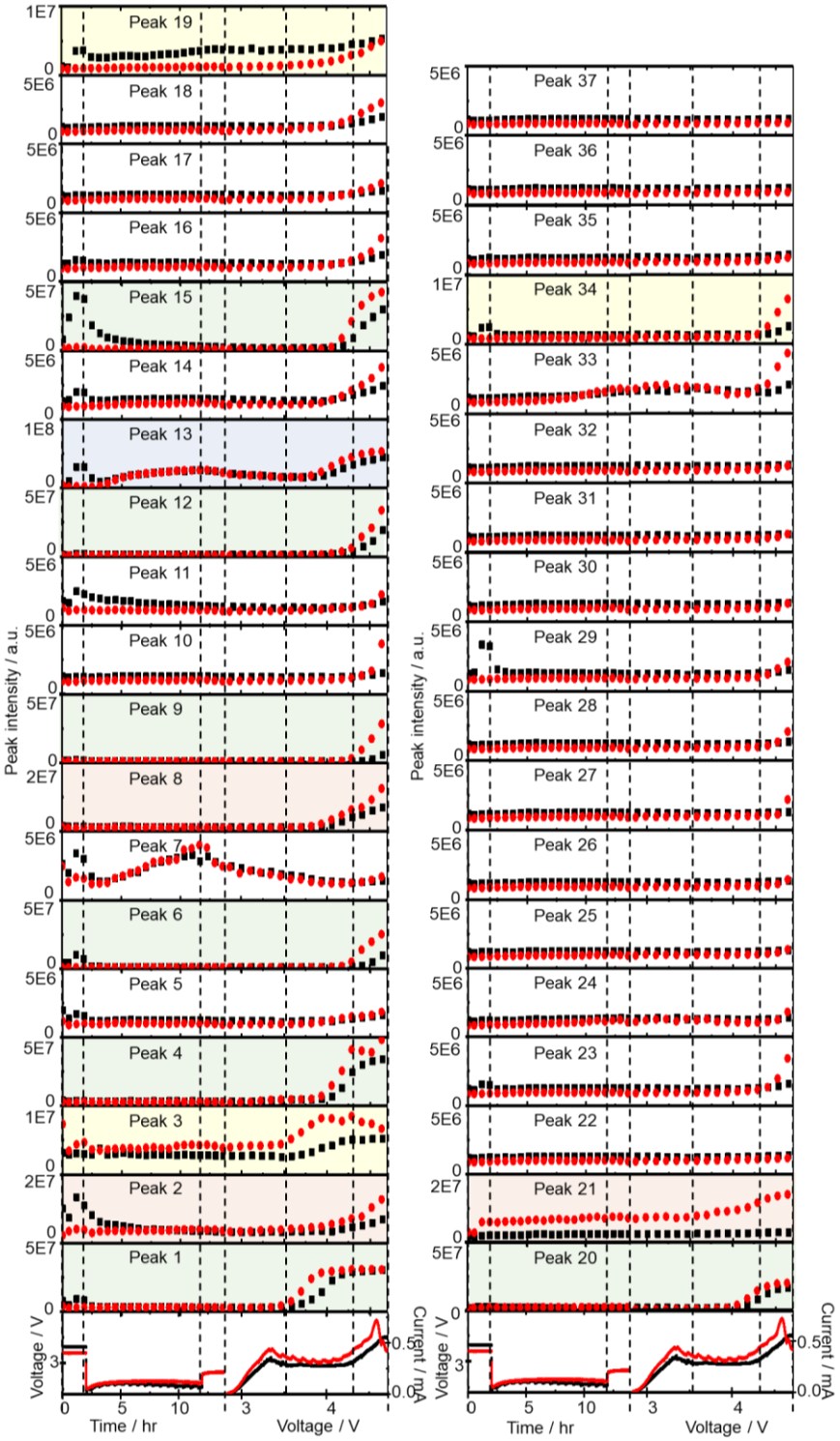

Figure 5-2. Effect of impurity levels in TEGDME on the variation of the intensities of 37 peaks during OCP, discharge, OCP, and voltage sweep charge. Voltage and current (bottom panels), and intensities of the peaks 1 – 37 in **Fig. 5-1(a)** (black) and **(b)** (red) during OCP, discharge, OCP, and voltage sweep charging. Data during OCP and discharge, and those during voltage sweep are presented as functions of time and voltage, respectively.

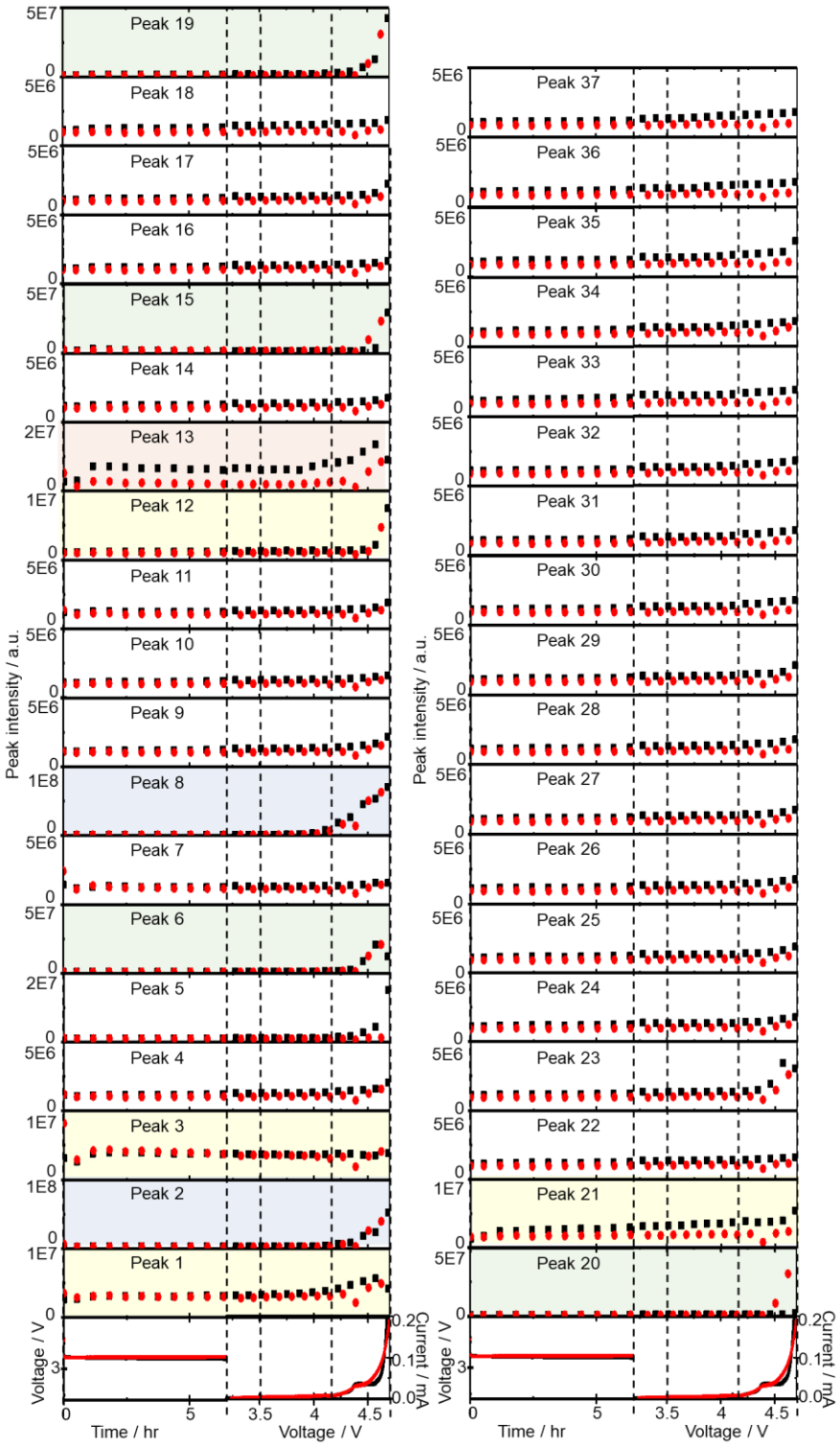

Figure 5-3. Effect of gas in the cell on the variation of the intensities of 37 peaks. Voltage and current (bottom panels), and intensities of the peaks 1 – 37 in **Fig. 5-1(c)** and **(d)** during OCP and voltage scan (red). Data during OCP and discharge, and those during voltage sweep are presented as functions of time and voltage, respectively.

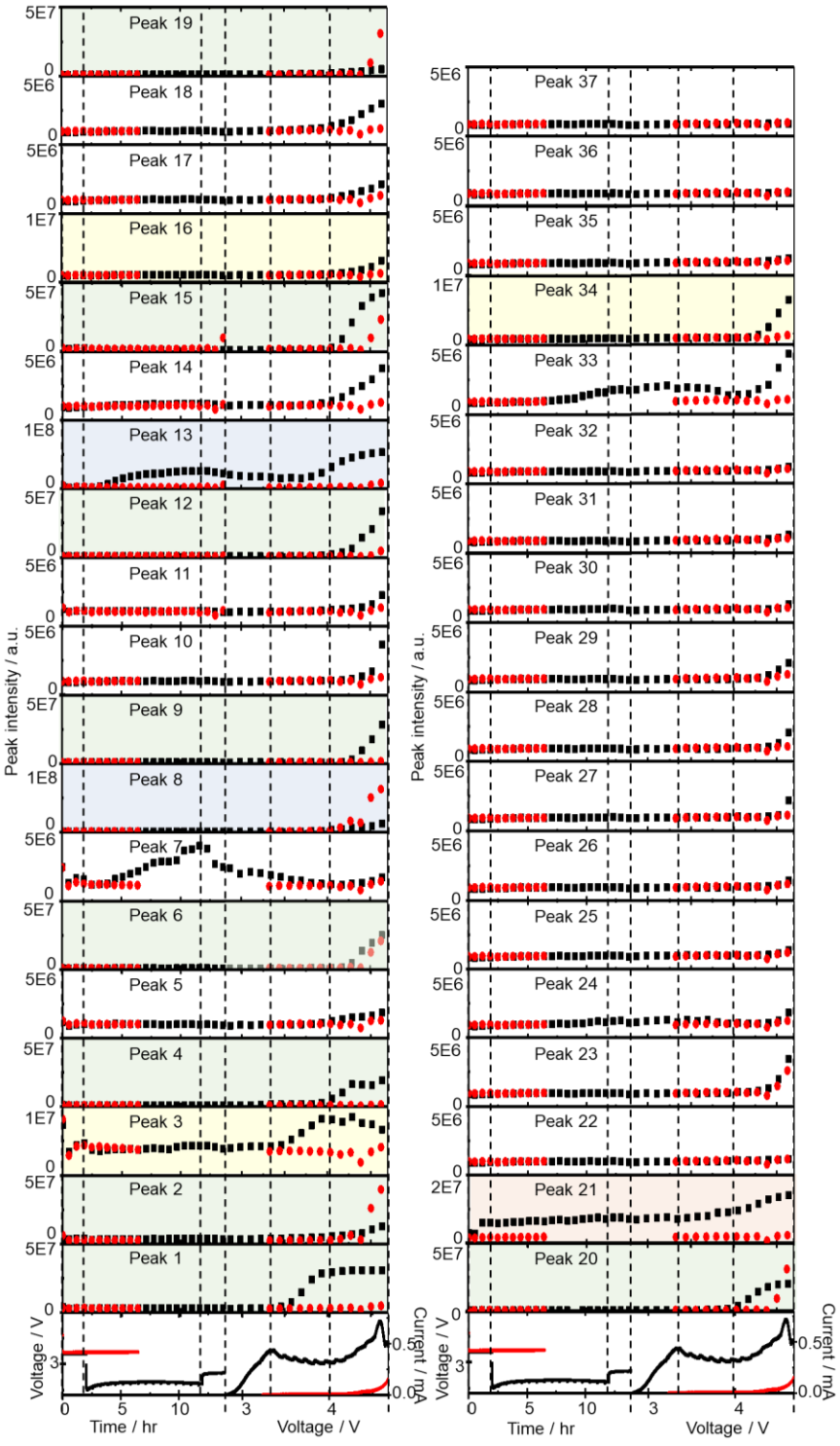

Figure 5-4. Effect of discharge on the variation of the intensities of 37 peaks. Voltage and current (bottom panels), and intensities of the peaks 1 – 37 in **Fig. 5-1(b)** during OCP, discharge, OCP, and voltage sweep charging (red) and those in **Fig. 5-1(d)** during OCP and voltage scan (red). Data during OCP and discharge, and those during voltage sweep are presented as functions of time and voltage, respectively.

Peak assignments were made by using GCMSsolution software (Shimadzu, ver.2) by comparing the mass spectrum of each peak with those in the NIST database attached to the software. Assignments were accepted only when the similarity between the mass spectrum of the peak and that of the proposed molecule was more than 90%. Final confirmation of the assignments were made by comparison with gas chromatograms obtained by using reference molecules. A total of 27 out of 37 peaks observed in **Fig. 5-1(a)** were assigned a molecular structure and so far 12 of them were confirmed by GC/MS of reference molecules.[32] Nine molecules detected in our previous TSP-GC/MS analysis[29] were found: *Mono*- (G1: peak 2), *Di*- (G2: peak 19), and *Tri*- (G3: peak 36) *ethyleneglycol dimethyl ether*, *Methoxy acetoaldehyde* (peak 6), *(2-Methoxyethoxy)ethene* (peak 7), *1-Methoxy-2-(methoxymethoxy)ethane* (peak 12); *2-Methoxy ethanol* (peak 13); *Acetic acid* (peak 27); and *Formic acid* (peak 30), as presented in **Table 5-1**.

It should be noted that peak intensity reflects the partial pressure (i.e., the concentration) of the corresponding molecule in the gas phase not in the solution. The partial pressure of each component is determined by the mole fraction (i.e., concentration) in the solution and vapor pressure of a pure liquid of each component in an ideal situation (Raoult's Law). Although it is not so simple in real systems, particularly in the multi-component systems like present system, vapor pressure is still important in evaluating the concentration of each molecule in the solution from the peak

height. Thus, vapor pressure data of the assigned molecules are also listed in **Table 5-1** together with boiling point data since for some assigned molecules vapor pressure values are missing but boiling point values available and there exists a good correlation between vapor pressure and boiling point as shown in **Figure 5-5**. Vapor pressure and boiling points were obtained from the database.

Table 5-1. List of GC/MS peaks with retention time, proposed molecular structures, similarity with database, vapor pressure, and boiling point. (Vapor pressure and boiling points were obtained from the database) Molecules of confirmed assignments by GC/MS analysis of reference molecule, and found by TSP-GC/MS analysis in our previous paper[29] are marked.

No.	Molecular structure	Retention time (min)	Confirmation*	TSP-GC/MS[29]	Similarity with DB (%)	Vapor pressure (25°C) / kPa	Boling point °C	No.	Molecular structure	Retention time (min)	Confirmation*	TSP-GC/MS[29]	Similarity with DB (%)	Vapor pressure (25°C) / kPa	Boling point °C
1		2.86	✓		98	16.93	64.60	20		7.82			93	N/A	190.90
2		3.20	✓	✓	97	10.19	85.00	21		8.12			94	0.34	165.00
3		3.40	✓		98	7.91	78.20	22		8.28	✓		97	0.40	150.00
4		3.70	✓		96	10.53	78.00	23	?	8.53			<90	—	—
5	?	4.09			<90	—	—	24		8.66			90	0.03	193.90
6		4.36		✓	95	54.17	92.00	25		8.71			90	1.8E-4	285.0
7		4.88		✓	97	5.42	108.80	26	?	8.75			<90	—	—
8		5.00	✓		96	5.08	101.00	27		8.87	✓	✓	97	2.09	117.80
9	?	5.30			<90	—	—	28	?	9.12			<90	—	—
10	?	5.67			<90	—	—	29		9.19			96	N/A	174.00
11	?	5.76			<90	—	—	30		9.48	✓	✓	97	5.68	100.70
12		6.18		✓	98	N/A	N/A	31		9.56			95	4.7E-4	233.9
13		6.36	✓	✓	98	1.27	193.90	32	?	9.67			<90	—	—
14		6.57	✓		97	1.26	131.00	33		9.77	✓		92	N/A	245.0-250.0
15	?	6.74			<90	—	—	34		9.83			92	N/A	208.50
16		6.89			96	N/A	128.10	35		10.00			94	N/A	175.10
17		7.09	✓		98	0.27	143.00	36		10.61	✓	✓	97	0.12 (20°C)	216.00
18	?	7.49			<90	—	—	37		10.86			95	N/A	96.0 (0.3 mmHg)
19		7.76	✓	✓	98	0.39	162.00								

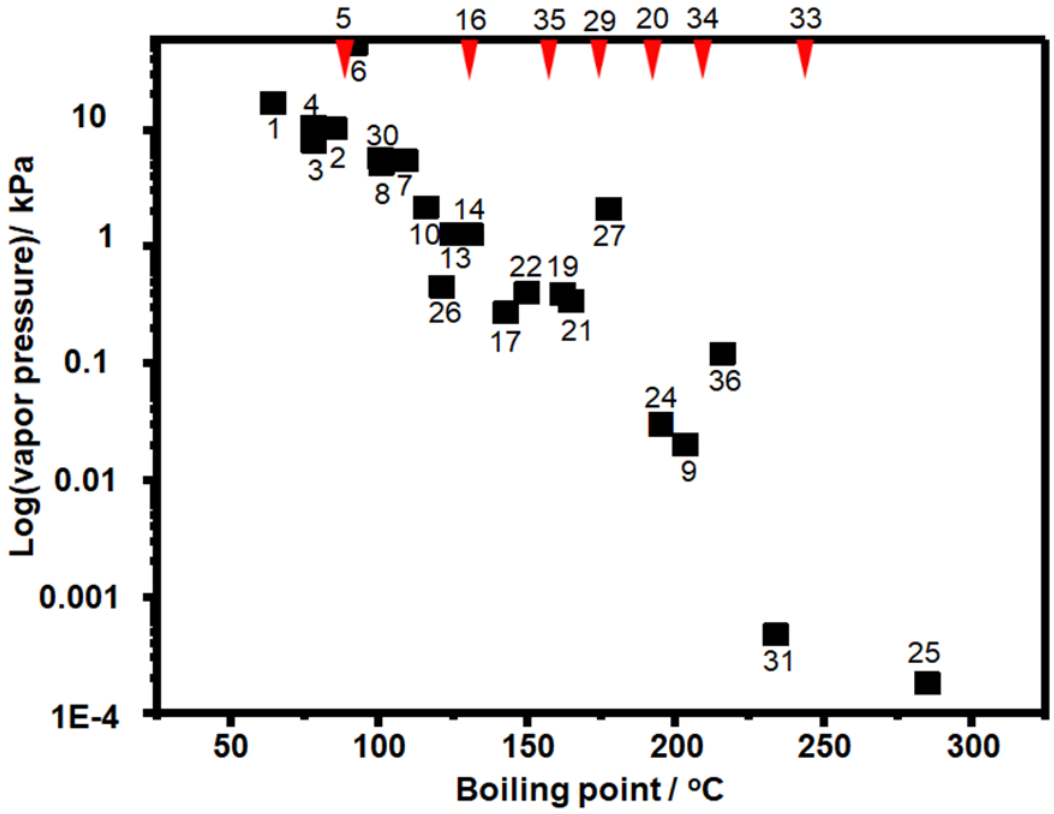

Figure 5-5. Correlation between the boing point and vapor pressure of assigned molecules in **Table 5-2**. The boiling points of molecules without vapor pressure data are shown above (red arrow).

Table 5-2. List of GC/MS peaks with retention time, proposed molecular structures, similarity with database, vapor pressure, boiling point, maximum peak height of each peak during whole operation, and the peak heights variation during OCP, discharge, OCP, and voltage sweep charge normalized by the maximum height (**Fig. 5-1**).

No.	Retention time (min)	Molecular structure	Similarity with DB (%)	Vapor pressure (25°C) / kPa	Boling point °C	Maximum peak intensity/ 10^7	OCP before discahrge	Discharge	OCP before charge	Charge		
										I (2.82-3.54 V)	II (3.54-4.3 V)	III (4.3-4.66 V)
1	2.86		98	16.93[a]	64.6[a]	2.38						
2	3.20		97	10.19[b]	85.0[a]	2.66						
3	3.40		98	7.91[a]	78.2[a]	0.47						
4	3.70		96	10.53[a]	78.0[a]	3.00						
5	4.09	?	<90	—	—	0.15						
6	4.36		95	54.17[c]	92.0[c]	2.87						
7	4.88		97	5.42[d]	108.8[a]	4.11						
8	5.00		96	5.08[a]	101.0[a]	4.98						
9	5.30	?	<90	—	—	2.52						
10	5.67	?	<90	—	—	0.32						
11	5.76	?	<90	—	—	0.26						
12	6.18		98	N/A	N/A	4.00						
13	6.36		98	1.27[a]	193.9[a]	4.11						
14	6.57		97	1.26[c]	131.0[a]	0.41						
15	6.74	?	<90	—	—	3.79						
16	6.89		96	N/A	128.1[f]	0.74						
17	7.09		98	0.27[a]	143.0[a]	0.23						
18	7.49	?	<90	—	—	0.40						
19	7.76		98	0.39[a]	162.0[a]	2.61						
20	7.82		93	N/A	190.9[e]	2.64						
21	8.12		94	0.34[e]	165.0[g]	0.95						
22	8.28		97	0.40[b]	150.0[b]	0.27						
23	8.53	?	<90	—	—	1.79						
24	8.66		90	0.03[a]	193.9[a]	0.47						
25	8.71		90	1.8E-4[a]	285.0[a]	0.43						
26	8.75	?	<90	—	—	0.30						
27	8.87		97	2.09[a]	117.8[a]	0.59						
28	9.12	?	<90	—	—	0.52						
29	9.19		96	N/A	174.0[a]	1.73						
30	9.48		97	5.68[a]	100.7[a]	0.31						
31	9.56		95	4.7E-4[a]	233.9[h]	1.05						
32	9.67	?	<90	—	—	0.75						
33	9.77		92	N/A	245.0-250.0[i]	1.55						
34	9.83		92	N/A	208.5[f]	2.95						
35	10.00		94	N/A	175.1[e]	0.61						
36	10.61		97	0.12 (20°C)[a]	216[a]	0.24						
37	10.86		95	N/A	96.0 (0.3 mmHg)[j]	0.35						

Vapor pressure and boiling points were obtained from the following database. aPubChem: https://pubchem.ncbi.nlm.nih.gov/, bNIST: https://www.nist.gov/, cTGSC: http://www.thegoodscentscompany.com/, dChemSpider: http://www.chemspider.com/, eChemSrc: https://www.chemsrc.com/en/, fChemeo: https://www.chemeo.com/ gAmerican Elements: https://www.americanelements.com/, h Chemenu: https://www.chemenu.com/, iChemical Book; https://www.chemicalbook.com/ProductIndex_EN.aspx

The time dependencies of the peak intensity during OCP and discharge can be categorized into at least three groups represented by peaks 1 (*Methanol*), 7 (*(2-Methoxyethoxy)ethene*), and 15 (unassigned) as shown in **Figure 5-6(a)**, in which intensities of these peaks obtained in two TEGDMEs are plotted as a function of time. During OCP, peak intensity increased initially for all three molecules because the concentrations of impurity molecules in the initial sampling were lowered by the flow of O_2 gas that was passed through the cell before the first sampling, and then it took time for the concentrations of the molecules in the gas phase to increase and reach vapor/solution equilibrium. Intensities of peaks were higher for BG-TEGDME than for HP-TEGDME as already shown in **Fig. 5-2**. As shown in **Fig. 5-1(c, d)**, even though the cell was kept at OCP much longer (6 hr: red lines) than the case in **Fig. 5-1(a, b)**, no marked decreases of peak intensities were observed, confirming that the decomposition of the molecules did not take place during OCP without discharge. Generally, peaks assigned to the molecules with relatively high and low vapor pressure gradually decreased and increased, respectively, during OCP; these behaviors reflected the time to reach vapor/liquid equilibrium.

After the initial increase during OCP, peaks 1, 7, 15 decreased rather quickly in the case of BG-TEGDME as discharge started. The changes were clear in the case of HP-TEGDME as initial intensities were low (**Fig. 5-6(a)**). Intensities of peak 1 remained at almost zero through discharge in both cases; those of peak 7 increased gradually

throughout discharge in both cases; and those of peak 15 decreased gradually throughout discharge in the case of BG-DME but remained almost 0 in the case of HP-TEGDME. At the start of discharge, active oxygen species such as superoxide and singlet oxygen, as well as lithium superoxide and lithium peroxide, are generated, leading to the decomposition of organic molecules. The concentration of each molecule should be determined by the initial concentration, decomposition rate, and generation rate from TEGDME. Because initial concentrations of impurities were higher, initial decreases were clearer in BG-TEGDMS. Only a few molecules such as *(2-Methoxyethoxy)ethene* (peak 7), *2-Methoxy ethanol* (peak 13), and *G2* (peak 19) increased their intensities during discharge. The increase of these molecules indirectly suggests the decomposition of G4.

Many more peaks were detected during charge than during discharge (**Fig. 5-1(a, b)**). The voltage dependencies of the peaks were categorized into at least three groups represented by peaks 1, 7, and 8 (*1,4-Dioxane*) as shown in **Figure 5-6(b)**, in which intensities of these peaks obtained during voltage scan (charge) in two TEGDMEs are plotted as a function of voltage. Results obtained in HP-TEGDME but without discharge (**Fig 5-1(d)**) are also plotted. Peak 1 started to increase at around 3.5V but not without discharge. Ethanol (peak 3) behaved similarly. On-line Q-mass analysis showed generation of water started at this voltage. These results suggest that generation of small alcohols is initiated by the same precursor, which generates H_2O. The intensities of

some peaks such as peak 8 started to increase during the latter part of the charge, or relatively positive voltage. Actually, these peaks started to increase at almost the same voltage with or without discharge, showing that they were generated purely or partly by electrochemical oxidation. Peak 7 decreased from as charge started but slightly increased at the last part of charge.

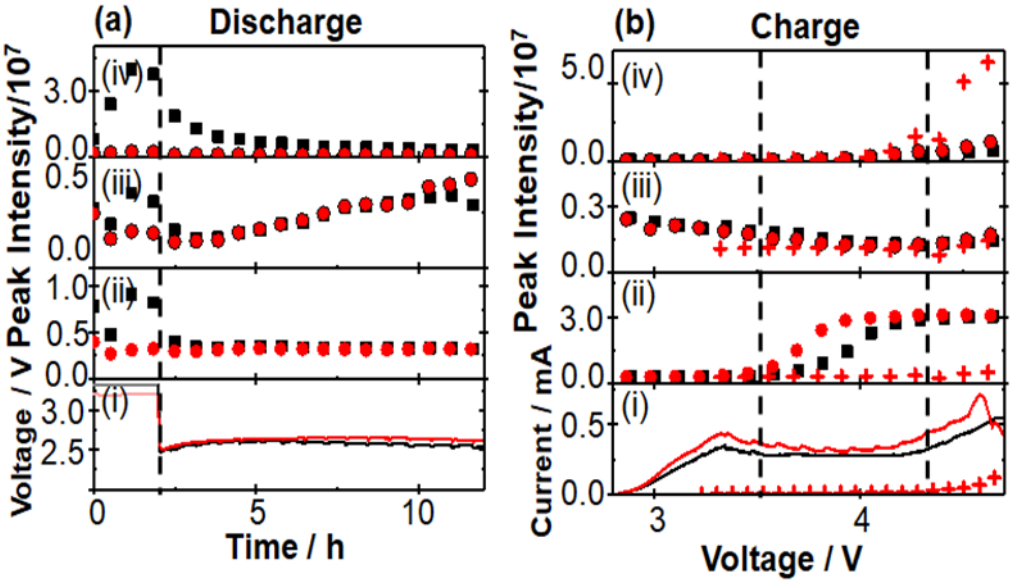

Figure 5-6. (a) Voltage (bottom panel) and normalized intensities of peaks **1** (ii), **7** (iii), and **15** (iv) (top panel) as a function of time during OCP and discharge for the cells using BG-(■) and HP-(●) TEGDME. (b) Current (i) and the intensities of peaks **1** (ii), **7** (iii), and **8** (iv) as a function of voltage for the cells using BG-(■) and HP-(●) TEGDME with discharge and for HP-(●) TEGDME without (+) discharge.

5.2.2 CTPC-GC/MS analysis during the constant current discharge/charge

5.2.2.1 CTPC-GC/MS analysis during the first discharge and charge

Sampling and analysis were started immediately after the cell was connected to the charge/discharge system and filled with O_2 gas. **Figure 5-7(a)** shows GCs of 1M

LiTFSI in BG-TEGDME obtained every 40 min during the 1st discharge/charge cycle, i.e., OCP (2 hr), constant-current (0.4 mA, 10 hr) discharge, OCP (2 hr), and constant-current (0.4 mA, 4.66 V cut off) charging. **Fig. 5-7(b)** shows GCs of 1M LiTFSI in HP-TEGDME obtained initially, 30 min after O_2 flow, then every 90 min during the 1st discharge/charge cycle, i.e., OCP (2 hr), constant-current (0.4 mA, 10 hr) discharge, OCP (2 hr), and constant-current (0.4 mA, 4.5 V cut off) charging. A total of 37 peaks were observed and 27 of them were assigned to specific molecules as presented in 5.2.1 (**Table 5-1 and Table 5-2**). Time dependencies of voltage (bottom panels; solid line) and the peak intensities of all 37 peaks (□) during OCP, discharge, OCP, and charge are shown in **Figure 5-8**. Many peaks were detected even before discharge started, showing the presence of impurity molecules in TEGDME.

When discharge was started, intensities of most peaks decreased. Intensities of only a few peaks such as peaks 7 (*(2-Methoxyethoxy)ethene*), 13 (*2-Methoxy ethanol*), 22 (*Methyl 2-hydroxyl acetate*), and 24 (*(2-(2-Methoxyethoxy)ethanol)*) increased at the later stage of discharge.

Many more peaks were detected during charge as shown in **Fig. 5-7(a)/(b)**. It must be noted that peaks corresponding to the molecules, which were not detected in the previous TSP-GC/MS study[20] such as methanol (Peak 1) and ethanol (Peak 3), were observed. The peak corresponding to G1 (peak 2) was stronger than that of G2 (peak 19) in the present study, while the G2 peak was stronger than G1 peak in the TSP-GS/MS

analysis, although the conditions of GC operation were the same in both cases. These results confirmed that molecules of low adsorption strength were replaced by those of high adsorption strength during sample collection by column adsorption in the TSP-GC/MS analysis[20] and showed the advantage of the present CTPC-GC/MS system over the previous method, i.e., the collection by column followed by post TSP-GC/MS analysis.

Although the intensities of most peaks increased during charge, the onset voltage for the peak increase varied with the peaks. Intensities of several peaks such as 1, 2 and 3 corresponding to relatively small and simple fragments of TEGDME increased from the early stage of charge but most other peaks increased from the middle or the last stage of charge when the voltage was relatively high. Peaks 7, 13, and 24, which increased at the last stage of discharge, behaved differently as they decreased at the early stage of charge but increased again at the later stage of charge as other peaks. Intensity increase in the middle and last stages of charge suggests the involvement of electrochemical oxidation at high voltage in the degradation process and/or the requirement of the accumulation of precursor molecules for the generation of complex molecules.

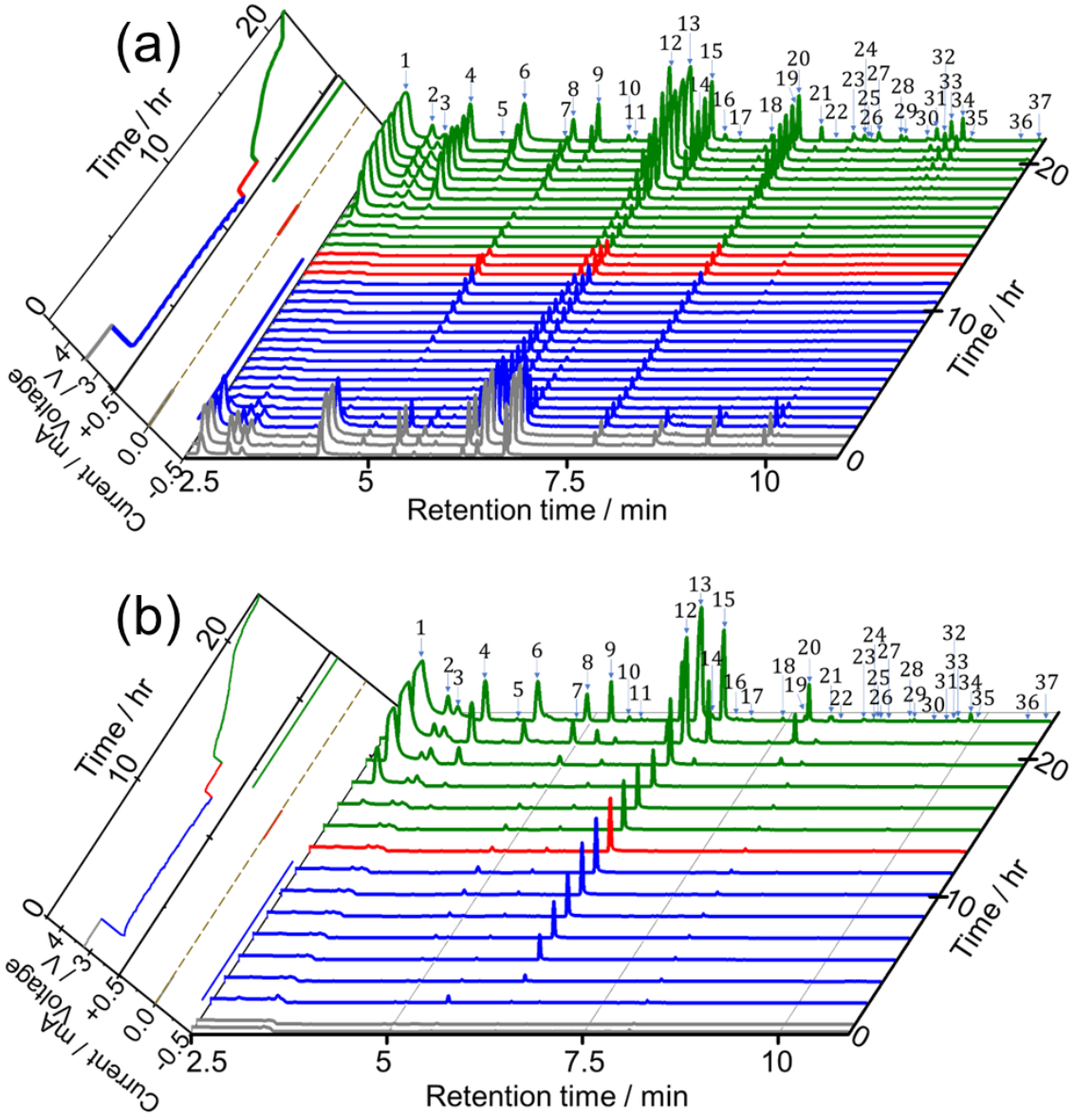

Figure 5-7. GCs of head space gas of the LOB during OCP (grey), constant current discharge (blue), OCP (red), constant current charge (green) prepared using **(a)** TEGDME (BG) and **(b)** TEGDME (HP). Left panel: voltage and current as a function of time. Color coding is as of gas chromatograms.

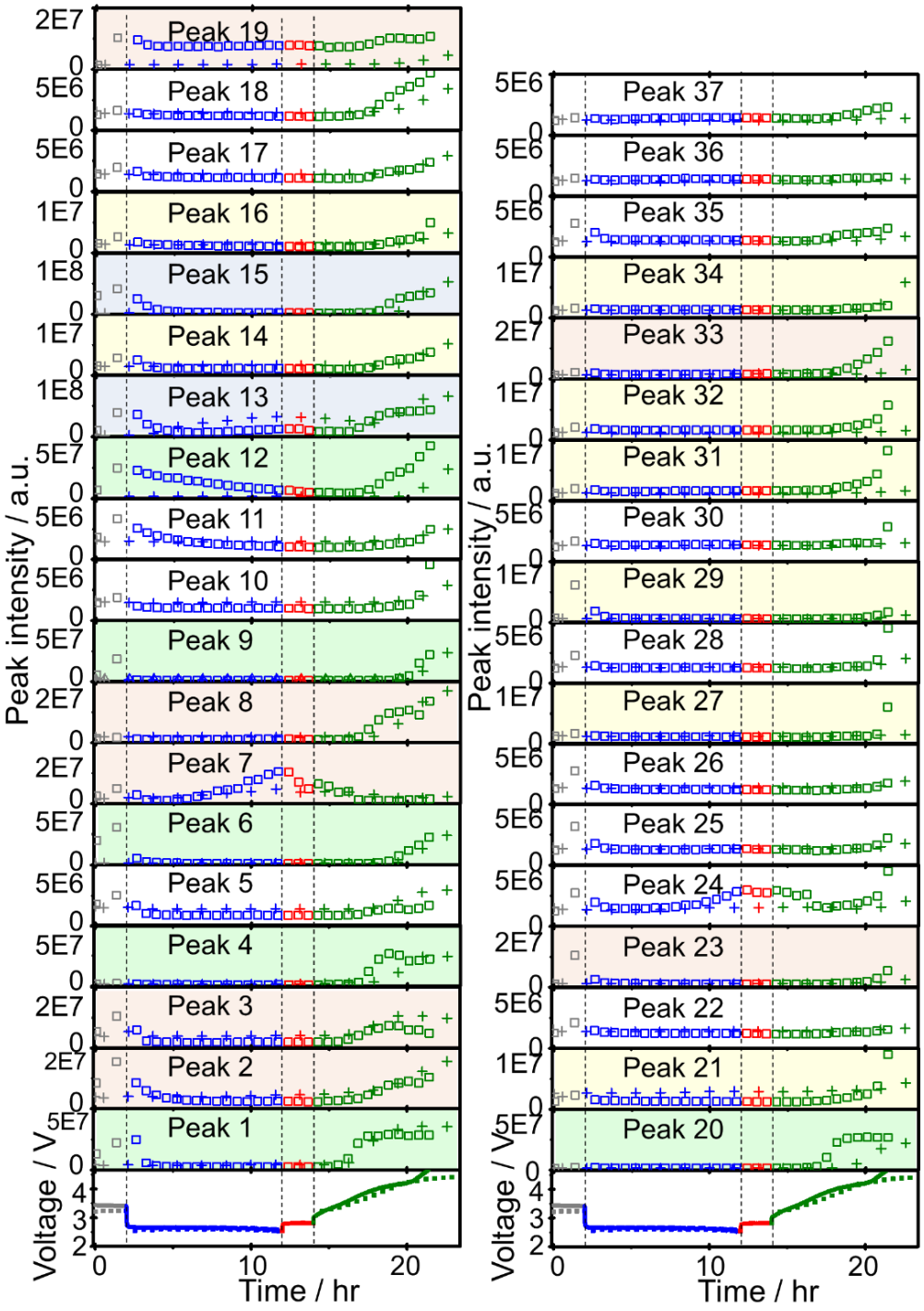

Figure 5-8. Voltage (bottom panels) and intensities of peaks 1 – 37 as a function of time for LOBs using TEGDME (BG) (☐) and TEGDME (HP) (+). Color coding is as of fig. **5-7 (a)** and **(b)**.

5.2.2.2 CTPC-GC/MS analysis during the discharge/charge cycles

CTPC-GC/MS analysis was then carried out during discharge/charge cycles. Sampling was started immediately after the cell assembly, 5 hr after discharge, and then every 90 min to minimize the sampling effect on the cell performance. **Figure 5-9** shows time dependencies of voltage and current (left panel) and GCs of head space gas of the LOB, sampled during 4 cycles of OCP (2 hr), constant current (0.4 mA) discharge (10 hr or 2V cut off), OCP (2 hr), constant current (0.4 mA) charge (10 hr or 4.5 V cut off). Time dependencies of voltage (bottom panels) and the peak intensities of all 37 peaks during 4 cycles are shown in **Figure 5-10**. The full capacity (10 hr) discharge was possible in the first 3 discharge, but the 4th discharge was terminated by cut-off at 2 V (6.1 hr). On the other hand, charge was terminated by cut-off at 4.5 V even from the 1st charge (9.7 hr) and charge duration (capacity) decreased as the cycle number increased (2nd: 9.4 hr, 3rd: 5.9 hr, and 4th: 1.6 hr). One reason for rather low cycle number is the lean electrolyte condition (15 μL $(2\ cm)^{-2}$) for the present cell operation.

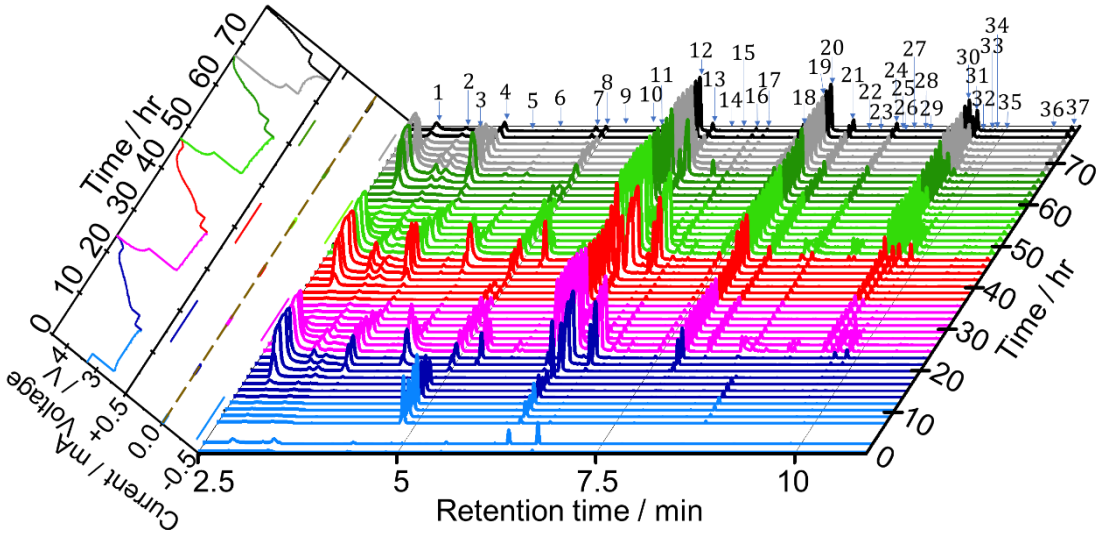

Figure 5-9. GCs of head space gas of the LOB, which was prepared by using TEGDME (BG), sampled during 4 cycles of OCP, discharge, OCP, and charge. Left panel: voltage and current as a function of time. Blue, pink/red, green, and grey/black lines are for the 1st, 2nd, 3rd, and 4th cycle, respectively. Lines of lighter color are of OCP and discharge, and of darker color are of OCP and charge.

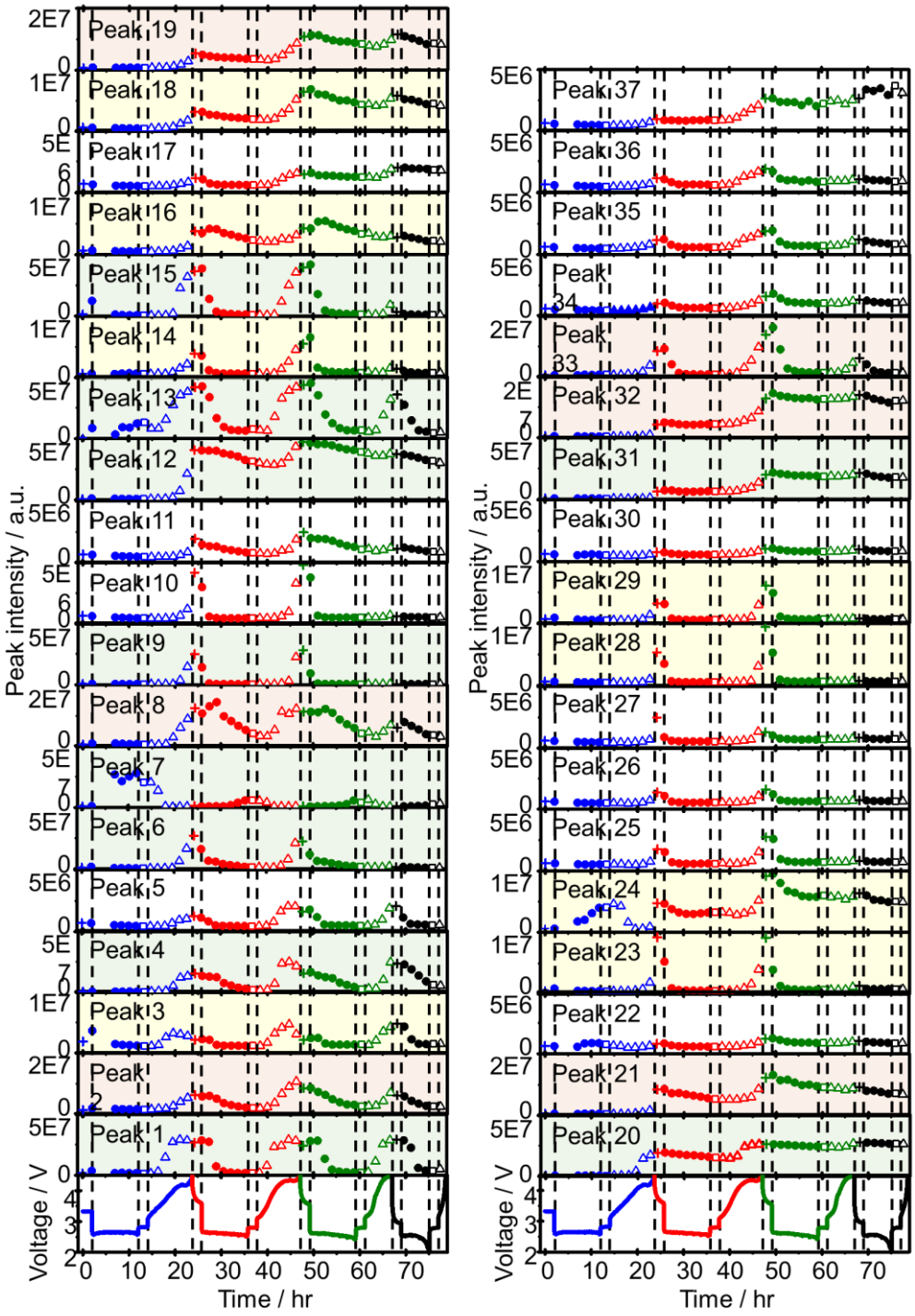

Figure 5-10. Voltage (bottom panels) and intensities of the peaks 1 – 37 during 4 cycles of OCP (+), discharge (●), OCP (□), and charge (△) as a function of time. Blue, red, green, and black lines/symbols are for the 1st, 2nd, 3rd, and 4th cycle, respectively.

Peak intensities varied in very complex manners during discharge/charge cycles. Intensities of most peaks decreased during discharge and increased during charge repeatedly as cycles but the rate and quantity of increase and decrease during discharge and charge, respectively, depending on the peak.

As shown in **Fig. 5-10**, intensities of most peaks decreased during the discharge in the following cycles; some peaks, e.g., 6 (*2-Methoxy acetaldehyde*), 13, and 14 (*Methyl 2-methoxyacetate*), started to decrease immediately and some peaks, e.g., 1, 3, and 4 (*1,3-Dioxolane*), started to decrease with delay. Peaks such as 8 (*1,4-Dioxane*) and 16 (*1,3,5-Trioxepane*) slightly increased at the initial stage of discharge before decrease. Peaks 7, 13, 22, and 24 increased at the last stage of the 1st discharge but only peak 7 increased during discharge in the following cycles. Peaks 13, 22, and 24 increased and decreased during charge and discharge, respectively, from the 2nd cycle as same as most other peaks behaved. Decay rates of some peaks such as 1, 2, 3, 4, and 29 (*Ethylene glycol diformate*) were high and these peaks became nearly zero at the end of discharge and those of some other peaks such as 12 (*1-Methoxy-2-(methoxymethoxy) ethane*), 16, 19, 20 (*2,2'-Bis(1,3-dioxolane)*) and 37 (*2-[2-(2-Methoxyethoxy)ethoxy]-1,3-dioxolane*) were low and these peaks remained at the end of discharge. Peak intensities increased again during the 2nd charge even more than those during the 1st charge and therefore, intensities of most peaks were higher at the end of the 2nd cycle than those at the end of the 1st cycle.

Similar trends were observed during the 3rd discharge/charge cycles but the increases of peak intensities during charge were generally less than those in the 2nd charge with exceptions for some peaks such as 1, 3, and 4, which increased as much as during the 2nd charge. In the 4th cycle, while behaviors during the discharge were almost the same as those in the previous cycles, almost no changes were observed during charge as it was terminated only in 1.6 hr and only one sampling was made during the charge.

Based on the above results, peaks can be categorized into at least four groups represented by peaks 1 (*Methanol*), 19 (G2), 7 (*(2-Methoxyethoxy)ethene*), and 25 (*Triethylene glycol*) as shown in **Figure 5-11**, in which voltage and intensities of these peaks are plotted as a function of time during OCP and discharge, and OCP and charge for the 1st, 2nd, 3rd, and 4th cycle. Peak 1 increased and decreased during charge and discharge, respectively, by almost the same amount up to the 4th discharge. Peak 19 increased and decreased during charge and discharge, respectively, as peak 1 but the amount of decrease during discharge was less than that of increase during charge and, therefore, the peak intensity gradually increased as the cycle was repeated. Peak 25 increased and decreased during charge and discharge, respectively, as other peaks but it increased at the very last stage of charge and decreased and disappeared at the very early stage of discharge. Peak 7 was the only peak that increased during discharge and decreased during charge, repeatedly, while other peaks increased during charge and

decreased during discharge.

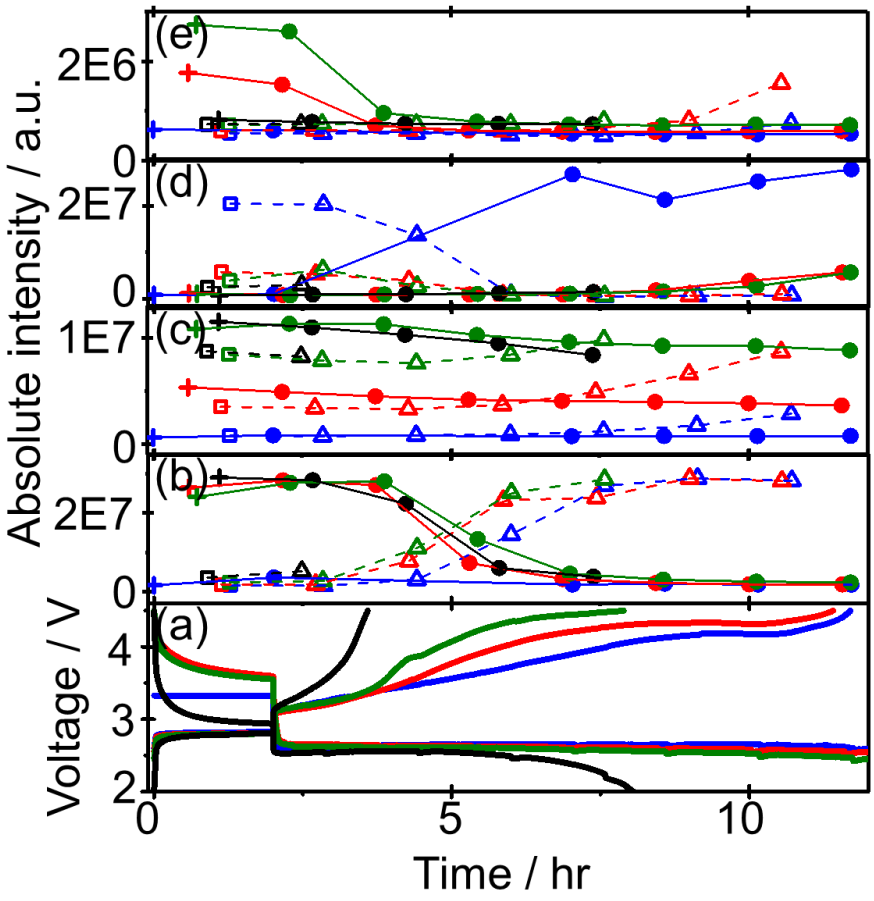

Figure 5-11. Voltage (a) and intensities of peak 1 (b), 19 (c), 7 (d), and 25 (e) of **Fig. 5-10** as a function of time during OCP (+) and discharge (●) (broken lines), and OCP (□) and charge (△) (solid lines) in the 1st (blue), 2nd (red), 3rd (green), and 4th (black) cycle.

CTPC-GC/MS analysis was also carried out for the LOB prepared by using TEGDME (HP). Sampling was started immediately after the cell was connected to the charge/discharge system, 30 min after O_2 gas flow, and then every 90 min. Time dependencies of voltage and current (left panel) and GCs of head space gas of the LOB, sampled during 4 cycles of OCP (2 hr), constant current (0.4 mA) discharge (10 hr or

2V cut off), OCP (2 hr), constant current (0.4 mA) charge (10 hr or 4.5 V cut off) are shown in **Figure 5-12** and time dependencies of voltage and the peak intensities of all 37 peaks during 4 cycles are shown in **Figure 5-13**.

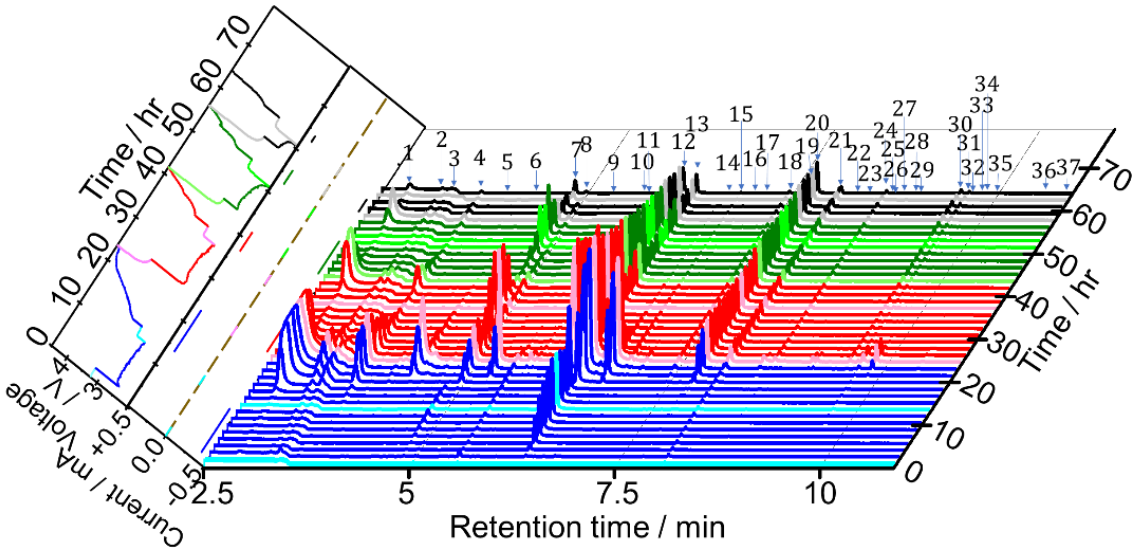

Figure 5-12. GCs of head space gas of the LOB, which was prepared by using TEGDME (HP), sampled during 4 cycles of OCP, discharge, OCP, and charge. Left panel: voltage and current as a function of time. Blue, pink/red, green, and grey/black lines are for the 1st, 2nd, 3rd, and 4th cycle, respectively. Lines of lighter color are of OCP and discharge, and of darker color are of OCP and charge.

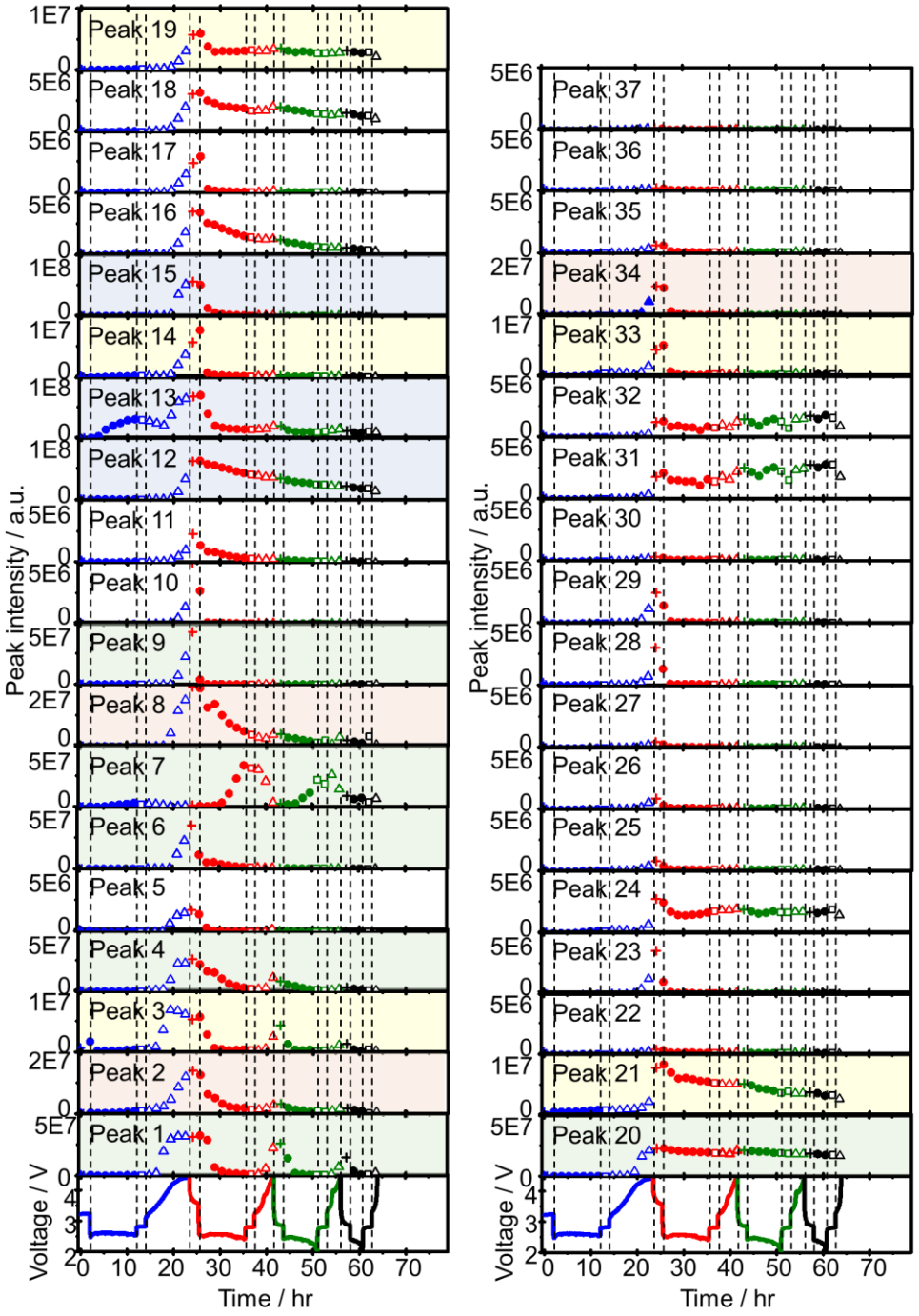

Figure 5-13. Voltage (bottom panels) and intensities of the peaks 1 – 37 during 4 cycles of OCP (+), discharge (●), OCP (□), and charge (▵) as a function of time. Blue, red, green, and black lines/symbols are for the 1st, 2nd, 3rd, and 4th cycle, respectively.

Results for the 1st cycle taken from **Fig. 5-12** are shown in **Fig. 5-7 (b)** time

dependencies of voltage and current (left panel) and GCs, and in **Fig. 5-8** time dependencies of voltage and the peak intensities of all 37 peaks together with the results of the LOB prepared by using TEGDME (BG). It is clear that initial impurity levels were much less in the LOB with TEGDME (HP) than in the LOB with TEGDME (BG) and, therefore, the decrease of peak intensities during the 1st discharge observed in the LOB with TEGDME (BG) was not observed in the LOB with TEGDME (HP). The increase of intensities at the last stage of charge observed for many peaks in the LOB with TEGDME (BG) were much less in the LOB with TEGDME (HP), reflecting smaller voltage rise in this cell than in the LOB with TEGDME (BG). Other features were essentially the same in both cells, although the absolute amount of intensity changes were different.

Cycle performance of the LOB with TEGDME (HP) was lower than that with TEGDME (BG) but the essential features presented in **Fig. 5-11** for the LOB with TEGDME (BG) were similar in the LOB with TEGDME (HP) as shown in **Figure 5-14**. The increases of peaks during the 2nd, 3rd, and 4th charge in the LOB with TEGDME (HP) were generally less significant than in the LOB with TEGDME (BG), which may be because of the short charge time.

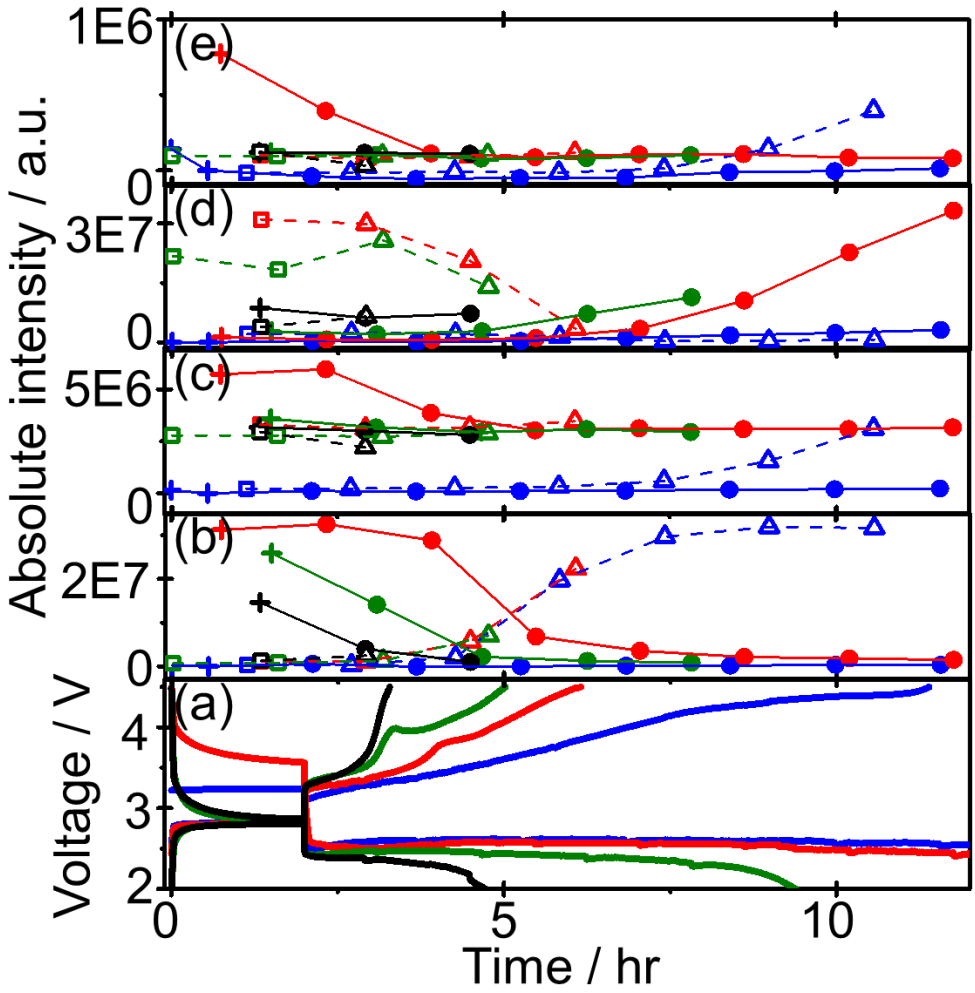

Figure 5-14. Voltage (a) and intensities of peak 1 (b), 19 (c), 7 (d), and 25 (e) of **Fig. 5-13** as a function of time during OCP (+) and discharge (●) (broken lines), and OCP (□) and charge (△) (solid lines) in the 1st (blue), 2nd (red), 3rd (green), and 4th (black) cycle.

5.2.3 CTPC-GC/MS analysis of dual-salt electrolytes

Lithium nitrate ($LiNO_3$) is commonly used as an additive in Li-S cells to protect the Li-negative electrode from further reactions with polysulfides. Recently, the use of $LiNO_3$ as a lithium salt in LOBs has attracted the attention of researchers as it has been found to exhibit superior performance in LOBs. The enhanced performance of LOBs

can be attributed to two aspects. One is that $LiNO_3$ can stabilize the lithium cathode by forming a strong SEI on the lithium cathode through reaction (14), the other is that NO_2^- formed by the reduction of nitrate ions on the anode acts as a redox mediator and helps to reduce the charge voltage.

$$2Li + LiNO_3 \rightarrow Li_2O + LiNO_2 \quad (14)$$

Despite the above-mentioned benefits of $LiNO_3$ for LOBs, the detection of nitrogen-containing groups on the surface of the carbon cathode indicates that $LiNO_3$ is unstable under cell operating conditions[31] Thus, combining lithium salts with different advantages into the multi-salt electrolytes seems to improve the performance of LOBs through a synergistic effect. This may be the reason for the recent popularity of dual-salt electrolytes. In this part, the dual electrolyte 0.5 M LiTFSI and 0.5 M $LiNO_3$ dissolved in TEGDME (HP) was tested.

Figure 5-15(a), (b) show the GCs obtained every 40 min during OCP, constant-current discharge, OCP, and voltage-sweep & constant current charge of cells with 0.5 M LiTFSI and 0.5 M $LiNO_3$ in HP-TEGDME, respectively. The GCs present similar behavior and compared with 1 M LiTFSI in HP-TEGDME (**Fig 1(b)**), 2 more peaks, which are suggested as *Diethyl carbonate* (5.5 min) and *1-Methyl-2-pyrrolidone* (10.42 min), were detected as shown in **figure 5-16**. These 2 peaks are also marked as yellow color in **Fig 5-15**. However, the generation of these two molecules is mechanistically

difficult, and their real existence needs to be confirmed by further, e.g., real molecular mass spectrometry analysis.

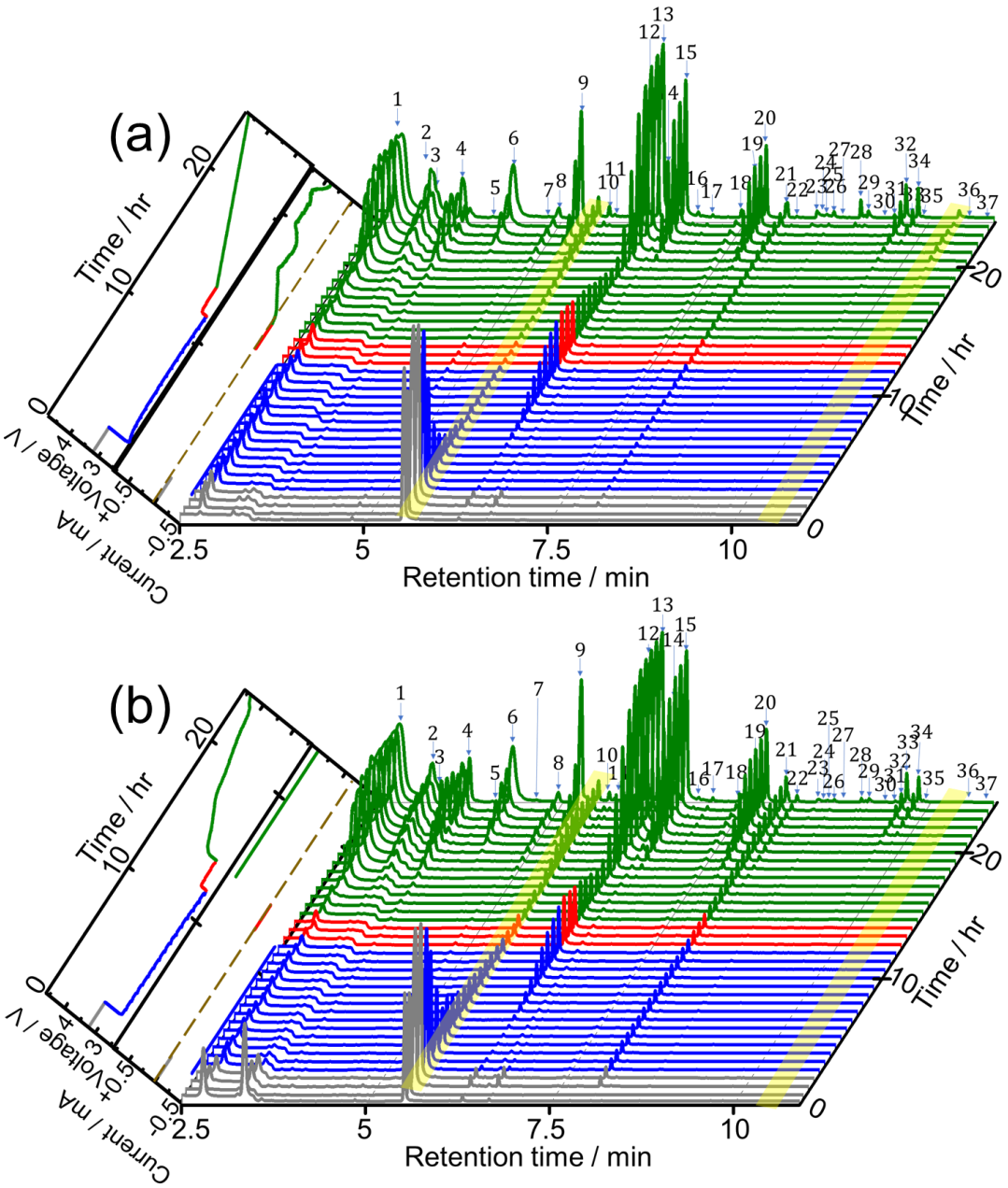

Figure 5-15. GCs of head space gas sampled by CTPC-GC/MS every 40 min during OCP (2 hr: gray), constant-current discharge (0.4 mA, 10 hr, cut off at 2 V: blue), OCP (ca. 2.82 V, 2 hr: red), and charge by voltage sweep (0.05 mV s^{-1} from OCP (~2.82 V) to 4.7 V: green) **(a)** and constant current (0.4 mA, 10 hr, cut off at 4.5 V: green) **(b)** of the cells prepared using 0.5 M LiTFSI and 0.5 M $LiNO_3$ in TEGDME (HP). Left panel: voltage and current as a function of time. Color coding is as of gas chromatograms.

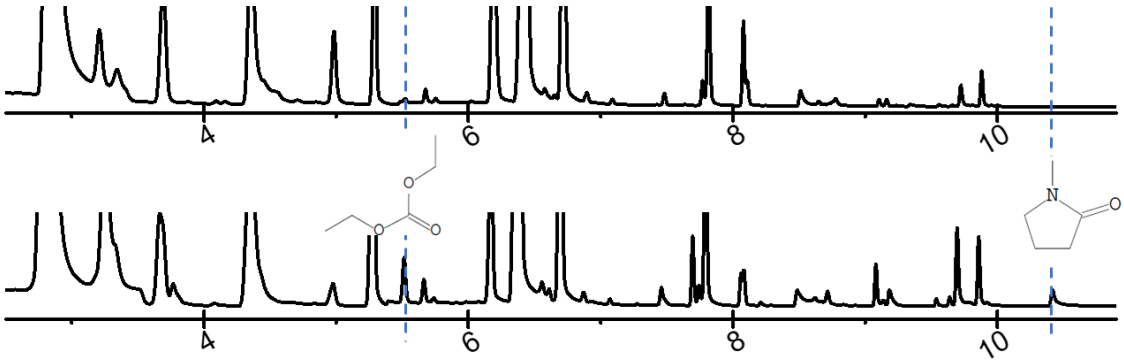

Figure 5-16. Gas chromatograms of head space gas sampled by CTPC-GC/MS of the cells prepared using 1 M LiTFSI (top panel) and 0.5 M LiTFSI and 0.5 M $LiNO_3$ dissolved in TEGDME (HG) (bottom panel).

The full results for peak intensities comparison as a function of time during OCP, discharge, and OCP, and of voltage during voltage scan of 0.5 M LiTFSI and 0.5 M $LiNO_3$ in HP-TEGDME (**Fig. 5-15(a)**) and 1 M LiTFSI in HP-TEGDME (**Fig. 5-1(b)**) is shown in **Figure 5-17**.

As can be seen from the charge/discharge curves, the discharge curve does not show a big difference, but the voltage scan of the charge curve, dual-salt electrolyte shows a wider second current peak appearing at a lower overpotential. And all the remaining peaks showed stronger peak intensities in the dual-salt electrolyte (0.5 M LiTFSI and 0.5 M $LiNO_3$ in HP-TEGDME) except for a few peaks, i.e., 1, 3, 6, and 21. Thus, the results are contrary to the expected results, with the dual-salt electrolyte producing more decomposition. In addition, constant current charge/discharge experiments (**Figure 5-18**) show dual-salt electrolyte producing more decomposition even at a voltage lower than 4.5 V.

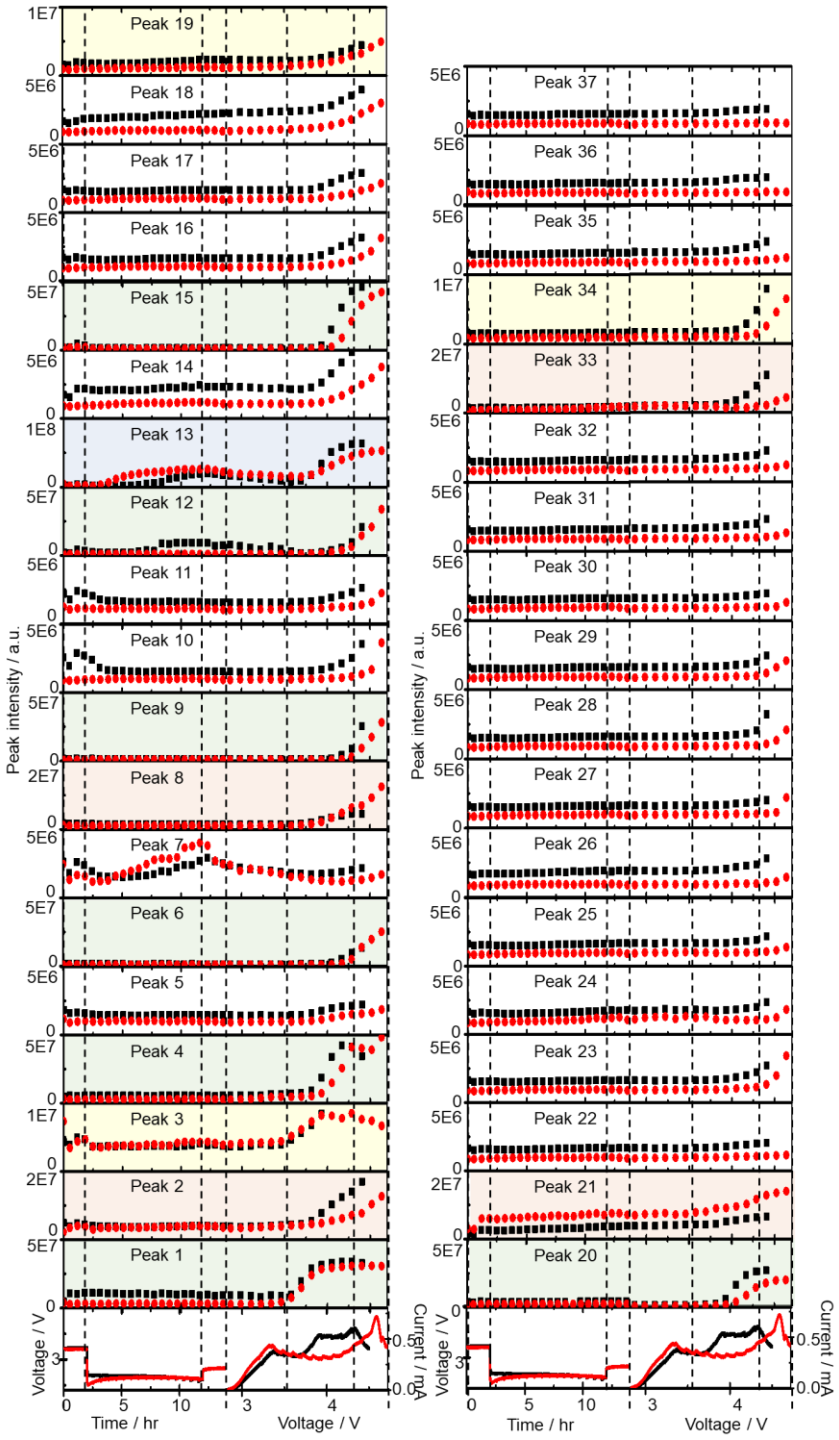

Figure 5-17. Effect of salt in HP-TEGDME on the variation of the intensities of 37 peaks during OCP, discharge, OCP, and voltage sweep charge. Voltage and current (bottom panels), and intensities of the peaks 1 – 37 in **Fig. 5-15(a)** (0.5 M LiTFSI and 0.5 M $LiNO_3$ in HP-TEGDME; black) and **Fig. 5-1(b)** (1 M LiTFSI in HP-TEGDME; red) during OCP, discharge, OCP, and voltage sweep charging. Data during OCP and discharge, and those during voltage sweep are presented as functions of time and voltage, respectively.

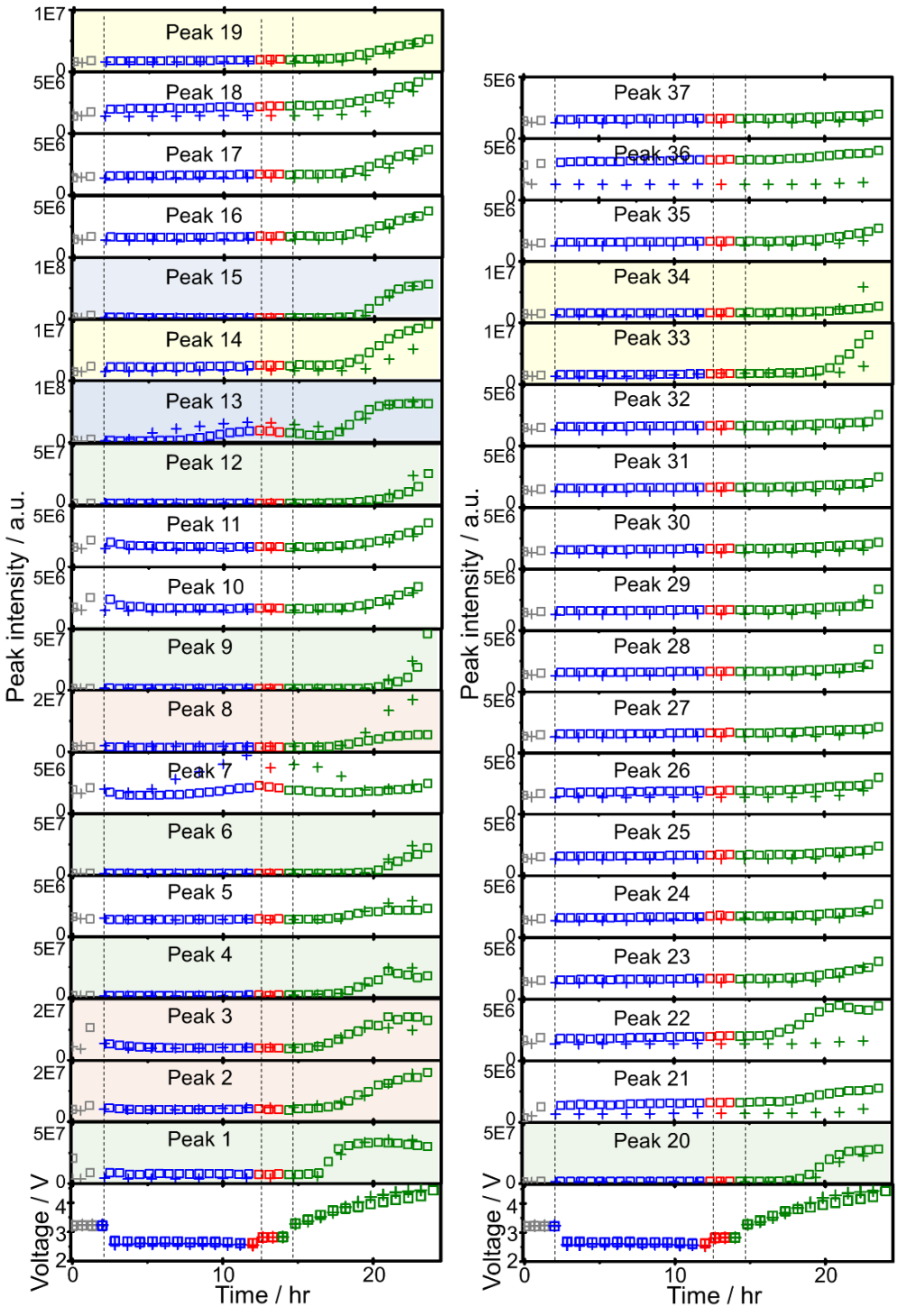

Figure 5-18. Voltage (bottom panels) and intensities of peaks 1 – 37 as a function of time for LOBs using 0.5 M LiTFSI and 0.5 M $LiNO_3$ in HP-TEGDME (□) and 1 M LiTFSI in HP-TEGDME (+ and dotted line). Colour coding is as of **Fig. 5-15 (b)** and **Fig. 5-7(b)**.

5.3 Conclusions

Although active oxygen species such as superoxide and singlet oxygen are considered to play key roles in the degradation of electrolyte in LOB[4,7,8-10] and these species were generated during both discharge and charge, degradation processes during discharge and charge were found to be quite different. During the charge, many molecules were generated particularly at the middle and last stage of charge. During discharge, only a few molecules were generated, and most molecules generated during charge were decomposed. Thus, TEGDME was decomposed, and many fragments and their reacted products were formed during the 1st charge. While small/simple fragments such as methanol, ethanol, and G1 were formed at relatively low voltage induced by active oxygen, which is released from Li_2O_2, more complex molecules were formed at the middle and last stages of charge possibly because of the involvement of electrochemical oxidation partly or fully (aldehyde and acid formation) and reactions of accumulated precursor molecules. In the 2nd discharge, almost all molecules generated during the 1st charge were decomposed. Delay in the decrease or even increase of the some peaks mainly due to small/simple molecules may be caused by the decomposition of more complex molecules. Small molecules were generated as degraded products of more complex molecules and decomposed by active oxygen species at the same time. As the decomposition of larger molecules became slower with time, the decomposition of small molecules, which seemed to proceed faster, became dominant and they were totally decomposed. Degradation of complex molecules led to the generation of smaller

molecules and also the formation of oligomers of ethylene glycol dimethyl ethers as reported before.20 Increase of the peak intensities during the 2nd charge was more than during the 1st charge in the LOB with TEGDME (BG) but less in the LOB with TEGDME (HP). Behaviors of molecules during 3rd discharge and charge and 4th discharge were essentially the same as those in the previous cycles but peak changes were less significant.

In conclusion, the degradation products of LAB with LITFSI/TEGDME electrolyte solution during discharge and charge were detected in real-time by using an on-line CTPC-GC/MS system. Although only a few molecules were detected during the discharge, a total of 37 molecules were detected during charging. A comparison with the results obtained under voltage scan without discharge confirmed that active oxygens was involved in the generation of some of the detected molecules, whereas others were generated at high cell voltages by direct electrochemical oxidation of TEGDME without involvement of active oxygen species.

Based on the current GCMS results, the possible degradation routes of TEGDME can be deduced with various detected (bold) and undetected molecules (**Scheme 5-1**). These schemes should not be considered as the actual reaction mechanisms but are simple modes, showing how detected molecules can be generated.

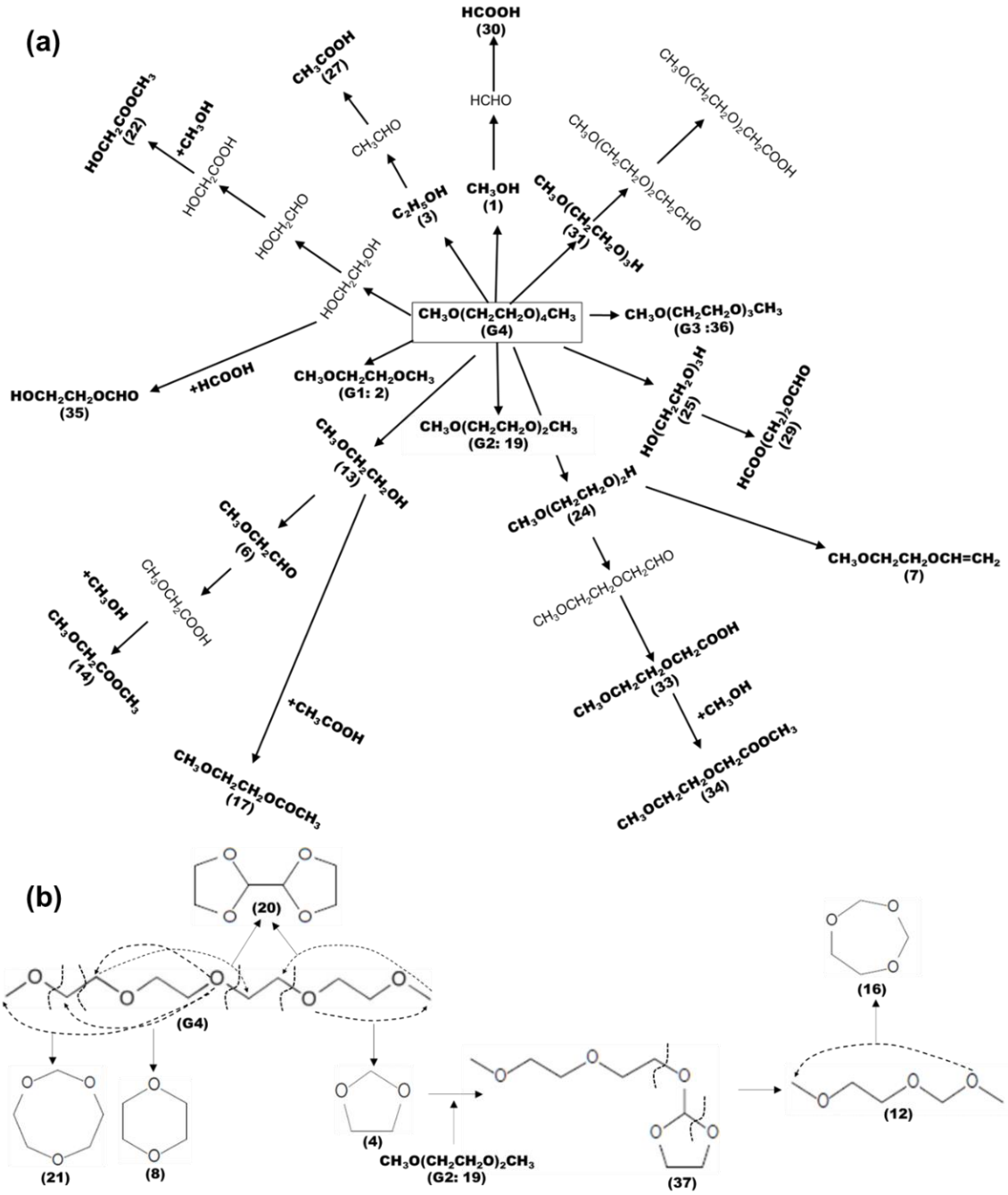

Scheme 5-1. Possible generation routes of various products from TEGDME: (a) Fragments of TEGDME and their relatively simple derivatives such as alcohols, aldehyde, acids, esters, etc. (b) More complicated molecules with ring structures.

References

1. Thackeray, M. M.; Wolverton, C.; Isaacs, E. D., Electrical energy storage for transportation—approaching the limits of, and going beyond, lithium-ion batteries. Energy & Environmental Science 2012, 5 (7), 7854-7863.

2. Kanamura, K. Large Scale Batteries for Green Energy Society. In *Electrochemical Science for a Sustainable Society: A Tribute to John O'M. Bockris*, Uosaki, K., Ed.; Springer, **2017** pp 175 – 193.

3. Winter, M.; Barnett, B.; Xu, K., Before Li ion batteries. Chemical reviews 2018, 118 (23), 11433-11456.

4. Li, M.; Lu, J.; Chen, Z.; Amine, K., 30 years of lithium-ion batteries. Advanced Materials 2018, 30 (33), 1800561.

5. Kwak, W.-J.; Rosy; Sharon, D.; Xia, C.; Kim, H.; Johnson, L. R.; Bruce, P. G.; Nazar, L. F.; Sun, Y.-K.; Frimer, A. A., Lithium–oxygen batteries and related systems: potential, status, and future. Chemical Reviews 2020, 120 (14), 6626-6683.

6. Imanishi, N.; Luntz, A. C.; Bruce, P. *The Lithium Air Battery: Fundamentals*; Springer, **2014**, pp 1-21.

7. Abraham, K.; Jiang, Z., A polymer electrolyte-based rechargeable lithium/oxygen battery. Journal of the Electrochemical Society 1996, 143 (1), 1.

8. Matsuda, S.; Ono, M.; Yamaguchi, S.; Uosaki, K., Criteria for evaluating lithium–air batteries in academia to correctly predict their practical performance in industry. Materials Horizons 2022, 9 (3), 856-863.

9. Aurbach, D.; McCloskey, B. D.; Nazar, L. F.; Bruce, P. G., Advances in understanding mechanisms underpinning lithium–air batteries. Nature Energy 2016, 1 (9), 1-11.

10. Kwak, W.-J.; Rosy; Sharon, D.; Xia, C.; Kim, H.; Johnson, L. R.; Bruce, P. G.; Nazar, L. F.; Sun, Y.-K.; Frimer, A. A., Lithium–oxygen batteries and related systems: potential, status, and future. Chemical Reviews 2020, 120 (14), 6626-6683.

11. Wu, Z.; Tian, Y.; Chen, H.; Wang, L.; Qian, S.; Wu, T.; Zhang, S.; Lu, J., Evolving aprotic Li–air batteries. Chemical Society Reviews 2022.

12. Girishkumar, G.; McCloskey, B.; Luntz, A. C.; Swanson, S.; Wilcke, W., Lithium− air battery: promise and challenges. The Journal of Physical Chemistry Letters 2010, 1 (14), 2193-2203.

13. Xu, W.; Xu, K.; Viswanathan, V. V.; Towne, S. A.; Hardy, J. S.; Xiao, J.; Nie, Z.; Hu, D.; Wang, D.; Zhang, J.-G., Reaction mechanisms for the limited reversibility of Li–O2 chemistry in organic carbonate electrolytes. Journal of Power Sources 2011, 196 (22), 9631-9639.

14. McCloskey, B. D.; Bethune, D.; Shelby, R.; Mori, T.; Scheffler, R.; Speidel, A.; Sherwood, M.; Luntz, A., Limitations in rechargeability of Li-O2 batteries and possible origins. The journal of physical chemistry letters 2012, 3 (20), 3043-3047.

15. Shao, Y.; Ding, F.; Xiao, J.; Zhang, J.; Xu, W.; Park, S.; Zhang, J. G.; Wang, Y.; Liu, J., Making Li-air batteries rechargeable: Material challenges. Advanced Functional Materials 2013, 23 (8), 987-1004.

16. Yao, X.; Dong, Q.; Cheng, Q.; Wang, D., Why do lithium–oxygen batteries fail: parasitic chemical reactions and their synergistic effect. Angewandte Chemie International Edition 2016, 55 (38), 11344-11353.

17. Laoire, C. O.; Mukerjee, S.; Abraham, K.; Plichta, E. J.; Hendrickson, M. A., Influence of nonaqueous solvents on the electrochemistry of oxygen in the rechargeable lithium− air battery. The Journal of Physical Chemistry C 2010, 114 (19), 9178-9186.

18. Freunberger, S. A.; Chen, Y.; Peng, Z.; Griffin, J. M.; Hardwick, L. J.; Bardé, F.; Novák, P.; Bruce, P. G., Reactions in the rechargeable lithium–O2 battery with alkyl carbonate electrolytes. Journal of the American Chemical Society 2011, 133 (20), 8040-8047.

19. Black, R.; Adams, B.; Nazar, L., Non-aqueous and hybrid Li-O2 batteries. Advanced Energy Materials 2012, 2 (7), 801-815.

20. Lu, Y.-C.; Gallant, B. M.; Kwabi, D. G.; Harding, J. R.; Mitchell, R. R.; Whittingham, M. S.; Shao-Horn, Y., Lithium–oxygen batteries: bridging mechanistic understanding and battery performance. Energy & Environmental Science 2013, 6 (3), 750-768.

21. Liu, T.; Vivek, J. P.; Zhao, E. W.; Lei, J.; Garcia-Araez, N.; Grey, C. P., Current challenges and routes forward for nonaqueous lithium–air batteries. Chemical reviews 2020, 120 (14), 6558-6625.

22. Wang, F.; Li, X.; Xie, Y.; Lai, Q.; Tan, J., Effects of Porous Structure on Oxygen Mass Transfer in Air Cathodes of Nonaqueous Metal–Air Batteries: A Mini-review. ACS Applied Energy Materials 2022, 5 (5), 5473-5483.

23. Song, C.; Ito, K.; Sakata, O.; Kubo, Y., Operando structural study of non-aqueous Li–air batteries using synchrotron-based X-ray diffraction. RSC advances 2018, 8 (46), 26293-26299.

24. Yao, K. P.; Kwabi, D. G.; Quinlan, R. A.; Mansour, A. N.; Grimaud, A.; Lee, Y.-L.; Lu, Y.-C.; Shao-Horn, Y., Thermal stability of Li2O2 and Li2O for Li-air batteries: in situ XRD and XPS studies. Journal of The Electrochemical Society 2013, 160 (6), A824.

25. Gittleson, F. S.; Yao, K. P.; Kwabi, D. G.; Sayed, S. Y.; Ryu, W. H.; Shao-Horn, Y.; Taylor, A. D., Raman spectroscopy in lithium–oxygen battery systems. ChemElectroChem 2015, 2 (10), 1446-1457.

26. Tomita, K.; Noguchi, H.; Uosaki, K., Effect of Water and HF on the Distribution of Discharge Products at Li–O2 Battery Cathode. ACS Applied Energy Materials 2018, 1 (7), 3434-3442.

27. McCloskey, B. D.; Bethune, D. S.; Shelby, R. M.; Girishkumar, G.; Luntz, A. C., Solvents' critical role in nonaqueous lithium–oxygen battery electrochemistry. The Journal of Physical Chemistry Letters 2011, 2 (10), 1161-1166.

28. Marchini, F.; Herrera, S.; Torres, W.; Tesio, A. Y.; Williams, F. J.; Calvo, E. J., Surface study of lithium–air battery oxygen cathodes in different solvent–electrolyte pairs. Langmuir 2015, 31 (33), 9236-9245.

29. Ue, M.; Asahina, H.; Matsuda, S.; Uosaki, K., Material balance in the O 2 electrode of Li–O 2 cells with a porous carbon electrode and TEGDME-based electrolytes. RSC advances 2020, 10 (70), 42971-42982.

30. Naitoh, K.; Inai, Y.; Hirabayashi, T.; Tsuda, T., Direct temperature-controlled trapping system and its use for the gas chromatographic determination of organic vapor released from human skin. Analytical chemistry 2000, 72 (13), 2797-2801.

31. Giordani, V.; Walker, W.; Bryantsev, V. S.; Uddin, J.; Chase, G. V.; Addison, D., Synergistic Effect of Oxygen and LiNO3 on the Interfacial Stability of Lithium Metal in a Li/O2 Battery. Journal of The Electrochemical Society 2013, 160 (9), A1544.

Chapter 6 General conclusions and future prospects

In this thesis, the degradation mechanism of LOB using 1 M LiTFSI in TEGDME as the electrolyte was investigated in-situ using on-line QMS and CTPC-GC/MS, and ex-situ post-analysis of organic compounds, which were collected by adsorption in small columns during the discharge and charge, using TSP-GC/MS.

In **Chapter 3**, on-line QMS and TSP-GC/MS were employed for real-time monitoring of generated gaseous products during charging. To qualitatively understand the energetics of the product formation during charging process, a linear voltage sweep (LSV: 0.05 mV s^{-1}) and voltage step modes were employed in additional to constant current charging. The presence of two distinctly different types of Li_2O_2, one being decomposed in wide range of relatively low voltages (2.8 – 4.2 V) (l-Li_2O_2) and the other being decomposed at higher voltage of around 4.2 V (h-Li_2O_2), was confirmed by both LSV and step experiments. H_2O generation started when O_2 generation reached a peak, and around 50% O atom in H_2O originated from the discharge gas, the other 50% O atom in H_2O originated from the solvent decomposition or the initial water amount in the electrolyte. CO_2 generation took place accompanied with the decomposition of h-Li_2O_2, and around 70% O atom in CO_2 originated from the discharge gas, the 30% originated from the solvent decomposition.

In **Chapter 4**, on-line QMS was introduced combining with isotope experiments, to follow and analysis products generation during charging process. $^{12}CD_3$_TEGDME, $^{13}CH_3$_TEGDME and $^{12}CH_3$_TEGDME were used as solvent, and $^{18}O_2$ and $^{16}O_2$ were used as the discharge gas. A total of 17 compounds were identified as the battery reaction products by mass spectrometry. From the detected products, battery degradation products can be divided into two types: generates from high overpotential induced degradation reactions (electrochemical reactions), such as *1,4-Dioxane*, *Methylal*, and *Methoxyethene*, and active species triggered decomposition reactions (chemical reactions), such as *Methanol*, *Ethanol*, etc. Notably, some degradation products are generated by both of the two reactions, such as *Methyl formate*.

In **Chapter 5**, on-line CTPC-GC/MS system was constructed to detect reaction products of LABs during discharge and charging in real-time with high accuracy. During cell operation, the generation of organic molecules was tracked over time by repeatedly sampling the cell's headspace gas for very short periods of time, such as 15 s, and for a fixed period of time, such as 40 min. By controlling the sampling time and period, loss of generated molecules by gas flow can be minimized. The CTPC-GC/MS system was operated under constant-current discharge and constant-current or voltage-sweep charging. A total of 37 peaks were detected and 27 of them were assigned to specific molecules. Several molecules were present as impurities in TEGDME even before discharge and a few molecules were generated during discharge but most of the

molecules were generated during charging. The results obtained under voltage scan without discharge showed that some of the molecules generated at the end of charging were also generated without discharge, indicating these molecules were formed by direct electrochemical oxidation without involvement of reactive oxygen.

Degradation of TEGDME in LOB during discharge/charge was investigated by monitoring the generation and decomposition molecules in real-time by mass spectrometry systems. Most of the molecules were generated during charge as a result of the degradation of TEGDME by reactive oxygens and electrochemical oxidation. These molecules were decomposed during discharge by reactive oxygens. In the future, ①more molecules assignment will be kept on going for more detailed degradation mechanism, mass spectrometry systems were committed to applying to the degradation of various electrolytes. ②Researches on the effect of various additives and singlet oxygen quenchers in inhibiting battery degradation will be conducted. ③Many ex-situ and operand techniques such as SEM, TEM, XPS, surface enhanced Raman scattering (SERS), etc. will be introduced into subsequent studies to characterize the reaction mechanism of the cell more intuitively.

Appendix I

Ionization table 1

	C0			C1					C1		C1
	H0			H0	H2		H4		D3	D4	H4
	O2		O1	O1	O2		O1		O		O0
molecule	16O2	18O2	H2O	CO	CO2	HCOOH	HCHO	CH3OH	CD3OH	CD3OD	CH4
MW	32		18	28	44	46	30	32	35	36	16
b.p./°C	-183		100	-191.5	-78.48	100.72	-21.11	64.61	65	65.4	-161.5
vapor pressure(25° C)/kPa	> 1000		3.17	2E+07	6439.5	5.68	518.62	16.93	2.8 - 20°	2.9 - 20°	62128.23
2								0.30			
12				4.7	8.71	3.30	1.00	0.20	0.50005	0.70007	3.8
13						2.90	1.00	0.60			10.69
14						0.40	1.00	1.69	1.10011	1.49015	20.42
15							2.00	12.39	0.40004		88.8
16	21.903		0.90	1.7	9.61	5.20		0.10	3.30033	4.59046	100
17			21.22			17.12		0.30	1.80018		1.64
18			100.00					0.70	26.1226	29.993	
19			0.50			0.20		0.10			
20			0.30								
22					1.9						
28				100	9.81	17.22	24.00	4.59	4.10041	6.79068	
29				1.2	0.1	100.00	100.00	44.59	6.71067	0.10001	
30						1.70	58.01	6.49	39.644	50.6951	
31						0.60	0.50	100.00	4.30043	0.50005	
32	100	0.419				0.20		74.40	5.0005	5.79058	
33	0.0744	0						1.19	100	0.10001	
34	0.409	1.586						0.10	10.6111	100	
35		0.286							71.6672	1.10011	
36		100							2.80028	70.5971	
37									1.40014	0.80008	
44					100	10.01					
45					1.2	47.64					
46					0.4	60.96					
47						1.00					
48						0.30					

Appendix I

Ionization table 2

	C_2					
	H_4					
	O_1	$O2$		O_0	O_1	
molecule	CH3CHO	CH3COOH	CH3OCHO	C2H6	C2H5OH	CH3OCH3
MW	44	60	60	30	46	46
b.p./°C	20.2	117.77	31.50	-88.6	78.20	-24.8
vapor pressure(25° C)/kPa	120.25	2.09	78.09	4194.18	7.91	593.28
2		0.20		0.20		
12	0.90	0.60	0.40	0.40	0.20	0.20
13	2.99	2.09	0.90	1.00	1.39	0.70
14	10.89	4.89	2.09	3.00	1.45	2.20
15	36.49	17.09	18.79	4.40	6.64	24.12
16	5.69	2.39	0.30	0.10		1.10
17	0.30	0.99	0.30		0.70	0.50
18	1.09	2.79	0.99		0.55	0.30
19	0.10				2.79	0.10
24	0.70	0.20		0.50	0.61	
25	2.39	0.40		3.50	2.46	
26	5.49	0.50		23.22	9.85	
27	3.59	0.10		33.23	22.41	0.20
28	3.29	4.09	4.89	100.00	3.45	1.00
29	100.00	8.49	45.49	21.52	29.85	38.73
30	1.19	0.40	6.09	26.22	8.12	1.10
31	0.30	2.49	100.00	0.50	100.00	3.40
32		0.10	45.79			0.10
33			0.80		0.31	
40	1.09	0.80				
41	5.09	3.59			1.37	0.10
42	12.79	13.09	0.10		4.74	0.30
43	47.49	100.00	0.40		11.44	1.40
44	82.60	2.49	1.39		0.71	0.60
45	2.79	90.40	0.99		51.50	100.00
46		1.09	0.10		21.63	60.76
47		0.20			0.73	1.30
55		0.10				
56			0.10			
57		0.20				
59			0.70			
60		74.80	37.99			
61		1.99	0.99			
62		0.20	0.20			

Appendix I

Ionization table 3

	C3				C4
	H6		H8		H8
		O1	O2	O1	O2
molecule	ring	CH3OC2H3	CH3OCH2OCH3	CH3OC2H5	ring
MW	74	58	76	60	88
b.p./°C	78	5.5	41.60	7.4	101
vapor pressure(25° C)/kPa	10.53	175.45	53.30	199.05	5.08
2					
12	0.20	4.00	0.90	1.00	0.21
13	0.80	9.71	2.00	2.40	0.49
14	3.99	24.62	6.51	6.81	3.00
15	21.49	100.00	41	25.02	9.11
16	3.69	0.80	1.30	0.90	0.40
17	0.20	0.10	0.90	0.60	0.10
18	0.90	0.20	0.10	0.10	0.22
19	4.49			0.10	0.38
24		1.30		0.20	0.11
25	0.30	5.61		1.10	
26	2.09	28.93	0.10	8.01	9.68
27	11.19	60.26	0.20	20.42	19.01
28	2.19	65.97	2.30	7.91	100.00
29	43.89	62.87	43.84	49.04	41.03
30	2.49	5.61	3.10	3.40	14.57
31	7.29	40.34	11.71	19.92	19.11
32	0.50	2.60	0.60	2.10	0.51
33		0.20	0.20	1.90	
34				0.10	
35		0.10			
36	0.40	0.20			
37		0.10		0.10	
38		0.20	0.10	0.10	
39		0.60		0.20	0.45
40	0.10	0.80	0.10	0.10	0.20
41	0.40	2.70	0.10	0.80	0.98
42	4.29	19.92	0.30	1.70	3.57
43	21.39	68.57	0.80	6.91	17.15
44	63.70	1.80	2.20	0.80	6.87
45	29.79	0.20	100.00	100.00	6.00
46	0.80		2.20	2.30	0.19
47	0.10		3.20	0.20	
52		0.10			
53		0.10			
54		0.10			
55		0.50		0.10	0.20
56		0.20		0.10	
57		4.70		0.20	13.18
58		77.58		0.50	40.81
59		2.70	0.10	10.81	2.01
60		0.20		25.82	0.16
61				0.90	0.12
62				0.10	
69					0.16
71	0.40				
72	0.10				
73	100.00				
74	5.69				
75	0.60		43.74		
76			1.40		
77			0.20		
87					6.13
88					52.08
89					2.26
90					0.36

Appendix II

Isotope experiments mass behavior of m/z = 12~25. Table 1

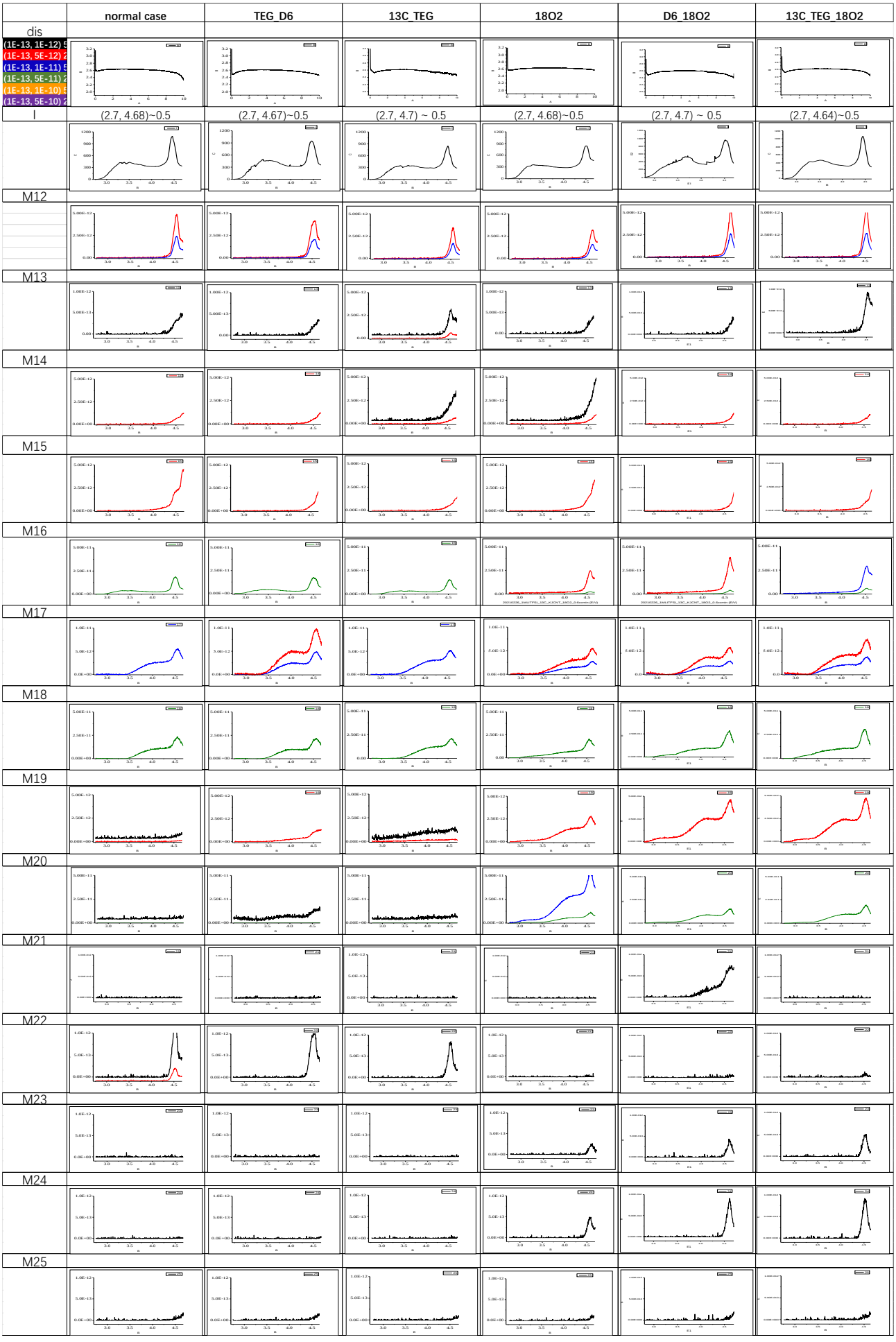

Appendix II

Isotope experiments mass behavior of m/z = 26~42. Table 2

	normal case	TEG_D6	13C_TEG	18O2	D6_18O2	13C_TEG_18O2
M26	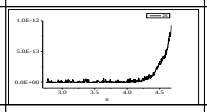	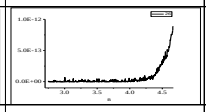	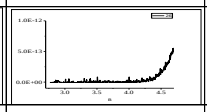	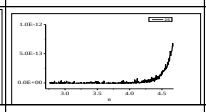	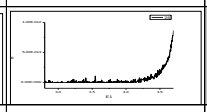	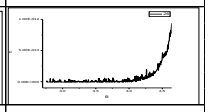
M27	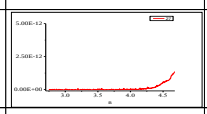	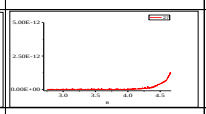	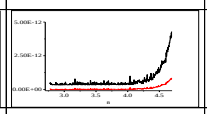	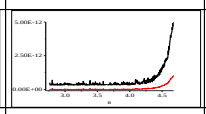	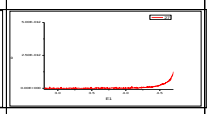	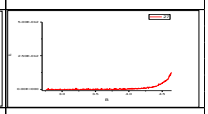
M28	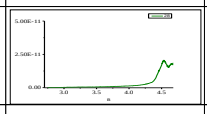	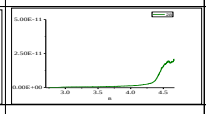	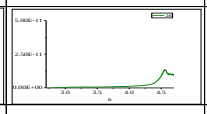	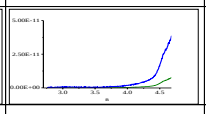	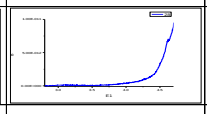	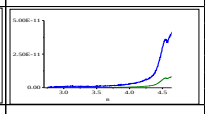
M29	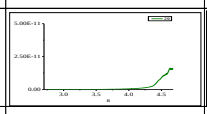	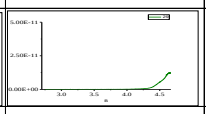	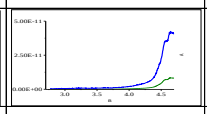	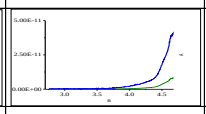	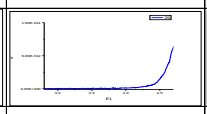	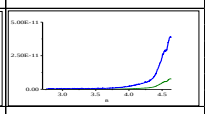
M30	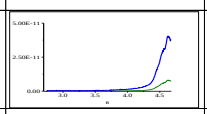	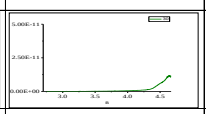	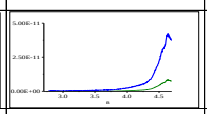	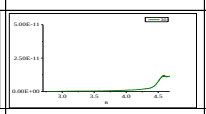	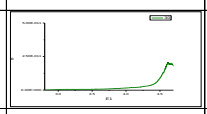	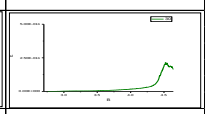
M31	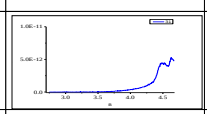	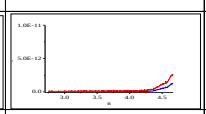	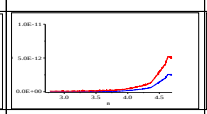	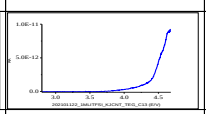	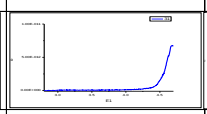	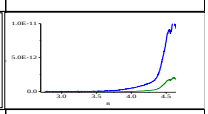
M32	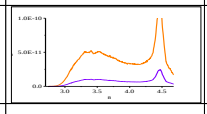	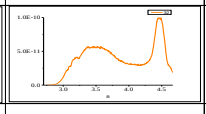	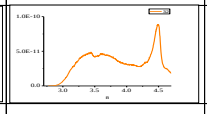	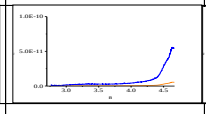	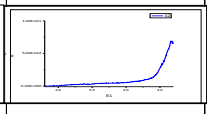	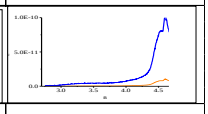
M33	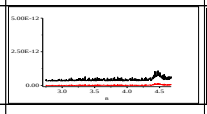	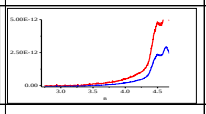	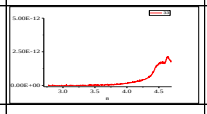	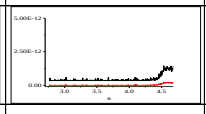	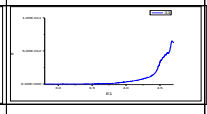	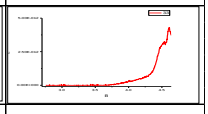
M34	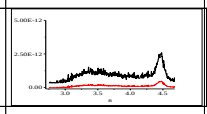	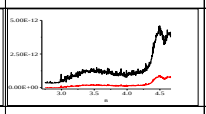	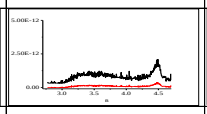	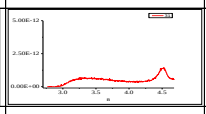	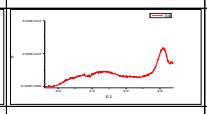	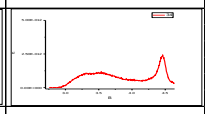
M35	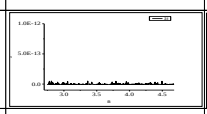	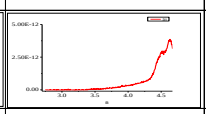	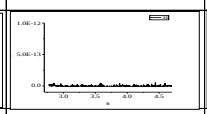	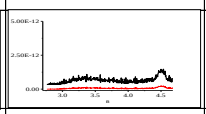	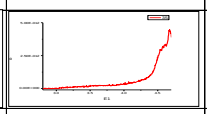	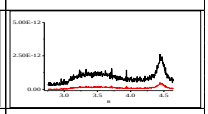
M36	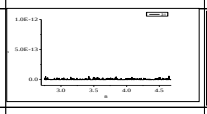	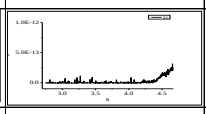	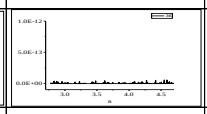	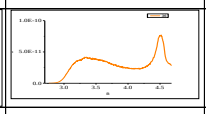	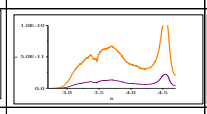	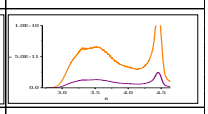
M37	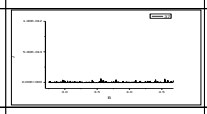	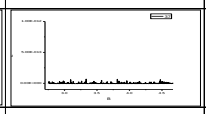	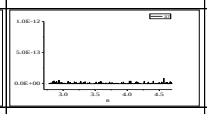	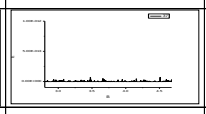	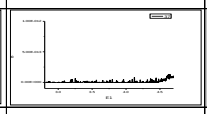	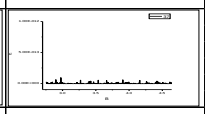
M39	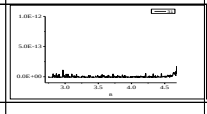	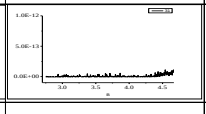	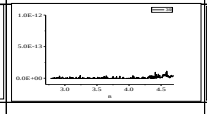	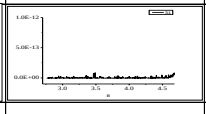	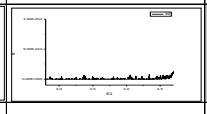	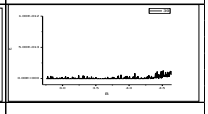
M40	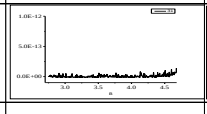	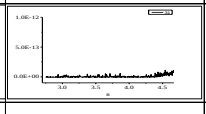	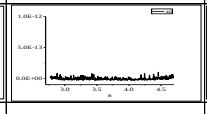	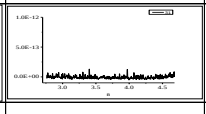	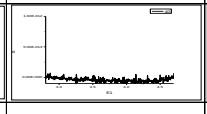	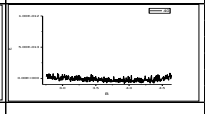
M41	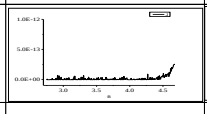	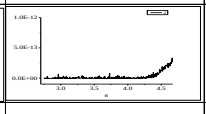	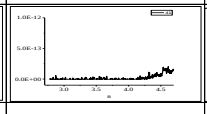	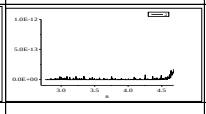	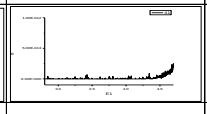	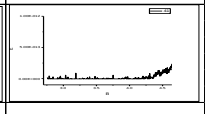
M42	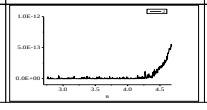	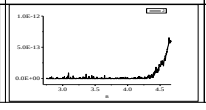	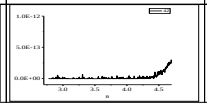	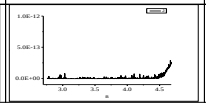	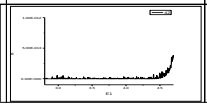	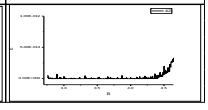

Appendix II

Isotope experiments mass behavior of m/z = 43~61. Table 3

	normal case	TEG_D6	13C_TEG	18O2	D6_18O2	13C_TEG_18O2
M43	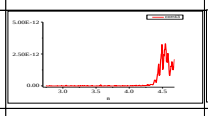	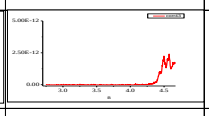	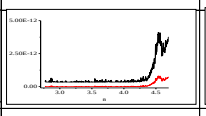	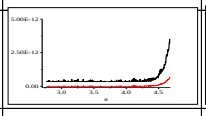	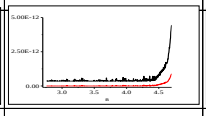	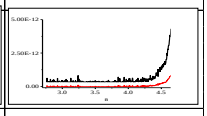
M44	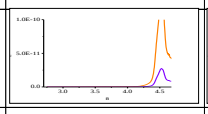	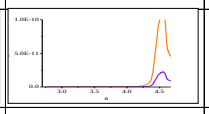	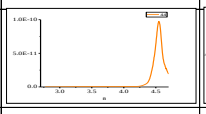	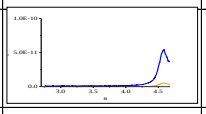	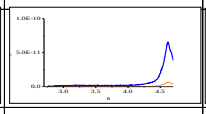	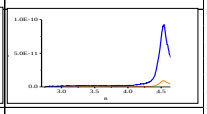
M45	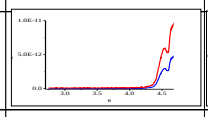	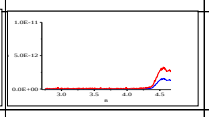	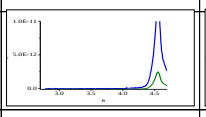	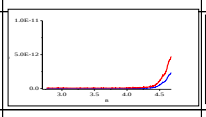	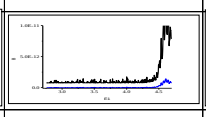	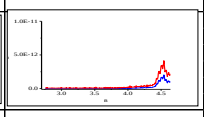
M46	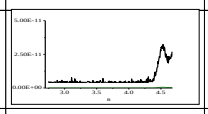	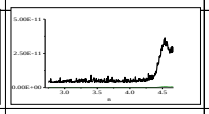	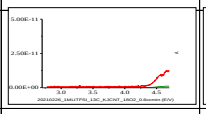	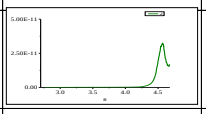	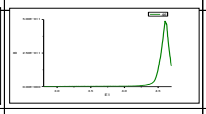	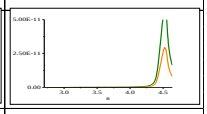
M47	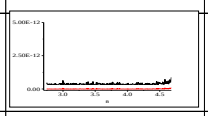	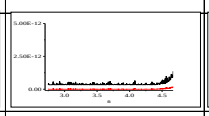	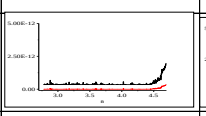	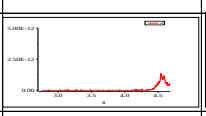	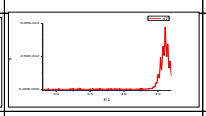	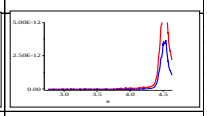
M48	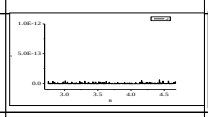	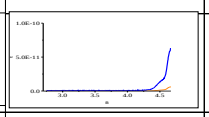	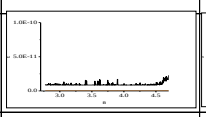	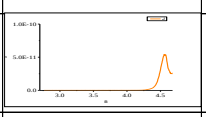	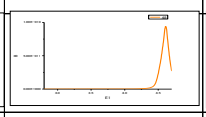	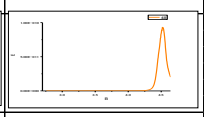
M49	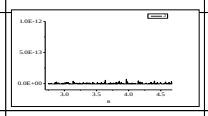	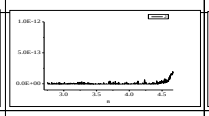	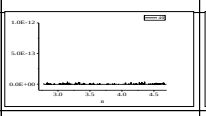	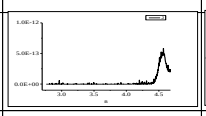	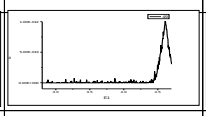	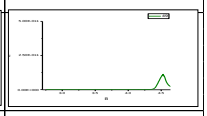
M50	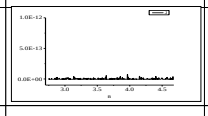	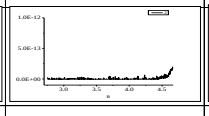	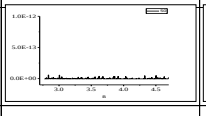	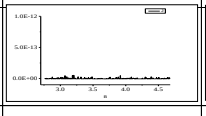	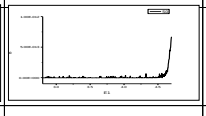	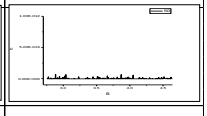
M52	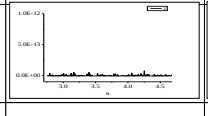	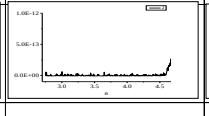	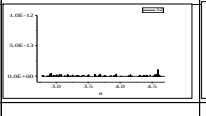	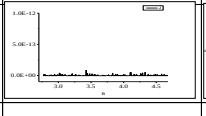	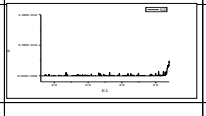	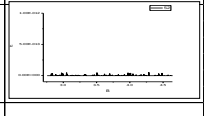
M53	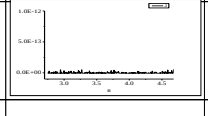	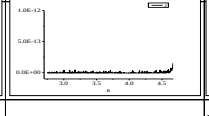	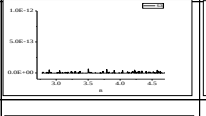	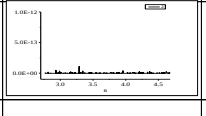	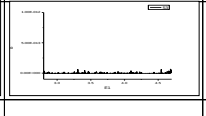	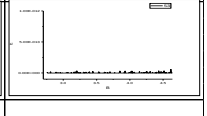
M56	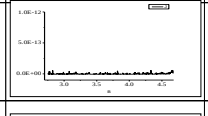	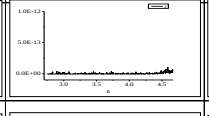	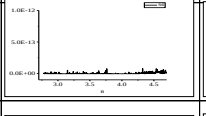	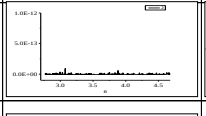	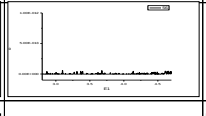	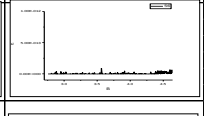
M57	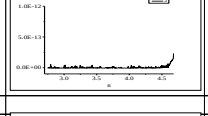	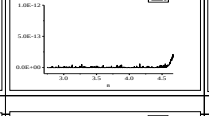	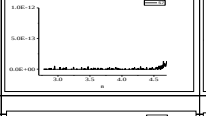	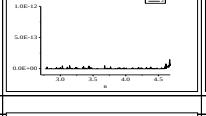	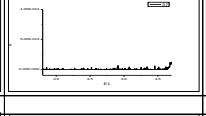	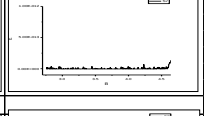
M58	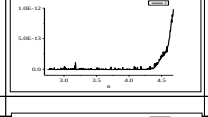	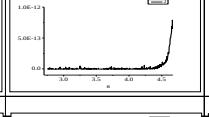	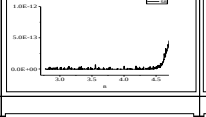	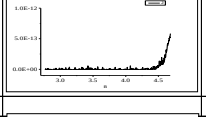	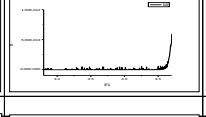	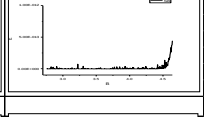
M59	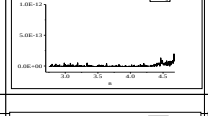	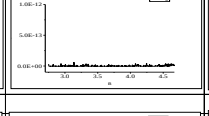	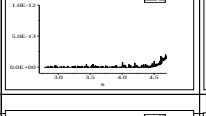	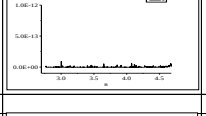	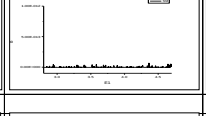	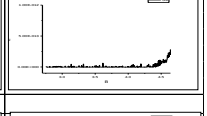
M60	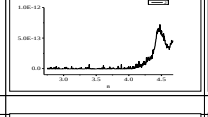	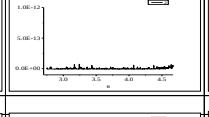	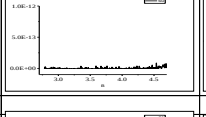	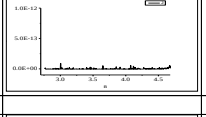	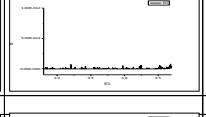	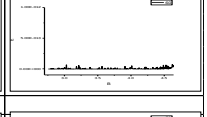
M61	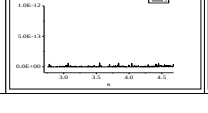	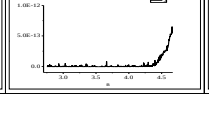	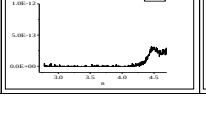	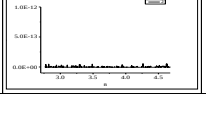	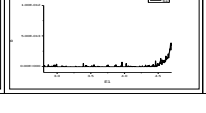	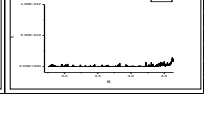

Appendix II

Isotope experiments mass behavior of m/z = 62~88. Table 4

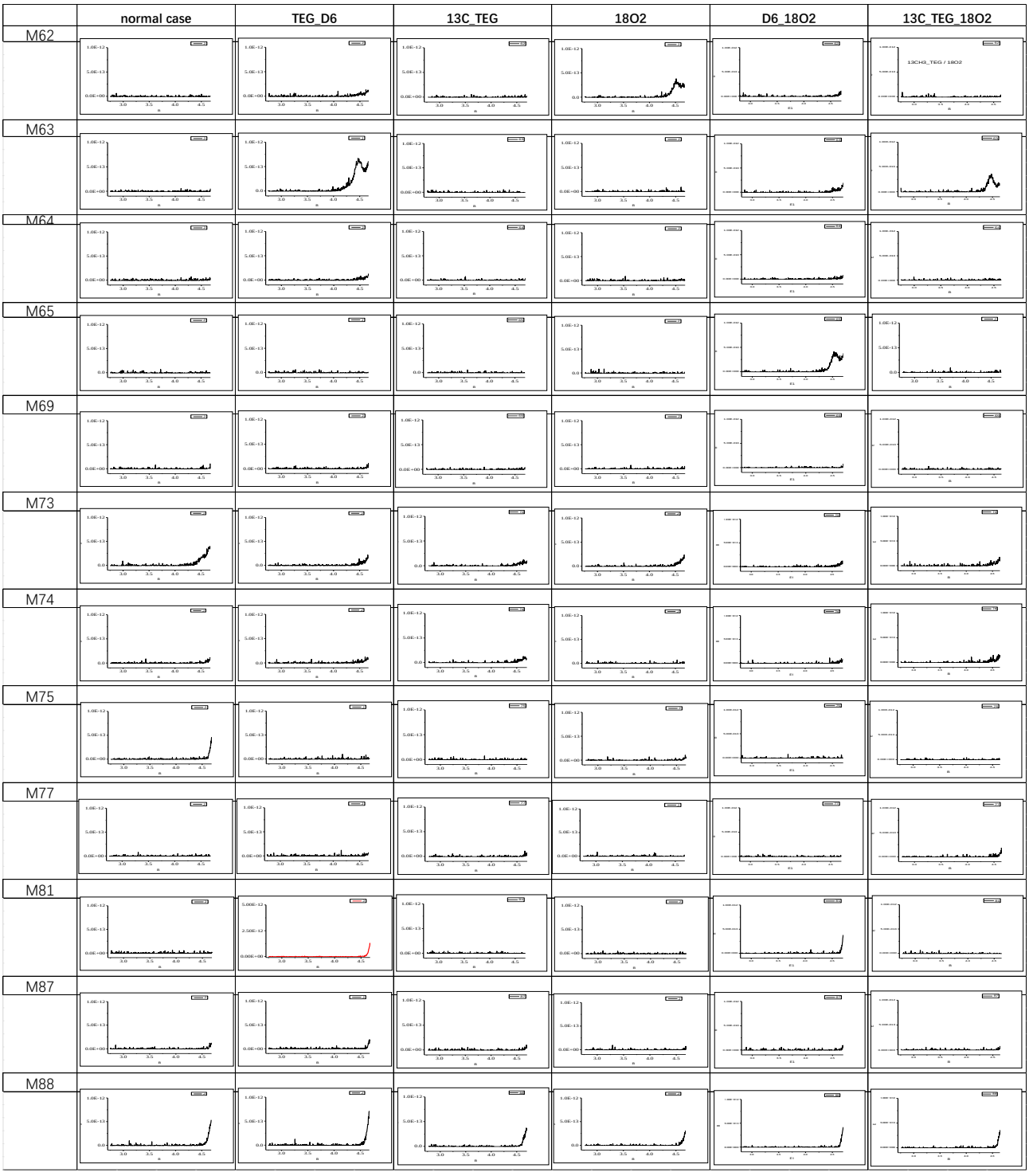

The different color line represents different Y-axis scale.

black line ~ (0, 1E-12) 5E-13,

red line ~ (0, 5E-12) 2.5E-12,

blue line ~ (0, 1E-11) 5E-12,

green line ~ (0, 5E-11) 2.5E-11,

orange line ~ (1E-13, 1E-10) 5E-11,

purple line ~ (1E-13, 5E-10) 2.5E-10.

Appendix III

Assignment process of oxygen/carbon dioxide/water/1,4-Dioxane/ Methylal, of m/z = 12~30

table 1-1

	normal case	O2_32	CO2_44	H2O_18	ring_88	CH3OCH2OCH3_75
M12		M12-M44*0.033				
	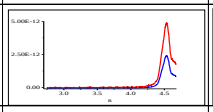	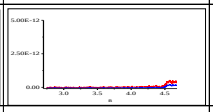	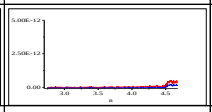	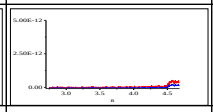	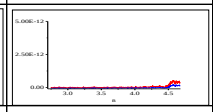	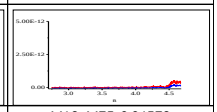
M13						M13-M75*0.04572
	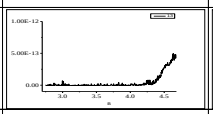	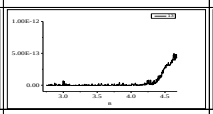	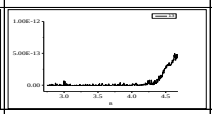	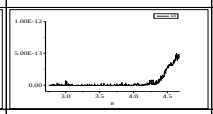	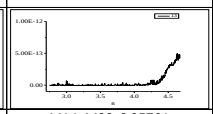	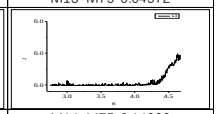
M14					M14-M88*0.05761	M14-M75*0.14883
	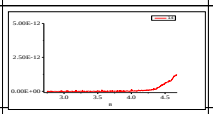	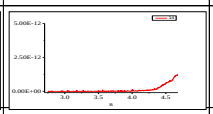	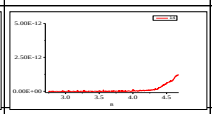	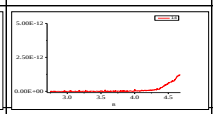	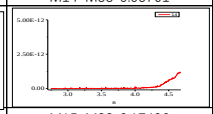	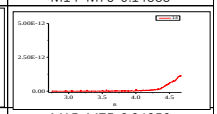
M15					M15-M88*0.17496	M15-M75*0.94056
	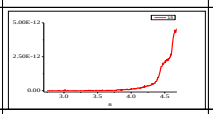	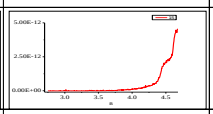	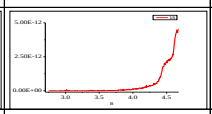	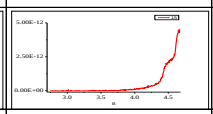	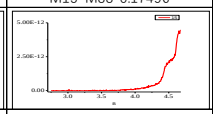	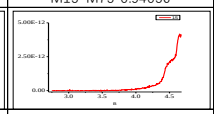
M16		M16-M32*0.075	M16-M44*0.0075	M16-0.0009*M18		
	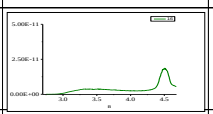	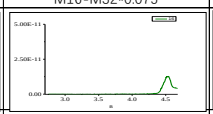	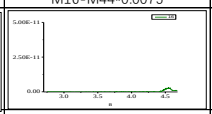	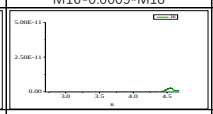	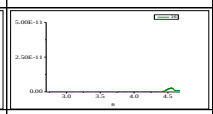	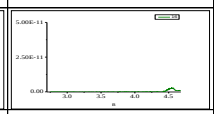
M17				M17-M18*0.243		
	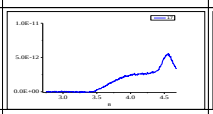	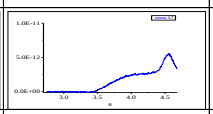	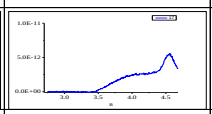	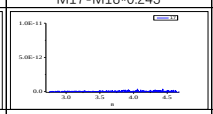	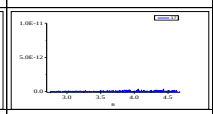	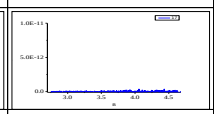
M18						
	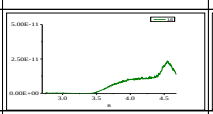	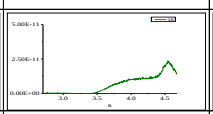	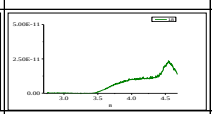	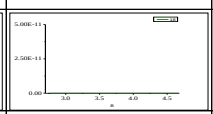	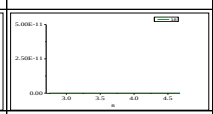	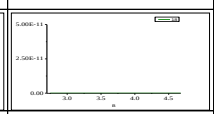
M19						
	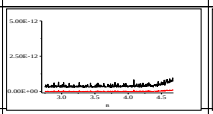	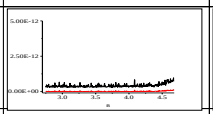	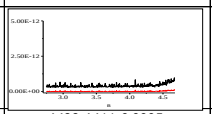	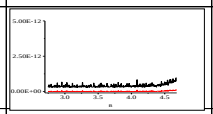	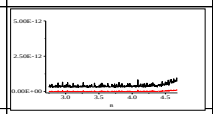	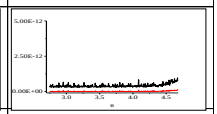
M22			M22-M44*0.0095			
	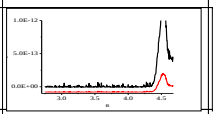	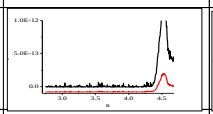	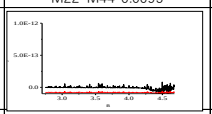	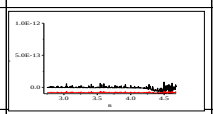	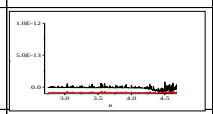	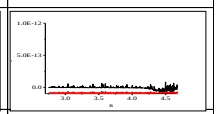
M25						
	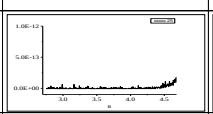	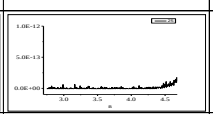	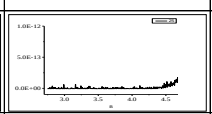	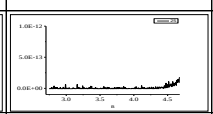	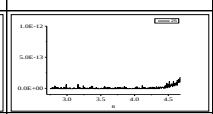	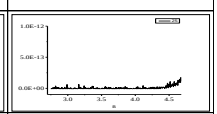
M26					M26-M88*0.1859	
	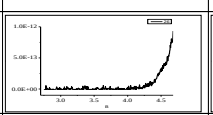	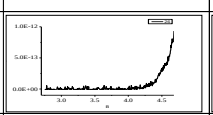	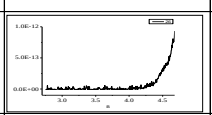	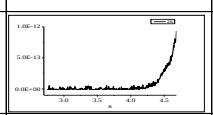	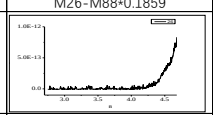	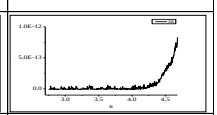
M27					M27-M88*0.36509	
	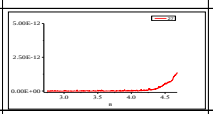	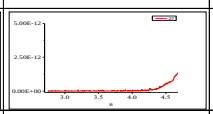	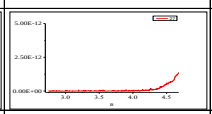	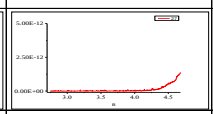	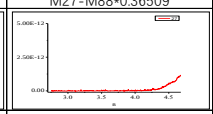	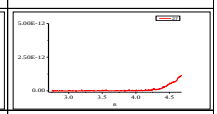
M28			M28-M44*0.09		M28-M88*1.9203	M28-75*0.05258
	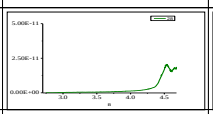	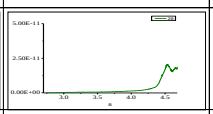	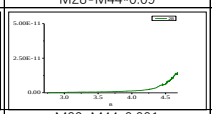	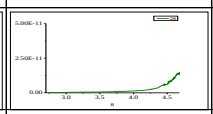	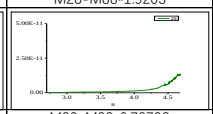	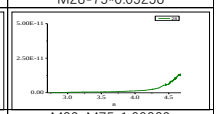
M29			M29-M44*0.001		M29-M88*0.78798	M29-M75*1.00229
	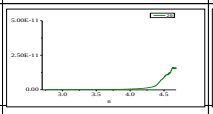	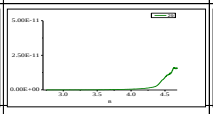	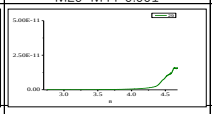	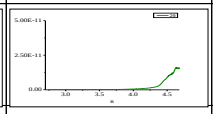	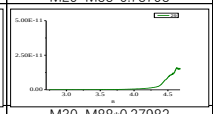	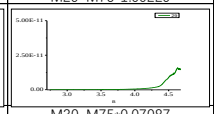
M30					M30-M88*0.27982	M30-M75*0.07087
	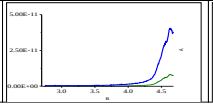	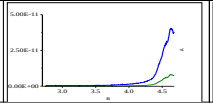	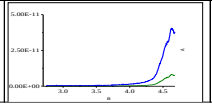	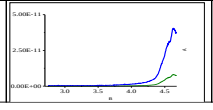	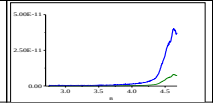	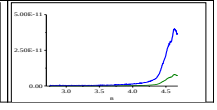

Appendix III

Assignment process of oxygen/carbon dioxide/water/1,4-Dioxane/ Methylal, of m/z = 31~57

table 1-2

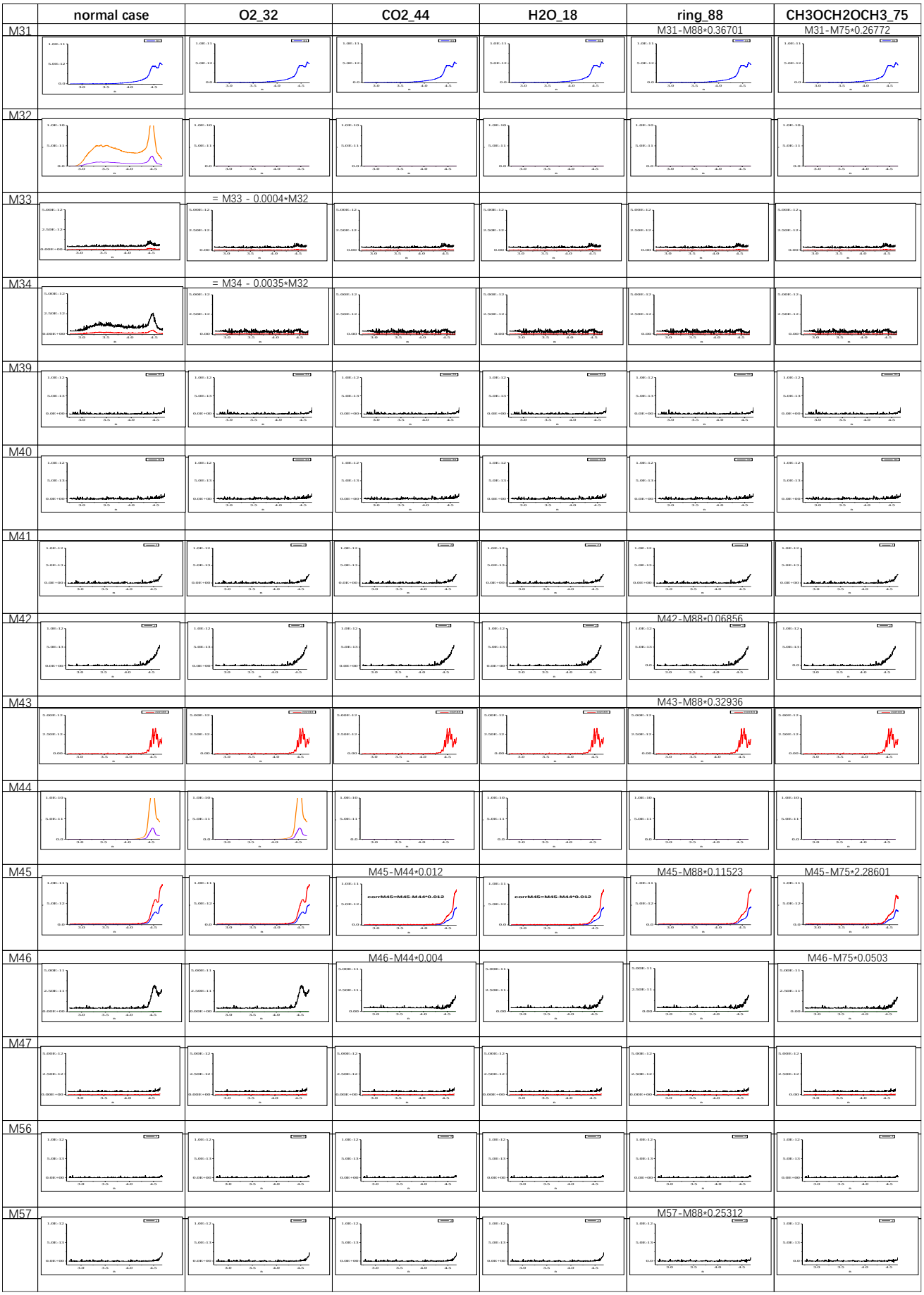

Appendix III

Assignment process of oxygen/carbon dioxide/water/1,4-Dioxane/ Methylal, of m/z = 58~88

table 1-3

	normal case	O2_32	CO2_44	H2O_18	ring_88	CH3OCH2OCH3_75
M58					M58-M88*0.78375	
M59					M59-M88*0.0386	
M60						
M73						
M74						
M75						
M87					M87-M88*0.11773	
M88						

Appendix III

Assignment process of 1,3-dioxolane/Methyl formate/Methoxyethene/Ethanol/Dimethyl ether/Methoxyethane, of m/z = 12~30 table 2-1

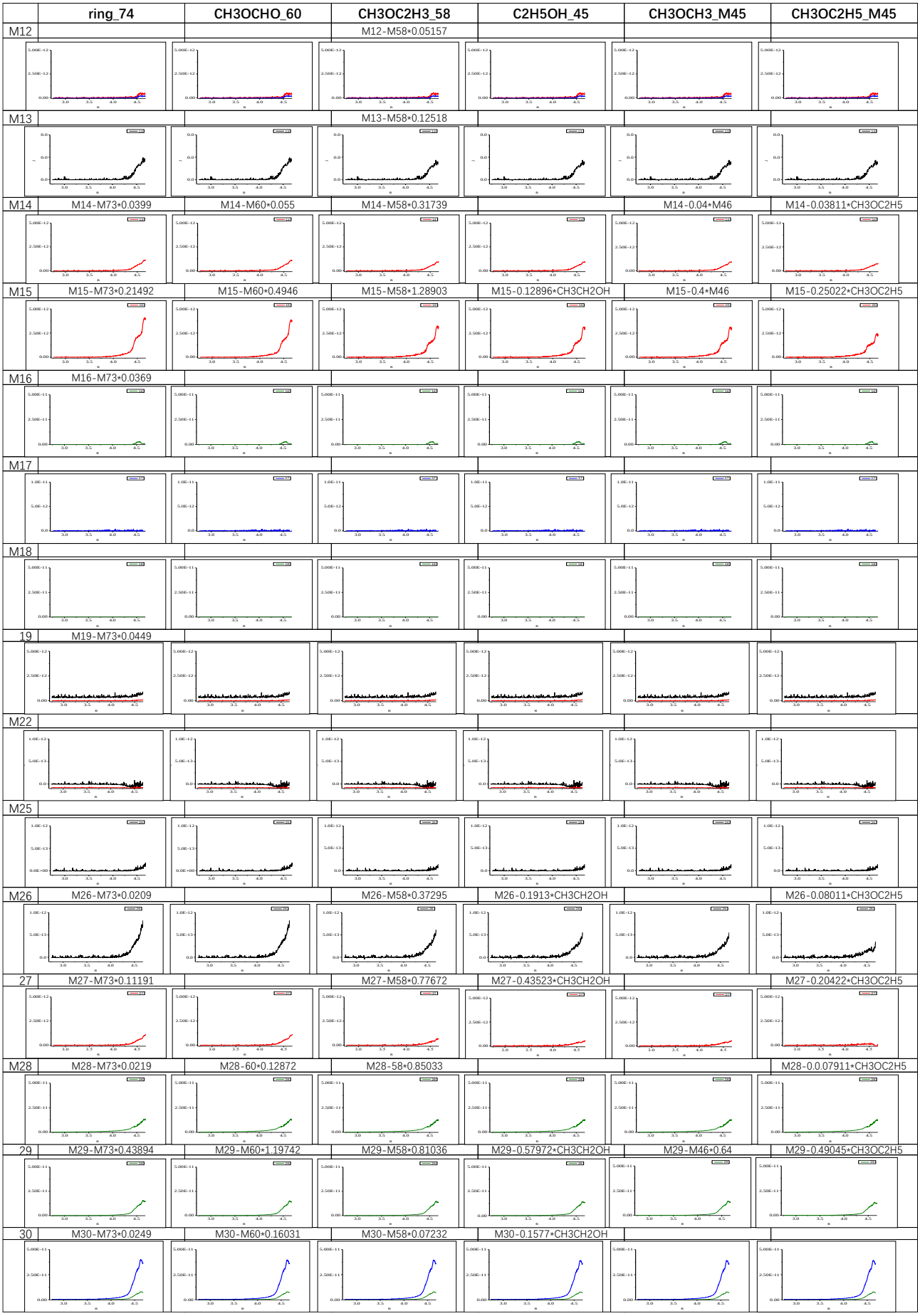

Appendix III

Assignment process of 1,3-dioxolane/Methyl formate/Methoxyethene/Ethanol/Dimethyl ether/Methoxyethane, of m/z = 31~57 table 2-2

	ring_74	CH3OCHO_60	CH3OC2H3_58	C2H5OH_45	CH3OCH3_M45	CH3OC2H5_M45
M31	M31-M73*0.07291	M31-M60*2.63201	M31-M58*0.52005	M31-1.94193*CH3CH2OH		M31-0.0.19922*CH3OC2H5
M32						
M33						
M34						
M39						
M40						
M41						
M42	M42-M73*0.0429		M42-M58*0.2568			
M43	M43-M73*0.21392		M43-M58*0.88385	M43-0.22218*CH3CH2OH		M43-0.06911*CH3OC2H5
M44						
M45	M45-M73*0.29793	M45-M60*0.02606		M45-CH3CH2OH	M45-1.65*M46	M45-CH3OC2H5
M46				M46-0.42008*CH3CH2OH		
M47						
M56						
M57			M57-M58*0.06059			

Appendix III

Assignment process of 1,3-dioxolane/Methyl formate/Methoxyethene/Ethanol/Dimethyl ether/Methoxyethane, of m/z = 58~88 table 2-3

	ring_74	CH3OCHO_60	CH3OC2H3_58	C2H5OH_45	CH3OCH3_M45	CH3OC2H5_M45
M58						
	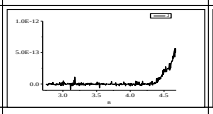	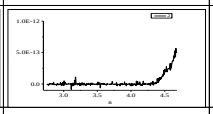	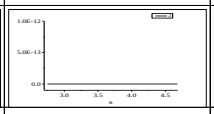	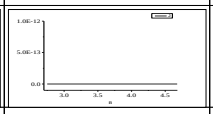	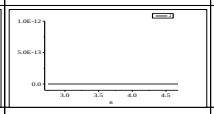	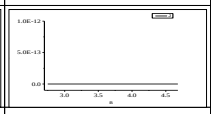
M59						
	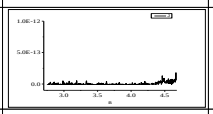	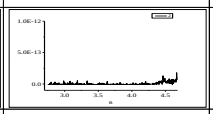	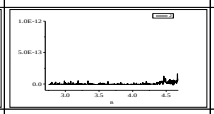	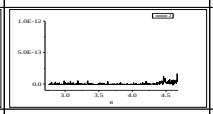	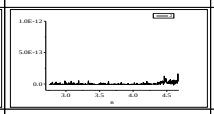	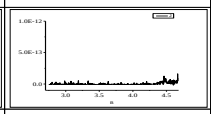
M60						
	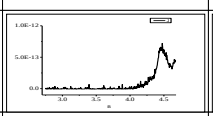	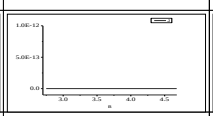	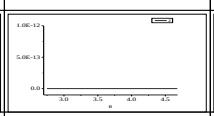	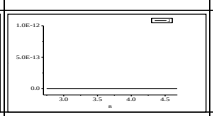	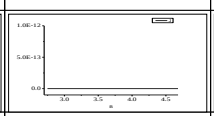	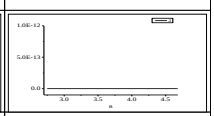
M73						
	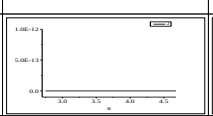	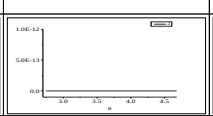	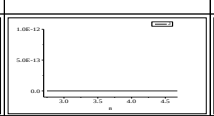	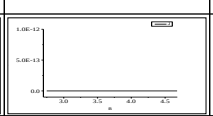	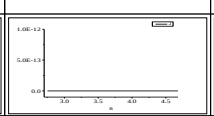	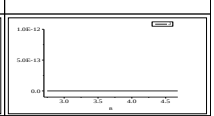
M74	M74-M73*0.05691					
	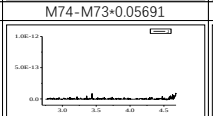	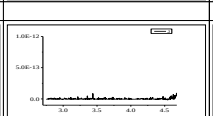	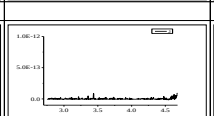	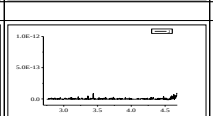	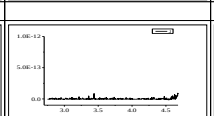	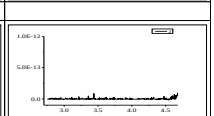
M75						
	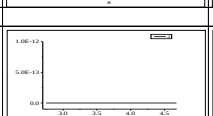	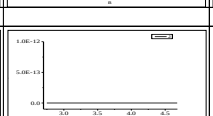	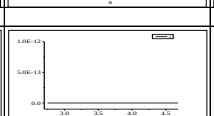	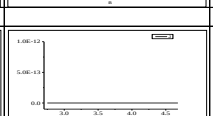	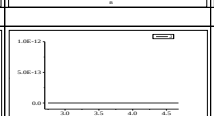	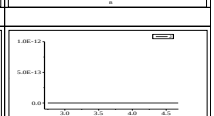
M87						
	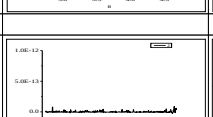	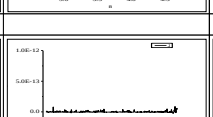	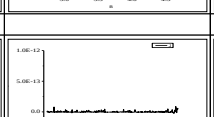	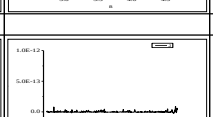	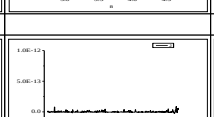	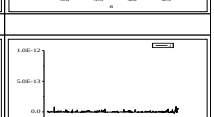
M88						
	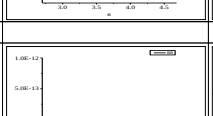	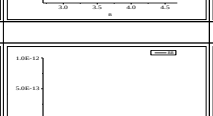	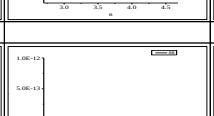	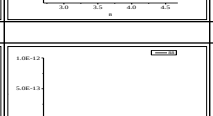	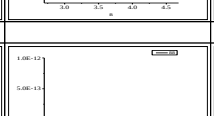	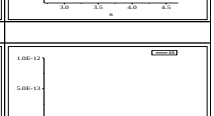

Appendix III

Assignment process of Acetic acid/Methanol/Ethane/Formaldehyde/Carbon monoxide/Methane, of m/z = 12~30

table 3-1

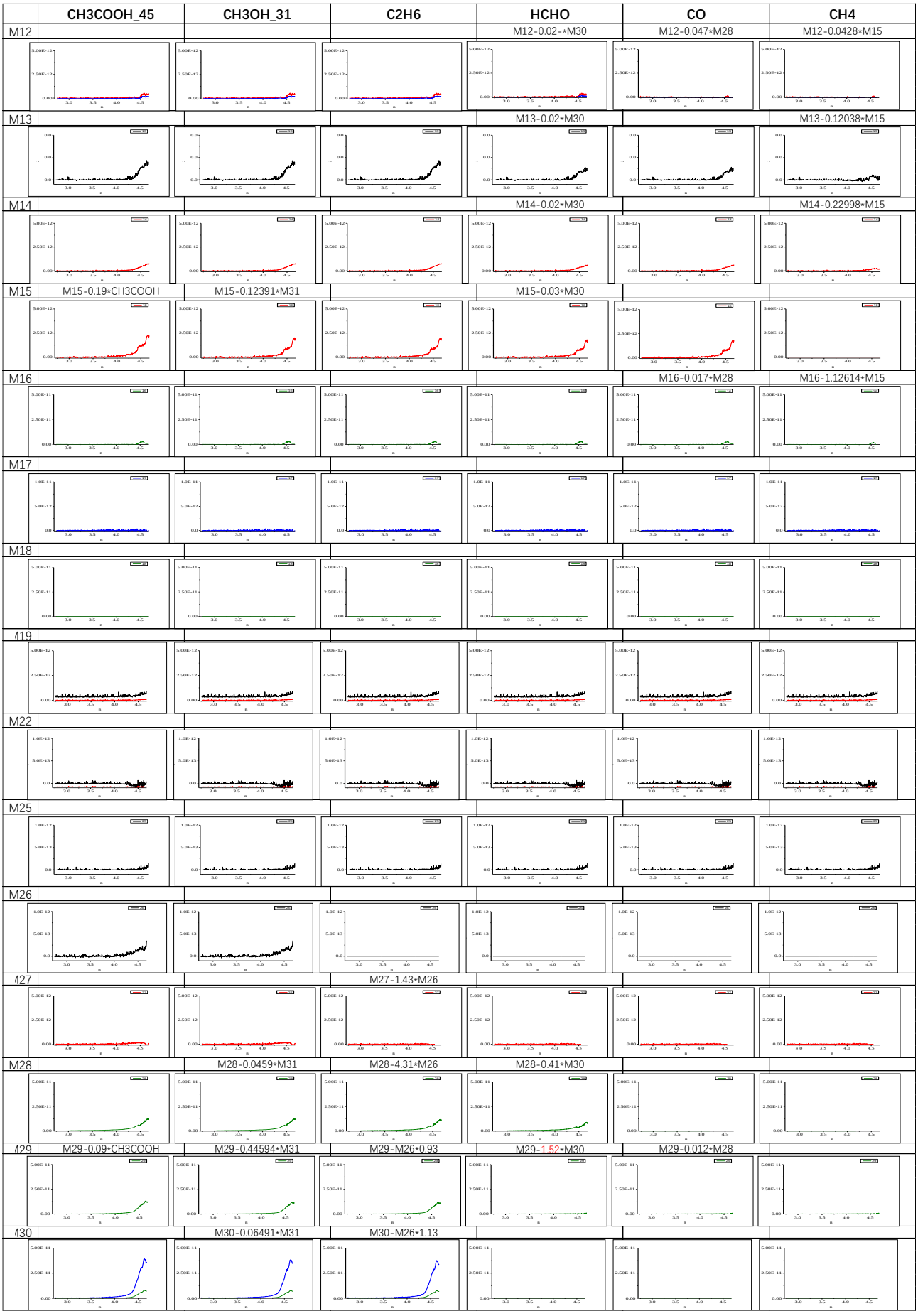

Appendix III

Assignment process of Acetic acid/Methanol/Ethane/Formaldehyde/Carbon monoxide/Methane, of m/z = 31~57

table 3-2

Appendix III

Assignment process of Acetic acid/Methanol/Ethane/Formaldehyde/Carbon monoxide/Methane, of m/z = 58~88

table 3-3